NIRS－M－84

特別研究「重粒子線によるがん治療法に関する調査研究」　論 文 集

第　2　集

（平成２年４月－平成３年３月）

放射線医学総合研究所

Collected Papers of Project Research
"Cancer Treatment and its Modalities using Accelerated Heavy Ions"

No. 2

(April 1990 — March 1991)

March, 1992

National Institute of Radiological Sciences
9-1, Anagawa 4-chome, Chiba-shi, 260 Japan

序

重粒子線は Bragg peak を持つ高 LET 放射線である。線量分布に難のある速中性子線では、十分に果せなかった高 LET 放射線の癌治療に果す意義が明確になるものと期待されている。

重粒子線治療の臨床トライアルは平成５年度に開始される予定であるが、それ以前に、治療に必要な物理・生物学的基礎研究の成果を集積すると共に、治療計画システムを完成せねばならない。

前臨床研究は、理科学研究所の生物ビームポートを利用して始められたが、このビームポートの整備は松平所長の決断に負うところが大きい。治療計画システムの中で、最も重要な役割を担う三次元治療計画装置の製作には多くの困難が予想されるが、重粒子線治療の要となる装置として完成させなければならない。

平成２年度に掲載された論文別刷をもとに特別研究・論文集を編集したが、その中にパンコースト腫瘍の速中性子線治療に関する論文がある。すでに、速中性子線治療の適応となる疾患の確認も進んでいるが、パンコースト腫瘍に関する適応確認は、放医研のグループが世界に先駆けて果した業跡の１つである。

速中性子線治療に内容、特に晩期放射線反応の経過を詳細に分析して、重粒子線治療の実行に遺漏なきよう実施計画を整える所存である。

最後に、特別研究に協力していただいた各位に感謝の詞を奉げます。

特研研究、班長

恒　元　　博

目　次

1．基礎的研究

2．画像診断

3．治　　療

4．そ　の　他

1. 基礎的研究

Medical Dosimetry, Vol. 15, pp. 79–81
Printed in the U.S.A.

0739-0211/90 $3.00 + .00

DOSIMETRY OF 70 MeV PROTON BEAMS FROM THE NIRS CYCLOTRON*

T. HIRAOKA, PH.D., K. HOSHINO, PH.D., A. FUKUMURA, B.S., and K. KAWASHIMA, PH.D.

Division of Physics, National Institute of Radiological Sciences, 9–1, Anagawa-4-chome, Chiba-shi 260, Japan

Abstract—Dosimetry of 70 MeV proton beams for radiotherapy was carried out using various ionization chambers. The beam irradiation conditions, dose estimation with an ionization chamber, measurement of dose distributions, and calculation of isodose curves for the proton beams will be discussed.

Key Words: **Proton dosimetry, proton radiotherapy, absorbed dose, Bragg curve.**

INTRODUCTION

High energy proton beams have been regarded as one of the more attractive particles for use in radiotherapy since Wilson[1] suggested the application of the high energy proton beams for radiological purposes. In the National Institute of Radiological Sciences, clinical trials of proton beams started in 1979 using the spot scanning system[2] in order to obtain the irradiation of large fields with homogeneous dose distributions. Superficial treatment of less than 4 cm depth in tissue is possible because of the maximum energy of the proton beams. At the present time over 60 patients, who mainly had eye tumors, were treated by the beams.

Dosimetry with ionization chambers can be considered as one of the most useful methods for absolute dose determination because it has characteristics of being reliable, easy to handle with good repeatability, good accuracy, and high resolution for many types of radiations.

MEASUREMENT METHOD

Irradiation condition

Proton beams of 70 MeV from the AVF cyclotron were directed by a switching magnet and the beams are then delivered to a treatment room. The beams pass through an upstream monitor, vertical and horizontal scanning magnets, a main monitor, and a range modulator. Details of the dose delivery system were published in a separate paper.[2]

The transmission monitor ionization chamber which have thin aluminum plates is located at 30 cm upstream from the treatment site. Nitrogen gas with a flow rate of 40 ml per minute was used as the chamber gas and −1000 volts is applied on the high voltage plate. Ionization current reduction by ion recombination loss was less than 0.2% for the ranges of dose rate in patient treatment. The saturation characteristics of proton beams for chambers are described in other paper.[3]

Absorbed dose determination

The Bragg–Gray cavity theory can be used to determine absorbed dose in the medium. The absorbed dose in tissue for proton beams is given by

$$D_T = \frac{Q \times Wp/e \times (Sp)w,g \times K}{M \times (Sp)w,t}, \qquad (1)$$

where D_T is tissue absorbed dose in Gy, Q is charge collected in coulomb, Wp is the average energy required to produce an ion pair in joule, e is the charge of the electron in coulomb, $(Sp)w,g$ is the average stopping power ratio of the chamber wall relative to the chamber gas for the proton beams including secondary charged particles, $(Sp)w,t$ is also the same ratio of the chamber wall relative to tissue for their particles, K is the correction factor including ion recombination loss, ambient temperature and pressure, etc., and M is the mass of gas in kg. The mass of gas in a chamber is determined by irradiation of the chamber in a photon field (Co-60). The intensity of the field can be measured using ionization chambers whose calibration is traceable to the national standardizing laboratory. The expression used for estimation of the mass of the gas is given by,

$$M = \frac{2.58 \times 10^{-2} \times Qg \times Wg/e \times (Sg)w,g}{0.957 \times X \times Aeq \times (\mu en/\rho)w,t}, \qquad (2)$$

where Qg is the charge collected in coulomb, X is exposure in C/kg. Aeq is the cap correction factor, $(\mu en/\rho)w,t$ is the mass energy absorption coefficient ratio of the chamber wall relative to tissue. Other factors with the subscript, g, denotes the value applicable to the calibration in gamma-ray field.

* Corresponding author: Takeshi Hiraoka, Ph.D.

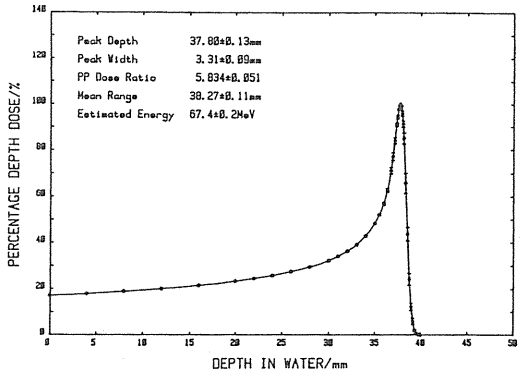

Fig. 1. Central axis depth dose curve of 70 MeV proton beams.

Depth dose distribution

The depth dose distributions were measured with a parallel plate ionization chamber the volume of which is 0.603 ml estimated by ^{60}Co gamma ray calibrations. The wall material is Lucite with a dag coating. A methane based tissue equivalent gas was used with a flow rate of 10 ml per minute. The ionization currents were measured with a vibrating reed electrometer Cary model 401 and read with a digital voltmeter. A water phantom was located in front of the chamber and the thickness of the phantom was selected by a remote control system. The thickness was measured with a large micrometer and the value was read on a TV monitor.

Isodose distribution

In the proton spot scanning system, spatial dose distributions in the field can be calculated by superposition of dose distribution for one spot beam in a given depth. The central axis depth dose distribution of the spot beam is measured with a small ionization chamber of 0.004 ml volume. Measurements are made for unmodulated and modulated beams with the range modulators of 10, 15, 20, 25, and 30 mm thick. The lateral dose distributions of the spot beams for various depth in phantom is also measured with the chamber. From data obtained for one spot beam at any depth, we can compute isodese distributions for desired fields. More detailed calculation method is described in elsewhere.[4]

Table 1. Results of absorbed dose obtained by three different types of ionization chambers.

Chamber-Gas	M ($\times 10^{-7}$ kg)	Q ($\times 10^{-10}$ C)	D (cGy/mu)
PP-1-AIR	7.218	2.431	1.367
PP-1-TEG	6.303	2.852 ± .010	1.376
IC-18-AIR	1.580	0.5380 ± .0056	1.382
IC-18-TEG	1.391	0.6312 ± .0058	1.379
IC-17-AIR	11.38	3.885 ± .017	1.386
IC-17-TEG	9.982	4.566 ± .049	1.391

$(Wp/e)_{air}$ = 35.3 J/C, $(Wp/e)_{TEG}$ = 30.4 J/C

RESULTS AND DISCUSSION

Figure 1 shows the results of the depth dose distribution in water which was measured on seven separate days. The curve was drawn through the mean value of each point and error bars show a standard deviation. Bragg peak depth, peak width (FWHM), peak to plateau dose ratio, and mean range deduced from the curve were 47.81 ± 0.13 mm, 3.31 ± 0.09 mm, 5.834 ± 0.051, and 38.27 ± 0.11 mm, respectively. The estimated incident energy from the mean range is 67.4 ± 0.2 MeV using the range-energy table.[5]

Three different shapes of the ionization chamber for determination of absorbed dose is shown in Fig. 2. A parallel plate ionization chamber, made at the NIRS, has dag-coated Lucite walls (we designated pp-1). Commercially available ionization chambers, Model IC-17 and IC-18 (Far West Technology, Goleta, CA), are made of A-150 plastic. For these

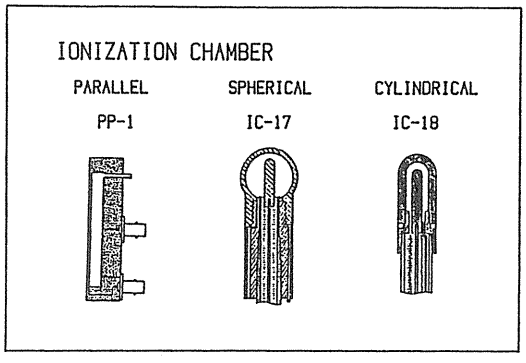

Fig. 2. Ionization chambers used for absorbed dose determinations.

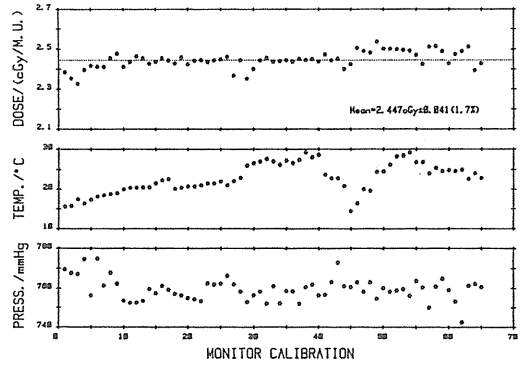

Fig. 3. Plot of constancy of the monitor chamber gathered with room temperature and atmospheric pressure.

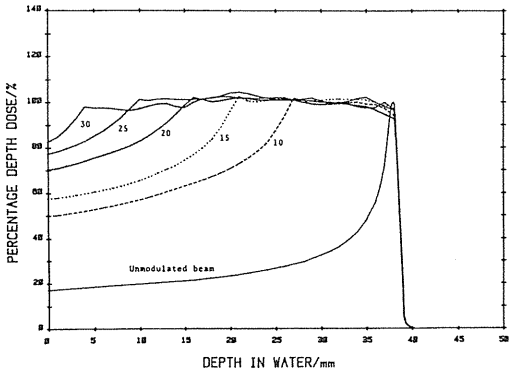

Fig. 4. Depth dose curves for modulated beams and unmodulated beam.

chambers, two ionization gases were used for absorbed dose determinations. Table 1 shows the chamber to gas combination, mass of the ionization gas, and the charge collected which was measured at the entrance plateau for the unmodulated beam. Using the equation (1), tissue absorbed dose per monitor unit was calculated and given in the last column. The value is quite acceptable. The small differences appearing among the chambers depend on the chamber shapes in which the proton beams will travel in the wall material. The absorbed dose values were confirmed by a proton dosimetry intercomparison between Japan and USA.[6]

A plot of the constancy of the thin walled transmission monitor chamber which was checked before irradiation is shown in Fig. 3. The figure also shows the results of changes in room temperature and atmospheric pressure at the calibration time. It seems that the stability is rather good as a proton beam monitor.

In order to obtain desired spread out Bragg peak, some rotating range modulators were constructed. Figure 4 shows depth dose curves for the modulated beams which were obtained with the range modulators of 10, 15, 20, 25, and 30 mm thick. The unmodulated depth dose curve is also shown in the figure for

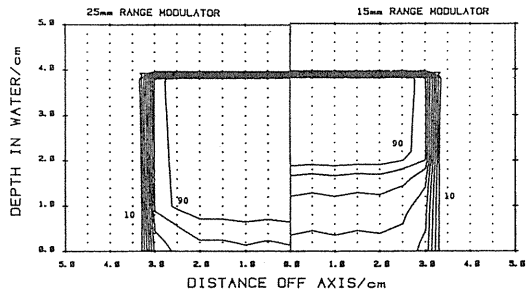

Fig. 5. Calculated isodose curve for both 25 (left hand side) and 15 mm (right hand side) range modulators in 6 cm × 6 cm field.

comparison. The thickness of the modulators were designed for Lucite for which the effective thickness is equivalent to 1.15 times for water. We have only used the 25 mm thick range modulator for regular radiotherapy except for some special requirements.

Figure 5 shows calculated isodose distributions of the modulated beams for both 25 and 15 mm modulators. The penumbra is very small because of a block collimator made of brass. It has been found that the both calculated and observed isodose curves agree within 1 mm width at any dose level greater than 10%.

REFERENCES

1. Wilson, R.R. Radiological use of fast protons. *Radiology* **47**:487–491; 1946.
2. Kanai, T.; Kawachi, K.; Kumamoto, Y.; Ogawa, H.; Yamada, T.; Matsuzawa, H.; Inada, T. Spot scanning system for proton radiotherapy. *Med. Phys.* 7:365–369; 1980.
3. Hiraoka, T.; Kawashima, K.; Hoshino, K. Ion recombination loss in ionization chambers irradiated by proton beams. *Br. J. Radiol.* **55**:585–587; 1982.
4. Hiraoka, T.; Kawashima, K.; Hoshino, K.; Kawachi, K.; Kanai, T.; Nakamura, Y.K. Dose distributions of 70 MeV proton scanning beams for radiotherapy. *Proc. of the 7th ICCR.* 377–381; 1980.
5. Janni, J.F. Proton range-energy tables, 1 keV-10 GeV. *Atomic Data and Nuclear Data Tables.* **27**:147–529; 1982.
6. Hiraoka, T.; Kawashima, K.; Hoshino, K.; Kawachi, K.; Kanai, T.; Ito, A.; Verhey, L.J.; McDonald, J.C.; Ma, I-Chang. Small scale dosimetry intercomparison between Japan and USA. *Jpn. Radiol. Phys.* **9**:135–141; 1989.

Nuclear Instruments and Methods in Physics Research A302 (1991) 158–164
North-Holland

An irradiation facility and a beam simulation program for proton radiation therapy

Tatsuaki Kanai [a], Kiyomitsu Kawachi [a] and Takeshi Hiraoka [b]

[a] *Division of Accelerator Research,* [b] *Division of Physics, National Institute of Radiological Sciences, 9–1, Anagawa 4-chome, Chiba-shi, Chiba 260, Japan*

Received 14 May 1990 and in revised form 12 December 1990

A new beam course dedicated to proton radiation therapy was constructed at NIRS (National Institute of Radiological Sciences, Japan). The vertical beamline, which is assumed to be suitable for radiation therapy, has a scatterer, wobbler magnets, monitor ionization chambers, a range shifter, a range modulator, a multileaf collimator and other patient-positioning devices. A simulation program for beam propagation in a beam port was developed in order to estimate beam profiles for any proton radiotherapy beam course. The results of the beam profile obtained by the simulation program were compared with the experimental results and were found to be in good agreement.

1. Introduction

Protons are promising for use in radiation therapy owing to their excellent dose localization, compared to conventional photon or electron radiation [1,2]. The excellent dose localization of protons is realized due to their physical characteristics: to penetrate in materials, for example, their relatively small degree of multiple scattering and their small amount of energy-loss straggling are important factors. On the other hand, these characteristics make it difficult to realize an appropriate irradiation field size for treatment. Usually, an accelerated proton beam with a diameter of several mm is delivered to the irradiation site. If the beam is injected without any modulation, it creates a very sharp hot spot in the irradiated material. For treatment purposes, therefore, it is necessary to spread the beam uniformly over a size of about 10 cm in diameter. Such a uniformly spread beam should be collimated so as to fit the shape of the targeted region of the patient. Secondly, monoenergetic proton beams show a sharp Bragg peak near the stopping region in the depth dose distribution. In radiation therapy, it is most important to uniformly irradiate the target volume in order to reduce any damage to normal tissue. Therefore, the sharp Bragg peak should also be spread uniformly over the target volume. The proton irradiation facility should have the above-mentioned beam modulation functions, as well as a precise irradiation dose control function, and a precise patient-positioning function.

A new irradiation facility for proton radiation therapy with the above-mentioned functions was constructed at NIRS (National Institute of Radiological Sciences), Japan, for the use of 70–90 MeV protons. This facility was constructed in order to provide a vertical beam which is suitable for radiation therapy. Devices to broaden narrow proton beams and to spread the sharp Bragg peak should be inserted in the beam course for proton radiation therapy. The quality of the radiation field, such as the physical penumbra, depends on the position of the devices in the beam course.

At present, the beam-course arrangement for proton radiation therapy and the method to spread a narrow beam and the sharp Bragg peak have not been fixed. So far, we have not had much experience to construct a proton therapy facility. Furthermore, it is often necessary to modify the beam course. It would be very useful if there exists a simulation program which can predict the beam profile or the best location for a scatterer, a range modulator or collimators. Although the various physical processes for describing beam transportation in a radiation therapy beam course are already clear, designing the geometrical layout of the devices will be difficult because of the complexity involved.

In this paper we describe our new irradiation facility as well as the measured physical characteristics of the facility for proton radiotherapy. Also described is a program which has been developed for evaluating beam propagation for many variations of the beam course. When we improve the irradiation facility, the simulation program will be a powerful tool to estimate the effect of any modifications.

0168-9002/91/$03.50

2. General description of the proton facility

The proton irradiation facility was constructed in the same room as the neutron radiation therapy facility [3]. The room is on the first basement of the NIRS cyclotron facility. The distance from the level of the horizontal beamline on the first floor to the floor level of the treatment room is about 4 m. The radius of curvature of the 90° bending magnet is 1.25 m. The irradiation site was set 1.0 m above the floor. The length of the straight section between the scatterer and the irradiation site, where it is possible to set beam-modifying devices, is only 2.79 m. Fig. 1. shows a conceptual layout of the vertical proton beamline.

The vertical beamline comprises four parts: (1) devices to produce uniform irradiation fields; (2) a depth dose modification device; (3) irradiation dose monitors; and (4) patient-positioning devices.

To broaden the proton beam uniformly, we have adopted a wobbler scanning method which was originally developed at Lawrence Berkeley Laboratory [4]. A scatterer and a pair of scanning magnets are used to broaden the beam uniformly. A multileaf collimator is used to produce irregular fields. The multileaf collimator comprises 12 leaves on each side; the width of each leaf is 10 mm. With this multileaf collimator, an irregular field can be formed in steps of 1 cm. The aperture of the multileaf collimator can be controlled, even during irradiation, in order to realize three-dimensional irradiation [5].

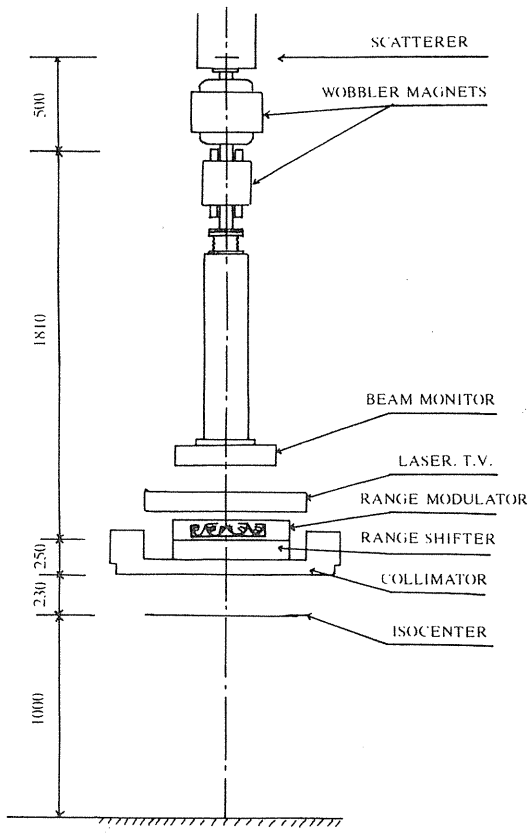

Fig. 1. Schematic illustration of the vertical beam course for proton radiation therapy.

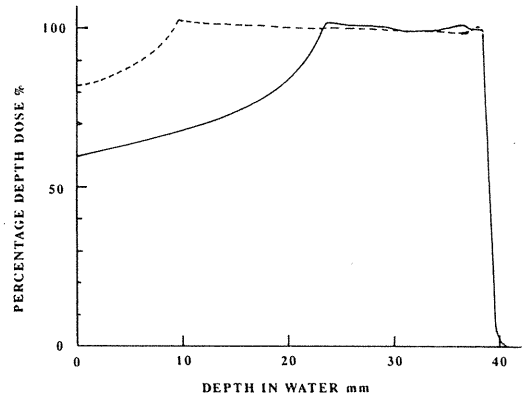

Fig. 2. Depth dose distributions for the spread Bragg peak of 70 MeV protons. The solid and dashed curves are the results for the cases of 15 and 30 mm width spreads of the Bragg peak, respectively.

In order to spread the Bragg peak a rotating range modulator was used [6]. For a 70 MeV proton beam, the range step for modulation is about 1 mm of water in equivalent thickness. The range modulator has 8 fan-shaped leaves which are fixed in a large wheel rotating at between 100 and 250 revolutions per minute. At this rotational speed the Bragg peak is swept between 13 and 33 times per second in the depth direction. Fig. 2 shows the results of the depth dose distribution for a Bragg-peak spread of 15 and 30 mm for 70 MeV protons. The 30 mm range modulator is made of aluminum in order to reduce the height of the ridge. The 15 mm range modulator is made of Lucite. The range shifter is used for adjusting the depth of the distal end of the spread Bragg peak. The range shifter comprises 7 aluminum sheets, each 0.25 to 16 mm in thickness. The range in the patient's body can be adjusted in steps of 0.53 mm owing to the stopping power ratio of aluminum and soft tissue.

This vertical beamline has three ionization chambers for monitoring both the irradiation dose and the beam profile. A multiwire ionization chamber is used for monitoring the beam profile. Two parallel-plate ionization chambers are used for monitoring the irradiation dose.

A laser marker and a TV camera are used for patient-positioning. With the TV monitor we can see the target marker on the beam's eye view.

3. Single-radius beam wobbling

At LBL the wobbling radius of the beam is changed during treatment in order to reduce the thickness of the scatterer [7]. For heavy-ion radiotherapy at LBL, energy losses in the scatterer are relatively large when obtaining appropriate scattered beams. Further, the use of a higher incident energy of heavy ions causes larger fragmentations in the scatterer and worse depth dose distributions. For the beam wobbling of multiple radii, however, uniform irradiation fields are not realized unless the doses are delivered in wobbled beams of all radii that are scheduled. Therefore, if the patient moves during irradiation, dose uniformity in the patient would not be maintained. In the case of proton radiotherapy, the energy loss in the scatterer is not so serious compared to the case of heavy ions. In order to improve the defect of the multiradius wobbler method, single-radius beam wobbling has been adopted. In this method a uniform irradiation field can be obtained in a period of beam wobbling when using the appropreate ratio of the radius of the circulating beam and the standard deviation of the scattered beam deflection. The optimum radius of beam wobbling is about 1.1 times the standard deviation of the scattered beam deflection, which is assumed to be Gaussian.

A golden scatterer of 0.1 mm thickness is used for a 70 MeV proton beam in order to obtain a large radiation field which is 140 mm in diameter. The energy loss in the scatterer is about 1 MeV. The range is reduced by about 1 mm because of the scatterer.

The physical specifications of the wobbler magnets are shown in table 1. By using this wobbler system it is possible to obtain a uniform field in 40 ms if the beam current is constant during this interval. In a typical treatment the beam current is about 25 nA. The dose rate in this case is about 1 Gy/s second. This means that the beam circulates 250 times in an irradiation of 10 Gy.

Table 1
Physical specifications of the wobbler scanning magnets

Magnetic rigidity	1.3661 Tm
Pole length	200 mm
Gap size	60 mm
Frequency	0–25 Hz
Inductance	4.5 mH
Maximum current	200 A
No. of turns	58

Fig. 3 shows a typical example of the transversal intensity distribution for an optimized irradiation field which was obtained by measuring the blackening of X-ray films. The lower intensity at the central part results from a larger radius of beam wobbling than for the case displayed in the figure; the smaller size of the irradiation field results from a smaller radius of beam wobbling. The ratio of the number of protons used in a uniform irradiation field to the total number of protons transported to the scatterer is about 26%.

In the case of the wobbler method, it is easy to tune the beam before a treatment. During beam tuning, the scatterer, range modulator and range shifter are removed and the wobbler magnets are turned off. To confirm the beam image, an intensifying screen for X-rays is placed at the isocenter. The transport line is tuned so as to focus the beam onto the screen. After tuning the transport line, a uniform irradiation field is obtained by only putting a regular scatterer and exciting the wobbler magnets. In the case of the beam flattening method, which uses double scatterers and an occluding ring [8], any misadjustment of the beam profile at the occluding ring causes a great deviation in the flat radiation field at the isocenter. It therefore takes a longer

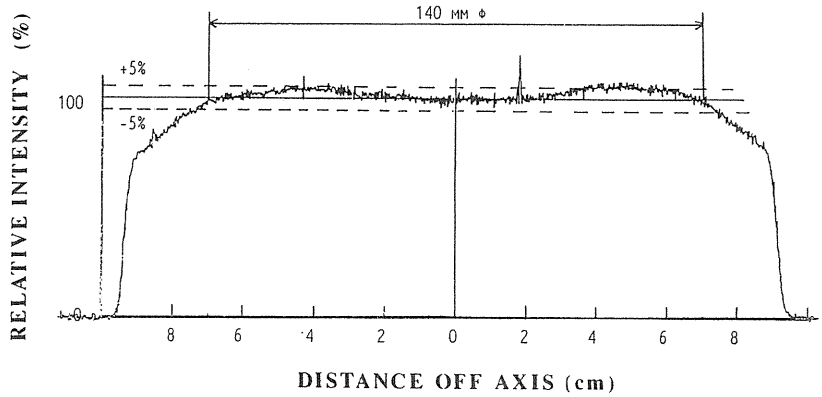

Fig. 3. Typical example of the transversal intensity distribution of an optimized irradiation field of maximum size.

time to tune the beam for radiation therapy than when using the single-radius wobbler method.

4. Simulation program for beam propagation

It usually requires much work to change the arrangement of the beamline. After doing so, a large amount of checking of the physical characteristics of the beamline must be carried out before any radiation treatment is performed. It is therefore very important to develop a computer program which can estimate the dose distribution for any type of irradiation facility. The principal purpose of the developed simulation program is to estimate the beam profile for any beamline configuration. The program should be capable of answering questions as to where is the best location to place the range modulator, the range shifter or the collimator for eliminatinging useless scattered particles; it must also deal with the question as to how large is the penumbra of the radiation fields for any beam port configuration. There already exist many programs describing beam development in an electromagnetic beam transport line; we have therefore restricted our program to the beam irradiation system. Therefore, in this program, for a given beam condition at the exit of the beam transport line (which is the entrance of the beam irradiation system) the beam profiles at the isocenter are calculated. In order to take into account the complex geometry of the collimator, or the entrance beam profile, it is almost impossible to calculate the beam profile analytically. A Monte Carlo simulation method was therefore used to estimate the beam profile. The Monte Carlo code was written with recourse to Berger's textbook [9].

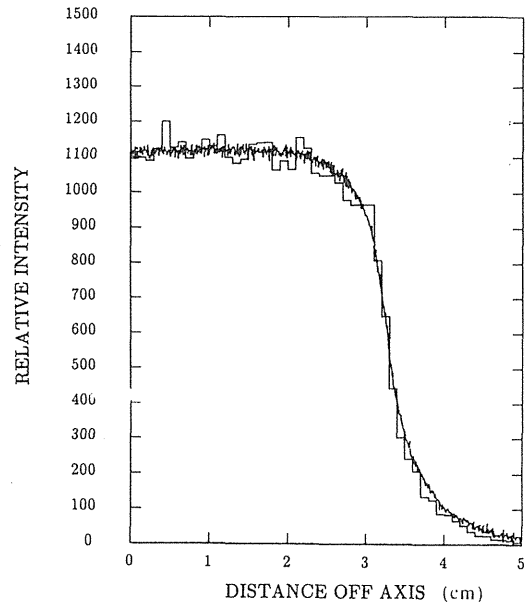

Fig. 5. Beam profile at the isocenter. A 30 mm range modulator and a 6×6 cm^2 square field collimator were used. The solid curve and the dashed histogram represent experimental measurements by X-ray film and the result of a Monte Carlo simulation, respectively.

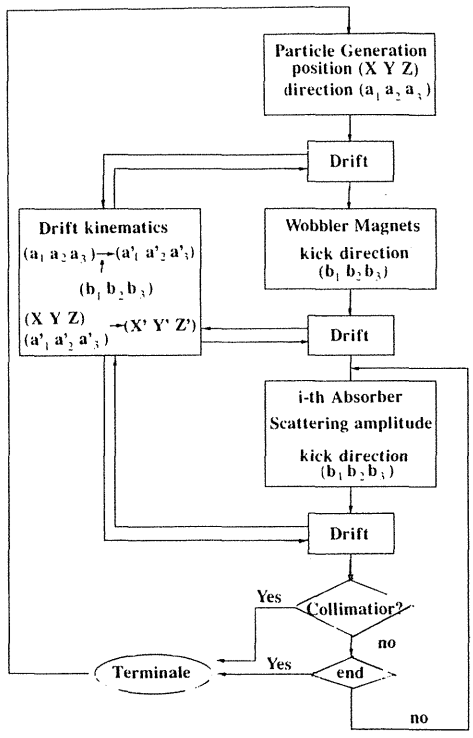

Fig. 4. Block diagram of a Monte Carlo calculation regarding beam propagation in the proton radiation therapy course.

As described in the former section, the irradiation system comprises a pair of wobbler magnets, a scatterer, collimators, a range modulator and dosimetric monitors. Using the wobbler magnets the particles are kicked so as to have a circular trajectory at the isocenter. When the beam passes through the other materials of the devices as well as free air – the flight path between the devices – the particles experience both energy loss and multiple scattering. The physical processes which are taken into account in this program are: (1) the energy loss in various materials and (2) multiple scattering in these materials. In a preparatory program the beam path in the irradiation system was divided into small slabs. The injecting and ejecting energies of the beam for each slab were calculated by the Bethe formula, in which the values of the average ionization potentials were those reported in the ICRU report [10]. Energy-loss straggling was neglected in the calculation. The angular

distribution, $A_M(\omega)$, of the multiple scattering in each slab was calculated according to Molière's theory, as follows:

$$A_M(\omega)\omega\,d\omega = \sqrt{\sin\omega/\omega}\,\theta\,d\theta\{2\exp(-\theta^2) + f^{(1)}(\theta)/B + f^{(2)}(\theta)/B^2\},$$

where ω is the deflection angle and θ is the reduced scattering angle defined as $\theta = \omega/(\chi_c\sqrt{B})$. Further, $f^{(1)}$ and $f^{(2)}$ are numerical functions tabulated by Bethe [11]. χ_c and B are parameters defined in Berger's textbook [9]. The cumulative probability distribution for each slab was deduced by integrating the angular distribution. These cumulative probability distributions of

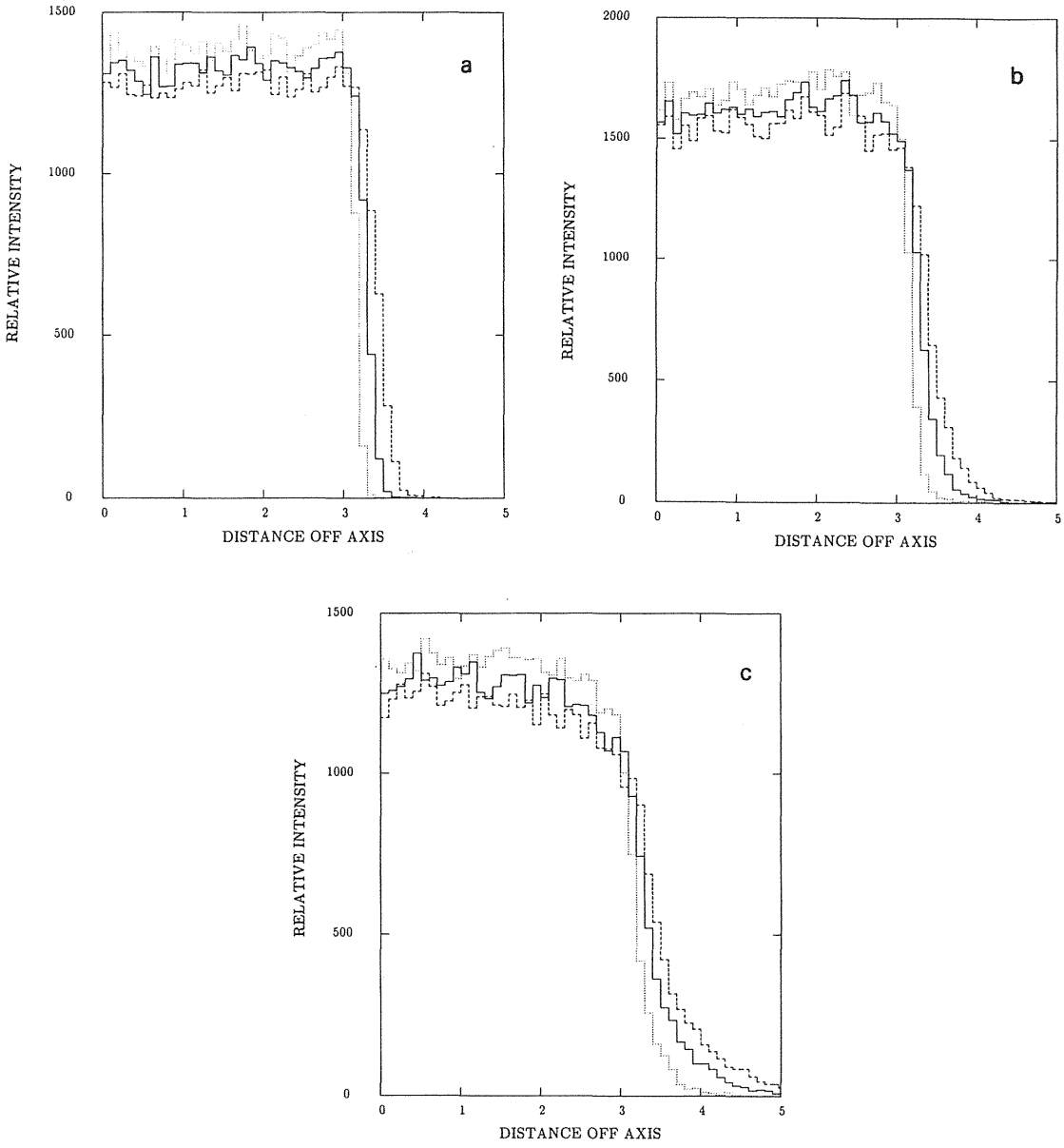

Fig. 6. Results of a Monte Carlo simulation for the 70 MeV proton beams in the proton radiation therapy course. The dotted, solid and dashed histograms represent results for the intensity distribution 10 cm upstream from the isocenter, at the isocenter and 10 cm downstream from the isocenter, respectively. (a) Results without the range modulator, (b) results with the 15 mm range modulator, (c) results with the 30 mm range modulator.

the deflecting angle were tabulated for all slabs in the preparatory program.

A Monte Carlo simulation was performed which generated histories at the entrance of the beamline. The beam characteristics, such as the beam profile and the angular distributions, can be taken into account in the program. Regarding the propagation of each step, the histories are pursued by a random-walk looking up of the accumulated probability distribution of multiple scattering. Then, the particle drifts to the next step with a kinematically determined angle. Regarding the free drift during each step, the history is terminated if a particle hits the collimator. The calculation procedure is briefly outlined in fig. 4.

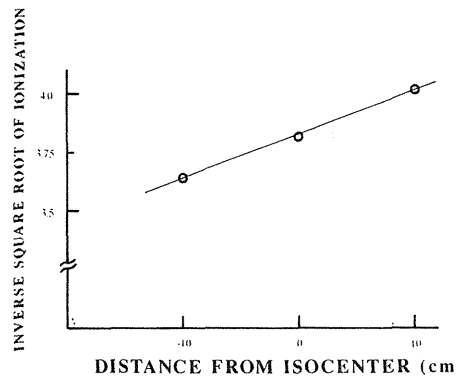

Fig. 7. Inverse square root of the dose rate versus the distance from the isocenter for the case of the 30 mm range modulator.

5. Results and discussions

Experimental beam profiles were obtained by exposing X-ray films and measuring their blackening density. Fig. 5 shows the results of the beam profile at the isocenter. The radius of beam wobbling and the thickness of the scatterer were set so as to produce a uniform field of 140 mm in diameter (fig. 3). The uniform field was collimated to a 6×6 cm^2 field with the multileaf collimator. The 30 mm thick range modulator was used to spread the Bragg peak. The histogram in the figure shows the result of the Monte Carlo calculation for the corresponding case. As shown in the figure, the Monte Carlo calculation satisfactorily agrees with the experimental results of the beam profile. In fig. 6, the results of the Monte Carlo calculations are plotted for uniform radiation fields collimated to a 6×6 cm square field by the multileaf collimator. The solid, dotted and dashed histograms represent beam profiles at the isocenter as well as 10 cm higher and 10 cm lower than the isocenter, respectively. Figs. 6a, b and c show the results obtained without the range modulator and with the 15 mm and the 30 mm range modulator, respectively. As shown in fig. 6, the results of the Monte Carlo calculations show the general characteristics of the beam port for proton radiation therapy. The amount of beam divergence and the physical penumbra for a beam using a thicker range modulator are much larger than those for a beam using either a thinner modulator or even no range modulator.

The exposures for the unit monitor output at three heights on the central beam axis (i.e. at the isocenter, 10 cm upstream and 10 cm downstream from the isocenter) were measured using a parallel-plate ionization chamber. Fig. 7 shows the change in the dose rate due to the height of the measured locations for the case of the 30 mm range modulator. The vertical axis shows the inverse square root of the measured ionization charge. The measured data fell on a straight line within the region displayed in the graph. The point at which this line crosses the horizontal line is at about -200 cm. This means that the dose rate decreases as the inverse of square of the distance from a virtual focal point 200 cm upstream from the reference point. The position of the scatterer or the wobbler magnets is more than 2.8 m upstream from the reference point. The downward displacement of the virtual focal point from the position of the scatterer is caused by scattering in the range modulator. The position of the virtual focal point therefore moves up and down for the various range modulators. Actually the virtual center of the beam divergence without the range modulator and with the 15 mm range modulator was about 225 cm upstream from the isocenter. This is due to the fact that the amplitude of multiple scattering in the 30 mm range modulator was much larger than that in the 15 mm range modulator.

In fig. 8 the field size is plotted against the height of the measured point. The open squares, triangles and circles indicate the experimental results without the range modulator and with the 15 mm and the 30 mm range modulator, respectively. The solid marks indicate the results of Monte Carlo calculations for the cases of the corresponding open marks. For the cases of no modualtor and the 15 mm range modulator, the results of Monte Carlo calculations coincided with the experimental results. The experimental results shown in fig. 8 fall on straight lines. All of the lines cross the horizontal axis, which corresponds to a field size of 60 mm at around -23 cm. The multileaf collimator was placed at this location. The slope of the lines is steeper for the 30 mm range modulator than that for the 15 mm range modulator. The slopes for no range modulator and the 15 mm modulator were not different from each other.

The size of the physical penumbra is plotted against the height of the measured point in fig. 9. The distances from the 80% dose level to the 20% dose level were taken as the physical penumbra. The experimental results fell on lines which intercepted the horizontal axis

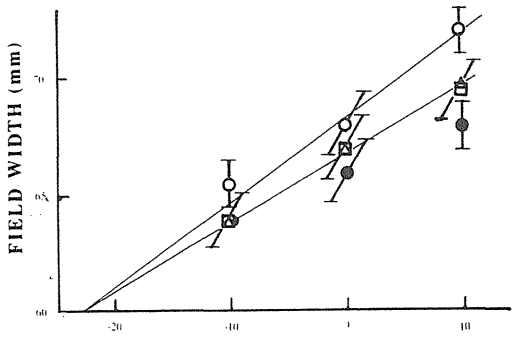

Fig. 8. Field size versus the distance from the isocenter. A 6×6 cm^2 field collimator was used. The open circles, squares and triangles represent experimental results without the range modulator and with the 15 mm and 30 mm range modulators, respectively. The closed circles are the results of a Monte Carlo simulation. The simulation results were similar for the three cases of range modulators.

at −23 cm. This location is the same collimator position as in the case of the field size. Just as in the case of the field size, the slopes were the steeper for the thicker range modulator.

Regarding the case of small irradiation fields, such as used in eye treatments, the physical penumbra was too large to use. In this case, a small collimator (which can be set very close to a patient) is used to define the final irradiation fields. The physical penumbra for these cases were examined, as shown in fig. 10. The 30 mm range modulator was used in these measurements. If the physical penumbra is less than 1.5 mm, the small collimator must be set 1 cm from the patient.

In order to realize a sharp edge for the irradiation fields by the wobbler method, it has been found that the ratio of the distance from the range modulator to the collimator to the distance from the collimator to the

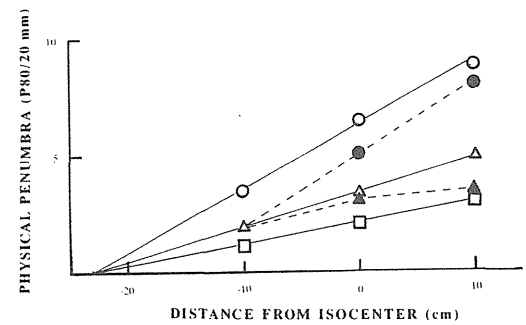

Fig. 9. Physical penumbra, which is defined as the distance from the 80% dose level to the 20% dose level, versus the distance from the isocenter.

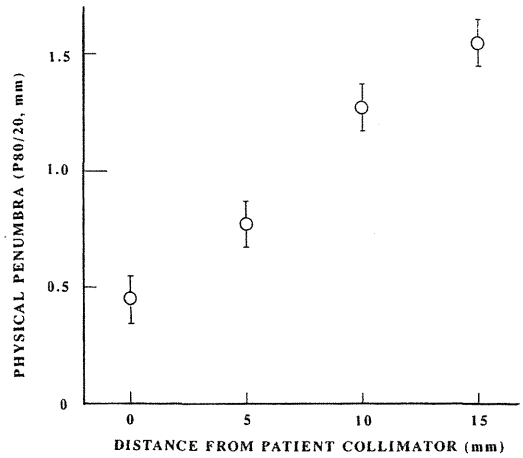

Fig. 10. Size of the physical penumbra versus the distance from the collimator. For small irradiation fields, the distance from the collimator to the patient is as small as possible in order to reduce the physical penumbra.

isocenter should be large. On the other hand, if the range modulator is placed very far upstream of the beamline, the doses at the proximal part of the spread Bragg peak are reduced due to scattering by the thicker part of the range modulator. Therefore in designing the range modulator we must consider the dose reduction due to multiple scattering in the range modulator, which can usually be neglected. It is therefore very important to simulate the beam profile when designing either the range modulator or the layout of the beamline.

References

[1] H.D. Suit, M. Goitein, J.E. Tepper, L. Verhey, A.M. Koehler, R. Schneider and E. Graroudas, Int. J. Radiat. Oncol. Biol. Phys. 3 (1977) 115.
[2] S. Graffman and B. Larsson, Atomkernenergie 27 (1976) 148.
[3] H. Ogawa, T. Yamada, V. Kumamoto, Y. Sato and T. Hiramoto, IEEE. Trans. Nucl. Sci. NS-26 (1979) 1988.
[4] W.T. Chu, S.B. Curtis, J. Llacer, T.R. Renner and R.W. Sorensen, IEEE Trans. Nucl. Sci. NS-32 (1985) 3321.
[5] T. Kanai, K. Kawachi, H. Matsuzawa and T. Inada, Med. Phys. 10 (1983) 344.
[6] A.M. Koehler, R.J. Schneider and J.M. Sisterson, Nucl. Instr. and Meth. 131 (1975) 437.
[7] T.R. Renner and W.T. Chu, Med. Phys. 14 (1987) 825.
[8] A.M. Koehler, R.J. Schneider and J.M. Sisterson, Med. Phys. 4 (1977) 297.
[9] M.J. Berger, Methods in Computational Physics, ed. B. Alder (Academic Press, New York, 1963) p. 135.
[10] ICRU report, 37 (1984).
[11] H.A. Bethe, Phys. Rev. 89 (1953) 1256.

日本医放会誌：50（4），404—411，1990（平2）

超高エネルギー中性子線の線量および線質特性

筑波大学基礎医学系
稲田哲雄　早川吉則
北海道大学医学部
有本卓郎
放射線医学総合研究所
平岡武　佐藤眞一郎
横浜市立大学医学部
窪田宜夫

（平成元年6月26日受付）
（平成元年10月3日最終原稿受付）

Characterization of Ultra High Energy Neutron Beam Generated by 500 MeV Proton Beam

Tetsuo Inada and Yoshinori Hayakawa
Institute of Basic Medical Sciences, University of Tsukuba
Takuro Arimoto
School of Medicine, Hokkaido University
Takeshi Hiraoka and Shin-ichiro Satoh
National Instutute of Radiological Sciences
Nobuo Kubota
School of Medicine, Yokohama City University

Research Code No. : 203

Key Words : High energy neutron, Dose distribution, RBE

An ultra high energy neutron facility was constructed at PARMS, University of Tsukuba, to produce a neutron beam superior to an X-ray beam generated by a modern linac in terms of dose distribution. This has been achieved using the reaction on a thick uranium target struck by 500 MeV proton beam from the booster-synchrotron of High Energy Physics Laboratory. The percentage depth dose of this neutron beam is nearly equivalent to that of X-rays at around 20 MV and the dose rate of 15 cGy per minute. Ralative biological effectiveness of this neutron beam has been estimated on the cell killing effect by the use of HMV-I cell line. Resultant survival curve of cells after the neutron irradiation shows the shoulder with n and Dq of 8 and 2.3 Gy, respectively. RBE value at 10^{-2} survival level for the present neutron, compared with ^{137}Cs γ-rays is 1.24. The result suggests that the biological effects of high energy neutrons are not practically large enough whenever the depth dose distribution of neutrons becomes superior to high energy linac X-rays.

I. 緒　言

サイクロトロンなどの粒子加速器により発生させた速中性子線ががん治療に使用され，これまでに世界の20余の施設で1万例を越える症例数をえ

た．この間にそれぞれの施設で多様な工夫・改善が加えられたにもかかわらず，唾液腺などの一部[1)~8)]を除くと従来の放射線治療成績と比較して有意な差を認めえない[9)~17)]．また，とくに深部臓器がんに対する治療において，重篤な後障害の発生が有意に多い施設がある．その原因の主なものとして，これらの中性子線の深部線量分布がライナックX線のそれより劣ることが挙げられる．

筑波大学粒子線医科学センターに設置した中性子照射システムは，高エネルギー物理学研究所の500MeV陽子線をウラニウム・ターゲットに入射して前方に発生した中性子線を利用するもので，世界に類を見ない研究施設である．この中性子線には核破砕反応と核分裂反応による最高500MeVに至る連続したエネルギー分布の中性子線が含まれており，従来のがん治療に用いられたものより高エネルギーであり，深部線量の増加が期待された．本研究では，この超高エネルギー中性子線の線量分布および生物効果を求め，そのがん治療への適用について基礎的検討を行った．

II. 装置の概要

照射設備の概念図をFig. 1に示す．高エネルギー物理学研究所のブースターシンクロトロンにより加速された500MeVパルス陽子線をウラニウムターゲットに入射することにより，最高エネルギー500MeVのパルス中性子線が発生する．ターゲットより発生した中性子線は，ターゲットの直後にある鉛コリメータの開口部を通過し，さらにビームシャッターおよび多葉コリメータを通過して被照射体に入射する．鉛コリメータはターゲットの周囲間隙を通過する一次陽子線を遮蔽する．多葉コリメータは厚さ2cm，長さ1mの鉄板が上下各10葉あって，これらを動かすことによって最大20×20cm²の照射野の形状を調節するものである．ターゲットから被照射体までの距離は約3.5mである．このように大きな距離をとった理由は，このウラニウム・ターゲットが，中性子物理学の研究に共用され，前方以外の照射場では，その研究のために長時間照射が行われるので，その時間に物理学実験室に生ずる中性子線による医療用照射室の放射化を防ぐためである．

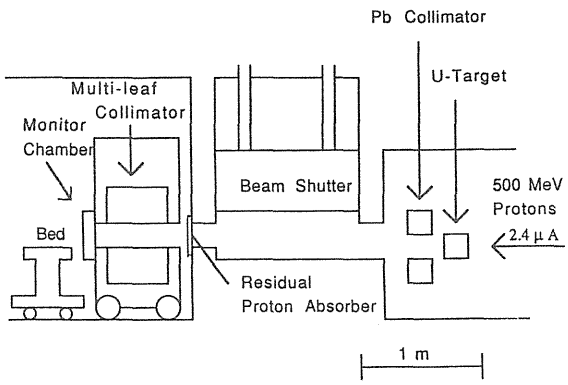

Fig. 1　Arrangement of irradiation apparatus for p (500)+U neutrons at PARMS.

中性子線量の決定は，A-150プラスチックを用いた組織等価壁の指頭形電離箱に組織等価ガスの1気圧フローにて行った．深部線量分布測定には，水槽による三次元駆動装置（Therados社製）を使用した．これに用いた電離箱および半導体線量系の特性は，上記の組織等価電離箱で確かめた．線量モニターは平行平板形電離箱を多葉コリメータの直後に設置して使用した．

III. 結　果

1. 線量率

この中性子発生用ターゲットとして当初はタングステンを使用し，最近になって中性子発生効率を高めるためにウラニウム・ターゲットに変更された[18)]．タングステン・ターゲットより発生する中性子エネルギー分布が，放射化法とunfolding法により求められており[19)]，これにウラニウム・ターゲットに変更して核分裂中性子の増加により，線量が約2.3倍に増加したとの仮定にもとづいて，Fig. 2のようにエネルギー分布を推定した．このスペクトルによるカーマ平均エネルギーは約43MeVであった．

組織等価電離箱による線量の測定はBragg-Grayの理論より組織線量

$$Dt = Qn \cdot Wn \cdot Sn/(e \cdot M)(Gy)$$

で与えられる．ここで

Qn：電離箱に集められた電荷（C）

M：電離ガスの質量（kg）

Wn：1イオン対を作るのに必要な平均エネ

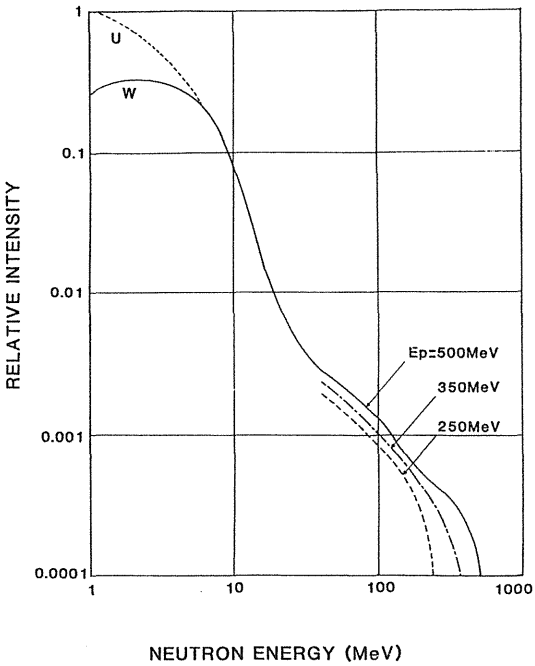

Fig. 2 Neutron energy distribution estimated by unfolding of activation data and by superposing uranium fission neutron spectrum.

ルギー（J）

e：素電荷（1.6×10^{19}C）

Sn：2次粒子にたいする平均阻止能比

である．この電離箱の組織等価ガスの質量Mはコバルト-60標準場における測定から求められた．

W値WnについてICRU report 31によれば組織等価ガスのW値は

陽子線に対して　W＝31.0（寄与0.7）

アルファ線に対して　W＝31.1（寄与0.2）

電子に対して　W＝29.4（寄与0.1）

上のような寄与率にたいして平均のW値は30.9 J/Cとなりこれらの寄与率が少々変わってもあまり変化しない．

阻止能比SnについてA-150と組織等価ガスの阻止能比は1.015と算定された．以上は正確にはA-150の吸収線量であるが，筋肉の線量はこれに中性子のスペクトルからえられた平均のkerma factor 0.974をかければ得られる．

多葉コリメータより30cmの距離にある20×20 cm²照射野において，組織等価電離箱による深さ5 cmのMix　DPの中で求めた全線量率は，約15 cGy/min at 2.4μA proton beamであった．ここでproton beamはシンクロトロンの1加速周期時間2.54秒に43パルスが供給され，パルスあたりに約8×10^{11}個の陽子が含まれる．よって1分間では，約1.9×10^{14}個の500MeV陽子がウラニウム・ターゲットに入射するが，上記線量率の“約”はこの入射一次陽子線の変動に伴うものである．また，本中性子線は，高エネルギー成分が多いために，非水素電離箱においても感度が高いのでn，γ線量の分離測定を従来の対電離箱法で行うことは困難であった．

2. 深部量百分率

水中での深部線量曲線をFig. 3に示す．実線が20×20cm²の本中性子線によるものである．比較のために示した破線は放医研サイクロトロンによる30MeV重陽子をベリリウム・ターゲットに入射してえられた中性子線のもので，ターゲット—表面距離175cmで，50%線量深は約10cmにあり，ほぼ^{60}Coγ線（SSD＝100cm）に相当する．本中性子線に若干のビルドアップが認められるが不明瞭であり，照射野の設定やその他の幾何学的条件により変化し，表面より数cmに亘り，ほぼ平坦な線量分布とみなしうる．これは，Fig. 2に示したように，中性子エネルギーが低エネルギーまで連続的に分布するので，その変動に起因すると考えられる．使用した水槽中の線量計駆動範囲の最大深は約33cmであり，ここでの深部量百分率は56%であり，50%線量深は外挿により約38cmと算定された．すなわち，ピーク後の減弱が従来の中性子線に比べて著しく小さく，濾過効果による高エネルギー中性子の寄与が大きいことを示す．

3. 側方向線量分布

Fig. 4に10×10cm²および20×20cm²の多葉コリメータより50cmにおける水中5cm深部照射野の側方線量分布を示した．平坦度に±5%程度の傾斜が認められるが，これはターゲット周囲の漏洩一次陽子線遮蔽のために追加した鉛コリメータの設定不良によるものと考えられる．その再設定を直ちに行うことは困難であり，適当な機会に行われよう．照射野辺縁の形状は，従来の速中性子

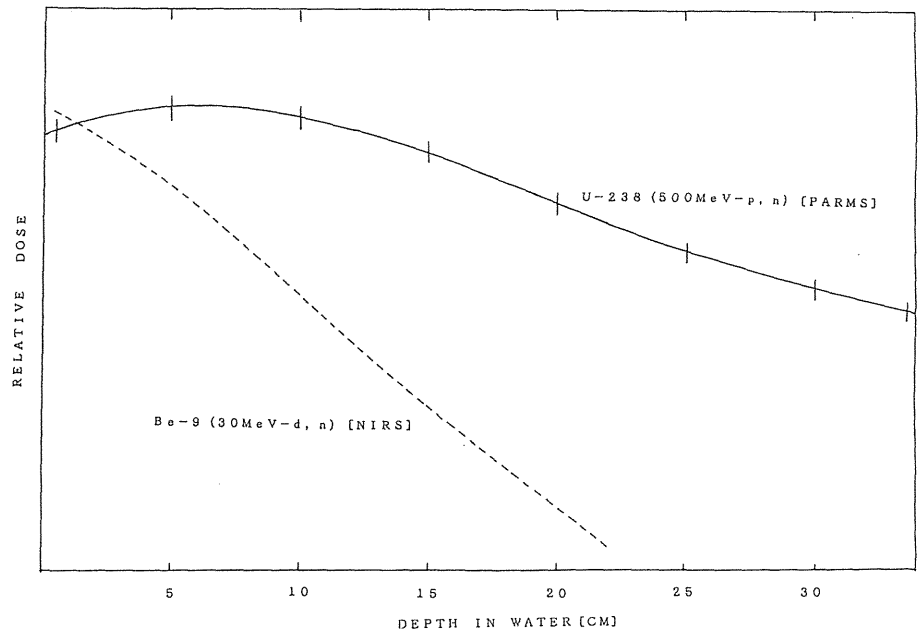

Fig. 3　Depth dose curve of p (500)+U neutrons in water (solid line) compared with that of d (30)+Be neutrons (broken line).

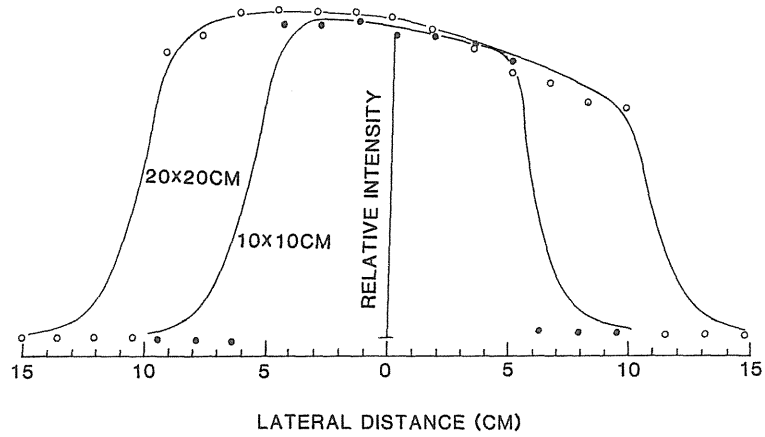

Fig. 4　Lateral dose distribution of neutrons at 5cm depth in water and 50cm distance from collimater illustrated in Fig. 1. Collimater openings are 10×10 and 20×20cm² where survival fractions of cultured HMV-I cells have been checked as shown by closed and open circles, respectively.

線よりもさらに不明瞭であった.

4. 細胞不活性化による生物学的効果比

これまでにも各種の中性子線の線質を評価する生物学的効果比（RBE）決定の指標に用いてきた[20]ヒト悪性黒色腫由来の培養細胞，HMV-I[21]の不活性化をγ線と比較して求め，Fig. 5にその結果を示した．中性子線およびγ線照射後に50個以上のコロニーを形成した細胞を活性とし，単層培養およびスフェロイド細胞について，照射後播種して15日間37℃，5％炭酸ガス培養後にコロニー計測を行った．スフェロイドは回転培養法にて作成し[22]，直径約300μmにて使用した．

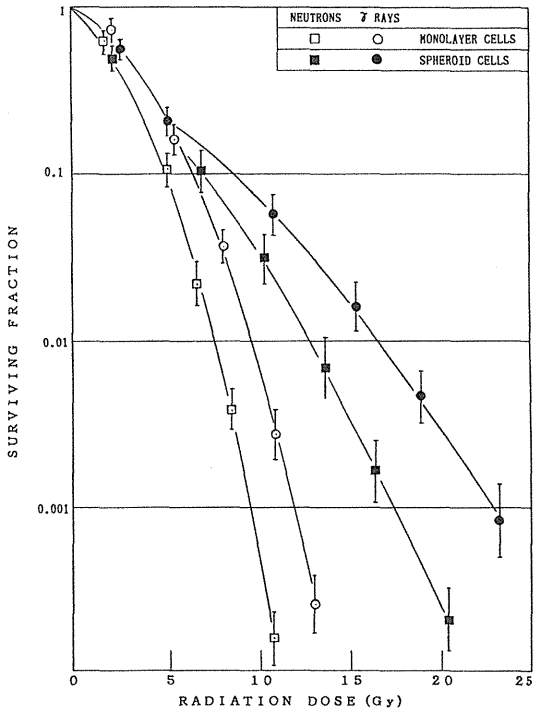

Fig. 5 Survival curves of cultured HMV-I cells after p (500)+U neutron irradiation (squares) in comparison with those after ^{137}Cs gamma ray irradiation (circles). Open and closed marks show data on monolayer and spheroid cells, respectively.

単層培養細胞（open marks）の中性子線照射生残率曲線においても肩が認められ（Dq＝2.3Gy, n＝8），1％生残率におけるRBEは1.24であった．また，スフェロイド細胞（closed marks）は中性子線に対しても明瞭な低感受性を示し，1％生残率でのRBEは1.29であった．

IV. 考　察

1. 線量率について

がん治療のためには，従来の放射線では1Gy/min以上の線量率を確保することが通常であり，特殊な場合を除けば照射時間を3分以内に抑えることが望まれる．本施設の中性子ターゲットが，中性子物理実験施設との共用という事情により，医療照射室の放射化を軽減するためには，ターゲットと照射室間に十分な遮蔽壁を設ける必要があり，これが線量率の低下を招いた．専用ターゲットを設けることとして，ターゲットより2m以内の距離で照射可能な施設であれば，このような中性子源により，約60cGy/minの線量率が確保されよう．もとより，医療専用ターゲットの設置も考えたが，このような特殊なターゲット設備の設計・製作とその後のメンテナンスに格別の配慮を要することから断念した．

2. 深部百分率について

現在，中性子線治療を行っている施設のうちの4施設は60数MeV陽子をベリリウム・ターゲットに入射して，ポリエチレン・フィルタで低エネルギー成分を減少させて，6MV強のX線相当の深部線量曲線をえており[23]，これまでの中性子線治療では，高い深部量百分率を示してきた．しかしながら，深部臓器がんの治療には10MeV以上のX線を使用する現状では，十分とは言えない．

今回の中性子線は，Fig. 3に示すように，従来報告された深部線量曲線と比較して明らかに深部線量を増大させるものである．γ線の混在については，このような透過力を示すエネルギーγ線が十分な線束で発生する可能性はないので，とくに深部においては中性子線量が大部分とみることができる．ウラニウムの核分裂中性子による低エネルギー成分をフィルタにより除去すれば，さらなる改善も期待できる．

3. 側方向線量分布について

これまでの中性子線についても，そのコリメータによる照射野辺縁は，$^{60}Co\gamma$線より不明瞭であったが，本中性子線ではさらに不明瞭である．この中性子線の透過力が高いので，コリメータ終端部の鉄中を通過する成分があることを示している．従来のものより長い1mの鉄コリメータを使用しており，線源より十分に距離があり，ほぼ平行ビームと見做せる条件であるから，さらに長いコリメータを用いても大きな改善は望みえない．

Fig. 4に示したopen and closed circlesはHMV-I細胞を側方向線量分布を測定した位置に設置して10Gy照射後の致死率を最大100％として，線量百分率と同様にリニアープロットしたものである．この細胞不活性化分布ではより明瞭にターゲット形状に一致した照射野を示した．

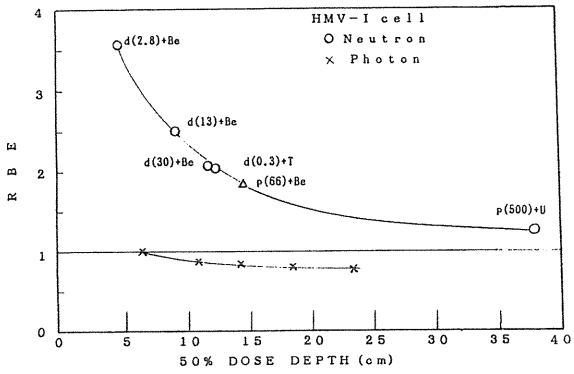

Fig. 6　RBE values on 1% cell survival of HMV-I cells for several neutron irradiations (open circles) plotted against 50% dose depths of these neutron beams in water compared with data for several photon beams (×marks) and with datum on V79 CH cells for p (66)+Be neutrons (open triangle)[23].

4. 生物学的効果比（RBE）について

本研究で使用したHMV-I細胞は，ヒト悪性黒色腫より培養系として確立[21]されてから約20年を経過し，300代以上の継代培養により，その放射線感受性は安定している．この間に数次のクローニングを行い雑菌の汚染を防いできた．これまでにもエネルギーの異なる各種中性子線について，その不活化RBEを求めてきたが[20]，それらの値を中性子線深部線量の50%線量深についてプロットしたものがFig. 6である．参考のためにFermi研究所（米国）の66MeV陽子＋Beターゲットによる V79CH 細胞の不活化よりえられているデータ（⊿）[24]も併せて示した．これらのデータと今回のものとは著しく異なるものであるが，図示するように50%線量深についてプロットした曲線上にスムースに合致する．対比すべき光子放射線についても，50%線量深の増加とともに線質の変化が認められる(×)．しかし，その変化は，中性子線におけるそれと比べて著しいものではない．従って，高エネルギー中性子線を導入して深部線量を改善すれば，RBEの減少を伴うことになる．

さて，多くのRBEの指標とともに酸素増感比（Oxygen Enhancement Ratio：OER）が培養細胞についていわゆるhypoxic chamberを用いて評価されてきたが，ここではがん治療効果を推定するために生体内細胞を近似する実験系としてスフェロイドを使用した．これは単層培養に用いたHMV-I細胞による多細胞系で，表層部を除けば低酸素状態にある[22]．Fig. 5に示した結果において，1%生存率におけるX線および中性子線のOERに対応する線量増加比は，それぞれ1.71および1.68であり，有意差は認められない．すなわち，X線に対して抵抗性の細胞は本中性子線に対しても抵抗性であることを示唆する．

このような，いわゆる超高エネルギー中性子線による生物効果が，これまでにも報告されている[25][26]．これらはCERNのシンクロサイクロトロン陽子線のベリリウムターゲット入射による最高600MeVおよび400MeV中性子線についてマウスの睾丸重量減少および白内障の発症におけるRBEを求めたものである．中性子線量率がそれぞれ14および5～6.5cGy/hrと低く，1Gy以下の照射による効果であるから，ただちに我々の結果と比較できないが，概して低エネルギー中性子線（1.5MeVおよびfission）と比べて低いRBE値をえているが，d-T中性子（15MeV）によるRBEとはほぼ等しく，睾丸重量減少で1.9～2.2，白内障発症で6と報告されている．なお，この中性子線のエネルギー分布には約200MeVに幅の広いピークがあり，よって，深部線量分布に急激がビルドアップを認めたとしている．しかし，最近の知見[27]や我々のスペクトルでは，このようなピークは認められず，線束はエネルギーの低下とともに単調に増大すると考えるのが妥当であろう．

V. 結　論

500MeV陽子線をウランターゲットに入射してえられる中性子線の線質について，次のような結果をえた．

1. ターゲットより約3mの前方照射野20×20 cm²における線量率は，平均2.4μAの陽子線入射について約15cGy/minであった．

2. 深部線量分布において表面より数cmに幅の広いピークが認められ，50%線量深は約38cmと推定された．

3. 鉄1mコリメータによっても，照射野辺縁は

従来の中性子線と比べて不明瞭であった.

4. 培養細胞HMV-Iの不活性化を指標としたRBEは，単層細胞で1.24，スフェロイド細胞で1.29であった.

これらの結果より，深部臓器がん治療のために高エネルギー中性子線の使用により，深部量百分率を改善することは，相対的に生物学的効果比の減少をもたらすこととなり，中性子線治療の本質的利点をある程度削減すると考えられる．また，中性子発生や照射野形成などに伴う技術的困難もあり，高エネルギー中性子線の導入には問題が多いと結論された.

本研究の遂行にあたり，放射線管理に関して，小林克巳，多田順一郎両氏にお世話頂いた．ビームの供給に関して高エネルギー物理学研究所の関係各位に，また測定作業に関して粒子線医科学センター各位に深甚の謝意を表する．この研究は科研費一般研究（B）（課題番号63480248）によった.

文　献

1) Medical Research Council Neutron Therapy Working Group: A comparative review of the Hammersmith (1971—75) and Edinburgh (1977—82) neutron therapy trials of certain cancers of the oral cavity, oropharynx, larynx and hypopharynx. Brit J Radiol 59: 429—440, 1986
2) Errington, R.D.: Advanced carcinoma of the paranasal sinuses treaten with 7.5 MeV fast neutrons, Bull. Cancer (Paris), 73: 569—576, 1986
3) Richard F, Renard L, Wambersie A: Current results of neutron therapy at the UCL, for soft tissue sarcomas and prostatic adenocarcinomas. Bull Cancer (Paris) 73: 562—568, 1986
4) Duncan W, Orr JA, Arnott SJ, et al: Fast neutron therapy for squamous cell carcinoma in the head and neck region: Results of a randomized trial. ibid 13: 171—178, 1987
5) Catterall M, Errington RD: The implications of improved treatment of malignant salivary gland tumors by fast neutron radiotherapy. ibid 13: 1313—1318, 1987
6) Saroja KR, Mansell J, Hendrickson FR, et al: An update on malignant salivery gland tumors treated with neutrons at Fermilab. ibid 13: 1319—1326, 1987
7) Pickering DG, Stewart JS, Rampling R, et al: Fast neutron therapy for soft tissue sarcoma. ibid 13: 1489—1496, 1987
8) Griffin BR, Laramore GE, Russell KJ, et al: Fast neutron radiotherapy for advanced malignant salivary gland tumors. Radiotherapy Oncology 12: 105—111, 1988
9) Breteau N, Destembert B, Favre A, et al: An interim assessment of the experience of fast neutron boost in inoperable rectal carcinomas in Orleans. Bull Cancer (Paris) 73: 591—595, 1986
10) Duncan W, Williams JR, Kerr GR, et al: An analysis of the radiation related morbidity observed in a randomized trial of neutron therapy for bladder cancer. Int J Radiat Oncol Biol Phys 12: 2085—2092, 1986
11) Battermann JJ, Mijnheer BJ: The Amsterdam fast neutron therapy project: A final report. ibid 12: 2093—2100, 1986
12) Duncan W, Orr JA, Arnott SJ, et al: An evaluation of fast neutron irradiation in the treatment of squamous cell carcinoma in cervical lymph nodes. ibid 13: 1793—1796, 0000
13) Russell KJ, Laramore GE, Krall JM, et al: Eight years experience with neutron radiotherapy in the treatment of stages C and D prostate cancer: Updated results of the RTOG 7704 randomized clinical trial. Prostate 11: 183—193, 1987
14) Schmitt G, Bamberg M, Budach V: Preliminary results of neutron irradiation of patients with spinal gliomas. Br J Radiol 60: 320—321, 1987
15) Maor MH, Gillespie BW, Peters LJ, et al: Neutron therapy in cervical cancer: Results of a phase III RTOG study. Int J Radiation Oncology Biol Phys 14: 775—891, 1988
16) Laramore GE, Griffeth JT, Boespflug M, et al: Fast neutron radiotherapy for sarcomas of soft tissue, bone, and cartilage: in press
17) Tsunemoto H, Morita S, Satho S, et al: Present status of fast neutron therapy in Asian countries, Strahlentheraple und Onkologie, 165: 330—336, 1989
18) 熊田俊明，佐々木寛，増田康博，他：スパレーション・パルス中性子源用劣化ウランターゲットシステムの安全解析，KEK Internal, 88—11, October, 1988
19) Ban S, Hirayama H: ICANS-IV (KEK, Oct 20—24, 1980) KENS Report II, 1981
20) Inada T, Kawachi K, Kanai T, et al: Inactivation of cultured human tumor cells irradiated by cyclotron neutrons and protons. J Ra-

diat Res 22 : 143—153, 1981
21) 春日　孟, 古瀬　健, 大沼直躬, 他：人癌培養細胞の放射線治療への応用, 医学のあゆみ, 90 : 326—335, 1974
22) Kubota N, Matsui K, Satoh S, et al : Radiation response of HMV-I human malignant melanoma cells grown in vitro as multicellular spheroids. J Radiat Res 25 : 215—224, 1984
23) Mijnheer BJ : Clinical dosimetry of high energy neutron beams : Future developments, Radiat. Protection Dosimetry 23 : 373—380, 1988
24) Hall EJ, Withers HR, Geraci, J.P, et al : Radiobiological intercomparisons of fast neutron beams used for therapy in Japan and the United States. Int J Radiat Oncol Biol Phys 5 : 277—283, 1979
25) DiPaola M, Caffarelli V, Coppola M, et al : Biological response to varions neutron energies from 1 to 600 MeV I. Testes weight loss in mice. Radiat Res 84 : 444—452, 1980
26) DiPaola M, Coppola M, Baarli J, et al : Biological responses to various neutron energies from 1 to 600 MeV II. Lens opacification in mice. Radiat Res 84 : 453—461, 1980
27) Nakamura T, Uwamino Y : Neutron energy spectra and yields produced from thick targets by light-mass heavy ions. Proc. Advisory Group Meeting on Properties of Neutron Sources. IAEA-TECDOC-410 : 80—89, 1987

Nuclear Science Applications
1991, Vol. 4, pp. 47–56
Reprints available directly from the publisher
Photocopying permitted by license only

REPAIR OF SUBLETHAL AND POTENTIALLY LETHAL DAMAGE IN MOUSE SQUAMOUS CELL CARCINOMA CELLS FOLLOWING MIXED NEUTRON AND X-RAY IRRADIATION: RELEVANCE TO EARLY CF-252 IMPLANT

H. MAJIMA,[1,2,3] H. OHARA,[4] M. URANO,[3] H. MAEZAWA[3] and Y. MARUYAMA[3]

[1] *Nihon University, School of Dentistry, Tokyo, Japan*
[2] *Department of Radiation Biology, Tokyo University, Tokyo, Japan*
[3] *Department of Radiation Medicine, University of Kentucky Medical Center, Lexington, Kentucky U.S.A.*
[4] *National Institute of Radiological Sciences, Chiba, Japan*

The effects of mixed neutron–photon irradiations on the cultured murine squamous cell carcinoma Sq-1979 cells were studied. Neutrons were produced by the NIRS cyclotron by bombarding 30 MeV deuterons on a beryllium target and photons were 200 kVp X-rays. The cells were irradiated with split-dose schedules to investigate SLD repair. Time-recovery curves were obtained in 4 irradiation schedules, i.e., X–X, X–N, N–X, N–N, using X-ray and neutron doses of 6 Gy and 4 Gy respectively. SLD repair was maximal following split X-ray doses. The use of mixed beams inhibited the repair of sublethal damage and this inhibition was maximal for two neutron doses. Mixed beam irradiations (X–N or N–X) given with a treatment interval of 3 hrs inhibited SLD repair. At a treatment interval of 22 hours N–X and N–N regimens continued to demonstrate a synergistic effect. The X–N regimen lost the synergism within 22 hours, but N–X continued to show the synergism. PLD repair was also inhibited by neutron irradiation. The results indicate that the synergistic effect between Low- and High-LET mixed beam may be related to the cellular capability for repairing SLD and PLD and that the use of neutrons as the priming or first dose had a much greater and prolonged effect.

INTRODUCTION

Repair of the sublethal damage (SLD) has been observed in cells irradiated with photons[1] while this type of repair is non-existent or minimal[2–7] in cells irradiated with high-linear energy transfer (LET) radiation such as neutrons. Other biological effects of High-LET radiations include lower OER,[8,9] inhibition of PLD repair,[10,11] large RBE, and minimal dependency of radiation sensitivity on cell cycle.[12–14] These biological features favor use of High-LET radiations for radiotherapy for malignant tumors. It has been reported, however, that High-LET radiations can cause higher rates of normal tissue injury[15–17] compared to low-LET photons. Mixed Low- and High-LET radiation therapy was proposed to reduce this problem and was tested in the U.S.A. and Japan.[18,19] Likewise, Cf-252 has been used with success for radiotherapy.[20] Its radiations are mixed and Cf-252 is used in mixed sequences with photon therapy, but the sequence can greatly affect outcome.

The biological effects of mixed beam irradiation have been studied by Barendsen *et al.* who reported that the killing effects on cells by mixed

alpha-particles and X-rays were synergistic.[21] In contrast, cell killing by mixed neutrons and X-rays[22] and mixed Neon particles and X-rays[23] were additive. The results of Railton *et al.*[4] and Durand and Olive[24] show that SLD repair in cells irradiated with mixed neutrons and X- or gamma-rays at intervals of 3 or 4 hours, was inhibited regardless of the sequence of the irradiations. Ngo *et al.*[23] reported that the synergistic effect on cell killing between mixed Neon particles and X-rays was lost when the fractionation interval between both irradiations was prolonged.

These results suggest that the synergistic effect between the two mixed radiations is related to effects on the capability of cells to repair SLD.

We investigated the effect of mixed radiations using 6 Gy of photons and 4 Gy of neutrons since these doses are isoeffective.[25] Fractionated irradiations were carried out using X-rays, neutrons, and mixed neutrons and X-rays, and the kinetics of SLD repair were investigated.

MATERIALS AND METHODS

Cells and Culture

Cell Culture: Sq-1979 (derived from C3H mouse squamous cell carcinoma) cells were cultured in Eagle MEM medium supplemented with 10% fetal calf serum at 37°C in 95% air and 5% CO_2. The population doubling time of cells was about 14 hours and plating efficiency for colony formation was 30–50%.

Preparation of Sample: Exponentially growing cells were trypsinized with trypsin-EDTA solution and resuspended in complete medium. Cells were plated in plastic flasks (Falcon #3012) and incubated in a CO_2-incubator for 2–3 hours at 37°C to allow attachment to the flask. After irradiation with X-rays or neutrons, cells in the flasks were incubated to allow the colony formation.

For experiments of PLD repair we used cells in the density-inhibited stationary phase. Immediately after irradiation cells were incubated in air plus 5% CO_2. After various post-irradiation times, cells were trypsinized to a single cell suspension and seeded to assay viability using colony formation assay.

Irradiation

X-rays: An X-ray unit (Shimazu, Shin-ai #259) was operated at 200 kVp and 20 mA with 0.5 mm Cu plus 0.5 mm Al filter (H.V.L. = 1.2 mm Cu.) at a source surface distance of 50 cm. Dose rate was 1.0 Gy/min. Samples were irradiated on a rotating table at room temperature.

Neutrons: Thirty MeV deuterium-on-beryllium fast neutron beams produced by the NIRS cyclotron were used. Two lucite plates (10 mm thick) each were placed above the samples. Dose rate was about 0.7 Gy/min (0.1 ml ionization chamber, EG & G) at room temperature.

RESULTS

1) Cell Survival After X-rays or Neutrons Irradiation:

Survival curves were fitted to the linear-quadratic (LQ) model in the low dose region (0–9 Gy for X-rays; 0–6 Gy for neutrons) and the multitarget model in the high dose region (9–15 Gy for X-rays; 5–9 Gy for neutrons) (Figure 1). RBE was

3.72 at 90% survival level, 2.03 at 50%, 1.52 at 10% and 1.45 at 5%, respectively. D_0 was 1.38 Gy and n was 20 for X-rays; for fast neutrons, $D_0 = 0.81$ Gy and $n = 52$. By the LQ model for X-rays, $\alpha = 0.035\ \text{Gy}^{-1}$; $\beta = 0.039\ \text{Gy}^{-2}$; for neutrons, $\alpha = 0.299\ \text{Gy}^{-1}$ and $\beta = 0.038\ \text{Gy}^{-2}$.

2) PLD Repair of Cells Irradiated with X-Rays or Neutrons:

Sq-1979 cells in the stationary phase were exposed to 12 Gy of X-Rays or 8 Gy of neutrons. Single dose survival curves showed that these doses were isoeffective. After irradiation, the cells were incubated up to 8 hours.

Results are shown in Figure 2. The surviving fractions of cells exposed to neutrons were nearly constant during the incubation period for 8 hours. The survival of cells irradiated with X-rays and incubated for 2 hours was two times higher compared to survival of cells plated immediately after irradiation, indicating that these cells repaired PLD.

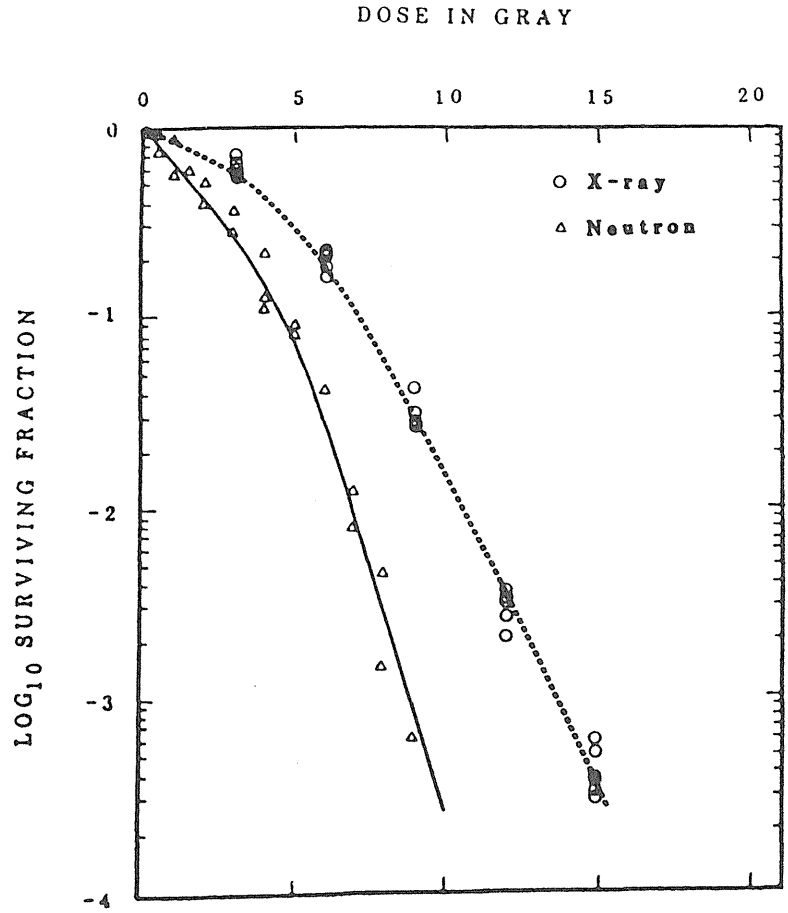

FIGURE 1 Dose effect–survival curves of Sq-1979 cells vs various doses of NIRS cyclotron-produced 30 MeV ($d^+ \rightarrow Be$) neutron, and 200 KVp X-rays. Curves were fitted by linear-quadratic model for low dose level, i.e., 0 ~ 9 Gy for X-rays, and 0 ~ 6 Gy for neutrons, and by multi-target model for high dose level, i.e., 9 ~ 15 Gy for X-rays, and 5 ~ 9 Gy for neutrons. From Majima[25] with permission of Nippon Acta Radiol.

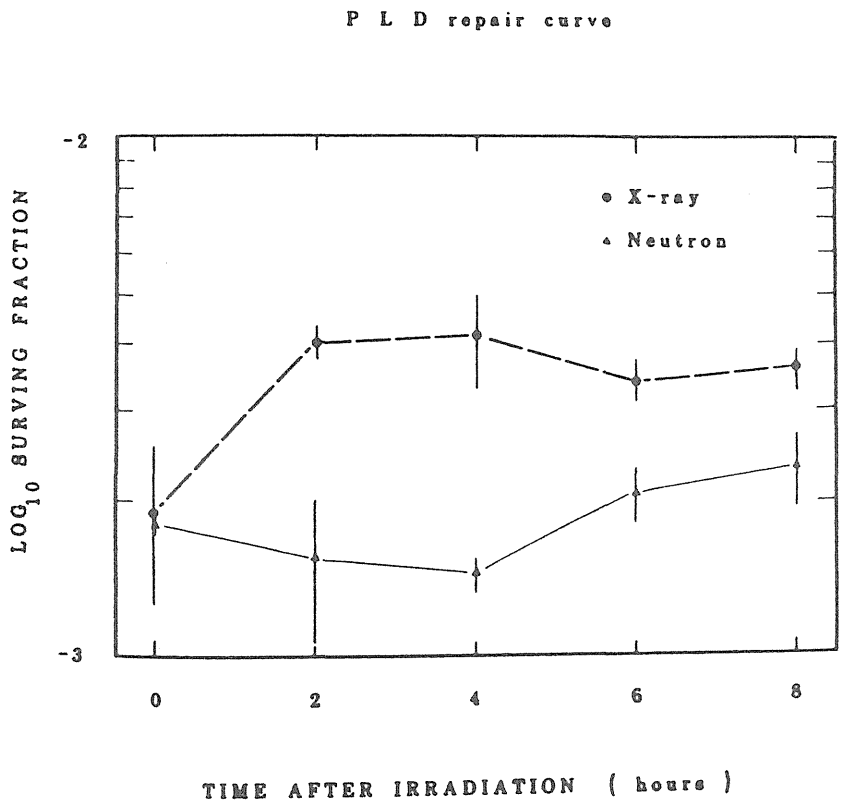

FIGURE 2 Repair of potentially lethal damage (PLD) in Sq-1979 cells. The cells were irradiated with 200 kVp X-rays (12 Gy) or NIRS 30 MeV ($d^+ \rightarrow Be$) neutrons (8 Gy) in the density inhibited stationary phase of growth and subcultured up to 8 hrs after the exposure. The bars indicate the standard deviations. From Majima[25] with permission of Nippon Acta Radiol.

3) Repair of SLD in Cells Following Irradiation by X-rays, Neutrons and Mixed Neutrons and X-rays:

Split-dose experiments were carried out in 4 irradiation schedules: (1) The D_1 priming radiation and the second D_2 test dose were X-rays (X–X), (2) X-rays and neutrons (X–N), (3) neutrons and neutrons (N–N) and (4) neutrons and X-rays (N–X). Six Gy of X-rays and 4 Gy of neutrons were given. Figure 3 shows the time-survival curves for SLD repair in the 4 irradiation schedules.

Following X–X irradiation, cell survival rose rapidly, reached a maximum at 3 hours and became constant at 10 hours. Following N–N the recovery curve showed no peak at 3 hours. The survival at 22 hours was lowest in this schedule compared to those in the other 3 irradiation schedules. The survival at 30 hours in the N–N schedule was about 30% of that in the X–X schedule.

The shape of the recovery curve in the X–N schedule was similar to that in the X–X schedule but the peak at 3 hours was smaller than the peak in the X–X schedule. Survival increased with increasing time intervals from 5 hours to 22 hours, and reached almost the same level as in the X–X schedule at 22 hours.

There was no rise in survival at 3 hours in the N–X schedule. Survival increased very slowly with increasing time to 22 hours.

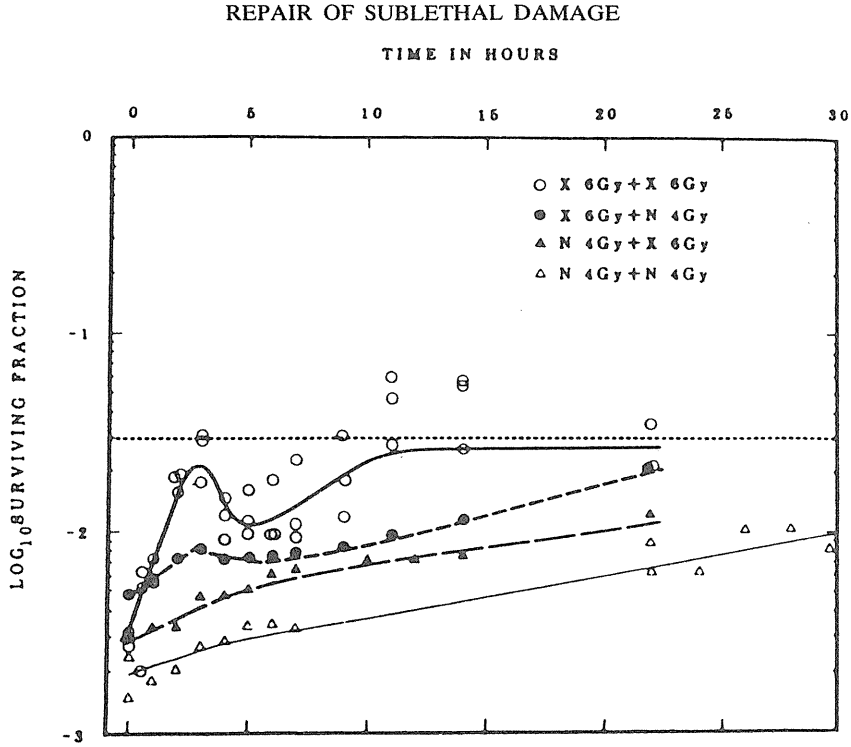

FIGURE 3 Spilt-dose experiments with Sq-1979 cells. Iso-effect dose, i.e., 6 Gy for 200 kVp X-rays and 4 Gy for 30 MeV ($d^+ \rightarrow Be$) neutrons, were chosen for each fraction of doses. The survival changes in four groups, X–X (○), X–N (●), N–X (▲), N–N (△), were obtained as a function of various time intervals. Short dashed line shows theoretical full level of SLD repair. From Majima[25] with permission of Nippon Acta Radiol.

4) Dose Survival Curves Following the Second Dose Given 3 or 22 Hours After Priming Dose:

Dose survival curves to the second dose were studied at 3 or 22 hours after the first priming dose[25] (Figures 4, 5). D_1 of 6 Gy X-rays or 4 Gy of neutrons were followed by graded doses of X-rays or neutrons. Two hypothetical curves are also presented in the figures: one is the curve for cells which fully repaired SLD and the other is the curve where cells did not repair SLD. In the X + N, N + X and N + N schedules with a 3 hour interval (Figure 4), the experimental points fell between these two hypothetical curves. The 22 hour survival curves following a D_1 of X-rays showed complete repair while those following a D_1 of neutrons demonstrated a persistent defect and deficiency for SLD repair. Cells were irradiated with a priming dose of 6 Gy X-rays or 4 Gy neutrons and received graded test doses of X-rays or neutrons (X + N or N + X) as shown for 22 hours in Figure 5. The survival curve for the N + X schedule was steeper at 22 hours after neutrons than after initial irradiation with X-rays.

The data show that after the priming X-radiation exposure, SLD repair capacity was intact and cellular recovery complete. After the priming neutron irradiation, recovery and SLD repair were always incomplete and fell below the full recovery curves. The neutron SLD lesions were still present 22 hours later (Figure 5). Similar observations have been noted by others.[23,24]

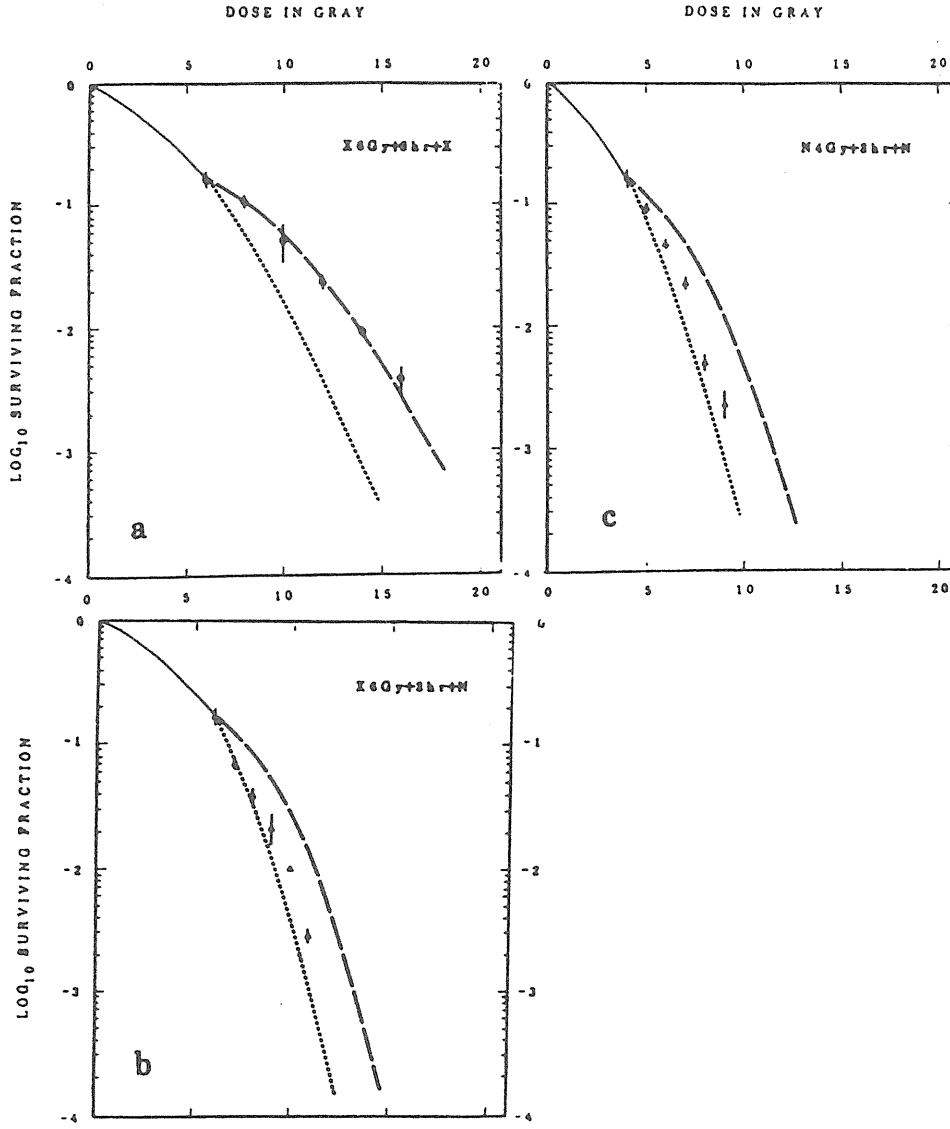

FIGURE 4 Survival data of Sq-1979 cells irradiated with graded test doses of neutrons or X-rays with 3 hrs. incubation after priming exposure of X-rays (6 Gy) or neutrons (4 Gy). Long dashed lines show theoretically defined curves for full repair, and dotted lines indicate no repair. The bars indicate the standard deviations. From Majima[25] with permission of Nippon Acta Radiol.

DISCUSSION

The RBE of fast neutrons produced by the NIRS cyclotron varied between 1.45–3.72 depending on the size of dose per fraction.[27,28] The survival curve of Sq-1979 cells irradiated with X-rays had a wide shoulder in the low dose region. There was a narrow shoulder in the survival curve for neutrons for these cells.

Damage produced in Sq-1979 cells by X-rays were of the SLD type and

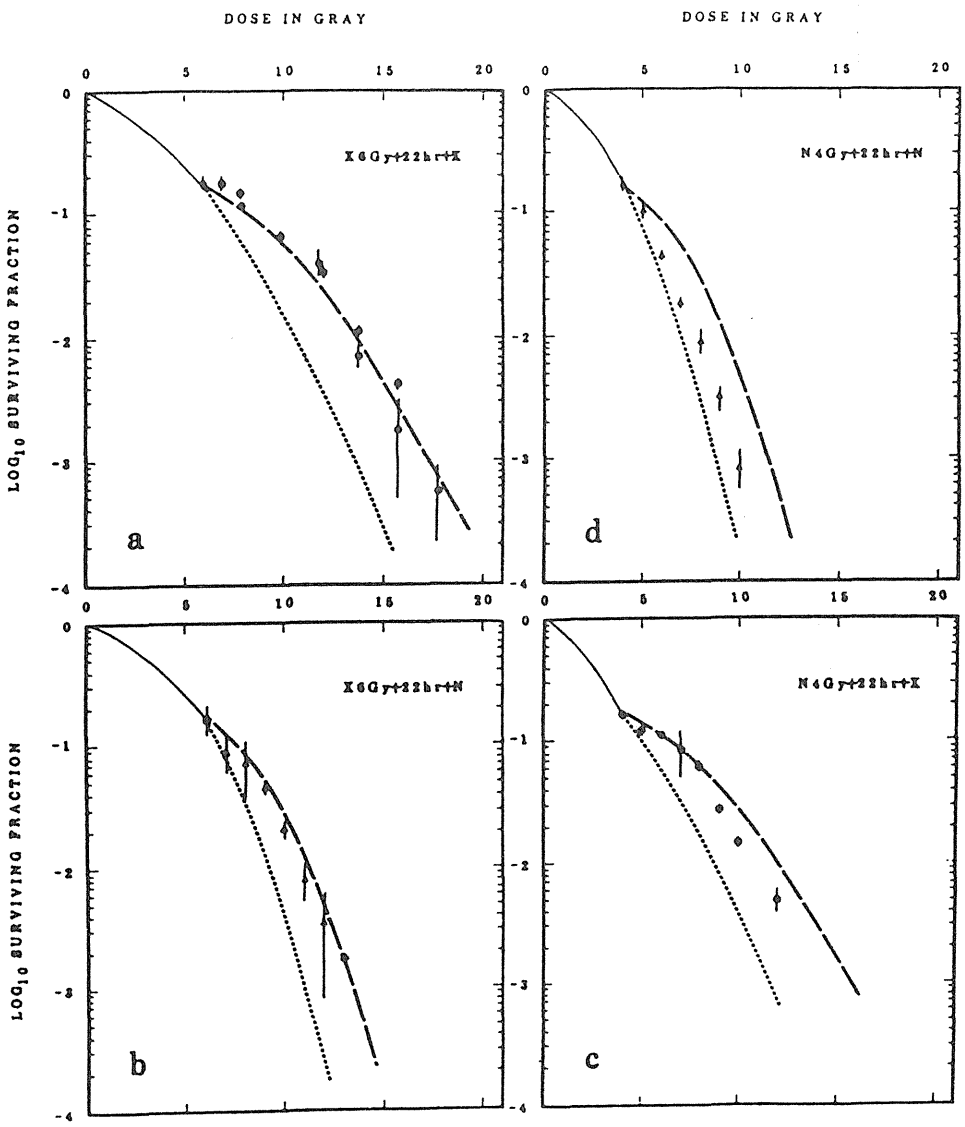

FIGURE 5 Survival data of Sq-1979 cells irradiated with graded test doses of neutrons or X-rays 22 hrs incubation after priming exposure of X-rays (6 Gy) or neutrons (4 Gy). Long dashed lines show theoretically defined curves for full repair, and dotted lines indicate no repair. The bars indicate the standard deviations. From Majima[25] with permission of Nippon Acta Radiol.

repairable when X-rays were the priming dose for the 4 irradiation schedules. Repair was complete after X-irradiation. Survival after the second irradiation depended on the initial radiation and the test irradiation schedule (X + X, X + N, N + X, N + N), providing that adequate time for SLD repair was allowed. When X-ray was the priming radiation in the mixed beam irradiation, full or partial repair was observed at 3 hours.

When the priming dose was neutrons there was no SLD repair. It is well known

that SLD damage produced by neutrons are not repaired.[2–7,11] When neutrons were the priming radiation no survival peak was observed at 3 hours. When neutrons were the priming radiation the survival to graded doses of X-rays was between the theoretically defined curves *for* full repair and no repair *for* at least 22 hrs. These results indicate that the effects on cell survival of mixed beam was synergistic but the magnitude of this synergism depended on the LET of the priming radiation, the time interval of the split doses and the type of second radiation.

When neutrons were given first, the rise in survival i.e., SLD repair, was not observed and survival increased only slowly with time. This indicates that the SLD produced by neutrons was repaired at a slow rate and with low efficiency compared to photon-induced SLD repair. The slow increase in survival may be partially due to cell repopulation. The present results indicate that SLD repair following initial neutron irradiation could be greatly inhibited for long periods of time.

PLD repair[29] was observed in Sq-1979 cells irradiated after X-rays (Figure 2) but no PLD was observed after neutrons (Figure 2). This indicates that PLD in Sq-1979 cells was repaired after Low-LET radiation but no repair occurred after neutrons. Similar results have been reported for neutrons by Gragg *et al.*[30] and for Cf-252 by Schroy *et al.*[31]

Figure 4 shows the survival of cells irradiated with graded test doses 3 hours after the priming exposure. The slope of the survival curve following graded neutron doses given immediately after a X-ray dose of 6 Gy were steeper and indicates that the effects of mixed irradiation with the two different radiations were synergistic. Railton *et al.*[4] investigated the survival curves of cells after simultaneous irradiation with a beam with X-rays to High-LET ratio of 50%:50% or 75%:25%. Their results showed that the steepness of the survival curves was increased and the width of the shoulder reduced with increasing proportion of High-LET radiation. Ngo *et al.*[23] reported that the steepness of the survival curve of cells irradiated with 50%:50% mix was greater than that obtained by assuming that the effect on cell killing was additive.

In the present studies, when cells were exposed to mixed X-rays and neutrons the cell killing effect by the mixed radiations was synergistic. Railton *et al.*[4] and Ngo *et al.*[23] observed that the survival curve was steeper with increasing proportion of High-LET radiation in the total dose from the two radiations.

The results in the present experiments indicate that the survival of cells irradiated with mixed X-rays and neutrons changed according to the proportion of high-LET and low-LET radiations, the type of initial radiation, the time interval between 2 doses and the radiation dose. The damage produced by X-rays was not independent of those by neutrons i.e., they were synergistic. The independence of damage produced by each radiation increased with an increase in the time interval between the split doses, up to 22 hours, and a priming neutron dose greatly inhibited the repair of SLD to subsequent X-rays. The SLD produced by the priming X-rays were least repairable when the high-LET irradiation followed X-rays in the split schedule.

We conclude that:

1) No PLD repair was observed in cells exposed to neutrons.
2) SLD induced by neutrons repaired only slowly.
3) SLD repair was incomplete after neutrons for at least 22 hours (when the neutrons were given first).

Mixed X-rays and neutrons produced:

1) Synergistic cell killing if two doses were given with an interval of 3 hrs. regardless of the priming radiation.
2) Synergistic cell killing, when neutrons were the priming radiation were observed for treatment intervals up to 22 hrs.

These results are highly pertinent to the clinical experiences using Cf-252 neutrons.[20] There, up-front neutrons followed by fractionated photon therapy produced much better results than delayed boost neutrons.[32] The synergism between neutrons and photons used in the early implant schedule was supported by the finding of a long-lived suppression of SLD and PLD repair induced by the initial high-LET neutron treatment. This synergism between neutrons and photons may have contributed to increase the efficacy of subsequent photon irradiations in clinical Cf-252 radiotherapy trials.[32]

ACKNOWLEDGEMENTS

We thank Mrs Jean Kennedy and Ms Rita House for expert assistance.

REFERENCES

1 Elkind, M. M. and Sutton, H. (1960), *Radiat. Res.*, **13**, 556.
2 Schneider, D. O. and Whitmore, G. G. (1963), *Radiat. Res.*, **18**, 286.
3 Nias, A. H. W., Greene, D. and Major, D. (1971), *Int. J. Radiat. Biol.*, **20**, 145.
4 Railton, R., Lawson, R. C. and Porter, D. (1975), *Radiat. Biol.* **27**, 75.
5 Hall, E. J., Roizin-Towle, L., Theus, R. B. and August, L. S. (1975), *Radiology*, **117**, 173.
6 Ngo, F. Q. J., Han, A., Utsumi, H. and Elkind, M. (1977), *Int. J. Radiat. Oncol. Biol. Phys.*, **3**, 187.
7 Durand, R. E. and Olive, P. L., (1977), *Brit. J. Radiol.*, **50**, 423.
8 Raju, M. R. and Jett, J. H. (1974), *Radiat. Res.*, **60**, 473.
9 Barendsen, G. W., Koot, C. J., van Kersen, G. R. *et al.* (1966), *Int. J. Radiat. Biol.*, **10**, 317.
10 Hall, E. J. and Kraljevic, U. (1976), *Radiology*, **121**, 731.
11 Shipley, W. U., Stanley, J. A. and Courtenay, V. D. (1975), *Cancer Res.*, **35**, 932.
12 Withers, H. R., Mason, K., Dubravsky, N., Barkley, H. T., Brown, B. W. and Smathers, J. B. (1974), *Cancer*, **34**, 39.
13 Hall, E. J., Bird, R. P., Rossi, H. H., *et al.* (1977), *Radiat. Res.*, **70**, 469.
14 Raju, M. R., Bain, E., Carpenter, S. G. and Jett, J. (1980), *Radiat. Res.*, **84**, 152.
15 Stone, R. S. (1948), *Am. J. Roentgenol Radium Therapy*, **59**, 771.
16 Hussey, D. H., Fletcher, G. H. and Caderao, J. B. (1974), *Cancer*, **34**, 65.
17 Catterall, M. (1977), *Int. J. Radiat. Oncol. Biol. Phys.*, **3**, 247.
18 Hussey, D. H., Parker, R. G. and Rogers, C. C. (1977), *Int. J. Radiat. Oncol. Biol. Phys.*, **3**, 255.
19 Peters, L. J., Hussey, D. H., Fletcher, G. H., *et al.* (1979), *Am. J. Roentgenol*, **132**, 637.
20 Maruyama, Y. (1984), *Nucl. Sci. Appl.*, **1**, 677.
21 Barendsen, G. W., Beusker, T. L. J., Vergroesen, A. J. and Budke, L. (1960), *Radiat. Res.*, **13**, 841.
22 Masuda, K. (1970), *Radiat Res.*, **11**, 107.
23 Ngo, F. Q. H., Blakely, E. A. and Tobias, C. A. (1981), *Radiat. Res.*, **87**, 59.
24 Durand, R. E. and Olive, P. L. (1983), *Int. J. Radiat. Biol.*, **30**, 539.
25 Majima, H. (1983), *Nippon Acta. Radiat.*, **43**, 1307.
26 Todd, P., Geraci, J. P., Furchinitti, P. S., Rossi, R. M., Mikage, F., Theus, R. B. and Schroy, C. B. (1978), *Int. J. Radiat. Oncol. Biol. Phys.*, **4**, 1015.
27 Ohara, H., Mikage, F. and Maruyama, Y. Presented at the first "High LET and Allied Area in Radiotherapy" seminar under the US-Japan Cooperative Cancer Research Program, May 22–23, 1979, Kyoto University, Kyoto, Japan.

28 Urano, M., Nesumi, N., Anod, K., Koike, S. and Ohnuma, N. (1976), *Radiology,* **118,** 447.
29 Little, J. B., Hahn, G. M., Frindel, E. and Tubiana, M. (1973), *Radiology,* **106,** 689.
30 Gragg, R. L., Humphrey, R. M. and Meyn, R. E. (1977), *Radiat. Res.*, **71,** 161.
31 Schroy, C. B., Goud, S. N., Magura, C., Feola, J. M. and Maruyama, Y. (1986), *Nucl. Sci. Appl.*, **2,** 743.
32 Maruyama, Y., Berner, B. and Feola, J. (1989), *Endocuriether. Hypertherm. Oncol.*, **5,** 39.

RADIATION RESEARCH 123, 182–191 (1990)

Chromosome Aberration Frequencies Produced by a 70-MeV Proton Beam

SHO MATSUBARA,* HIROSHI OHARA,† TAKESHI HIRAOKA,† SACHIKO KOIKE,† KOICHI ANDO,† HIROSHI YAMAGUCHI,† YUJI KUWABARA,* MASAO HOSHINA,* AND SOJI SUZUKI*

*Department of Radiology, Tokyo Medical and Dental University, School of Medicine, Tokyo, and †National Institute of Radiological Science, Chiba, Japan

MATSUBARA, S., OHARA, H., HIRAOKA, T., KOIKE, S., ANDO, K., YAMAGUCHI, H., KUWABARA, Y., HOSHINA, M., AND SUZUKI, S. Chromosome Aberration Frequencies Produced by a 70-MeV Proton Beam. *Radiat. Res.* 123, 182–191 (1990).

The effectiveness of a 70-MeV proton beam in the induction of chromosome aberrations was studied. We employed peripheral lymphocytes and analyzed the frequencies of dicentrics and rings after irradiation at doses ranging from 0.1 to 8.0 Gy at various depths within a Lucite phantom. The frequency of chromosome aberrations after irradiation with an unmodulated proton beam at 5 mm showed a dose–response relationship similar to that of ^{60}Co γ rays. However, irradiation at greater depths with the spread-out Bragg peak induced higher aberration frequencies at doses lower than those with γ rays. Furthermore, the distribution curve of chromosome aberration frequencies as a function of depth was found to be slightly different from the physically measured depth–dose curve. With the spread-out Bragg peak the biological effects were more marked at greater depths, resulting in a distribution of relative biological effectiveness values. The results obtained from chromosome aberration analysis may not be related directly to those for the relationship between dose and cell killing. Slight differences in values for relative biological effectiveness due to the change of dose and site of proton beam irradiation may not be important for practical proton beam therapy, but may be important in the prevention of late radiation injuries.

INTRODUCTION

It is widely believed that the greatest advantage of a high-energy proton beam in radiotherapy is its precise and selective spatial dose distribution, although its relative biological effectiveness (RBE) has been considered to differ little from that of a photon beam. The radiation dose delivered by a proton beam has a sharp maximal point, called the Bragg peak, due to particle deceleration, and shows a low level of lateral scatter. For radiotherapy (*1–7*), by varying the energy and the number of protons accelerated, the Bragg peak can be shaped to deliver homogeneous doses of radiation to irregularly outlined three-dimensional volumes. Values found in a number of studies undertaken to investigate the RBE of protons, mostly by assessing the cell-killing effect, have ranged from about 0.8 to 2.0 (*8–15*). A survey of RBE values reported for high-energy protons indicates that RBE is a function of the biological end point as well as beam parameters (*9–12*). Chromosome analysis using peripheral lymphocytes is now accepted as a sensitive and reliable indicator of biological effect (*6, 8, 16–22*). No effect of spreading the Bragg peak of the proton beam was detected using cell killing as the end point. In this study, we have employed analysis of chromosome aberrations to detect differences in the effects of the different segments of a 70-MeV proton beam.

MATERIALS AND METHODS

Dose Distribution and Dosimetry

A cyclotron unit at the National Institute of Radiological Science, Chiba, was used in this study. A parallel plate ionization chamber with a guard plate was employed to determine the absorbed dose and dose distribution. This chamber (FWT Model EIC-1) was made of A150 plastic and was small in size and filled with methane-based tissue-equivalent gas (TE). Based on the calibration of ^{60}Co γ rays, the active collecting volume of the chamber was determined to be 0.348 ml. The proton beam with a maximum initial energy of 70 MeV from the unit demonstrated a sharp Bragg peak at 31.8 mm in the Lucite phantom (Fig. 1). In Fig. 2, the relative dose as a function of depth for a Bragg peak, spread out and flattened by a range modulator, is shown. The physical measurement of dose distribution in the spread-out peak was made at 0.5-mm increments in depth in the Lucite phantom located behind a range modulator which consisted of a rotating wheel with blades of various thickness. Mean dose-averaged values for linear energy transfer (LET) of the modulated beam were calculated using Janni's stopping-power table (*24*). The marked increase in LET values observed with increase in depth, even after beam modulation (Fig. 3), is considered due to the significant dependence of stopping power on proton energy. The sharp change in the curve, calculated as a function of depth (Fig. 3), corresponds to the build-up point on the depth–dose curve in Fig. 2.

0033-7587/90 $3.00

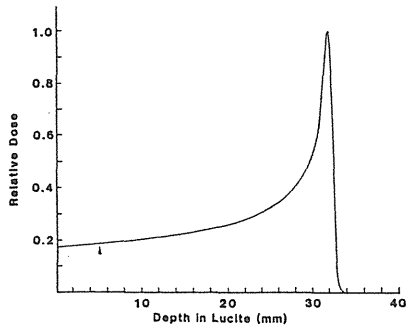

FIG. 1. Depth–dose distribution of a 70-MeV proton beam in an unmodulated form within a Lucite phantom. The arrowhead indicates the position at which the blood sample was irradiated to obtain a dose–response relationship for chromosome aberrations.

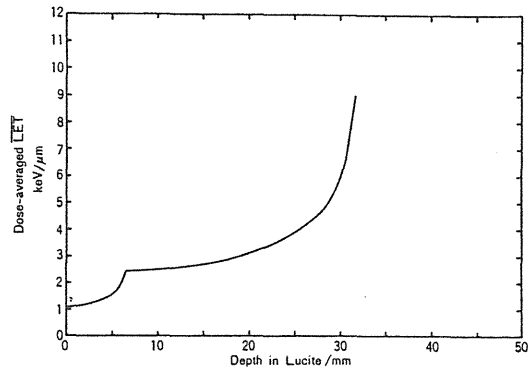

FIG. 3. Mean dose-averaged LET values of the 70-MeV modulated proton beam were calculated using Janni's stopping-power table (*24*). LET values of the modulated beam are clearly demonstrated to increase with increasing depth.

Exposure to Proton Beam

Venous blood was drawn from healthy 20-year-old donors who had no history of exposure to ionizing radiation, except for routine chest X-ray examinations. The heparinized blood was irradiated in small plastic tubes (outer diameter 5.3 mm; inner diameter 4.0 mm; No. 1693, Shibata) set in a special stand of a Lucite phantom. Employing modulated as well as unmodulated beams, we irradiated 0.3-ml blood samples in a central portion of a 4 × 4-cm broad-beam irradiation portal at a distance of 6.0 m from the 1-mm aluminum scattering foil. The plastic tube was 2 cm long, and the dose distribution was quite uniform, varying not more than 1.0%. The dose rates we used were 2.0 and 6.0 Gy per minute.

Dose–response relationships at various depths. Irradiation was performed to obtain the dose–effect relationship of chromosome aberration frequencies in blood samples in small plastic tubes placed in a Lucite phantom at depths of 5, 15, and 25 mm. The depths at which the blood was irradiated were obtained by using the Lucite absorbers, as illustrated in Fig. 4. The irradiation at the 5-mm position (a) was performed using only the unmodulated beam, but the modulated beam was used at 15 mm (b) and 25 mm (c). The radiation doses we employed were 0.1, 0.2, 0.5, 1.0, 2.0, 3.0, 4.0, 6.0, and 8.0 Gy at a dose rate of 2.0 Gy per minute. The dose–effect relationship thus obtained was then compared with that observed after irradiation with 0.1, 0.2, 0.3, 0.5, 1.0, 2.0, 3.0, 4.0, 6.0, and 8.0 Gy of ^{60}Co γ rays at a dose rate of 0.8 Gy per minute.

Depth–dose distribution within the phantom. The whole blood in small plastic tubes was exposed to fixed proton beam doses, i.e., radiation doses of 1.0 and 2.5 Gy were used in the first experiment and doses of 4.0 and 6.0 Gy in the second, to determine the change in RBE values derived from chromosome aberration frequencies induced in samples at various depths within the phantom. The dose rate was 6.0 Gy per minute. The depths as arranged by the placement of absorbers were 10, 17, 22, 26, 29, 31, and 32 mm. Irradiation was at room temperature, and blood culture was started within 2 h of the completion of irradiation.

Lymphocyte Culture, Slide Preparation, and Chromosome Analysis

After irradiation, the blood was cultured in 5 ml RPMI-1640 culture medium with 1 ml fetal bovine serum after the addition of 0.2 ml phytohe-

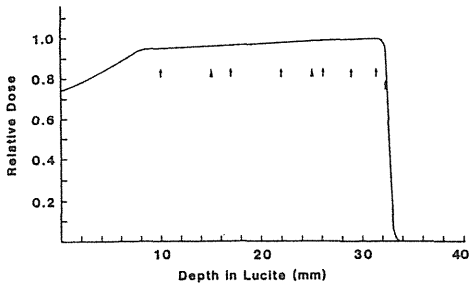

FIG. 2. Depth–dose distribution of a 70-MeV proton beam in a modulated form within a Lucite phantom. The spread-out Bragg peak is illustrated. The arrowheads indicate the positions at which blood samples were irradiated to obtain dose–response relationships of chromosome aberrations. Arrows indicate the positions at which blood samples were irradiated to obtain RBE values based on chromosome analysis.

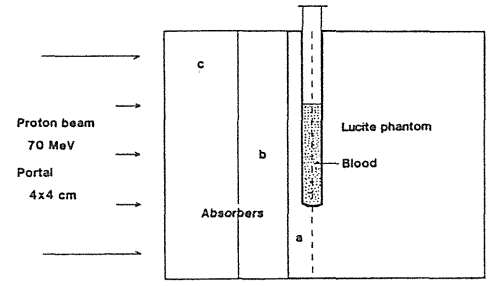

FIG. 4. Plastic tubes of 4-mm inside diameter containing the blood samples were placed in a Lucite phantom and irradiated with a 70-MeV proton beam through a lateral 4 × 4-cm portal. The depths at which the blood samples were irradiated were arranged using absorbers b and c, and the dose–response relationship was obtained. To investigate the depth–dose relationship, various other kinds of absorbers were used.

TABLE I

Distributions of Dicentrics and Rings among the Cells Irradiated with 70-MeV Proton Beams at Depth of 5 mm

Radiation dose (Gy)	Number of cells scored	Number of dicentrics and rings	Number of cells with indicated number of dicentrics and rings								Mean (dicentrics and rings per cell) ± SE	σ^2/Y	U
			0	1	2	3	4	5	6	7			
0.1	600	4	596	4							0.007 ± 0.003	0.99	−0.10
		(2)[a]	(598)	(2)							(0.003 ± 0.002)	(1.00)	(−0.04)
0.2	400	4	396	4							0.01 ± 0.005	0.99	−1.23
		(0)	(400)	(0)							(0)	—	—
0.5	300	12	288	12							0.04 ± 0.01	0.96	−0.47
		(2)	(298)	(2)							(0.007 ± 0.005)	(1.00)	(−0.06)
1.0	300	18	282	18							0.06 ± 0.01	0.94	−0.72
		(4)	(296)	(4)							(0.013 ± 0.007)	(0.99)	(−0.14)
2.0	100	36	70	25	4	1					0.36 ± 0.06	1.04	0.29
		(7)	(93)	(7)	(0)	(0)					(0.07 ± 0.03)	(0.94)	(−0.46)
3.0	100	60	55	32	11	2					0.60 ± 0.08	0.98	−0.14
		(10)	(90)	(10)	(0)	(0)					(0.10 ± 0.03)	(0.91)	(−0.68)
4.0	100	96	38	35	21	5	1				0.96 ± 0.09	0.92	−0.5
		(18)	(84)	(14)	(2)	(0)	(0)				(0.18 ± 0.04)	(1.05)	(0.37)
6.0	100	206	9	29	34	13	8	4	3		2.06 ± 0.14	0.95	0.36
		(32)	(70)	(28)	(2)	(0)	(0)	(0)	(0)		(0.32 ± 0.05)	(0.81)	(−1.30)
8.0	50	162	0	4	15	12	7	8	4		3.24 ± 0.21	0.65	−1.73
		(27)	(28)	(18)	(3)	(1)	(0)	(0)	(0)		(0.54 ± 0.10)	(0.92)	(−0.41)

[a] Centric and acentric rings in parentheses.

magglutinin (PHA, M-type). The cultures were incubated at 37°C for 48 h and Colcemid (demecolcine) was added at a final concentration of 0.5 μg/ml at 24 h after the start of incubation. The harvested lymphocytes were treated with a hypotonic solution of 0.075 *M* KCl and stained with Giemsa solution after fixation. To confirm whether we could exclude the presence of second-division cells in the present lymphocyte culture method, another culture technique with fluorescence plus Giemsa staining was also employed using 4.0- and 6.0-Gy-irradiated and nonirradiated control blood (*16*). For these 48 h of culture, 5-bromodeoxyuridine (BrdU) and Colcemid were added at the start of incubation and 24 h before har-

TABLE II

Distributions of Dicentrics and Rings among the Cells Irradiated with 70-MeV Proton Beams at Depth of 15 mm

Radiation dose (Gy)	Number of cells scored	Number of dicentrics and rings	Number of cells with indicated number of dicentrics and rings								Mean (dicentrics and rings per cell) ± SE	σ^2/Y	U
			0	1	2	3	4	5	6	7			
0.1	450	6	444	6							0.013 ± 0.005	0.99	−0.18
		(1)[a]	(449)	(1)							(0.002 ± 0.002)	(1.00)	(0)
0.2	400	12	388	12							0.03 ± 0.01	0.97	−0.41
		(5)	(395)	(5)							(0.013 ± 0.006)	(0.99)	(−0.16)
0.5	300	17	283	17							0.06 ± 0.01	0.95	−0.67
		(3)	(297)	(3)							(0.010 ± 0.006)	(0.99)	(−0.10)
1.0	200	27	173	24	3						0.15 ± 0.03	1.06	0.56
		(8)	(192)	(8)	(0)						(0.040 ± 0.014)	(0.96)	(−0.38)
2.0	100	46	64	27	8	1					0.46 ± 0.07	1.03	0.22
		(5)	(95)	(5)	(0)	(0)					(0.050 ± 0.022)	(0.96)	(−0.32)
3.0	100	68	50	35	13	1	1				0.68 ± 0.08	0.98	−0.14
		(12)	(88)	(12)	(0)	(0)	(0)				(0.12 ± 0.03)	(0.89)	(−0.82)
4.0	100	104	36	34	20	10					1.04 ± 0.10	0.93	−0.50
		(15)	(85)	(13)	(2)	(0)					(0.17 ± 0.04)	(1.08)	(0.59)
6.0	100	199	7	31	34	16	9	2	1		1.99 ± 0.12	0.73	−1.85
		(22)	(78)	(16)	(6)	(0)	(0)	(0)	(0)		(0.28 ± 0.06)	(1.16)	(1.16)
8.0	—												

[a] Centric and acentric rings in parentheses.

TABLE III

Distributions of Dicentrics and Rings among the Cells Irradiated with 70-MeV Proton Beams at Depth of 25 mm

Radiation dose (Gy)	Number of cells scored	Number of dicentrics and rings	Number of cells with indicated number of dicentrics and rings								Mean (dicentrics and rings per cell) ± SE	σ^2/Y	U
			0	1	2	3	4	5	6	7 8 9			
0.1	550	9	541	9							0.016 ± 0.005	0.99	−0.26
		(2)[a]	(548)	(2)							(0.004 ± 0.003)	(1.00)	(−0.04)
0.2	400	14	387	12	1						0.035 ± 0.006	1.11	1.62
		(6)	(394)	(6)	(0)						(0.015 ± 0.006)	(0.99)	(−0.19)
0.5	200	17	185	13	2						0.09 ± 0.02	1.16	1.60
		(5)	(195)	(5)	(0)						(0.025 ± 0.011)	(0.98)	(−0.22)
1.0	200	32	169	30	1						0.16 ± 0.03	0.91	−0.97
		(7)	(193)	(7)	(0)						(0.035 ± 0.013)	(0.97)	(−0.33)
2.0	100	46	62	31	6	1					0.46 ± 0.07	0.94	−0.43
		(9)	(91)	(9)	(0)	(0)					(0.09 ± 0.03)	(0.92)	(−0.60)
3.0	100	80	48	31	14	7					0.80 ± 0.09	1.09	0.64
		(14)	(86)	(14)	(0)	(0)					(0.14 ± 0.04)	(0.87)	(−0.96)
4.0	100	113	31	37	22	8	2				1.13 ± 0.10	0.91	−0.64
		(19)	(81)	(19)	(0)	(0)	(0)				(0.19 ± 0.04)	(0.82)	(−1.31)
6.0	100	197	8	28	34	22	6	1	1		1.97 ± 0.11	0.67	−2.35
		(20)	(82)	(16)	(2)	(0)	(0)	(0)	(0)		(0.20 ± 0.05)	(1.01)	(0.07)
8.0	100	353	0	7	27	26	16	10	6	3 2 3	3.53 ± 0.19	0.98	−0.14
		(61)	(60)	(23)	(14)	(2)	(1)	(0)	(0)	(0) (0) (0)	(0.61 ± 0.09)	(1.26)	(3.08)

[a] Centric and acentric rings in parentheses.

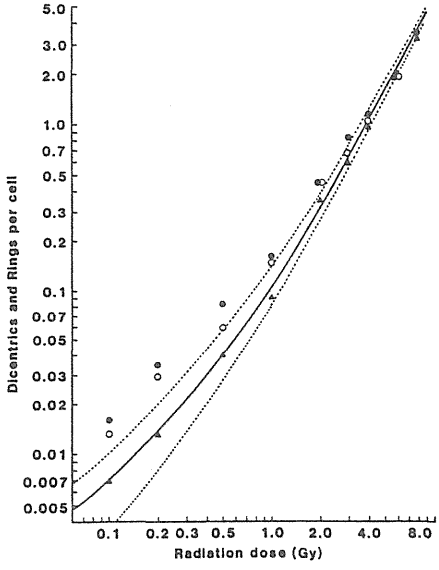

FIG. 5. Dose-response relationships of chromosome aberration frequencies obtained at three depths. Solid triangles: irradiated at 5 mm with the unmodulated beam, indicated by the arrowhead in Fig. 1. Open circles: irradiated at 15 mm with the modulated beam, indicated by one of the arrowheads in Fig. 2. Closed circles: irradiated at 25 mm with the modulated beam, indicated by another arrowhead in Fig. 2. A solid line indicates the dose-response relationship due to ^{60}Co γ irradiation with 95% confidence limits (shown as dotted lines).

vest, respectively. The metaphase slides were processed with hypotonic solution and fixed, treated with Hoechst-33258 solution, exposed to ultraviolet light, and finally stained with Giemsa solution. Metaphases beyond first division were identified by the harlequin-stained figures on chromosome slide preparations. The slides were coded before being scored.

In the present chromosome analysis, only dicentrics and centric and acentric rings were analyzed, because they could be scored easily and accurately and are commonly recognized as a biological dosimeter. The number of cells examined ranged from 100 to 600, a larger number of cells being examined for the lower dose ranges. However, for depths of 5 and 15 mm, only 50 and 25 cells, respectively, could be scored for the 8.0-Gy dose point; the results for 15 mm are not reported. For analysis of the dose-effect relationship, the data were fitted by least-squares regression analysis to a linear-quadratic model.

RESULTS

We determined the effectiveness of both the unmodulated beam and the spread-out Bragg peak for the induction of chromosome aberrations in samples of blood irradiated in the beams as shown in Figs. 1 and 2.

No second mitotic figures were observed among the metaphases of 4.0- and 6.0-Gy-irradiated lymphocytes or in the nonirradiated controls on the preparation slides obtained by the fluorescence plus Giemsa technique, although no further detailed data are given in this paper. Therefore, we evaluated cells processed by the conventional method with the addition of Colcemid at 24 h after the start of incubation. For the control frequency of chromosome aberrations in unirradiated donor, 1050 metaphases were scored and two dicentrics were observed (0.0019 ± 0.0013). The dose-

TABLE IV
Distributions of Dicentrics and Rings among the Cells Irradiated with ^{60}Co γ Rays

Radiation dose (Gy)	Number of cells scored	Number of dicentrics and rings	Number of cells with indicated number of dicentrics and rings								Mean (dicentrics and rings per cell) ± SE	σ^2/Y	U
			0	1	2	3	4	5	6	7			
0.1	550	4	546	4							0.007 ± 0.004	0.99	−0.10
		(0)[a]	(550)	(0)							(0)	—	—
0.2	500	7	493	7							0.014 ± 0.005	0.99	−0.21
		(0)	(500)	(0)							(0)	—	—
0.3	400	9	392	7	1						0.02 ± 0.01	1.20	3.04
		(2)	(398)	(2)	(0)						(0.005 ± 0.004)	(1.00)	(−0.05)
0.5	300	12	288	12							0.04 ± 0.01	0.96	−0.47
		(2)	(298)	(2)							(0.007 ± 0.005)	(1.00)	(−0.06)
1.0	200	20	182	16	2						0.10 ± 0.02	1.11	1.08
		(3)	(197)	(3)	(0)						(0.02 ± 0.01)	(0.99)	(−0.12)
2.0	100	34	73	20	7						0.34 ± 0.06	1.08	0.58
		(4)	(96)	(4)	(0)						(0.04 ± 0.02)	(0.97)	(−0.25)
3.0	100	62	52	37	8	3					0.62 ± 0.08	0.94	−0.43
		(9)	(91)	(9)	(0)	(0)					(0.09 ± 0.03)	(0.92)	(−0.60)
4.0	100	105	32	41	17	10					1.05 ± 0.09	0.85	−1.00
		(14)	(86)	(10)	(2)	(0)					(0.14 ± 0.04)	(1.16)	(1.18)
6.0	100	229	7	24	27	23	13	6			2.29 ± 0.13	0.76	−1.71
		(47)	(53)	(30)	(4)	(3)	(0)	(0)			(0.47 ± 0.07)	(1.09)	(0.65)
8.0	100	360	0	11	10	27	28	12	8	4	3.60 ± 0.15	0.65	−2.49
		(63)	(37)	(25)	(13)	(4)	(0)	(0)	(0)	(0)	(0.63 ± 0.09)	(1.18)	(1.22)

[a] Centric and acentric rings in parentheses.

response relationship for the aberrations induced by the 70-MeV proton beam showed a trend somewhat similar to the relationship for ^{60}Co γ rays. However, there appeared to be some differences in efficiency of aberration induction among the lymphocytes irradiated at depths of 5, 15, and 25 mm (Tables I, II, and III) (Fig. 5). These aberration frequencies were expressed in equations based on a linear-quadratic model shown as $Y = \alpha D + \beta D^2$, where Y and D indicate the yield of dicentrics plus rings and the dose in grays, respectively. α and β are the coefficients giving a best fit to the data points. The dose–effect relationships can thus be expressed as follows at each depth.

$$5 \text{ mm:} \quad Y = (8.72 \pm 2.65) \times 10^{-2} \times D + (4.03 \pm 0.40) \times 10^{-2} \times D^2$$

$$15 \text{ mm:} \quad Y = (1.43 \pm 0.30) \times 10^{-1} \times D + (2.65 \pm 0.50) \times 10^{-2} \times D^2$$

$$25 \text{ mm:} \quad Y = (1.78 \pm 0.43) \times 10^{-1} \times D + (3.08 \pm 0.35) \times 10^{-2} \times D^2$$

The dose–response relationship of frequency of chromosome aberrations induced by ^{60}Co γ rays (Table IV) is given by the following equation:

$$Y = (6.11 \pm 0.49) \times 10^{-2} \times D + (5.03 \pm 0.14) \times 10^{-2} \times D^2.$$

Compared to the aberration frequencies due to ^{60}Co γ-ray exposure, no remarkable difference was elicited in the frequencies obtained by irradiation with the unmodulated proton beam at the site of 5-mm depth in all dose ranges.

TABLE V
RBE Values of 70-MeV Proton Beams at Different Depths of Irradiation

Proton dose (Gy)	Depth of irradiation		
	5 mm	15 mm	25 mm
0.1	1.0 ± 0.7[a]	1.8 ± 1.2	2.3 ± 1.2
0.2	0.9 ± 0.5	2.1 ± 1.0	2.5 ± 1.2
0.5	1.0 ± 0.4	1.5 ± 0.5	2.1 ± 0.8
1.0	0.9 ± 0.3	1.5 ± 0.3	1.6 ± 0.5
2.0	1.1 ± 0.3	1.3 ± 0.3	1.4 ± 0.3
3.0	1.0 ± 0.2	1.1 ± 0.2	1.4 ± 0.2
4.0	0.9 ± 0.1	1.0 ± 0.1	1.1 ± 0.2
6.0	0.9 ± 0.1	0.9 ± 0.1	0.9 ± 0.1
8.0	0.9 ± 0.1		1.0 ± 0.1

[a] Mean ± SE.

TABLE VI

Distributions of Dicentrics and Rings among the Cells Irradiated with 70-MeV Proton Beams at Different Depths (1.0 Gy)

Depth (mm)	Number of cells scored	Number of dicentrics and rings	Number of cells with indicated number of dicentrics and rings								Mean (dicentrics and rings per cell) ± SE	σ^2/Y	U
			0	1	2	3	4	5	6	7			
10	150	16	135	14	1						0.11 ± 0.03	1.03	0.22
		(2)[a]	(148)	(2)	(0)						(0.01 ± 0.01)	(0.99)	(−0.08)
17	200	23	177	23							0.12 ± 0.02	0.89	−1.13
		(1)	(199)	(1)							(0.01 ± 0.01)	(1.00)	—
22	300	37	264	35	1						0.12 ± 0.02	0.93	−0.82
		(5)	(295)	(5)	(0)						(0.02 ± 0.01)	(0.99)	(−0.18)
26	300	35	267	31	2						0.12 ± 0.02	1.01	0.10
		(9)	(291)	(9)	(0)						(0.11 ± 0.01)	(0.97)	(−0.35)
29	350	47	304	45	1						0.13 ± 0.02	0.91	−1.19
		(13)	(337)	(13)	(0)						(0.04 ± 0.01)	(0.97)	(−0.47)
31	250	45	208	40	1	1					0.18 ± 0.03	1.00	0.02
		(8)	(242)	(8)	(0)	(0)					(0.03 ± 0.01)	(0.97)	(−0.31)
32	250	46	210	34	6						0.18 ± 0.03	1.08	0.87
		(13)	(237)	(13)	(0)						(0.05 ± 0.01)	(0.95)	(−0.56)

[a] Centric and acentric rings in parentheses.

However, the modulated beam at 15 and 25 mm was more effective than the γ rays in the low-dose range. This was more marked at 25 mm.

The RBE values of the proton beam were obtained by comparing the chromosome aberration yields observed at 5 mm, 15 mm, and 25 mm with the yields induced by ^{60}Co γ irradiation. The results suggested RBE values of about 2 in the lower dose range at 15 and 25 mm and around unity at higher dose levels (Table V). However, at 5 mm no increase in RBE value was observed (Table V, Fig. 5).

The chromosome aberration frequencies induced by irradiation with the modulated beam at various depths in the Lucite phantom revealed a specific relationship between depth at which blood is irradiated and frequency of aberrations. The frequency of aberrations after exposure to 1.0 Gy starting at the 10-mm depth gradually increased and reached a maximum at 32 mm (Table VI). Thus the ratio of aberration frequencies for the 32-mm point relative to the 10-mm point was 1.6 (Fig. 6). The depth–dose distribution obtained by irradiation at 2.5 Gy also showed the same

TABLE VII

Distributions of Dicentrics and Rings among the Cells Irradiated with 70-MeV Proton Beams at Different Depths (2.5 Gy)

Depth (mm)	Number of cells scored	Number of dicentrics and rings	Number of cells with indicated number of dicentrics and rings								Mean (dicentrics and rings per cell) ± SE	σ^2/Y	U
			0	1	2	3	4	5	6	7			
10	200	52	156	35	7	1					0.26 ± 0.04	1.12	1.16
		(9)[a]	(191)	(9)	(0)	(0)					(0.045 ± 0.015)	(0.96)	(−0.43)
17	—	—											
		(–)											
22	200	68	149	37	11	3					0.34 ± 0.04	1.26	2.56
		(11)	(189)	(11)	(0)	(0)					(0.06 ± 0.02)	(0.95)	(−0.53)
26	200	85	129	58	12	1					0.43 ± 0.05	0.93	−0.66
		(14)	(186)	(14)	(0)	(0)					(0.07 ± 0.02)	(0.94)	(−0.68)
29	100	48	63	29	6	1	1				0.48 ± 0.07	1.16	1.15
		(10)	(90)	(10)	(0)	(0)	(0)				(0.10 ± 0.03)	(0.91)	(−0.67)
31	100	51	67	19	10	4					0.51 ± 0.07	1.37	2.61
		(13)	(87)	(13)	(0)	(0)					(0.13 ± 0.03)	(0.88)	(−0.89)
32	100	64	99	40	9	2					0.43 ± 0.05	1.05	0.36
		(10)	(140)	(10)	(0)	(0)					(0.07 ± 0.02)	(0.94)	(0.55)

[a] Centric and acentric rings in parentheses.

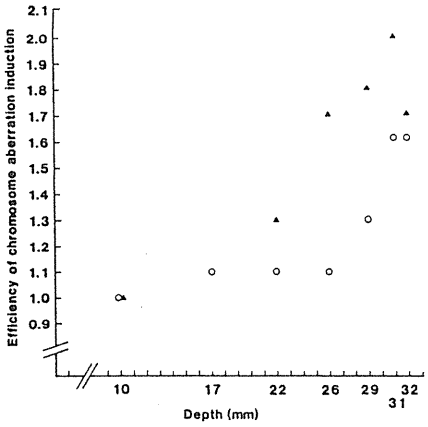

FIG. 6. Depth–dose distribution of the 70-MeV modulated proton beam estimated from chromosome aberration frequencies. The units on the ordinate are ratios of aberration frequencies along various depths. Open circles: 1.0 Gy; solid triangles: 2.5 Gy.

tendency seen for 1.0-Gy irradiation, although the aberration yield at 32 mm was slightly lower than the yields at 29 and 31 mm (Table VII). The maximum aberration frequency obtained at a depth of 31 mm was two times higher than that at 10 mm (Fig. 6). Another series of comparisons of the frequency of aberrations for 4.0 and 6.0 Gy at various depths (Table VIII and IX) resulted in almost the same distribution pattern described above, and the ratios of maximum aberration frequency at a depth of 29 mm relative to frequencies at 10 mm were 1.6 and 1.6, respectively (Fig. 7).

The spread-out peak of the 70-MeV proton beam in the present study revealed an almost flat contour in the physically measured dose distribution, not unlike that reported by other authors. However, the present results using chromosome aberration analysis as a measure of biological effectiveness suggest that relative dose is not constant over the spread-out Bragg peak but changes with depth between 10 mm and the deepest site of the spread-out peak. This result suggested the possibility of a more marked biological effect in deeper areas even within the spread-out peak.

DISCUSSION

Using chromosome aberrations as a biological end point of radiation damage, we investigated the dose–effect relationship for a 70-MeV proton beam and its depth–dose distribution. We also investigated the dose–effect relationship in the dose range down to 0.1 Gy, because the effect of proton irradiation on the induction of chromosome aberrations in such a low-dose range, which may exist in the peripheral and/or surrounding normal areas of radiotherapy portals, has not been studied extensively (*25*). The observed aberration frequencies for cells irradiated at 15 and 25 mm were found to be a little higher per unit dose than those caused by doses of less than 2.0 Gy of ^{60}Co γ rays. However, no enhanced values were observed at higher doses such as 4.0, 6.0, and 8.0 Gy. The dose–response relationships of chromosome aberration frequencies due to the proton beam irradiation have been reported by many authors, and the frequencies have been found to be largely dependent on proton energy (*8, 13, 16, 26, 27*). Radiation effects were

TABLE VIII

Distributions of Dicentrics and Rings among the Cells Irradiated with 70-MeV Proton Beams at Different Depths (4.0 Gy)

Depth (mm)	Number of cells scored	Number of dicentrics and rings	Number of cells with indicated number of dicentrics and rings								Mean (dicentrics and rings per cell) ± SE	σ^2/Y	U
			0	1	2	3	4	5	6	7			
10	100	83	42	40	12	5	1				0.83 ± 0.09	0.98	−0.18
		(14)[a]	(86)	(14)	(0)	(0)	(0)				(0.14 ± 0.03)	(0.87)	(−0.96)
17	100	102	33	41	18	7	1				1.02 ± 0.09	0.87	−0.91
		(13)	(87)	(13)	(0)	(0)	(0)				(0.13 ± 0.03)	(0.88)	(−0.89)
22	100	109	34	36	20	7	3				1.09 ± 0.11	1.00	0.02
		(18)	(83)	(16)	(1)	(0)	(0)				(0.18 ± 0.04)	(0.94)	(0.44)
26	100	123	25	38	26	11					1.23 ± 0.10	0.74	−1.86
		(23)	(78)	(21)	(1)	(0)					(0.23 ± 0.04)	(0.87)	(−0.95)
29	100	129	28	36	19	13	4				1.29 ± 0.11	0.99	−0.06
		(22)	(79)	(20)	(1)	(0)	(0)				(0.22 ± 0.04)	(0.88)	(−0.87)
31	100	49	69	20	7	2	1	1			0.49 ± 0.09	1.71	5.05
		(9)	(92)	(7)	(1)	(0)	(0)	(0)			(0.09 ± 0.03)	(1.14)	(1.06)
32	100	23	83	11	6						0.23 ± 0.05	1.31	2.19
		(7)	(93)	(7)	(0)						(0.07 ± 0.03)	(0.94)	(−0.46)

[a] Centric and acentric rings in parentheses.

TABLE IX

Distributions of Dicentrics and Rings among the Cells Irradiated with 70-MeV Proton Beams at Different Depths (6.0 Gy)

Depth (mm)	Number of cells scored	Number of dicentrics and rings	Number of cells with indicated number of dicentrics and rings								Mean (dicentrics and rings per cell) ± SE	σ^2/Y	U
			0	1	2	3	4	5	6	7			
10	100	176	9	35	36	12	7	1			1.76 ± 0.11	0.66	−0.17
		(29)[a]	(74)	(23)	(3)	(0)	(0)	(0)			(0.29 ± 0.05)	(0.93)	(−0.51)
17	100	185	12	28	34	17	7	2			1.85 ± 0.12	0.75	−0.13
		(21)	(81)	(17)	(2)	(0)	(0)	(0)			(0.21 ± 0.05)	(0.99)	(−0.07)
22	100	203	12	27	29	18	8	4	2		2.03 ± 0.14	0.96	−2.21
		(38)	(65)	(32)	(3)	(0)	(0)	(0)	(0)		(0.38 ± 0.05)	(0.79)	(−1.51)
26	100	218	4	32	30	16	13	4	1		2.18 ± 0.13	0.76	−1.67
		(35)	(68)	(29)	(3)	(0)	(0)	(0)	(0)		(0.35 ± 0.05)	(0.83)	(−1.23)
29	100	284	3	16	31	18	15	11	5	(1)	2.84 ± 0.16	0.85	−1.05
		(51)	(60)	(31)	(7)	(2)	(0)	(0)	(0)	(0)	(0.51 ± 0.07)	(1.01)	(0.07)
31	100	54	71	16	7	3	1	1	1		0.54 ± 0.11	2.22	8.69
		(12)	(90)	(8)	(2)	(0)	(0)	(0)	(0)		(0.12 ± 0.04)	(1.23)	(1.63)
32	100	19	85	11	4						0.19 ± 0.05	1.24	1.76
		(6)	(94)	(6)	(0)						(0.06 ± 0.02)	(0.95)	(−0.39)

[a] Centric and acentric rings in parentheses.

found to be influenced by the sites at which the cells were irradiated, as reported previously (*9–11*). Elevated chromosome aberration frequencies were found to be induced when the blood was irradiated at deeper sites within the beam spread out by a range modulator. Thus the RBE values obtained at 25 mm were suggested to be around 2 in a lower-dose range such as 0.1 to 0.5 Gy. Elevation of chromosome aberration frequencies was found to be less remarkable, and an RBE value of about 2 was estimated only at the doses of 0.1 and 0.2 Gy, when the blood was irradiated at 15 mm. The unmodulated proton beam irradiation at a depth of 5 mm in the Lucite phantom did not induce an elevation in chromosome aberration frequencies even in the low-dose range compared to the aberrations induced by ^{60}Co γ rays, resulting in RBE values of around unity over the dose range 0.1 to 8.0 Gy. Values for the RBE of a proton beam ranging from 0.8 to 2.0 have been reported (*8–15*). In the present study, however, the dose and depth at which the blood was irradiated were found to have a considerable influence upon the RBE values of the proton beam.

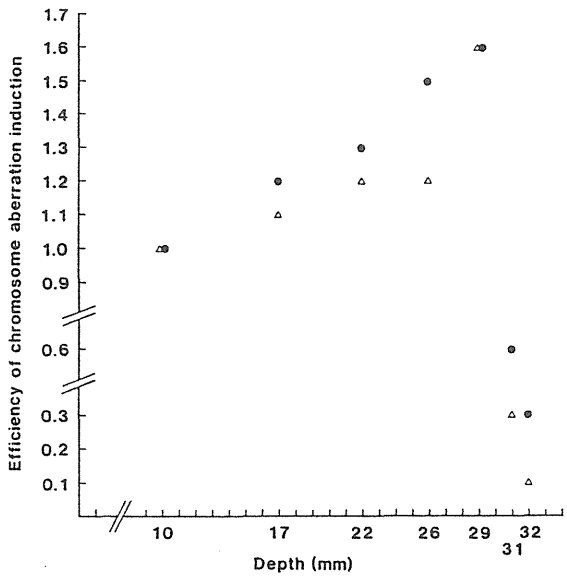

FIG. 7. Depth–dose distribution of the 70-MeV modulated proton beam estimated from chromosome aberration frequencies. The units on the ordinate are ratios of aberration frequencies along various depths. Solid circles: 4.0 Gy; open triangles: 6.0 Gy.

The measured RBE values as a function of depth based upon chromosome aberration frequencies revealed an appreciable slope even within the spread-out peak of the 70-MeV proton beam, i.e., the irradiation at deeper sites within the spread-out peak resulted in higher aberration frequencies per unit dose. The chromosome aberration frequencies observed at the deeper sites of the spread-out peak were 1.5 to 2.0 times higher than those seen at shallower sites within the same broadened peak. These results could be explained by the increase in LET with depth in the spread-out peak, which was calculated using Janni's atomic data and nuclear data table, as illustrated in Fig. 3. Furthermore, comparing the change in LET reflected in Fig. 3 and the change in the aberration frequencies in Figs. 6 and 7,

LET appears to have more influence on the induction of chromosome aberrations at lower doses than at higher doses.

In this study of proton beam dose distribution, we performed two experiments and observed slight discrepancies between them as illustrated in Figs. 6 and 7. This difference may be explained by the diameter of the small plastic tubes in which the blood was irradiated, which might have been a little too large for evaluation of the sharp reduction in the relative dose in the spread-out peak of the 70-MeV proton beam. It is possible that at this point in the beam, half of the blood within the tube did not receive a uniform dose, even though the remaining half was fully exposed to the proton beam. This possibility may be verified by the presence of more dispersed distribution of aberrations as shown in Tables VII to IX.

The value of RBE is not constant, but varies depending upon the biological end point and the dose. Differences between the RBE values obtained here and those reported by other investigators (*8–15*) can be explained as follows: (1) The chromosome aberration assay system that we employed in this study is much more sensitive than any other biological parameters. (2) The RBE values investigated in this study were for doses down to 0.1 Gy.

In radiotherapy, it is essential to restrict the radiation dose only to the target area of the tumor and to eliminate unnecessary irradiation to the surrounding normal tissue. For this requirement, the proton beam appears to give the ideal depth–dose distribution among the various types of external beam therapy. In fact, superior clinical results have been reported employing proton beam therapy for the control of selected malignant diseases in more than 5000 patients (*5*). Therefore, with respect to treatment with a high-energy proton beam, the increase in RBE values at low doses and also the possibility of a nonflat distribution of RBE values within the spread-out peak area may indicate factors to be considered for the prevention of late effects due to genetically injured but surviving cells.

RECEIVED: June 28, 1989; ACCEPTED: March 26, 1990

REFERENCES

1. J. O. ARCHAMBEAU, G. W. BENNETT, G. S. LEVINE, R. COWEN, and A. AKANUMA, Proton radiation therapy. *Radiology* **110,** 445–457 (1974).
2. I. V. CHUVILO, L. L. GOLDIN, S. V. KHOROSHKOV, S. E. BLOKHIN, V. M. BREYEV, I. A. VORONTSOV, V. V. ERMOLAYEV, Y. L. KLEINBOCK, M. I. LOMAKIN, M. F. LOMANOV, V. Y. MEDVED', N. A. MILIOKHIN, V. M. NARINSKY, L. M. PAVLONSKY, G. G. SHIMCHUCK, A. I. RUDERMAN, G. D. MONZUL, E. L. SHUVALOV, V. N. KISELIOVA, E. I. MAROVA, L. E. KIRPATOVSKAYA, E. I. MINAKOVA, V. A. KRYMSKY, A. F. BROVKINA, G. D. ZARUBEY, I. M. RESHETNIKOVA, and A. V. KAPLINA, ITEP synchrotron proton beam in radiotherapy. *Int. J. Radiat. Oncol. Biol. Phys.* **10,** 185–195 (1984).
3. A. M. KOEHLER and W. M. PRESTON, Protons in radiation therapy. *Radiology* **104,** 191–195 (1972).
4. J. E. MUNZENRIDER, M. AUSTIN-SEYMOUR, P. J. BLITZER, R. GENTRY, M. GOITEIN, E. S. GRAGOUDAS, K. JOHNSON, A. M. KOEHLER, P. MCNULTY, G. MOULTON, E. OSBORNE, J. M. SEDDON, H. D. SUIT, M. URIE, L. J. VERHEY, and M. WAGNER, Proton therapy at Harvard. *Strahlentherapie* **161,** 756–763 (1985).
5. J. M. SLATER, D. W. MILLER, and J. O. ARCHAMBEAU, Development of a hospital-based proton beam treatment center. *Int. J. Radiat. Oncol. Biol. Phys.* **14,** 761–775 (1988).
6. H. SUIT, M. GOITEN, J. MUNZENRIDER, L. VERHEY, P. BLITZER, E. GRAGOUDAS, A. M. KOEHLER, M. URIE, R. GENTRY, W. SHIPLEY, M. URANO, J. DUTTENHAVER, and M. WAGNER, Evaluation of the clinical applicability of proton beams in definitive fractionated radiation therapy. *Int. J. Radiat. Oncol. Biol. Phys.* **8,** 2199–2205 (1982).
7. H. TSUNEMOTO, S. MORITA, T. ISHIKAWA, S. FURUKAWA, K. KAWACHI, T. KANAI, and H. OHARA, Proton therapy in Japan. *Radiat. Res.* **104,** S235–S243 (1985).
8. D. BETTEGA, S. DUBINI, A. M. F. CONTI, T. PELUCCHI, and L. T. LOMBARDI, Chromosome aberrations induced by protons up to 31 MeV in cultured human cells. *Radiat. Environ. Biophys.* **19,** 91–100 (1981).
9. E. J. HALL, A. M. KELLERER, H. H. ROSSI, and Y. P. LAM, The relative biological effectiveness of 160 MeV protons, II. *Int. J. Radiat. Oncol. Biol. Phys.* **4,** 1009–1013 (1978).
10. P. J. KLIAUGA, R. D. COLVETT, Y. P. LAM, and H. H. ROSSI, The relative biological effectiveness of 160 MeV protons. I. Microdosimetry. *Int. J. Radiat. Oncol. Biol. Phys.* **4,** 1001–1008 (1978).
11. M. R. RAJU, H. I. AMOLS, E. BAIN, S. G. CARPENTER, R. A. COX, and J. B. ROBERTSON, A heavy particle comparative study. Part III: OER and RBE. *Br. J. Radiol.* **51,** 712–719 (1978).
12. J. B. ROBERTSON, J. R. WILLIAMS, R. A. SCHMIDT, J. B. LITTLE, D. F. FLYNN, and H. D. SUIT, Radiobiological studies of a high-energy modulated proton beam utilizing cultured mammalian cells. *Cancer* **35,** 1664–1677 (1975).
13. S. L. TODOROV, Y. G. GRIGOR'EV, N. I. RIZHOV, B. A. IVANOV, T. S. MALYUTINA, and M. S. MILEVA, Dose–response relationship for chromosome aberrations induced by X-rays or 50 MeV protons in human peripheral lymphocytes. *Mutat. Res.* **15,** 215–220 (1972).
14. M. URANO, M. GOITEN, L. VERHEY, O. MENDIONDO, H. D. SUIT, and A. KOEHLER, Relative biological effectiveness of a high energy modulated proton beam using a spontaneous murine tumor *in vivo*. *Int. J. Radiat. Oncol. Biol. Phys.* **6,** 1187–1193 (1980).
15. M. URANO, L. VERHEY, M. GOITEIN, J. E. TEPPER, H. D. SUIT, O. MENDIONDO, E. S. GRAGOUDAS, and A. KOEHLER, Relative biological effectiveness of modulated proton beams in various murine tissues. *Int. J. Radiat. Oncol. Biol. Phys.* **10,** 509–514 (1984).
16. M. BAUCHINGER, Cytogenetic effects in human lymphocytes as a dosimetry system. In *Biological Dosimetry* (W. G. Eisert and M. L. Mendelsohn, Eds.), pp. 15–24. Springer-Verlag, Berlin, 1984.
17. A. A. EDWARDS, D. C. LLOYD, and J. S. PROSSER, The induction of chromosome aberrations in human lymphocytes by accelerated charged particles. *Radiat. Protect. Dosim.* **13,** 205–209 (1985).
18. D. C. LLOYD and A. A. EDWARDS, Chromosome aberrations in human lymphocytes: Effect of radiation quality, dose and dose rate. In *Radiation-Induced Chromosome Damage in Man* (T. Ishihara and M. S. Sasaki, Eds.), pp. 23–49. Alan R. Liss, New York, 1983.
19. D. C. LLOYD, An overview of radiation dosimetry by conventional

cytogenetic methods. In *Biological Dosimetry* (W. G. Eisert and M. L. Mendelsohn, Eds.), pp. 3–14. Springer-Verlag, Berlin, 1984.

20. S. MATSUBARA, Y. KUWABARA, J. HORIUCHI, S. SUZUKI, M. HOSHINA, and T. KATO, A comparative study of dose distribution of a high-energy electron beam and chromosome aberration frequencies. *Br. J. Radiol.* **59**, 1001–1005 (1986).
21. S. MATSUBARA, Y. KUWABARA, J. HORIUCHI, S. SUZUKI, and A. ITO, Dose distribution of neutron beam and chromosome analysis. *Int. J. Radiat. Oncol. Biol. Phys.* **14**, 503–509 (1988).
22. M. S. SASAKI, Radiation-induced chromosome aberrations in lymphocytes: possible biological dosimeter in man. In *Biological Aspects of Radiation Protection* (T. Sugahara and O. Hug, Eds.), pp. 81–91. Igaku-Shoin, Tokyo, 1971.
23. T. HIRAOKA, Studies of absorbed dose determinations and spatial dose distributions for high energy proton beams. *Nippon Acta Radiol.* **42**, 30–54 (1982).
24. J. F. JANNI, Proton range-energy tables, 1 keV–10 keV. *At. Data Nuclear Data Tables* **27**, 147–529 (1982).
25. M. M. URIE, J. M. SISTERSON, A. M. KOEHLER, M. GOITEIN, and J. ZOESMAN, Proton beam penumbra: Effects of separation between patient and beam modifying devices. *Med. Phys.* **13**, 734–741 (1986).
26. A. A. EDWARDS, D. C. LLOYD, J. S. PROSSER, P. FINNON, and J. E. MOQUET, Chromosome aberrations induced in human lymphocytes by 8.7 MeV protons and 23.5 MeV helium-3 ions. *Int. J. Radiat. Biol.* **50**, 137–145 (1986).
27. T. TAKATSUJI, H. TAKEKOSHI, and M. S. SASAKI, Induction of chromosome aberrations by 4.9 MeV protons in human lymphocytes. *Int. J. Radiat. Biol.* **44**, 553–562 (1983).

RADIATION RESEARCH 123, 345–347 (1990)

SHORT COMMUNICATION

Frequency of Micronuclei in Hepatocytes following X and Fast-Neutron Irradiations—An Analysis by a Linear-Quadratic Model

KOJI ONO, YASUSHI NAGATA, KEIZO AKUTA, MITSUYUKI ABE, KOICHI ANDO,* AND SACHIKO KOIKE*

*Department of Radiology, Faculty of Medicine, Kyoto University, Kyoto 606, Japan; and *Division of Clinical Research, National Institute of Radiological Science, Chiba 260, Japan*

ONO, K., NAGATA, Y., AKUTA, K., ABE, M., ANDO, K., AND KOIKE, S. Frequency of Micronuclei in Hepatocytes following X and Fast-Neutron Irradiations—An Analysis by a Linear-Quadratic Model. *Radiat. Res.* 123, 345–347 (1990).

The usefulness of the micronucleus assay for investigating the radiation response of hepatocytes was examined. The frequency was defined as the ratio of the total number of micronuclei to the number of hepatocytes examined. The dose–response curves were curvilinear after X rays and linear after neutrons. These dose–response curves were analyzed by a linear-quadratic model, frequency = $aD + bD^2 + c$. The a/b ratio was 3.03 ± 1.26 Gy following X irradiation. This value is within the range of the α/β ratios reported by others using the clonogenic assay of hepatocytes. While the a/b value for neutrons was 24.3 ± 11.7 Gy, the maximum relative biological effectiveness of neutrons was 6.30 ± 2.53. Since the micronucleus assay is simple and rapid, it may be a good tool for evaluating the radiation response of hepatocytes *in vivo*.

INTRODUCTION

Radiation therapy has not usually been considered for the treatment of primary and metastatic liver tumors, because most of the tumors are adenocarcinomas, which are generally considered to be refractory to radiation, and because the tolerance dose of the liver is low compared to the dose required for the successful treatment of tumors (*1*). However, since it has been shown that some hepatocellular carcinomas can be treated successfully with external-beam radiotherapy (*2*), and since radiolabeled anti-tumor antibodies which can deliver radiation to tumors fairly selectively have been developed (*3*), an interest in radiotherapy as a treatment for liver tumors is increasing among oncologists. To treat liver tumors successfully with radiotherapy, it is necessary to find the fractionation schemes or combination therapy which will spare the hepatocytes while increasing the damage to tumors. The radiation response of hepatocytes, which are in G_0 phase of the cell cycle and one of the targets of radiation-induced liver damage, can be evaluated by a transplantation assay developed by Jirtle *et al.* (*4*). However, this method is not easy to use, so we have examined the usefulness of the micronucleus assay for investigating the radiation response of hepatocytes. We have also analyzed our data using a linear-quadratic model, and compared them with the results obtained by others using the clonogenic assay.

MATERIALS AND METHODS

Eight- to 10-week-old female C3H/He mice were used for the experiments. For irradiations, each mouse was placed in a plastic tube in a way that restricted movement. The upper abdomen of each mouse including the liver was irradiated with 10 MV X rays or neutrons generated by a linear accelerator or cyclotron (NIRS), respectively.

Micronuclei will appear in the cytoplasm of cells irradiated after mitosis. Since the hepatocytes are in G_0 phase of the cell cycle, the production of micronuclei will be far from maximal. Therefore, a standard partial hepatectomy was performed immediately after irradiation to induce hepatocytes into a rapid cell cycle.

Several days after the partial hepatectomy, a laparotomy was done and a fine polyethylene tube was inserted into the portal vein. Through this tube, 2 ml of a mixture of 0.05% Trypsin and 0.02% EDTA at 37°C was infused slowly. After perfusion of the enzyme mixture, the liver was removed and minced. Fragments of the liver tissue were packed into a 2-ml syringe and pressed into 10 ml phosphate-buffered saline (PBS). The mixture of liver fragments and PBS was shaken gently and filtered through fine nylon mesh. To obtain a good single hepatocyte suspension, the filtrate was centrifuged at 500 rpm for 40 s and a pellet of hepatocytes was resuspended in 10 ml PBS. This procedure was repeated twice, and the pellet of cells was then resuspended in 3 ml complete medium containing 12.5% fetal calf serum to inhibit the action of residual trypsin. This cell suspension was centrifuged again and the pellet was fixed with 70% ethanol at 4°C for 24 h. The fixative was changed to Carnoy's fluid (3 vol ethanol and 1 vol acetic acid). Thirty microliters of this suspension was dropped onto a microslide glass and dried at room temperature.

Micronuclei in the hepatocytes were observed with a fluorescence microscope after staining with ethidium bromide. About 500 hepatocytes were examined, and the frequency was defined as a ratio of the total number of micronuclei to the number of hepatocytes examined.

The experiment was repeated at least twice, and 10 to 12 mice were used for each data point.

RESULTS AND DISCUSSION

The frequency of micronuclei increased and reached a maximum level 5 days after irradiation and partial hepatectomy. Thereafter, the frequency gradually decreased. The

0033-7587/90 $3.00

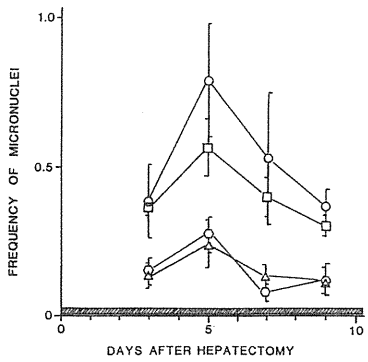

FIG. 1. The frequency of micronuclei in hepatocytes as a function of time (days) after treatment with X rays (△, 4 Gy; □, 6 Gy) and fast neutrons (⊙, 1.25 Gy; ○, 3.75 Gy). A partial hepatectomy was performed immediately after irradiation. Vertical lines represent standard deviations. Shaded area represents spontaneous micronucleus frequency.

pattern of the frequency of micronuclei in relation to the time after irradiation was similar for X rays and neutrons (Fig. 1). The decrease in the relative incidence of micronuclei after the fifth day can be explained by the elimination of micronucleus-positive cells and by an intensive proliferation of healthy hepatocytes. A similar pattern has been reported by others (*5*).

The dose–response curve for the incidence of micronuclei was constructed using the data obtained on the fifth day after irradiation and partial hepatectomy. The curve was curvilinear following X irradiation but linear after neutron irradiation (Fig. 2a). The relative biological effectiveness (RBE) of neutrons for hepatocytes was graphically obtained from these data. The RBE was 5.6 with 0.36-Gy neutrons; however, it decreased with an increase in radiation doses (2.4 with 2.5-Gy neutrons) (Fig. 2b). In the next step, the dose–response curve was analyzed using a linear-quadratic model, frequency = $aD + bD^2 + c$. This equation was transformed as (frequency $- c)/D = a + bD$. The mean data points were plotted in Fig. 3. The values at which the lines intercept the ordinate and the slopes of the lines correspond to a and b values, respectively. So the values at which the lines intercept the abscissa are $-a/b$ values. As determined by the weighted least-squares regression, a was 0.027 ± 0.0096 Gy^{-1} and b was 0.0089 ± 0.0019 Gy^{-2} for X irradiation. The a/b value was 3.03 ± 1.26 Gy. For neutron irradiation, a and b were 0.17 ± 0.032 Gy^{-1} and 0.0070 ± 0.0031 Gy^{-2}, respectively (Fig. 3). The a/b value for neutrons was 24.3 ± 11.7 Gy. The ratio of a values for neutrons and X rays provided a maximum RBE (RBE_m) of 6.30 ± 2.53. The frequency of micronuclei in hepatocytes following irradiation was reported by Fisher *et al.* (*5*). However, they analyzed their data in terms of the fraction of cells without micronuclei as a function of radiation dose and did not use a linear-quadratic model. Although only a part of the chromatid or chromosome aberrations appear as micronuclei (*6*), the dose–response curve for frequency of micronuclei after irradiation is closely related to the curve for cell survival (*7–10*). In particular, the a/b value agrees well with the α/β value of the cell survival curve (*8*). The α/β value of 1.0–2.1 Gy for the radiation response of hepatocytes was reported in the experiments using fractionated irradiation and the transplantation clonogenic assay (*11*). We analyzed the survival curve for hepatocytes reported by Jirtle *et al.* (*4*), and obtained an α/β value of 4.5 ± 0.46 Gy in the low-dose range (0–8.0 Gy), which corresponded to the doses in our study. Therefore, the a/b value of 3.03 ± 1.26 Gy obtained by the assay of micronuclei is comparable to the α/β values obtained with the clonogenic assay. Fisher *et al.* did not note a close correlation of the curves for frequency of micronuclei and for survival as determined by the clonogenic assay.

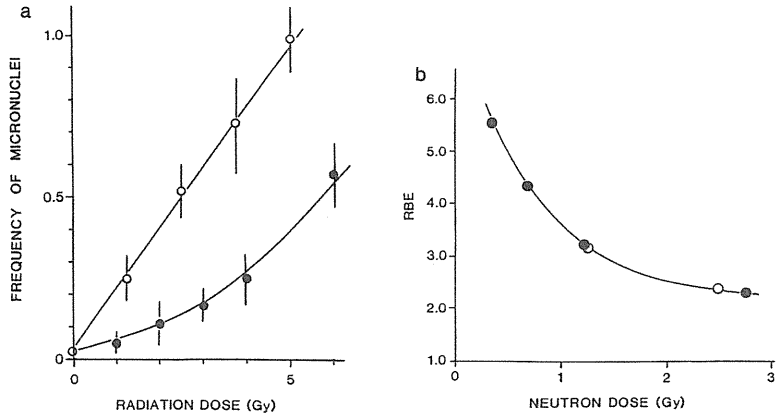

FIG. 2. (a) Frequency of micronuclei in hepatocytes following treatment with X rays (●) or fast neutrons (○). Vertical lines represent standard deviations. (b) RBE as a function of neutron dose. Closed symbols represent the data corresponding to X-ray doses of 2, 3, 4, and 6 Gy.

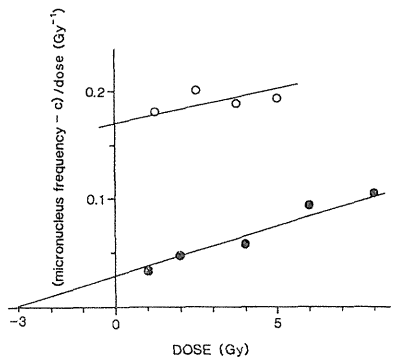

FIG. 3. Analysis of the frequency of micronuclei per hepatocytes using the linear-quadratic model: $aD + bD^2 + c$. (○) neutrons, (●) X rays.

The radiation response of hepatocytes has been studied using different criteria, such as the function assayed using ^{131}I-rose bengal (*12*) and histopathological changes (*13, 14*). The clonogenicity of hepatocytes following irradiation was assayed using the transplantation system of Jirtle *et al.* (*4*). This method is very reliable and elegant; however, it is labor intensive. The micronucleus assay in hepatocytes described here is much easier and more rapid than the clonogenic assay using a transplantation system, and the results are comparable to those obtained with the clonogenic assay. Therefore, the micronucleus assay should be an excellent tool for experimental determinations of the response of hepatocytes to radiation and combined treatments.

ACKNOWLEDGMENTS

This work was supported by a Grant-in-Aid for Cancer Research from the Ministry of Education, Science and Culture (01010020, 01010047, 01570588), and the Ministry of Health and Welfare (63-5)

RECEIVED: July 17, 1989; ACCEPTED: May 4, 1990

REFERENCES

1. P. RUBIN and G. M. CASARETT, A direction for clinical radiation pathology; Tolerance dose. *Front. Radiat. Ther. Oncol.* **6**, 1–16 (1972).
2. M. OHTO, M. EBARA, M. YOSHIKAWA, and K. OKUDA, Radiation therapy and percutaneous ethanol injection for the treatment of hepatocellular carcinoma. In *Neoplasm of the Liver* (K. Okuda and K. G. Ishak, Eds.), pp. 335–341. Springer-Verlag, Tokyo, 1987.
3. S. E. ORDER, G. B. STILLWAGON, J. L. KLEIN, P. K. LEICHNER, S. S. SIEGELMAN, E. K. FISHMAN, D. S. ETTINGER, T. HAULK, K. KOPHER, K. FINNEY, M. SURDYKE, S. SELF, and S. LEIBEL, Iodine 131 antiferitin, a new treatment modality in hepatoma: A radiation therapy oncology group study. *J. Clin. Oncol.* **3**, 1573–1582 (1985).
4. R. L. JIRTLE, G. MICHALOPOULOS, J. R. MCLAIN, and J. CROWLEY, Transplantation system for determining the clonogenic survival of parenchymal hepatocytes exposed to ionizing radiation. *Cancer Res.* **41**, 3512–3518 (1981).
5. D. R. FISHER, J. H. HENDRY, and D. SCOTT, Long-term repair *in vivo* of colony-forming ability and chromosomal injury in X-irradiated mouse hepatocytes. *Radiat. Res.* **113**, 40–50 (1988).
6. C. J. ROBERT, G. R. MORGAN, and P. D. HOLT, A critical comparison of the micronucleus yield from high and low LET irradiation of plateau-phase cell populations. *Mutat. Res.* **160**, 237–242 (1986).
7. J. MIDANDAR and L. REVESZ, The frequency of micronuclei as a measure of cell survival in irradiated cell populations. *Int. J. Radiat. Biol.* **38**, 237–242 (1980).
8. K. ONO, E. WANDL, K. TSUTSUI, K. SASAI, and M. ABE, The correlation between cell survival curve and dose response curve of micronucleus (MN) frequency. *Strahlenther. Onkol.* **165**, 824–827 (1989).
9. C. STREFFER, D. VAN BEUNINGEN, and M. MOLLS, Possibilities of the micronucleus test as an assay in radiotherapy. In *Progress in Radiooncology II* (K. H. Karcher, H. D. Kogelink, and G. Reinartz, Eds.), pp. 243–251. Raven Press, New York, 1982.
10. E. WANDL, K. ONO, K. H. KARCHER, A. U. SCHRATTER, R. KAIN, T. HERBSTHOFER, G. HIENERT, and K. HOBATH, Linear correlation between surviving fraction and the micronucleus frequency. *Int. J. Radiat. Biol.* **56**, 771–775 (1989).
11. D. R. FISHER and J. H. HENDRY, Dose fractionation and hepatocyte clonogens: $\alpha/\beta \simeq 1$–2 Gy, and β decreases with increasing delay before assay. *Radiat. Res.* **113**, 51–57 (1988).
12. S. S. KUROHARA, N. L. SWENSSON, J. A. USSELMAN, and F. W. GEORGE, Response and recovery of liver to radiation as demonstrated by photoscans. *Radiology* **89**, 129–135 (1967).
13. D. W. HEBARD and G. M. CHRISTENSEN, The chronological development of late radiation injury in the liver of the rat. *Radiat. Res.* **81**, 441–454 (1980).
14. D. C. WHITE, *An Atlas on Radiation Histopathology*, pp. 161–170. Technical Information Center, Office of Public Affairs, United States Energy Research and Development Administration, 1975.

1. 放射線による治癒とは何か

基礎面からみた腫瘍治癒

——腫瘍幹細胞数の重要性について——

安藤興一[*1]　福田寛[*1]
荒居竜雄[*2]　中野隆史[*2]

1. 放射線治療後の再発時期——ヒト原発腫瘍とマウス移植腫瘍の比較——

ラルストロンによる子宮頸癌の5年後治癒率を図1に示す[1]．A点線量の増大とともに治癒率の向上が明瞭に認められる．治療後再発するまでの時期を調べてみると，1年以内に再発（残存）した頻度は，2年目以降15年目までにおけるすべての再発とほぼ同数である（図2）[1]．5年経過以降に再発する頻度は，治療後15年目までの全再発数の10%であり，5年目に治癒率を求めることは十分根拠があることがわかる．マウス実験腫瘍（NFSa 線維肉腫）を用いて，放射線照射後の再発時期を調べると（図3）[2]，照射後100ないし120日目までの間に再発が多発するが，それ以降300日目くらいまでは再発頻度が低いことがわかり，ヒトの原発腫瘍とマウス移植腫瘍の間に類似性が認められる．一方，ヒトでの再発時期が年単位であり，マウスでの月単位よりも長い．この理由は，腫瘍体積倍加時間の差であり，growth fraction や cell loss がこの差に関与していると思われる．細胞固有の分裂周期はヒト腫瘍で20～30時間であり，マウス腫瘍のものの約2倍でしかない．マウスで照射後400日目以降に出現した腫瘍は，おそらく放射線発癌と思われる．

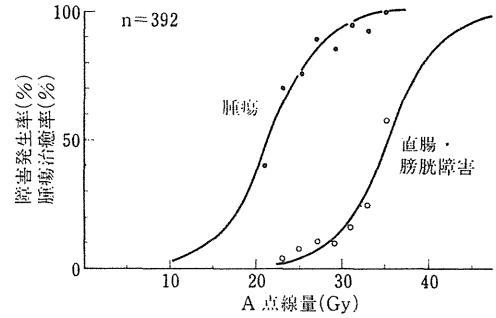

図1　子宮頸癌（Ⅰ期＋Ⅱ期）ラルストロン治療におけるA点線量と治療効果の関係（荒居，中野）

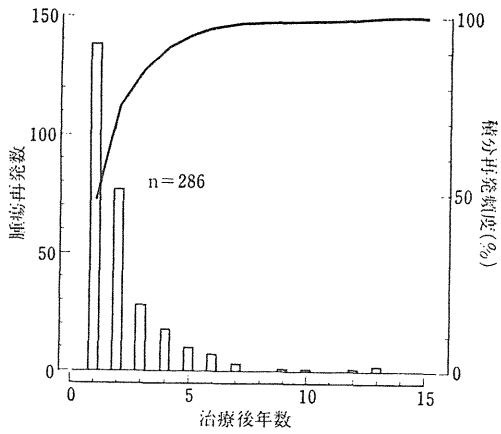

図2　子宮頸癌治療後の腫瘍再発時期

2. マウス腫瘍中の幹細胞数

図3は，C3Hマウスに同系線維肉腫NFSaを移植し，γ線や速中性子線で1回あるいは5分割照射した結果である．別の実験で求めたコロニー形成率を基にして，50%腫瘍治癒率における生存細胞を求めると，速中性子線1回照射を除いて1ないし4個であった（表1）[3]．すなわち，ほとんどすべての細胞を不活化しなければこの腫瘍の治癒は得られないことがわかる．このような少数の

*1 放射線医学総合研究所臨床研究部
*2 放射線医学総合研究所病院部

表 1　50%腫瘍治癒線量を受けた時に生残した細胞数

Radiation schemes	TCD_{50} (Gy)	Surviving fraction*	Number of cells
1 N	27.1 (24.8−29.6)†	$(3.7\pm 1.2)\times10^{-7}$†§	55.5
		$(4.3\pm 1.3)\times10^{-7}$‡§	64.1
5 N	35.8 (28.9−40.4)	$(1.1\pm2.06)\times10^{-8}$	1.6
1 γ	83.2 (68.2−87.6)	$(6.7\pm 16)\times10^{-9}$	1.0
		$(2.3\pm2.97)\times10^{-8}$‡	3.5
5 γ	104.4 (87.9−113.9)	$(1.7\pm 2.6)\times10^{-8}$	2.5
Mixed Beam	81.3 (66.9−83.4)	$(1.2\pm 2.1)\times10^{-8}$	1.8

(Ando, et al., 1985)

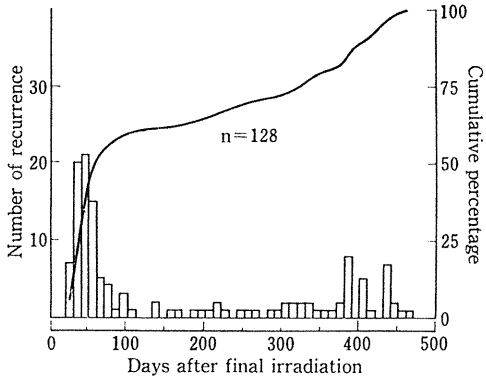

図 3　マウス線維肉腫に対する放射線照射後の再発時期（安藤，未発表データ）

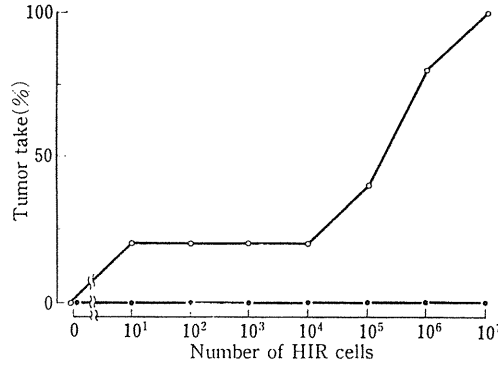

図 5　放射線不活化細胞添加による細胞造腫瘍性の増強（安藤，未発表データ）

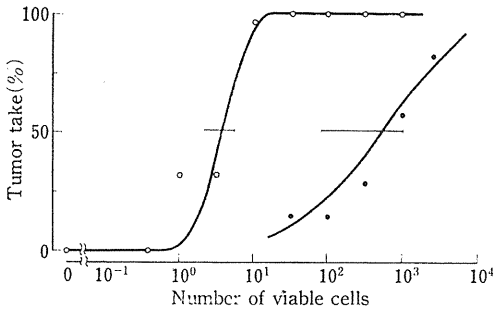

図 4　100% 腫瘍治療線量を受けた腫瘍内に移植された細胞の造腫瘍性（安藤，未発表データ）

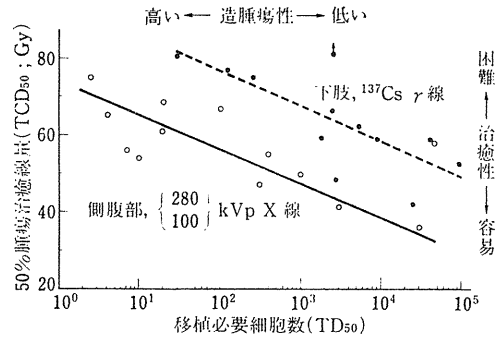

図 6　腫瘍幹細胞数と治癒線量との関係（Hill and Milas; 1989）

細胞が残っていても，腫瘍形成に至ることは移植実験で証明される．すなわち，腫瘍を含む下肢に100% 腫瘍治癒線量（速中性子線 40 Gy 1 回）を照射した後，この腫瘍内に新たに腫瘍細胞を移植して，TD_{50}（50%のマウスに腫瘍形成させるのに必要な移植細胞数）を調べると，それは約 4 個であった（図 4）[4]．非照射の下肢での TD_{50} は約 500 個であることから，照射された腫瘍には，生き（残っ）た細胞の増殖を助ける作用があることがわかる．この作用は Revesz effect と呼ばれており，放射線で不活化された細胞が多いほど生細胞による造腫瘍性が高まる（図 5）[4]．

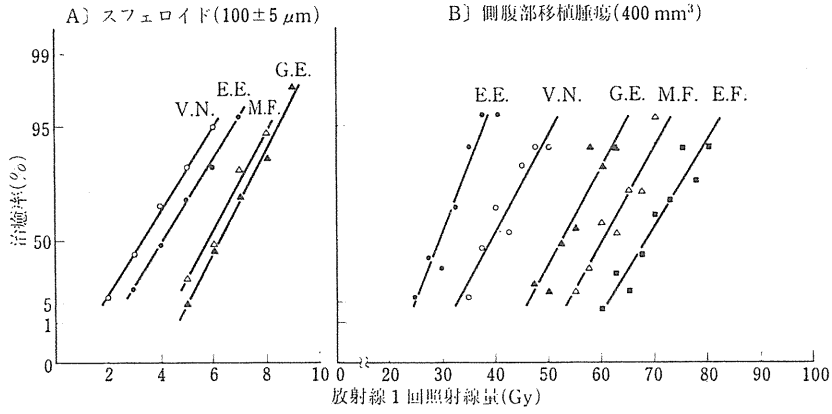

図 7　ヒトメラノーマの in vitro（スフェロイド）および in vivo（ヌードマウス）における放射線治癒曲線（Rofstad ら，1986，1989）

上記のごとく，移植に必要な細胞数は腫瘍放射線治癒に深く関わっているわけだが，この両者の関係を25種類の移植腫瘍について調べたところ，TD_{50} が小さい（すなわち幹細胞数が多い）腫瘍の TCD_{50} は大きい（すなわち治癒し難い）という傾向が認められている（図6）[5]．各腫瘍の間には，細胞固有の放射線感受性，低酸素分画の大きさ，そして潜在的致死損傷の回復能などの面で違いがあるはずである．それにもかかわらず，腫瘍幹細胞数と治癒線量の間に良い相関があるという事実は，腫瘍治癒を決定する要因として幹細胞数が重要であることを意味している．

3. ヒト腫瘍モデルの問題点

ヒト由来腫瘍の放射線治療実験を行うには二つの方法があり，一つは in vitro で多細胞球状体(Spheroid) を用いる方法であり，他の一つはヌードマウスに移植した in vivo 腫瘍を用いる方法である．5種類のヒト悪性黒色腫細胞をヌードマウス側腹部皮下に移植し，X線1回照射後の腫瘍治癒率を求めると，最大 37 Gy の違いが腫瘍間で認められる（図7右側）[6]．同じ腫瘍細胞を多細胞球状体にして in vitro での治癒を求めると，治癒線量の違いは約 3 Gy と小さくなり，しかも in vivo で感受性が高い腫瘍は，in vitro では必ずしも高い感受性の多細胞球状体であるわけではない（図7左側）[7]．in vivo で治癒しやすい腫瘍の TD_{50} は治癒し難い腫瘍の TD_{50} の50倍以上

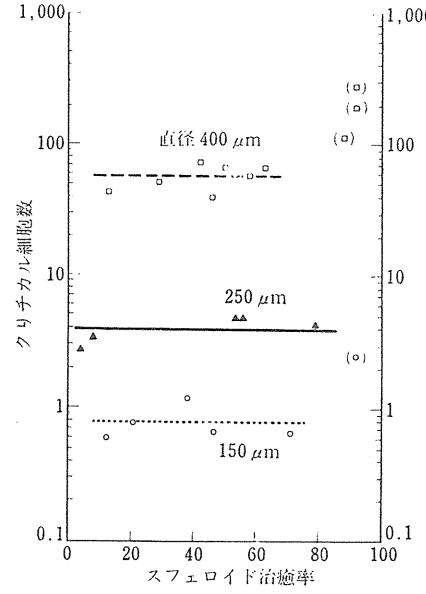

図 8　ヒトメラノーマ多細胞球状体におけるクリチカル細胞数（Kuwashima ら，1988）

も大きいが，免疫抑制しておくとこの違いが小さくなることから考えると，ヌードマウスにおける腫瘍治癒には，ヒト腫瘍に対するマウスの拒絶免疫反応が大きく影響するようだ．

免疫反応が関与しない多細胞球状体を用いて，再発に必要な生存細胞数を調べた場合には，興味深い結果が得られている[8]．ヒト悪性黒色腫 HMV-1 細胞を用いて，大きさの異なる球状体を

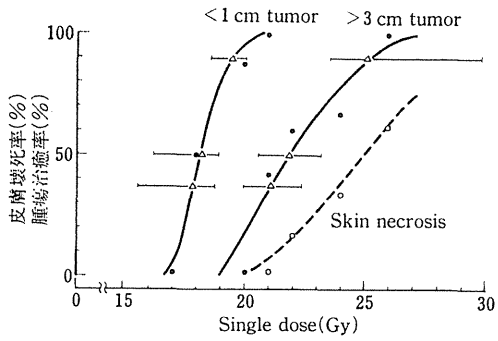

図 9　ヒト皮膚癌1回放射線治療による腫瘍治癒率（Trott ら，1984）

作り，X線照射したところ，小さい（150 μm）球状体の方が大きい（400 αm）球状体より治癒しやすい．ところが，球状体の再発に必要な生存細胞数を計算すると，大きな球状体の方が小さい球状体より50倍以上必要である（図8）．放射線で不活化された細胞数は，大きい球状体の方が小さい球状体よりも数桁多いわけであり，in vivo の結果とは矛盾している．もし，こうした in vitro での結果が普遍的現象であるとするならば，放射線で不活化された腫瘍細胞は，生存細胞に対して増強と抑制の両面性を示すことになる[9]．他の細胞を用いた追試実験が望まれる．

4. ヒト原発腫瘍中の幹細胞数

移植腫瘍や多細胞球状体のような実験では，幹細胞数を調べることができるが，ヒト原発腫瘍における幹細胞数を調べた報告は少ない．ヒト皮膚癌を実験的に1回照射して得られた線量―腫瘍治癒効果関係に基づいた計算によると，3ないし4 cm の皮膚癌中の幹細胞数は 10^7 以下であり，もし腫瘍全部が腫瘍細胞だと仮定すると，幹細胞が全腫瘍細胞中に占める割合は1％以下であるという（図9）[10,11]．ヒト腫瘍の初代培養成功率やヌードマウス移植率が低いことを併せて考えると，1％の正確さは別としても，ヒト原発腫瘍中の幹細胞数がかなり少ないことは十分考えられる．

まとめ

幹細胞数は腫瘍治癒線量を決定する重要な因子である．腫瘍により幹細胞数が異なる理由や，放射線で不活化された腫瘍細胞と生存幹細胞との関係などの不明な点を解明する研究が必要である．また，ヒト腫瘍中の幹細胞数を測定する方法を，今後開発することも大切であろう．

文　献

1) 荒居竜雄，中野隆史：未発表データ
2) 安藤興一：未発表データ
3) Ando, K. & Koike, S.: *Int. J. Radiat. Oncol. Biol. Phys.*, **11**: 1495-1502, 1985.
4) 安藤興一：未発表データ
5) Hill, R.P. & Milas, L.M.: *Int. J. Radiat. Oncol. Biol. Phys.*, **16**: 513-518, 1989.
6) Rofstad, E.K.: *Cancer Res.*, **49**: 3163-3167, 1989.
7) Rofstad, E.K., Wahl, A. & Brustad, T.: *Br. J. Radiol.*, **59**: 1023-1029, 1986.
8) Kuwashima, Y., Majima, H. & Okada, S.: *Int. J. Radiat. Biol.*, **54**(1): 91-104, 1988.
9) 佐々木武仁，増山洋二：組織培養研究，4(2): 12-16, 1985.
10) Trott, K.R., Maciejewski, B., Preuss-Bayer, G. & Skolyszewski, J.: *Radiother. Oncol.*, **2**: 123-129, 1984.
11) Trott, K.R.: Chapter 5 in the Biological Basis of Radiotherapy, 2nd edition ed. by Steel, G.G., Adms, G.E. and Horwich, A., Elsevier, Amsterdam, 1989.

ノート

ラット脳の放射線壊死作成およびMRIによる評価

橋本隆裕[1]，池平博夫[1]，安藤興一[1]，吉井与志彦[4]，
平岡　武[2]，柴山晃一[3]，福田　寛[1]，館野之男[1]

[1]放射線医学総合研究所臨床研究部　[2]同　物理研究部
[3]同　病院部　[4]筑波大学脳神経外科

はじめに

放射線照射に伴う正常脳への影響は病巣の反応とともに重要な問題である．すなわち，照射野内の正常脳の放射線障害による合併症が結局は照射線量を規定しているのが現状で，残念ながら現在の照射線量による治療のみで治癒の得られる脳腫瘍は極めて少ない[1]．臨床的に照射の効果および影響を評価するにはX線CT（computed tomography），MRI（magnetic resonance imaging），PET（positron emission tomography）などの画像診断が有力な手懸かりとなるが，臨床の場では純粋に放射線照射の影響のみを評価するには困難な場合が多い[2),3)]．実験的にも放射線照射に対する正常脳の反応を検討した報告は多く見られるが，従来の方法では小動物の脳局所照射を行うには線量分布の点で問題があり，また小動物の脳の *in vivo* での画像も満足できるものではなかった[4),5)]．

本研究の目的は照射野内の良好な線量分布の得られる陽子線（プロトン）を用いてラットの実験的局所脳障害を作成し，その障害の描出を高分解能MRIにて試み，脳照射に伴う正常脳障害の病態解明の第一歩とすることである．

対象および方法

10週齢の雄性Fischerラット20匹の頭部局所照射を以下の方法で行い，そのうち無作為に抽出した4匹を今回のMRIによる検討の対象とした．残りの動物は別の実験に供した．

照射方法：ラットを抱水クロラールの腹腔内投与（0.35 mg/kg）にて麻酔を得た後，脳の長軸が水平となるように下顎を約1 cmのアクリル板に乗せ，腹臥位にて固定した．照射は放射線医学総合研究所のサイクロトロンより得られる陽子線（プロトン，70 MeV，垂直ビーム）を用い，Bragg-peakを重ね合わせることで（spread out Bragg-peak），照射容積内の線量を均一とした．照射野はbregmaを中心とした前後10 mm，左右20 mmの矩形で，照射深度は頭皮より5 mmとし，60 Gyの一回照射（照射時間100秒前後）を行った．照射後動物は麻酔より覚醒させ，その後自由に餌，水を摂らせて飼育し，照射後5ヶ月目に以下のごとくMRI撮影を行った．

MRI測定：口径31 cmの水平型，超伝導2T磁石よりなる動物用MR装置（RS-200，Siemens-Asahi Medical Systems Ltd.，Tokyo）を用いた．撮影には動物を抱水クロ

キーワード　magnetic resonance imaging 〈MRI〉, radiation brain damage, radiation necrosis

ラールの腹腔内投与にて不動化し，H-1用Alderman-Grant型コイル（内径8cm，共鳴周波数85.26 MHz）の中に固定した．観測周波数および90°，180°パルスは動物をコイルに入れた状態で決定した．

パルス系列はスピンエコー（SE）法で，繰り返し時間/エコー時間＝500/30 msのT_1強調（T_1W）画像を撮影した．画像再構成は2D FT（dimensional Fourier transformation）によった．スライス幅は2㎜のシングルスライスで断層面は冠状断とし，積算回数は2ないし4回である．*In vivo*での血液脳関門（BBB）障害の指標として，Gd-DTPA（0.1 mmol/kg）を腹腔内投与後前記と同条件のT_1W SEを撮影した．

MRI撮影終了後，生理食塩水に溶解した2％Evans blue溶液（1 ml/kg）を股静脈より投与した．1時間後に脳を摘出してホルマリン中に固定し冠状断面を作成してGd-DTPA投与後のMRIと比較した．またLuxol Fast bule染色による組織学的検討も行った．

結　　果

照射後5ヶ月にわたる観察期間中に死亡した動物は見られず，摂食行動および運動機能にも異常は認めなかった（n＝20）．照射部位の脱毛は著明で，その周囲は図1のようにbregmaを中心に前後10㎜，左右20㎜と設定した照射野に良く一致していた．照射後5ヶ月目の頭部MRIを図2に示す．冠状断単純T_1W SE像にて両側側脳室の拡大および脳梁を中心に側脳室内側部に低信号域を認め（図2-A），Gd-DTPA投与後，T_1W SE像にて低信号を呈した部位にほぼ一致した造影効果を認めた（図2-B）が，単純MRIにて異常信号が明らかでなかった視床核の一部にも造影効果が見られた．照射野内の皮質および被殻にはMRI上異常信号は認めなかった．今回検討した4匹のMRI所見はいずれも上記の如くであった．

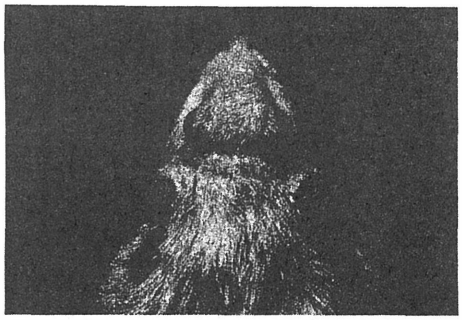

図1． 陽子線（プロトン）の60 Gy一回照射後5ヶ月経過したラットの頭部を示す．照射は頭頂部より垂直ビームを使用し，照射野は左右20㎜，前後10㎜の矩形で照射深度は頭皮より5㎜とした．脱毛の範囲が設定した照射野とよく一致している．

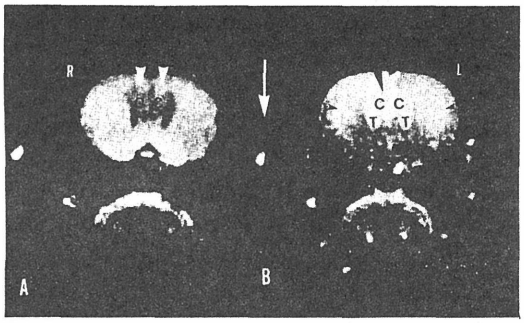

図2． 照射後5ヶ月経過時のラット頭部MRI冠状断を示す．(spin echo法，Tr/Te＝500/30 ms，2㎜幅)．単純では側脳室の拡大（小矢頭）と脳梁（cc）を中心に低信号域（大矢頭）を認め（A），Gd-DTPAによる造影では単純MRIにて低信号を呈した部分が増強効果を呈し，また視床核（T）にも造影効果が見られる．外包にも淡い造影効果が見られる(黒矢頭)．皮質部には異常信号を認めない(B)．図中央の矢印は照射の方向と深度(頭皮より5㎜）を示す．

Evans blue投与後に摘出した脳の冠状断面を図3-Aに示す．矢印のごとく脳梁を中心に側脳室の周囲に漏出が見られたが，側脳室よりの被殻にも漏出が見られた．ただ，脳梁には肉眼的

1991年2月8日受理　1991年4月22日改訂
別刷請求先　〒260　千葉市穴川4－9－1　放射線医学総合研究所臨床研究部　橋本隆裕

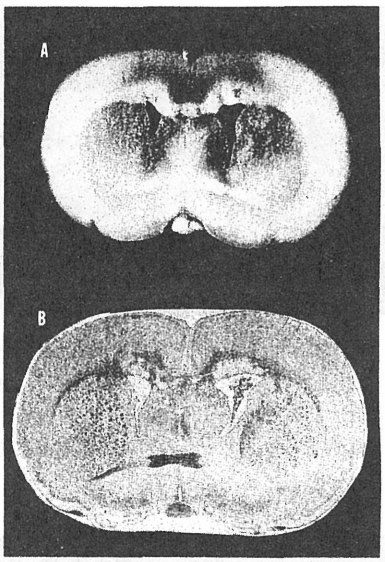

図3. 摘出脳の冠状断面を示す．A）Evans blue の漏出は脳梁を中心とした側脳室周囲に見られる．MRI にて造影効果の見られなかった被殻も漏出が及んでいる．脳梁には肉眼的にも壊死により多数の孔が見られるが Evans blue の漏出は見られない．B）脳梁は組織の脱落が明らかで，脱髄が著しい（Luxol Fast blue 染色）．

に多数の孔（vacuolation）が見られたものの脳梁自体には漏出は認めなかった．

図3-Bに示すように最も変化の大きかった脳梁は組織の脱落が著しく，組織学的に凝固壊死を呈する特徴的な放射線壊死で，著明な脱髄が見られ，脳梁周囲組織では血管壁の肥厚を認めた．Evans blue でのみ異常を呈した被殻にも局所的ではあるが血管壁の変化を認め，特に脳室に接する部分で顕著であった．

考　　察

今回は正常脳の放射線壊死の作成および評価法を開発するため，陽子線（プロトン）を用いてラット脳局所照射を行ない，その変化を高分解能 MR 装置にて捉えることを試みた．実験動物，特にラットなどの小動物の脳に外照射を行なう場合に最も問題となるのはやはり線量分布の精度である．従来使用されている外照射装置は^{60}Co およびリニアックで，一般に鉛を用いた遮蔽により照射野を設定するが[4]，口腔，咽頭，気管，食道などの近傍組織障害を引き起こす可能性が高く，ましてラット脳への精度の高い局所照射は不可能であった[6]．加えて，ラット脳の照射後の変化を *in vivo* の画像として検討することも高分解能 MR 装置なくしては困難であった．

陽子線（プロトン）は照射野内での線量分布が良好で，Bragg-peak を有する物理的特性がある[7]．この単一の Bragg-peak を用いてラット脳の照射を行ない，Evans blue により血液脳関門の障害を *in vitro* で検討した報告[5]があるが，この方法では脳深部のある限られた領域の照射には優れるものの均一な線量に対する脳の各構造の反応の違いを検討するには適していない．そこで今回は spread-out Bragg peak を用いて頭頂から脳内の5㎜までの範囲の線量分布が均一に 60 Gy となるように照射を行い，部位による反応の違いにも注目した．

図1に示したように，脱毛の範囲は設定した照射野に一致し，照射範囲外の組織，例えば眼球への影響は見られなかった．また図2，3のように MRI 所見および摘出脳でも異常所見は照射野にほぼ限局し陽子線の線量分布の精度の高さを良く反映していた．このように従来の照射法で見られた咽頭，口腔など脳以外の組織障害に起因する死亡を除外でき，今回のようにラット脳に限局した高線量一回照射後の長期間の観察が可能となる．脳への放射線照射には種々の程度の副作用を伴うが，臨床的に最も問題となるのはいわゆる late delayed radiation damage である[1]．とりわけ，放射線壊死は最も重大な合併症で照射後数カ月から数年の期間をおいて発生する．この期間（latent period）の意味は未だ十分には解明されていないが，放射線壊死の発生機序は血管内皮障害説が最も有力で，内皮細胞の障害が再生能を上回って顕性化するまでの時間を表すと考えられる．実際に線量や照射野容積が増えると障害発現までの期間は短くな

る[8]．従来の病理学的検討で，脳は部位により放射線感受性が異なり，ラットでは海馬采が最も障害を受けやすく，また照射線量により血管内皮細胞の障害とグリア細胞の障害では差があると指摘されている[6]．すなわち低線量ではグリアの障害が内皮細胞障害より先に発生し，今回行なった60 Gyの照射では内皮細胞とグリアはほぼ同時期に障害を来すと考えられ，再現性の良い脳壊死モデル作成には高線量照射が必要である．今回の検討では脳梁の病変が最も著明で，組織像は細胞の脱落および血管の変化からなる明確な放射線壊死で，脳梁周囲の組織にも変化を認めたが，大脳皮質は保たれていた．脳梁での変化が顕著であったのは血管内皮とグリアの両方の障害のためと思われ，白質が放射線障害を来しやすいとする従来の見解を支持したが，rodent脳では白質が少ないと言う欠点は否めない．

MRI導入後，放射線照射を受けた患者脳で脳萎縮，脳室に接近する白質の浮腫，及び広範な白質の異常信号などの所見を認めるとする報告が増加しており，これらは脱髄，血液脳関門の障害および血管周囲の炎症と考えられている[2),3)]．しかし，臨床ではMRI所見を裏付ける組織学的検討を行なうには困難な場合が多く，手術や化学療法また血管障害など内因性の病変の影響も加わっており，MRI所見も非特異的である．そのため正常脳の放射線障害の実験的研究には再現性の良い脳放射障害を作成し，そのMRIによる検討を行なうことは意義がある．猫での正常照射（35 Gy，6 MeV，photons）後の変化をMRIで観察した報告はあるが，異常所見を呈した頻度が低く（2/6），またその所見は一様ではなかった[9]．一方，今回の検討ではすべてMRI上の異常所見（4/4）が得られており，この相違は照射方法の精度ならびに先に述べたように照射線量の違いによると我々は考える．

正常脳では血液脳関門のために下垂体，脈絡叢などを除いて造影剤の血管外漏出は見られないため，造影剤の投与後にX線CTまたはMRIの造影効果の有無により血液脳関門の機能評価が可能である．特に，濃度分解能が高いMRIでの造影の有用性は臨床でも良く知られている．今回示した如くラット脳では空間分解能の精度の問題はあるものの，MRIは*in vivo*での血液脳関門の障害を知るには極めて都合が良い．臨床例で見られる放射線壊死の造影CTおよびMRIでは造影能が時間やステロイドによる治療により変化するが，今後，今回の手法を用いこの病態の解明も可能となるであろう．一方，Evans blueは静注後速やかに血中アルブミンと結合し，血管内に留まるが血液脳関門が破綻すると血管外に漏出するため摘出脳で容易に同定可能となる．今回のEvans blueの漏出とGd-DTPAの造影所見をまとめると，①Evans blueの漏出の範囲はMRI上の造影部分より広く，②著明なGd-DTPAの造影および組織変化の見られた脳梁ではEvans blueの漏出は無く，③またMRI上造影効果を見なかった被殻にEvns blueの漏出を認めた．これらの解釈は十分ではないが，Gd-DTPAとEvans blueの所見の相違は*in vivo*と*in vitro*による違いが最も大きいと考える．また上記の①，③についてはMRIの分解能の問題および血管内のEvans blueが死後に漏出した可能性が考えられ，②については，脳梁は組織の脱落が著明で，脳梁自体の血管はヒアリン化が著しく，もはや血管内から外への移行は見られなくなっている．一方，周囲組織から漏れた物質は拡散するが，Gd-DTPAはEvans blueより分子量も小さく，拡散しやすいために脳梁にGd-DTPAの造影効果が見られたと解釈した．Gd-DTPAとEvans blueの両者を検討した報告は見られないが，Hecht-Leavitt, et al.[9]はGd-DTPAの造影の有無について興味ある意見を述べている．すなわち，ネコ脳への照射後T_2強調画像で高信号を呈した部位がGd-DTPAにより造影される場合とされない場合があり，造影されないのは非炎症性の脱髄および壊死を表わし，これにより組織学的な差違を分けられるというのである．我々は照射後にGd-DTPA

にて造影される部分も時間が経つと造影がみられなくなることを確認しており（T. Hashimoto, unpublished data），造影の有無は照射後の組織の反応すなわち血管の状態の時間経過を反映するものと考えている．今回の検討では血液脳関門の機能障害の検出には *in vitro* の Evans blue のほうが *in vivo* の Gd-DTPA より鋭敏であったが，死後に漏出した可能性もあり他の *in vitro* の手法による評価が今後必要である．Gd-DTPA および Evans blue の投与量，投与後の時間経過，作用機序ならびにそれぞれの所見に違いはあるものの，血液脳関門障害の程度および状態が同じ線量の照射であっても部位により異なる可能性が示唆される．

結　　語

陽子線（プロトン）の極めて良好な線量分布を利用してラット脳の局所放射線壊死を作成し，MRI により放射線照射による変化を捉えた．60 Gy 1回照射後5ヶ月目の MRI で脳梁を中心に異常を促え，Gd-DTPA による造影を認めた．Gd-DTPA は血液脳関門の機能評価法として有用であるが，*in vitro* の Evans blue の漏出と一致しない部位があり，その解明が今後必要である．また実験的に照射後の経時的な MRI 所見と組織変化との関係を明らかにすることは脳の放射障害の病態を把握するために重要である．今回報告した手法を用いることで，今後放射線照射に生じる正常脳障害の病態の解明が推められることを期待する．

謝　　辞

プロトン照射に御尽力いただいた放射線医学総合研究所サイクロトロン管理課の皆様に深感謝します．本研究の一部は平成2年度文部省科学研究費（奨励研究 A 02770695）の助成を受けた．

文　　献

1) G. E. Sheline, W. M. Wara, V. Smith, et al. : Therapeutic irradiation and brain injury. Int J Radiat Oncol Biol Phys, 6 : 1215-1228, 1980.
2) L. S. Constine, A. Konski, S. Ekholm, et al. : Adverse effects of brain radiation correlated with MR and CT imaging. Int J Radiat Oncol Biol Phys, 15 : 319-330, 1988.
3) J. T. Cunes, D. W. Laster, M. R. Ball, et al. : MRI of radiation injury to the brain. AJR, 147 : 119-124, 1986.
4) E. H. Oldfield, R. Friedman, T. Kinsella, et al. : Reduction in radiation-induced brain injury by use of pentobarbital or lidocaine protection. J Neurosurg, 72 : 737-744, 1990.
5) M. P. Remler, W. H. Marcussen, J. Tiller-Borsich: The late effects of radiation on the blood brain barrier. Int J Radiat Oncol Biol Phys, 12 : 1965-1967, 1986.
6) W. Calvo, J. W. Hopewell, H. S. Reinhold, et al.: Time- and dose-related changes in the white matter of the rat brain after single doses of Xrays. Br J Radiol, 61 : 1043-1052, 1988.
7) E. J. Hall : Radiobiology for the radiologist (3rd Ed). pp271-274 J. B. Lippincott Company, Philadelphia, 1988.
8) J. R. Fike, C. E. Cann, K. Turowski, et al. : Radiation dose response of normal brain. Int J Radiat Oncol Biol Phys, 14 : 63-70, 1988.
9) C. Hecht-Leavitt, R. I. Grossman, W. J. Curran Jr, et al. : MR of brain radiation injury : Experimental studies in cats. AJNR, 8 : 427-430, 1987.

Development of Radiation Necrosis in Rat Brains and Its Evaluation with MRI

Takahiro HASHIMOTO[1], Hiroo IKEHIRA[1], Koichi ANDO[1],
Yoshihiko YOSHII[2], Takeshi HIRAOKA[3], Koichi SIBAYAMA[4],
Hiroshi FUKUDA[1], Yukio TATENO[1]

[1]*Divisions of Clinical Research,*
[3]*Physics, and* [4]*Hospital,*
National Institute of Radiological Sciences,
4-9-1 Anagawa, Chiba-shi, Chiba 260,
[2]*Department of Neurosurgery, Tsukuba University*

Radiation brain damage, especially radiation necrosis, is most critical and well-known sequelae after cranial irradiation. However, the etiology of radiation necrosis has not been fully understood. In order to characterize and to investigate the pathogenesis of radiation necrosis, the experimental techniques in small animals and the evaluation methods should be refined.

The authors developed focal radiation brain damage in rats utilizing protons of a single dose of 60Gy with superior dose distribution and demonstrated the lesions caused by radiation on MRI with 2T magnet. The damaged lesion was not uniform within the radiation field 5 months after radiation. The corpus callosum was the most vulnerable site which showed low intensity on T_1 weighted spin echo images with marked enhancement after Gd-DTPA administration. These MRI findings are common in patients with radiation necrosis. Discrepancy between the area of Gd-DTPA enhancement on MRI and that of Evans blue extravasation on excised brain might be attributed to the different response and pathological conditions in different brain structures following a single dose of radiation of 60Gy.

Further investigation on radiation brain damage in rats can be encouraged with the elegant methods of both protons radiation and high resolution MRI described here.

2. 画 像 診 断

Psychopharmacology (1991) 103:41–45

Psychopharmacology

Age-related changes in human D1 dopamine receptors measured by positron emission tomography

T. Suhara[1], H. Fukuda[1], O. Inoue[1], T. Itoh[2], K. Suzuki[1], T. Yamasaki[1], and Y. Tateno[1]

[1] Division of Clinical Research, National Institute of Radiological Sciences, 9–1 Anagawa 4-chome, Chiba-shi 260, Japan
[2] Department of Mathematics, Nihon Medical School, 2-297-2, Nakahara-ku, Kawasaki-shi, Japan

Received February 26, 1990 / Final version August 6, 1990

Abstract. The effects of age on the binding parameters of ^{11}C–SCH23390, the highly selective ligand for central D1 dopamine receptors, at specific binding sites in the brain were studied. Seventeen healthy male volunteers (20–72 years old) participated. Regional radioactivity in the brain was followed for 40 min by positron emission tomography (PET). A high accumulation of radioactivity was observed in the striatum and there was a conspicuous accumulation in the neocortex. A two-compartment model was used to obtain quantitative estimates of rate constants of association (k_3) and dissociation (k_4). The binding potential (k_3/k_4) of the dopamine D1 receptors in the striatum and frontal cortex decreased by 35% and 39%, respectively, with age. The value of k_3 decreased by 58% in the striatum and 83% in the frontal cortex, whereas the value of k_4 decreased by 35% in the striatum and 72% in the frontal cortex with age.

Key words: Positron emission tomography – Dopamine D1 receptor – SCH23390 – Aging – Striatum – Frontal cortex

Recent studies have demonstrated age-related changes in various neurotransmitter systems in the mammalian brain, including the dopaminergic system. Dopamine receptors are divided into two subtypes, D1 receptors which mediate the stimulation of adenylate cyclase and D2 receptors which are not associated with this enzyme or which mediate its inhibition. Although the D1 receptor was defined first, research on D1 receptor characteristics has been limited due to the previous lack of D1 selective compounds. SCH23390 (Iorio 1981) has been reported to be a selective high affinity D1 receptor antagonist (Hyttel 1983).

The decrease in D2 receptors with age has been widely accepted in recent years (Severson and Finch 1980; O'Boyle and Waddington 1984) through human experiments both in vitro and in vivo with positron emission tomography (PET) (Severson et al. 1982; Wong et al. 1984; Baron et al. 1986; Rinne 1987; Seeman et al. 1987). However, contradictory results concerning the age-related changes in the density of D1 receptors have been reported. In animal experiments, no change (O'Boyle and Waddington 1984), and a decrease (Giorgi et al. 1987; Battaglia et al. 1988; Gelbard et al. 1989; Hyttel 1989) in the D1 receptor density have been reported. Similarly in humans, a decrease (Hess et al. 1987; Seeman et al. 1987), increase (Morgan et al. 1987) and no change (Rinne 1987) in D1 receptor density have been reported.

In the present study, SCH23390 was labeled with ^{11}C and used to demonstrate D1 receptor binding in the brain (Farde et al. 1987) in order to investigate the human age-related change in D1 receptors by PET.

Offprint requests to: T. Suhara

Materials and methods

Subjects. Seventeen healthy male volunteers ranging in age from 20 to 72 years old participated in this study. The volunteers were considered to be healthy as determined by history, and physical and neurological examinations. Magnetic resonance imaging (MRI) of the brain of the older subjects (over age 50) showed no abnormalities. None of the paticipants were taking prescription or non-prescription drugs. Before the experiment, written informed consent was obtained from all participants.

Chemistry. Carbon 11-labeled SCH23390 was synthesized by methylation of the desmethyl precursor (0.5 mg/0.5 ml DMF, 80° C, 3 min) with ^{11}C-CH_3I which was produced by the same method, described elsewhere (Suzuki et al. 1985), using an AVF cyclotron at the National Institute of Radiological Sciences. The reaction mixture was purified on a reverse phase column, eluting with CH_3CN/0.03M–CH_3COONH_4/CH_3COOH (100/100/1). The ^{11}C–SCH23390 fraction was collected, evaporated to dryness, dissolved in sterile saline and filtered through a 0.22 μm Milex filter. The radiochemical purity was greater than 99% and the specific activity of ^{11}C–SCH23390 ranged from 12.25 to 54.50 GBq/μmol at the injection.

Positron emission tomography. The whole-body, three-ring positron emission tomography system was used to follow the radioactivity in five sections covering an axial field of view of 72 mm of the brain

(Takami et al. 1983). The intervals between the section midpoints were 18 mm. The spacial resolution for the reconstructed image was 13 mm FWHM at the center, and the in-plane and cross-plane slice thicknesses were 13 and 10 mm, respectively.

The subjects were carefully positioned according to the brain atlas (Matui and Hirano 1977) with the aid of a vertical laser line so that the lowest slice (first slice) included cerebellar hemispheres [10 mm above and parallel to the orbitomeatal (OM) line] and the third slice encompassed the striatum. A transmission scan for attenuation correction was performed using a ^{68}Ge-^{68}Ga source.

A dose of 385.17–679.69 MBq of ^{11}C–SCH23390 was injected intravenously from the antecubital vein with a 10 ml saline flush. Serial dynamic scans were performed for 40 min immediately after the injection.

Regions of interest were delineated on the image from 0 to 26 min after injection. The external border of the cerebellum was delineated manually by contours representing about 65% of maximal image intensity of the first slice. The external borders of striatum and frontal cortex were also delineated manually by contours representing about 75% and 55% of the maximal intensity of the third slice, respectively, with reference to the brain atlas (Matui and Hirano 1977). The experiments were performed at 11:45 a.m.

Calculation. Regional radioactivity, measured for each sequential image and corrected for ^{11}C decay, was divided by the injected radioactivity of ligand and expressed as the per cent dose/ml.

Kinetic analysis. A three-compartment model has been used in the calculation of receptor kinetics with PET (Wong et al. 1984). Under certain conditions, such as the presence of a receptor-free region, i.e. cerebellum (De Keyser et al. 1988b; Cortés et al. 1989) and poor penetration of radiolabelled metabolites across the blood-brain barrier (Andersen and Grønvald 1986; Farde et al. 1987), this model can be reduced to two compartments which include only the free and bound ligand concentrations (Eckernâs et al. 1987; Lundberg et al. 1989). The two-compartment model, when using high specific radioactivity, can be expressed by the following equation:

$$dC_b(t)/dt = k_3 * C_f(t) - k_4 * C_b(t) \quad (1)$$

where C_f and C_b are the free and bound ligand concentrations, respectively (Eckernâs et al. 1987). The rate constant, k_3, is the constant proportional to the bimolecular association rate constant (k_{on}) and number of receptors (B_{max}), whereas k_4 is the rate of dissociation from the receptor. The ratio k_3/k_4 is, assuming tracer conditions, equal to B_{max}/K_D (binding potential) (Mintun et al. 1984). K_D is the ratio of the molecular dissociation rate to the association rate. The total radioactivity in the cerebellum (M_c) was used as the estimate of the free radio ligand concentration (Farde et al. 1987). Specifically bound radioactivity (C_b) was defined as the difference between the measured radioactivity in the striatum or frontal cortex (M_s) and that in the cerebellum (M_c).

$$C_f = M_c \quad (2)$$

$$C_b = M_s - M_c \quad (3)$$

Equation (1) can be written

$$dC_b(t)/dt = k_3 * M_c(t) - k_4 * C_b(t) \quad (4)$$

The solution to equation (4) is

$$C_b(t) = k_3 \int_0^T M_c(t-\tau) * \exp(-k_4\tau) d\tau \quad (5)$$

Then optimal values of k_3 and k_4 were obtained by comparing $C_b(t)$ from equation (5) with the measured specifically bound radioactivity, using the non-linear least square fitting method.

Results

After the injection of ^{11}C–SCH23390, radioactivity rapidly increased with time and peaked at 7–11 min in the striatum and 1–3 min in the cerebellum, followed by a gradual decrease. The highest radioactivity in the brain was seen in the striatum, and relatively high radioactivity was seen in the neocortex in comparison to the cerebellum, a region with negligible density of dopamine receptors (Fig. 1). The level of radioactivity appeared to be similar in all neocortical regions.

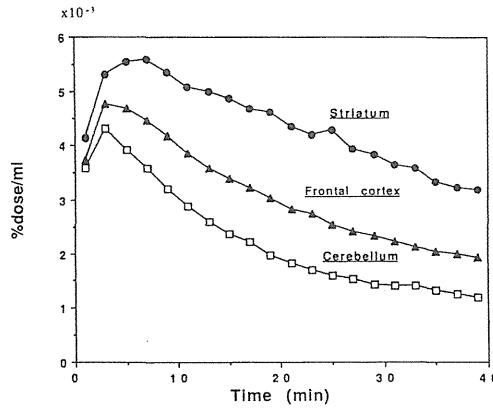

Fig. 1. The time course of ^{11}C–SCH23390 (551.3 MBq) accumulation in the striatum, frontal cortex, (mean values of the left and right region of interest) and cerebellum in a 55-year-old male volunteer. PET scanning was started immediately after the injection and was continued for a period of 40 min. The complete study consisted of a sequence of twenty 2-min images. *Abscissa:* time (min); *ordinate:* radioactivity (per cent dose/ml)

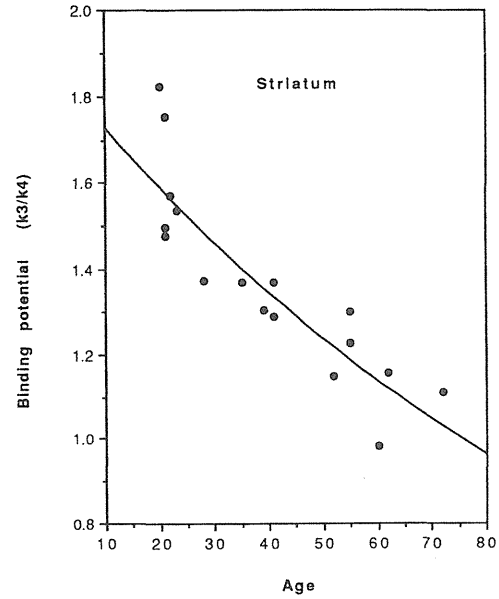

Fig. 2. Age-related decrease in D1 dopamine receptor in the striatum in 17 healthy male volunteers. The binding potential (k_3/k_4) decreased 35% over the age range (20–72 years) [$k_3/k_4 = 1.88 * 10^{(-0.00363*X)}$, where X is age]

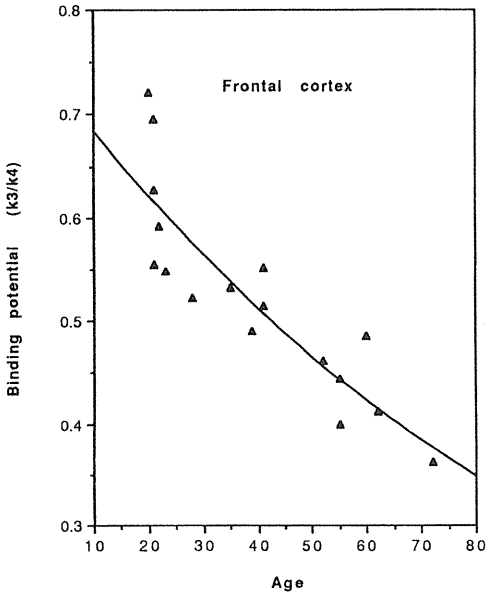

Fig. 3. Age-related decrease in D1 dopamine receptor in the frontal cortex in 17 healthy male volunteers. The binding potential (k_3/k_4) decreased 39% over the age range (20–72 years) [$k_3/k_4 = 0.754*10^{(-0.00419*X)}$, where X is age]

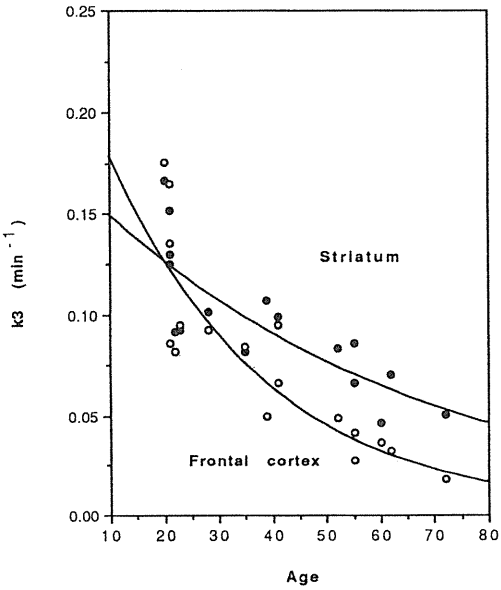

Fig. 4. k_3 values in the striatum and in the frontal cortex in 17 healthy male volunteers. The data in the striatum, fitted by an exponential function [$k_3 = 0.177*10^{(-0.00727*X)}$, where X is age], decreased with age by 58%. The data in the frontal cortex, fitted to [$k_3 = 0.252*10^{(-0.0149*X)}$, also decreased with age by 83%. Striatum (●); frontal cortex (○)

The values of rate constants k_3 and k_4 were calculated using the non-linear least square method, and k_3, k_4 and the binding potential (k_3/k_4) for the striatum and frontal cortex were plotted versus the age of the subjects (Figs. 2–5).

The plots revealed a decrease in D1 receptor binding with age. The data of the binding potential of the striatum (Fig. 2) were fitted using the exponential function [$k_3/k_4 = 1.88*10^{(-0.00363*X)}$, where X is age; $R^2 = 0.79$]. There was a decrease of 35% in the fitted function over the range of age (20–72 years).

There was a similar (39%) exponential decrease in the binding potential in the frontal cortex (Fig. 3) [$k_3/k_4 = 0.754*10^{(-0.00419*X)}$, $R^2 = 0.80$] but the values were lower compared to the striatum.

The rate constants k_3 and k_4 in the striatum and in the frontal cortex were separately plotted (Figs. 4 and 5) and showed decreases as a function of age. The k_3 values in the striatum were fitted by an exponential function [$k_3 = 0.177*10^{(-0.00727*X)}$, $R^2 = 0.71$] and the k_3 values in the frontal cortex were also fitted by an exponential function [$k_3 = 0.252*10^{(-0.0149*X)}$; $R^2 = 0.85$]. The decrease with age of the k_3 values was 58% in the striatum and 83% in the frontal cortex, respectively (Fig. 4).

The rate constants k_4 in the striatum and in the frontal cortex were also fitted by exponential function [$k_4 = 0.0942*10^{-0.00363*X)}$; $R^2 = 0.45$], [$k_4 = 0.334*10^{(-0.0107*X)}$; $R^2 = 0.84$] respectively (Fig. 5). The k_4 values in the frontal cortex were higher than that in the striatum and this tendency was more pronounced in young volunteers.

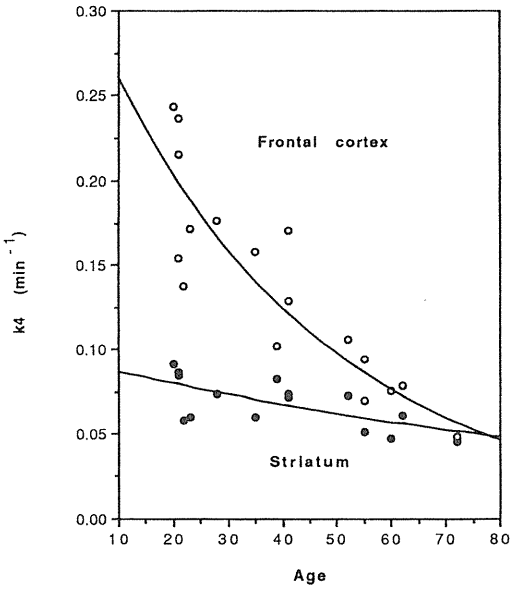

Fig. 5. k_4 values in the striatum and in the frontal cortex in 17 healthy male volunteers. The data in the striatum, fitted by an exponential function [$k_4 = 0.0942*10^{(-0.00363*X)}$, where X is age], decreased with age by 35%. The data in the frontal cortex, fitted to [$k_4 = 0.334*10^{(-0.0107*X)}$], also decreased with age by 72%. Striatum (●); frontal cortex (○)

The per cent decrease with age of k_4 was 35% in the striatum and 72% in the frontal cortex.

Discussion

Previous in vitro and in vivo animal experiments have demonstrated the high affinity and selectivity of ^{3}H–SCH23390 for central D1 dopamine receptors (Schultz et al. 1985; Andersen and Grønvald 1986). It is well known from in vitro studies that the striatum in animals as well as in humans has a high density of D1 dopamine receptors (Giorgi et al. 1987; Seeman et al. 1987).

Specific binding of ^{3}H–SCH23390 in the neocortex has also been demonstrated in animals and in humans, although the specificity for the D1 receptor in the cortex is somewhat controversial with regard to the serotonin S2 receptor (Andersen and Grønvald 1986; Bischoff et al. 1986; Savasta et al. 1986; De Keyser et al. 1988; Cortés et al. 1989). In a PET study by Farde et al. (1987) using ^{11}C–SCH23390, a high accumulation of radioactivity in the striatum and a conspicuous level of accumulation of radioactivity in the neocortex were reported; the levels of radioactivity were reported to be similar in all neocortical regions. These findings are consistent with our results.

The results of the present study indicated that the in vivo binding of ^{11}C–SCH23390 in the striatum and the frontal cortex decreases with age. The percentage of reduction of the binding potential (k_3/k_4) of the striatum and the frontal cortex was 35% and 39%, respectively, over the age range.

In the striatum the decrease in the binding potential was primarily due to the decrease in the k_3 value. As k_3 is the product of k_{on} and B_{max}, assuming that k_{on} does not change with age, a likely explanation for the decrease with age is that the number of receptors (B_{max}) decreases. In vitro studies with both animal and human tissues obtained at autopsy confirm the decrease in the density of ^{3}H–SCH23390 binding site with age (Giorgi et al. 1987; Seeman et al. 1987; Gelbard et al. 1989; Hyttel et al. 1989). However, contradictory results in the decrease in the density of D1 dopamine receptors with age have been reported. The difference in species does not seem to be the reason since in human experiments a decrease (Hess et al. 1987; Seeman et al. 1987), increase (Morgan et al. 1987), and no change (Rinne 1987) have been reported. However, all studies using SCH23390 have shown an age-related decrease in D1 dopamine receptor density in the striatum, so the difference in the results could be due to non-selective ligands for D1 receptors (O'Boyle and Waddington 1984; Morgan et al. 1987; Rinne 1987).

Several lines of experimental evidence indicate that D1 dopamine receptors lost during aging are located on the cell bodies of the striatal neurons rather than in the nerve ending of afferent fibers (Filleux et al. 1987). The turnover of the D1 receptors, that is the receptor production rate and receptor degeneration rate constants, is significantly decreased with age (Battaglia et al. 1988). The above findings are consistent with the view that the decrease in striatal D1 dopamine receptors with age can result from a loss of striatal neurons or from a decreased number of receptors per cell.

In the frontal cortex the binding potential was about one-third of that in the striatum, which nearly corresponds with the difference in the B_{max} value of D1 dopamine receptors in vitro (Cortés et al. 1989). However, the absolute k_4 value and the degree of its decrease with age were larger in the frontal cortex than in the striatum. These findings indicate that the changes in the binding potential in the frontal cortex are significantly affected by the dissociation rate from receptors. By in vitro studies, no significant difference in dissociation rate of ^{3}H–SCH23390 between these two regions was reported despite different numbers of binding sites (Reader et al. 1988). The reason for the larger changes in the k_4 value with age in the frontal cortex than in the striatum is unclear yet, thus further animal experiments are necessary to clarify the physiological roles of the different rate constants in vivo.

Although cerebral blood flow has been shown to decrease with age, the binding potential is reported to be not critically dependent on the blood flow (Mintun et al. 1984; Pantano et al. 1984; Frost et al. 1989). In the present study, to avoid the partial volume effect due to brain atrophy, the subjects over age 50 were examined by magnetic resonance imaging and were confirmed to have no significant atrophy.

The decrease in ^{3}H–SCH23390 binding with age may be relevant in view of the behavioral effects mediated by D1 dopamine receptors. Decreased intense grooming and increased vacuous chewing responses to the selective D1 agonist R–SK&F38393 have been shown with aging (Molloy and Waddington 1988). However, there are few reports in this area, and the functional role of D1 receptors is not completely understood at present. In addition, the presence of a significant functional interaction between D1 and D2 dopamine receptors has been reported (Arnt 1985; Saller and Salama 1985). Thus, further study examining the effects of aging on the functional changes of the dopaminergic neural system is necessary.

Acknowledgements. Demethylated SCH23390 was kindly supplied by Dr. Allen Barnett, Schering Corporation, Bloomfield, New Jersey, USA. We are grateful to Dr. A. Koseki, Dr. M. Nishio and S. Onozuka for their assistance in the PET study, and K. Tamate for his assistance in the preparation of ^{11}C–SCH23390.

References

Andersen PH, Grønvald FC (1986) Specific binding of ^{3}H–SCH23390 to dopamine D1 receptors in vivo. Life Sci 38:1507–1514

Arnt J (1985) Behavioural stimulation is induced by separate dopamine D–1 and D–2 receptor sites in reserpine-pretreated but not in normal rats. Eur J Pharmacol 113:79–88

Baron JC, Mazière B, Loc'h C, Cambon H, Sgouropoulos P, Bonnet AM, Agid Y (1986) Loss of striatal [^{76}Br]bromospiperone binding sites demonstrated by positron tomography in progressive supranuclear palsy. J Cereb Blood Flow Metab 6:131–136

Battaglia G, Norman AB, Creese I (1988) Age-related differential

recovery rate of rat striatal D-1 dopamine receptors following irreversible inactivation. Eur J Pharmacol 145:281–290
Bischoff S, Heinrich M, Sonntag JM, Krauss J (1986) The D-1 dopamine receptor antagonist SCH23390 also potently with brain serotonin (5-HT2) receptors. Eur J Pharmacol 129:367–370
Cortés R, Gueye B, Pazos A, Probst A, Palacios JM (1989) Dopamine receptors in human brain: autoradiographic distribution of D1 sites. Neuroscience 28:263–273
De Keyser J, Claeys A, De Backer JP, Ebinger G, Roels F, Vauquelin G (1988) Autoradiographic localization of D1 and D2 dopamine receptors in the human brain. Neurosci Lett 91:142–147
Eckernâs S-A, Aquilonius SM, Hartvig P, Hagglund J, Lundqvist H, Nagren K, Långström B (1987) Positron emission tomography (PET) in the primate brain: evaluation of a kinetic model using ^{11}C-N-methyl-spiperone. Acta Neurol Scand 75:168–178
Farde L, Halldin C, Stone-Elander S, Sedvall G (1987) PET analysis of human dopamine receptor subtypes using ^{11}C-SCH23390 and ^{11}C-raclopride. Psychopharmacology 92:278–284
Filloux FM, Wamsley JK, Dawson TM (1987) Presynaptic and postsynaptic D1 dopamine receptors in the nigrostriatal system of the rat brain: a quantitative autoradiographic study using the selective D1 antagonist [^{3}H]SCH23390. Brain Res 408:250–209
Frost JJ, Douglass KH, Mayberg HS, Dannals RF, Links JM, Wilson AA, Ravert HT, Crozier WC, Wagner HN Jr (1989) Multicompartmental analysis of [^{11}C]-carfentanil binding to opiate receptors in humans measured by positron emission tomography. J Cereb Blood Flow Metab 9:398–409
Gelbard HA, Teicher MH, Faedda G, Baldessarini RJ (1989) Postnatal development of dopamine D1 and D2 receptor sites in rat striatum. Brain Res 49:123–130
Giorgi O, De Montis G, Porceddu ML, Mele S, Calderini G, Toffano G, Biggio G (1987) Developmental and age-related changes in D1-dopamine receptors and dopamine content in the rat striatum. Dev Brain Res 35:283–290
Hess EJ, Bracha HS, Kleinman JE, Creese I (1987) Dopamine receptor subtype imbalance in schizophrenia. Life Sci 40:1487–1497
Hyttel J (1983) SCH23390 – the first selective dopamine D1 antagonist. Eur J Pharmacol 91:153–154
Hyttel J (1989) Parallel decrease in the density of dopamine D1 and D2 receptors in corpus striatum of rats from 3 to 25 month age. Pharmacol Toxicol 64:55–57
Iorio LC (1981) SCH23390. A benzazepine with atypical effects on dopaminergic systems. Pharmacologist 23:136
Lundberg T, Lindstöm LH, Hartvig P, Eckernâs SA, Ekblom B, Lundqvist H, Fasth KJ, Gullberg P, Långström B (1989) Striatal and frontal cortex binding of 11-C-labelled clozapine visualized by positron emission tomography (PET) in drug-free schizophrenics and healthy volunteers. Psychopharmacology 99:8–12
Matui T, Hirano A (1977) An atlas of the human brain for computerized tomography. Igaku Shoin Ltd, Tokyo
Mintun MA, Raichle ME, Kilbourn MR, Wooten GF, Welch M (1984) A quantitative model for the in vivo assessment of drug binding sites with positron emission tomography. Ann Neurol 15:217–227
Molloy AG, Waddington JL (1988) Behavioural responses to the selective D1-dopamine receptor agonist R-SK&F38393 and the selective D2-agonist RU24213 in young compared with aged rats. Br J Pharmacol 95:335–342
Morgan DG, Marcusson JO, Nyberg P, Wester P, Winblad B, Gorden MN, Finch CE (1987) Divergent change in D-1 and D-2 dopamine binding sites in human brain during aging. Neurobiol Aging 8:195–201
O'Boyle KM, Waddington JL (1984) Loss of rat striatal dopamine receptors with aging is selective for D-2 but not D-1 sites: association with increased non-specific binding of the D-1 ligand [3H]piflutixol. Eur J Pharmacol 105:171–174
Pantano P, Baron JC, Lebrun-Grandie P, Duquesnoy N, Bousser MG, Comar D (1984) Regional cerebral blood flow and oxygen consumption in human aging. Stroke 15:635–641
Reader TA, Brière R, Gottberg E, Diop L, Grondin L (1988) Specific [^{3}H]SCH23390 binding to dopamine D1 receptors in cerebral cortex and neostriatum: evidence for heterogeneities in affinity state and cortical distribution. J Neurochem 50:451–463
Rinne JO (1987) Muscarinic and dopaminergic receptors in the aging human brain. Brain Res 404:162–168
Saller CF, Salama AI (1985) Dopamine receptor subtypes: in vivo biochemical evidence for functional interaction. Eur J Pharmacol 109:297–300
Schultz DW, Wyrick SD, Mailman RB (1985) ^{3}H-SCH23390 has the charactristics of a dopamine receptor ligand in rat central nervous system. Eur J Pharmacol 106:211–212
Savasta M, Dubois A, Scatton B (1986) Autoradiographic localization of D1 dopamine receptors in the rat brain with [^{3}H]SCH23390. Brain Res 375:291–301
Seeman P, Bzowej NH, Guan HC, Bergeron C, Becker LE, Reynolds GP, Bird ED, Riederer P, Jellinger K, Watanabe S, Tourtellotte WW (1987) Human brain dopamine receptors in children and aging adults. Synapse 1:399–404
Severson JA, Finch CE (1980) Reduced dopaminergic binding during aging in the rodent striatum. Brain Res 192:147–162
Severson JA, Marcusson J, Winblad B, Finch CE (1982) Age-correlated loss of dopaminergic binding sites in human basal ganglia. J Neurochem 39:1623–1631
Suzuki K, Inoue O, Hashimoto K, Yamasaki T, Kuchiki M, Tamate K (1985) Computer-controlled large scale production of high specific activity [^{11}C]Ro15-1788 for PET studies of benzodiazepine receptors. Int J Appl Radiat Isot 36:971–976
Takami K, Ueda K, Okajima K, Tanaka E, Nohara N, Tomitani T, Murayama H, Shishido F, Ishimatu K, Ohgushi S, Inoue Y, Takakusa Y, Hayashi T, Nakase S (1983) Performance study of whole-body, multislice positron computed tomograph-positrosica II. IEEE Trans Nucl Sci NS-30:734–738
Wong DF, Wagner HN Jr, Dannals RF, Links JM, Frost JJ, Ravert HT, Wilson AA, Rosenbaum AE, Gjedde A, Douglass KH, Petronis JD, Folstein MF, Tung JKT, Burns D, Kuhar MJ (1984) Effects of age on dopamine and serotonin receptors measured by positron tomography in living human brain. Science 226:1393–1396

Printed in the U.S.A.

EFFECT OF DESIPRAMINE ON DOPAMINE RECEPTOR BINDING IN VIVO

Tetsuya Suhara[1,2], Osamu Inoue[1], Kaoru Kobayasi[1]

1. Division of Clinical Research, National Institute of Radiological Sciences, 9-1 Anagawa 4-chome, Chiba-shi 260, Japan; 2. Department of Psychiatry, Jikei University School of Medicine.

(Received in final form September 28, 1990)

Summary

Effect of desipramine (given i.p. 30 min prior to the tracer injection) on the in vivo binding of ^{3}H-SCH23390 and ^{3}H-N-methylspiperone (^{3}H-NMSP) in mouse striatum was studied. The ratio of radioactivity in the striatum to that in the cerebellum at 15 min after i.v. injection of ^{3}H-SCH23390 or 45 min after injection of ^{3}H-NMSP were used as indices of dopamine D1 or D2 receptor binding in vivo, respectively. In vivo binding of D1 and D2 receptors was decreased in a dose-dependent manner by acute treatment with desipramine (DMI). A saturation experiment suggested that the DMI-induced reduction in the binding was mainly due to the decrease in the affinity of both receptors. No direct interactions between the dopamine receptors and DMI were observed in vitro by the addition of 1 mM of DMI into striatal homogenate. Other antidepressants such as imipramine, clomipramine, maprotiline and mianserin also decreased the binding of dopamine D1 and D2 receptors. The results indicated an important role of dopamine receptors in the pharmacological effect of antidepressants.

The hypothesis that the dopamine system in the brain may play an important role in mood and mood disorders was reported by Randrup et al. (1). Recent reports have indicated that several antidepressants increase the activity of dopaminergic neurons, either by reducing the sensitivity of presynaptic dopamine receptors or by blocking the uptake mechanism (2,3).

Dopamine receptors have been divided into two subtypes, D1 dopamine receptors, which are positively linked to adenylate cyclase and D2 dopamine receptors which are negatively linked to adenylate cyclase (4). A number of studies on receptor binding have revealed that DMI has the least affinity for both D1 and D2 dopamine receptors (5,6). There are significant discrepancies regarding drug effects on receptor binding between in vitro and in vivo studies (7). With regard to antidepressants, Bischoff et al. have reported on the affinity change of dopamine D2 receptors in vivo after acute treatment with the atypical antidepressant bupropion (8). The present experiments were designed to examine the effects of the tricyclic antidepressant DMI and other antidepressants on the binding of ^{3}H-SCH23390 and ^{3}H-NMSP in vivo.

0024-3205/90 $3.00 +.00

Materials and Methods

^{3}H-labeled SCH23390 (specific activity: 70.7 mCi/μmol) and N-methylspiperone (90 mCi/μmol) were provided from New England Nuclear (Boston, MA). Antidepressants and other drugs were kindly supplied by the following corporations: desipramine HCl (DMI), imipramine HCl, clomipramine HCl, maprotiline from Ciba-Geigy (Takarazuka, Japan); mianserin HCl from Organon (Oss, The Netherlands); SCH23390 from Schering (Bloomfield, NJ) and N-methylspiperone from Sumitomo Heavy Industries (Tokyo, Japan). Ketanserin was purchased fom Research Biochemicals Inc. (Natick, MA). Male ddy mice (8 weeks old) weighing about 40 g were used for all animal experiments.

In vivo binding

All antidepressants were given intraperitoneally at a dose of 30 mg/kg at 30 min before the injection of the tracer. DMI was given at three different doses (3 mg/kg, 10 mg/kg, 30 mg/kg) 30 min before the injection of the tracer. Ketanserin was given at three different doses (3 mg/kg, 10 mg/kg, 30 mg/kg) 30 min before the injection of the tracer. Mice were injected into the tail vein with 0.2 ml (3-5 μCi) of ^{3}H-labeled SCH23390 or ^{3}H-NMSP, and were decapitated at 15 min and at 45 min, respectively after the injection of corresponding radio tracer. The brains were rapidly removed, and the striatum and cerebellum were dissected and weighed. Samples were solubilized in 2 ml Protosol (New England Nuclear), and 14 ml of scintillator (Hionic-Fluor, Packard) was added. Radioactivity of each brain region was measured by liquid scintillation counter, and values were expressed as percent of injected dose per gram of tissue (% dose/g). The ratios of radioactivity in the striatum to that in the cerebellum at 15 min for ^{3}H-SCH23390 and at 45 min for ^{3}H-NMSP after the tracer injection were used as indices of in vivo binding of dopamine D1 or D2 receptors, respectively (9-12).

In vivo saturation experiment

^{3}H-SCH23390 or ^{3}H-NMSP (0.2 ml) with various doses of corresponding carrier ligands (from 0.2 to 1000 μg/kg) were injected intravenously into control and DMI-treated (30 mg/kg, 30 min prior to tracer injection) mice. Radioactivity in the striatum and cerebellum at 15 min or 45 min after the injection of ^{3}H-SCH23390 or ^{3}H-NMSP was determined by the same method as described above. Radioactivity in the cerebellum was used for the estimation of non-specific binding and free-ligand concentration. Specific binding in the striatum was determined by subtraction of the radioactivity in the cerebellum.

In vitro receptor binding

The mice were decapitated and the brain was rapidly removed and dissected. The tissue was kept frozen at -70 °C until use. Tissues were homogenized in 10 vol. of ice-cold 0.32 M sucrose solution with a teflon-on-glass tissue homogenizer and centrifuged at 900 g for 10 min; supernatant was centrifuged at 11,500 g for 20 min. The pellets were resuspended in buffer and centrifuged at 11,500 g twice for 20 min. The final pellets were resuspended in buffer [50 mM Tris-HCl, pH 7.4, 120 mM NaCl, 5 mM KCl, 2 mM $CaCl_2$, 1 mM $MgCl_2$, 0.1% ascorbic acid for the binding of ^{3}H-SCH23390 (13); 120 mM NaCl, 5 mM KCl, 4 mM $MgCl_2$, 1.5 mM $CaCl_2$, 50 mM Tris-HCl, pH 7.4 for the binding of ^{3}H-NMSP (14)].

Tissue suspension 0.5 ml, with 0.3 ml buffer, 1 mM of DMI and 0.1 ml of various concentrations of the radioligands (^{3}H-SCH23390, ^{3}H-NMSP) ranging from 0.1 nM to 300 nM were incubated at 20 °C for 60 min. The incubations were terminated by filtration using a

glass fiber filter (Whatman GF/B). The filters were washed three times with 3.5 ml of buffer. The radioactivity of the filters was measured in a liquid scintillation counter. Specific binding was defined as the difference between the total counts in the absence of unlabelled ligand and the counts obtained in the presence of 30 μM of carrier compound.

Results

In vivo binding: The ratio of radioactivity in the striatum to that in the cerebellum following injection of ^{3}H-SCH23390 or ^{3}H-NMSP was decreased by the treatment with DMI in a dose-dependent manner (FIG. 1).

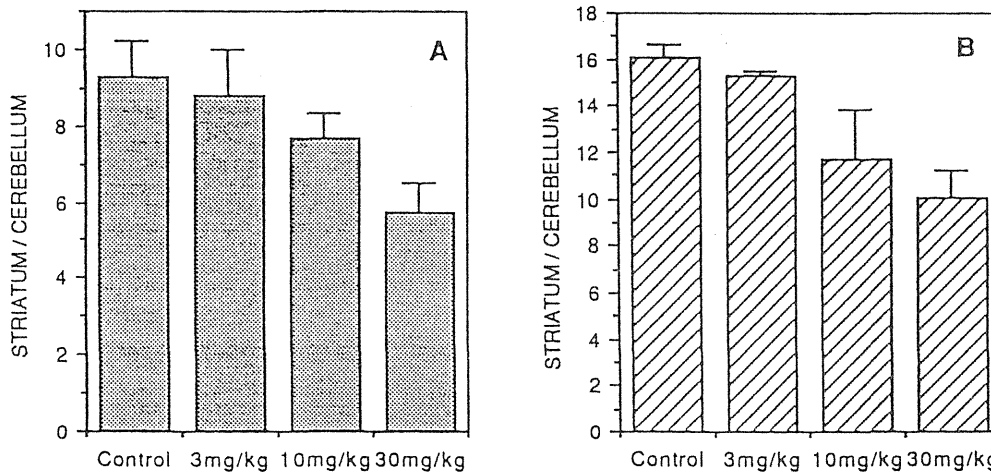

FIG. 1

The effect of DMI on the ratio of radioactivity in the striatum to that in the cerebellum. Three different doses of DMI (3 mg/kg, 10 mg/kg, 30 mg/kg) were administered intraperitoneally at 30 min before the injection of radio-tracer. A. The ratio of radioactivity at 15 min after the injection of ^{3}H-SCH23390. B. The ratio of radioactivity at 45 min after the injection of ^{3}H-NMSP.

In vivo saturation experiment: Mice were injected with various doses of corresponding carrier ligands (from 0.2 to 1000 μg/kg) together with radioligand. The accumulation of ^{3}H-SCH23390 and ^{3}H-NMSP in the striatum was significantly decreased in both control and DMI-treated mice with the increased doses of carrier up to 1000 μg/kg. In contrast, the accumulation of radioactivity in the cerebellum was not significantly changed by co-injection of carrier ligand following injection of either radioligand.

In mice pretreated with DMI (30 mg/kg i.p. 30 min prior to tracer injection), changes in saturation curves were observed (FIG. 2). From 0.2 μg/kg to 1000 μg/kg of carrier ligand, the difference of specific binding in the striatum between the control and the DMI-treated mice was highly significant with both ^{3}H-SCH23390 and ^{3}H-NMSP; these changes appeared to be due to the alteration of apparent affinities in vivo.

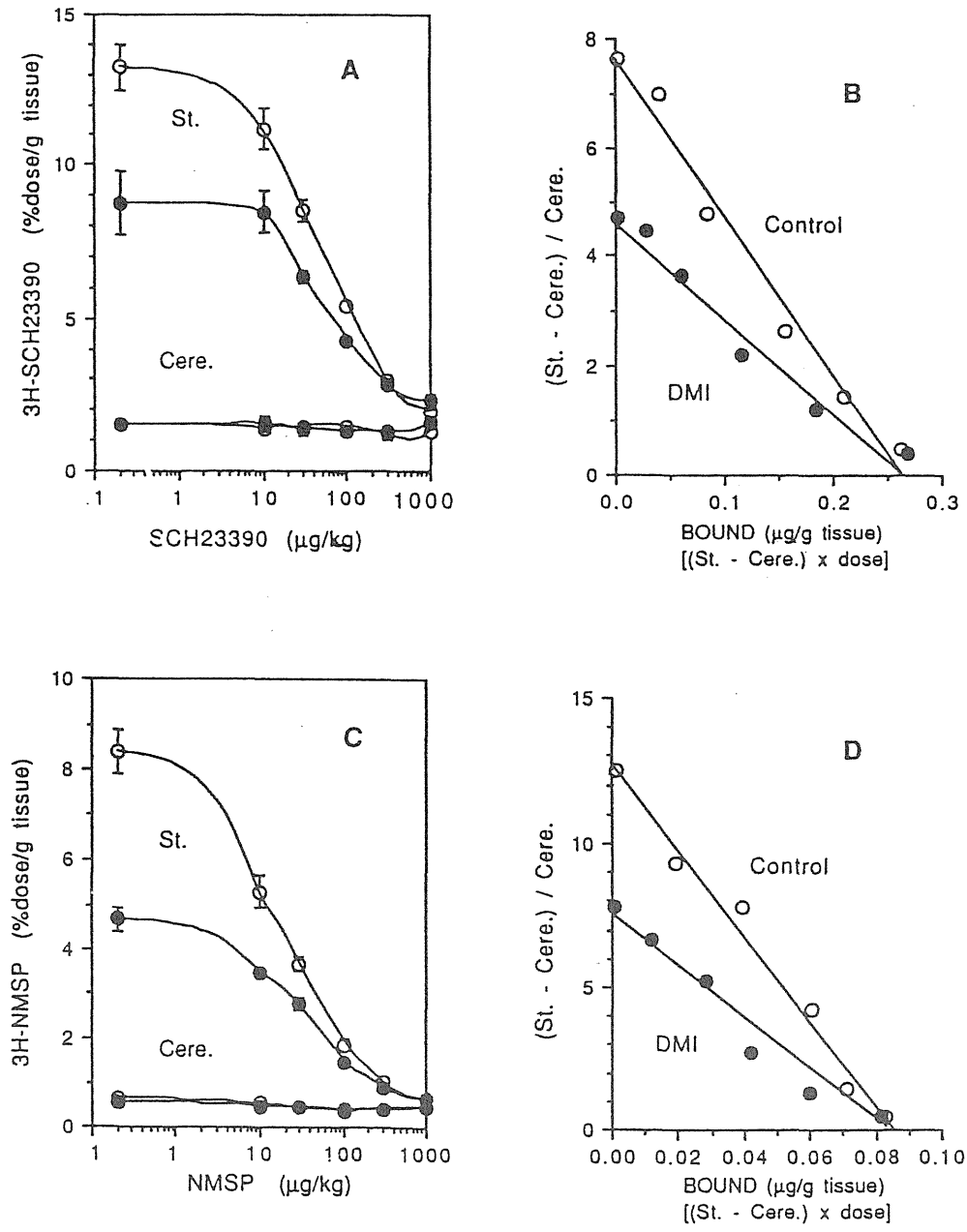

FIG. 2

Saturation experiment of in vivo binding of 3H-SCH23390 and 3H-NMSP in control and DMI-treated mice. Each point represents the average of 4 mice.The accumulation of radioactivity in the striatum (St.) and cerebellum (Cere.) at 15 min after the injection of ^{3}H-SCH23390 into control (○) and DMI-treated (●) mice (A, B). The accumulation of radioactivity in the striatum (St.) and cerebellum (Cere.) at 45 min after the injection of ^{3}H-NMSP into control (○) and DMI-treated (●) mice (C, D).

Scatchard plot of in vitro binding of ^{3}H-SCH23390 and ^{3}H-NMSP in the presence or absence of 1 mM of DMI (FIG. 3). There were no significant differences in the binding parameters (KD and Bmax) of the two different incubation conditions.

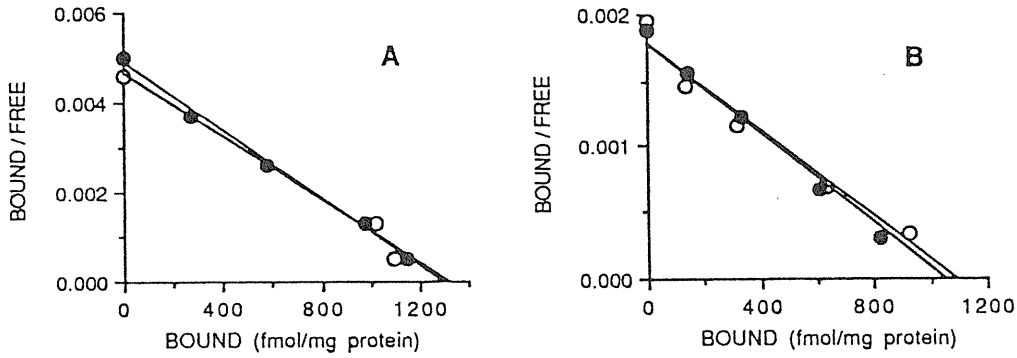

FIG. 3

In vitro Scatchard analysis in the absence (○) or presence (●) of 1 mM DMI. A. ^{3}H-SCH23390 binding. B. ^{3}H-NMSP binding.

Effect of other antidepressants: The classical tricyclic antidepressants imipramine, desipramine, clomipramine, and recently developed drugs maprotiline and mianserin were injected intraperitoneally into mice 30 min prior to the tracer injection. In all cases, a significant decrease in the binding of both ^{3}H-SCH23390 (FIG. 4A) and ^{3}H-NMSP (FIG. 4B) in vivo was observed.

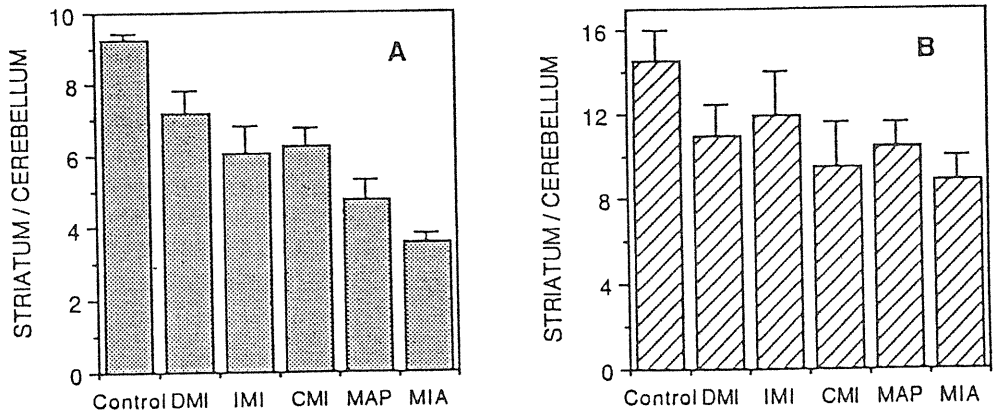

FIG. 4

The effect of a single administration of various antidepressants on dopamine D1 and D2 binding. Mice were administered 30 mg/kg of desipramine (DMI), imipramine (IMI), clomipramine (CMI), maprotiline (MAP), mianserin (MIA), 30 min prior to the administration of radio-tracer. A. Striatum/cerebellum ratio 15 min after the injection of ^{3}H-SCH23390. B. Striatum/cerebellum ratio 45 min after the injection of ^{3}H-NMSP.

Effect of ketanserin: Ketanserin was injected into mice 30 min prior to the tracer injection. The binding of both ^{3}H-SCH23390 (FIG. 5A) and ^{3}H-NMSP (FIG. 5B) in the striatum was decreased by treatment with ketanserin in a dose-dependent manner. In the cortex, the binding of ^{3}H-NMSP (FIG. 5B) was decreased significantly in a dose-dependent manner, whereas only a slight decrease was observed in the binding of ^{3}H-SCH23390 (FIG. 5A).

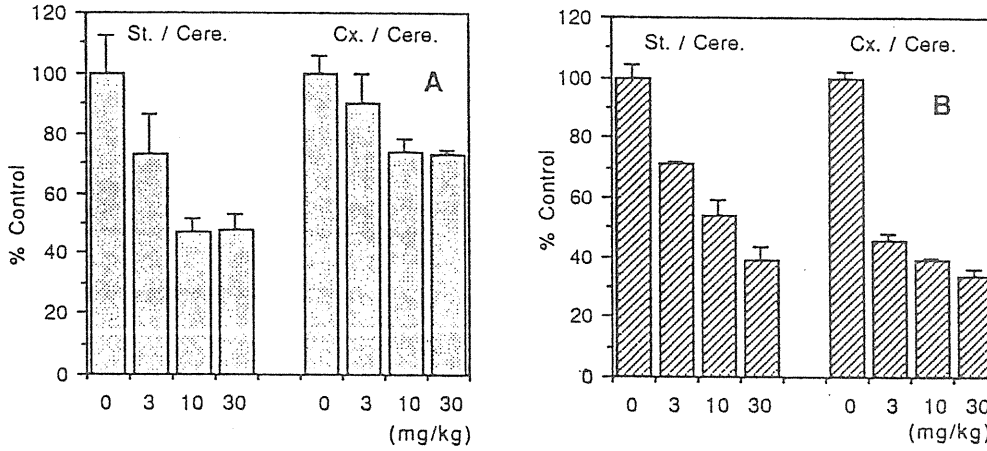

FIG. 5

The effect of ketanserin on the binding of ^{3}H-SCH23390 (A) and ^{3}H-NMSP (B) in the striatum and in the cortex. Three different doses of ketanserin (3 mg/kg, 10 mg/kg, 30 mg/kg) were administered intraperitoneally at 30 min before the injection of radio-tracer. The data represent the ratio of the radioactivity in the striatum (St.) and the cortex (Cx.) to that in the cerebellum (Cere.) expressed as a percentage of the control.

Discussion

As previously reported, D1 and D2 dopamine receptors can be labeled in vivo using the selective radioligands ^{3}H-SCH23390 and ^{3}H-NMSP, respectively. Both ^{3}H-SCH23390 and ^{3}H-NMSP are selectively accumulated in the striatum following intravenous administration. The cerebellum can be used as a reference region for the estimation of non-specific binding and free-ligand concentration in vivo, due to the negligible density of dopamine receptors. For the quantification of dopamine receptors in vivo, the ratio of radioactivity in the striatum to that in the cerebellum can be used as an index of receptor binding (9-11). In the present study the ratio at 45 min after the injection of the ligand was used for ^{3}H-NMSP binding(11), and that at 15 min after the injection for ^{3}H-SCH23390 binding (12).

In the present study we found a significant decrease in the striatum/cerebellum ratio of both D1 and D2 receptors labeled by ^{3}H-SCH23390 and ^{3}H-NMSP, respectively, after a single administration of DMI. This reduction was dose dependent in both D1 and D2 dopamine receptors (FIG. 1). Previous reports of the direct effect of various antidepressants on dopamine receptors in vitro have indicated that DMI is one of the least potent compounds on both D1 and D2 dopamine receptors (5,6). The present results confirmed that there is no direct effect of DMI on either ^{3}H-SCH23390 or ^{3}H-NMSP binding in vitro (FIG. 3). Therefore, the acute effect of DMI on the in vivo binding of both types of dopamine receptors can not be explained by direct interaction. Change in cerebral blood flow during the in vivo binding is not a likely explanation, since no changes in cerebral blood flow have been reported by a single administration of DMI

(10 mg/kg) (15). One possible explanation is that there is some DMI-induced alteration in an unknown factor at the receptor site, which affects in vivo binding. Although the receptor binding in vivo does not reach the equilibrium state, the results of the present saturation experiment suggest that in vivo apparent affinity of both D1 and D2 dopamine receptors appears to be altered by DMI (FIG. 2). The mechanism underlying this change is unknown. However with regard to the receptor binding in vivo, there might be a significant difference from that in vitro. For example Chugani et al.(7) reported a decrease in binding of ^{3}H-spiperone in vivo in reserpinized rat striatum without any changes in KD or Bmax values in vitro. They proposed agonist-mediated receptor internalization as the mechanism for the change in dopamine receptor binding in vivo. Following receptor internalization, endocytic vesicles would act as a diffusion barrier, restricting ligand diffusion away from the receptor. However, this hypothesis seems unlikely for the explanation of the present results, since the levels of dopamine, DOPAC and HVA in the brain are not altered by a single administration of DMI (16). Thus, the diffusion barrier might be altered by acute treatment of DMI through another mechanism, resulting in the alteration of apparent affinity (17).

Our results also indicated that both classic antidepressants and non-tricyclic antidepressants decreased the binding of dopamine D1 and D2 receptors (FIG. 4). However, mianserin (18) and maprotiline (19) have been reported to have no effect on ^{3}H-spiperone binding in the striatum in vivo. One possible explanation of these discrepancies may be the species difference (rats and mice), but the most probable explanation is the difference in the methods used for the in vivo binding (20), in paticular, the homogenation and filtration processes used in that experiment differed from those used in this study.

The antidepressants used here have been reported to have some 5-HT2 blocking properties (21), and ketanserin treatment also decreased the ^{3}H-SCH23390 and ^{3}H-NMSP binding in the striatum (FIG. 5). These results indicated the important role of serotonin receptors on the dopamine receptor bindings. Although ketanserin showed a significant effect on the ^{3}H-SCH23390 and ^{3}H-NMSP binding in the striatum and ^{3}H-NMSP binding in the cortex, only a minor decrease in ^{3}H-SCH23390 binding was observed in the cortex. The result was at variance with that in a previous report (22) in which on the binding of ^{3}H-spiperone in cortex was altered by SCH23390. In our experimental condition, the binding of ^{3}H-NMSP in the cortex, where the 5-HT2/dopamine ratio of receptor density is high, might be the direct effect of ketanserin on the 5-HT2 receptors. However in the striatum, the significant effect of ketanserin in vivo could not to be explained by simply a direct effect. Thus, there may be some indirect mechanism between the dopaminergic system and the serotonergic system through the neural network.

It has been reported that some antidepressants such as bupropion, which increase the synaptic level of dopamine, increase the affinity of dopamine D2 receptors in vivo after acute treatment (8). The reason for such discrepancy is unknown, but chronic administration of antidepressants that are reported to induce progressive subsensitivity in dopamine autoreceptors (3) and supersensitivity in some postsynaptic dopamine receptors (23) might lead to similar changes at dopamine receptors. Our preliminary data (unpublished) indicate that after chronic administration of DMI, the striatum/cerebellum ratio of both D1 and D2 receptors is slightly increased. Considering the mode of action of antidepressants, the adaptation mechanism of the acute effect might be more important and the adaptation mechanism of bupropion-like antidepressants and other antidepressants may differ. In this regard, further study is necessary to elucidate the mechanism of action of antidepressants in vivo.

In conclusion, the present data revealed an important role of the dopaminergic mechanism in several types of antidepressants in vivo.

References

1. A. RANDRUP, I. MUNKVAD, R. FOG, J. GERLACH, L. MOLANDER, B. KJELLBERG and J. SCHEEL-KRUGER, Curr. Dev. Psychopharmacol. 2 205-248 (1975).
2. P.C. WALDMEIER, J. Pharm. Pharmacol. 34 391-394 (1982).
3. L.A. CHIODO and S.M. ANTELMAN, Nature 287 451-454 (1980).
4. J.C. STOOF and J.W. KEBABIAN, Life Sci. 35 2281-2296 (1984).
5. E. RICHELSON and A. NELSON, J. Pharmacol. Exp. Ther. 230 94-102 (1984).
6. G. FAEDDA, N.S. KULA and R.S. BALDESSARINI, Biochem. Pharmacol. 38 473-480 (1989).
7. D.C. CHUGANI, R.F. ACKERMANN and M.E. PHELPS, J. Cereb. Blood Flow Metab. 8 291-303 (1988).
8. S. BISCHOFF, H. BITTIGER, J. KRAUSS, A. VASSOUT and P.WALDMEIER, Eur. J. Pharmacol. 104 173-176 (1984).
9. J.J. FROST, A.C. SMITH, M.J. KUHAR, R.F. DANNALS and H.N. WAGNER JR, Life Sci. 40 987-995 (1987).
10. M.J. KUHAR, L.C. MURRIN, A.T. MALOUF and N. KLEMM, Life Sci. 22 203-210 (1978).
11. D.F. WONG, H.N. WAGNER, JR., R.F. DANNALS, J.M. LINKS, J.J. FROST, H.T. RAVERT, A.A. WILSON, A.E. ROSENBAUM, A. GJEDDE, K.H. DOUGLASS, J.D. PETRONIS, M.F. FOLSTEIN, J.K.T.TOUNG, H.D. BURNS and M.J. KUHAR, Science 226 1393-1396 (1984).
12. P.H. ANDERSEN and F.C. GRONVALD, Life Sci. 38 1507-1514 (1986).
13. C. MISSALE, E. NISOLI, P. LIBERINI, P. RIZZONELLI, M. MEMO, M.BUONAMICI, A. ROSSI and P. SPANO, Brain Res. 483 117-122 (1989).
14. P. SEEMAN, N.H. BZOWEJ, H.C. GUAN, C. BERGERON, L.E. BECKER, G.P. REYNOLS, E.D. BIRD, P. RIEDERER, K. JELLINGER, S. WATANABE and W.W. TOURTELLOTTE, Synapse 1 399-404 (1987).
15. E. BUCHWEITZ, M. ROFFMAN and H.R. WEISS, Eur. J. Pharmacol. 106 19-26 (1984).
16. S. SUGITA, A. KOBAYASHI, S. SUZUKI, T. YOSHIDA and K. NAKAZAWA, Eur. J. Pharmacol. 165 191-198 (1989).
17. D.C. PERRY, K.B. MULLIS, S. OIE and W. SADEE, Brain Res. 199 49-61 (1980).
18. R. ORTMANN, S. BISCHOFF, E. RADEKE, O. BUECH and A. DELINI-STULA, Naunyn-Schmiedeberg's Arch. Pharmacol. 321 265-270 (1982).
19. A. DELINI-STULA, S. BISCHOFF and E. RADEKE, Drug Dev. Res. 2 543-55 (1982).
20. S. BISCHOFF, H. BITTIGER and J. KRAUSS, Eur. J. Pharmacol. 68 305-315 (1980).
21. S. O. OGREN, K. FUXE, L. F. AGNATI, J. A. GUSTAFSSON, G. JONSSON and A. C. HOLM, J. Neural Transm. 46 85-103 (1979).
22. S. BISCHOFF, M. HEINRICH, J. M. SONNTAG and J. KRAUSS, Eur. J. Pharmacol. 129 367-370 (1986).
23. V. KLIMEK and J. MAJ, J. Pharm. Pharmacol. 41 555-558 (1989).

《原　著》

ヒト前頭葉における ^{11}C-N-methylspiperone の結合能の加齢による変化

米澤　久司*,**　伊豫　雅臣*　伊藤　高司***　福田　寛*
山崎統四朗*　井上　修*　須原　哲也*　篠遠　仁*
西尾　正人*　東儀　英夫**　舘野　之男*

要旨　Positron emission tomography (PET) を用いて前頭皮質における ^{11}C-N-methylspiperone (NMSP) と serotonin S2 受容体との結合能の加齢にともなう変化について，22 歳から 72 歳までの健常ボランティア 11 例について検討した．前頭皮質での ^{11}C-NMSP の取り込みは静注後 5～15 分でピークに達し徐々に減少し，小脳では約 10 分でピークに達したのち速やかな減少を認めた．解析には 3-コンパートメントモデルを用いた．NMSP と特異的結合部位をもたない小脳を入力関数として，結合速度定数 k3・解離速度定数 k4 を求め，その比を結合能 (k3/k4) として定量評価した．結合能は加齢にともない著明な減少を認めた．この減少は主に結合速度定数 k3 の低下によるものであった．結合能は親和定数 Kd と最大結合数 Bmax を用いて Bmax/Kd で表わされるが，加齢にともなう結合能の低下は前頭皮質における serotonin S2 受容体の Bmax の減少によるものと考えられた．

I. はじめに

加齢に伴って中枢神経系の機能が低下することはよく知られた事実であり，その生化学的背景についても動物脳やヒト剖検脳を用いた多くの研究報告がなされている[1~3]．

近年種々の標識リガンドの動態を通して，各種神経受容体の分布やその結合特性の測定がポジトロン CT (PET) や SPECT を用いて直接ヒトを対象として可能となってきた．加齢にともなう脳血流量 (CBF) や糖代謝量の測定報告がいくつか見られるが，CBF は若干の低下に過ぎず代謝量もそれ程大きな変化はしていないという結果が多い[4~7]．

脳神経受容体については ^{11}C-N-methylspiperone (^{11}C-NMSP) を用いたヒト線条体における dopamine D2 受容体の in vivo 結合能 (BP＝B max/Kd) が加齢に伴って著明に低下することが報告されており[8]，われわれもそれを確認した[9]．

^{11}C-NMSP は大脳皮質にも特異的結合をすることが判明しており，それは主に serotonin S2 受容体との結合であるといわれている[8]．そこで今回健常ボランティア 11 例について ^{11}C-NMSP の大脳皮質における結合能の加齢にともなう変化をコンパートメントモデルを用いて定量解析したので報告する．

II. 方　法

1. 対　象

対象は先に伊豫ら[9]により報告された22歳から72歳の男性ボランティア10人に新たに検査を行っ

* 放射線医学総合研究所臨床研究部
** 岩手医科大学神経内科学講座
*** 日本医科大学数学科教室
受付：2 年 5 月 23 日
最終稿受付：2 年 10 月 1 日
別刷請求先：岩手県盛岡市内丸 19–1　(〒020)
岩手医科大学神経内科学講座
米　澤　久　司

た1人を加えた11人であり，全員神経学的に異常を認めずまた中枢に作用する薬物の服用はしていない．PET検査施行時に行った血算・生化学的検査にても異常を示さなかった．検査にあたって被験者には検査内容を十分に説明して同意を得た．

2. ^{11}C-NMSP の動態測定

^{11}C-NMSP注射薬はすでに報告した方法[10]に基づき製造した．比放射能は 17.9±5.7 GBq/μ mol であった．

約330 MBq (330±46 MBq) のトレーサー・^{11}C-NMSPを肘静脈より静注し，投与直後より2分間，引き続き5分間のダイナミック・スキャンをそれぞれ5回，10～16回繰り返し行い経時的な脳内放射能を測定した．脳内放射能はポジトロジカ II (日立メディコ社製)[11]にて測定した．この装置は3リングで，スライス間隔18 mmで5スライスのデータを同時に収集できる．スライス厚は約13 mm (FWHM) であり，空間分解能は約10 mm (FWHM) である．測定は最下層のスライスが被験者の orbito-meatal line から10 mm 上方で平行になるようにし安静閉眼仰臥位にして行った．

また，一部の被験者についてはトレーサー静注後経時的に反対側肘静脈から1回1～2 mlずつ14回の採血を行い，遠心分離後，血漿1 mlの放射能をウエル型カウンターにて測定し半減期補正を行った．

再構成した経時的画像も半減期補正を行い，画像上に関心領域を小脳および左右の前頭葉に設定した．前頭皮質では左右の平均の放射能値を用いて，小脳，前頭皮質の両領域および血漿の時間放射能曲線を作成した．

3. データの解析

^{11}C-NMSP と前頭葉との結合能を Fig. 1 に示した3コンパートメントモデルを用いて解析した．

各分画のトレーサー濃度の時間変化を速度定数 (k1～k4) を用いて表わすと

$$\begin{aligned} dCe/dt &= k1\cdot Cp-(k2+k3)\cdot Ce+k4\cdot Csp \\ dCsp/dt &= k3\cdot Ce-k4\cdot Csp \end{aligned} \qquad (1)$$

ここで Ce は脳内遊離リガンド濃度＋非特異的結合リガンド濃度，Csp は特異的結合リガンド濃度，Cp は血漿中リガンド濃度である．

前頭葉のリガンド濃度 Cfrt は，

$$Cfrt=Ce+Csp \qquad (2)$$

また小脳には特異的結合部位がないことから小脳では2コンパートメントモデルが考えられる (Fig. 1)．ここで Cce は小脳内遊離リガンド濃度＋非特異的結合リガンド濃度を表すが，皮質における k1，k2 と小脳における k1′，k2′ はほぼ等しく k3，k4 に比較すると非常に大きいと考えられるので，脳内での遊離リガンド濃度＋非特異的結合リガンド濃度 Ce に近似できるとされる[8,12]．

したがって (2) 式は次のように表すことができる．

$$Cfrt\fallingdotseq Cce+Csp \qquad (3)$$

各部位の放射能は各リガンド濃度に比例するので

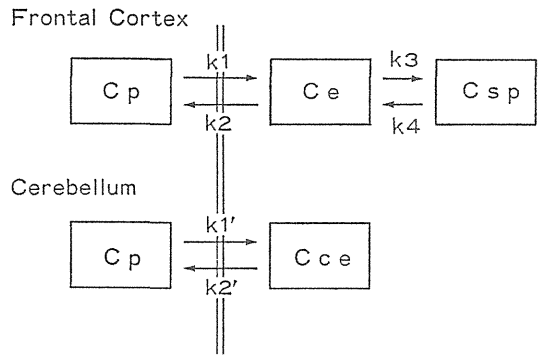

Cp : ligand concentration in plasma

Ce : ligand concentration of free plus nonspecific binding in the brain

Csp : ligand concentration of specific receptor-binding

Cce : ligand concentration of free plus nonspecific binding in cerebellum

k1, k1′ : rate constant from the plasma to tissue

k2, k2′ : rate constant from the tissue to plasma

k3 : rate constant from the tissue to receptor

k4 : rate constant from the receptor to tissue

Fig. 1 Three compartment model used for the quantification of k3 and k4 value. The cerebellum was used as a reference region for the estimates of non-specific bind plus free ligand concentration.

小脳の放射能を A ce (t)，前頭皮質の放射能を A frt (t)，前頭皮質で特異的結合している放射能を A sp (t) とすると (1), (3) 式は，

$$dA\,sp\,(t)/dt = k3 \cdot A\,ce\,(t) - k4 \cdot A\,sp\,(t) \quad (4)$$

$$A\,frt\,(t) = A\,ce\,(t) + A\,sp\,(t) \quad (5)$$

(4) 式を A sp (0)=0, A ce (0)=0 の境界条件のもとで解くと

$$A\,sp\,(t) = k3 \cdot \int_0^t A\,ce\,(t-\tau) \cdot e^{-k4\tau}\,d\tau \quad (6)$$

である．

A sp (t) は (5) 式より実測値の A frt (t), A ce (t) を用いて

$$A\,sp\,(t) = A\,frt\,(t) - A\,ce\,(t) \quad (7)$$

で推定できる．

以上から (6), (7) 式により最小二乗法を用いて k3, k4 を決定した．

Kon (association rate constant), Koff (dissociation rate constant) を用いると解離定数 Kd, 速度定数 k4 は次のように定義される．

$$Kd = Kon/Koff$$

$$k4 = Koff$$

また，k3 は最大結合部位数を B max とすると Kon・B max に比例する[13]ことが知られている．k3/k4=Bmax/Kd であり，これを結合能 (Binding Potential: BP)[23] として評価した．

III. 結　果

前頭皮質の ^{11}C-NMSP の取り込みは7～15分で最高になりその後緩やかに減少した．側頭葉，頭頂葉についても前頭葉とほぼ同様の取り込みを示した．各部位での取り込みに左右差は認めなかった．一方小脳では10分で取り込みは最高になりその後速やかに減少した (Fig. 2)．この小脳における放射能動態を入力関数にして最小二乗法により決定した k3, k4, および結合能 (k3/k4) を Fig. 3, 4 にそれぞれ示した．結合能 (Binding Potential: BP) の加齢 (x) にともなう変化は負の相関が認められ，一次回帰式は BP=−0.00821x+1.297 (r=−0.711) であり (Fig. 3), k3 および k4 についても負の相関で得られた回帰式は k3=−0.0006011x+0.0520 (r=−0.885), k4=−0.00435x+0.0461 (r=−0.706) であった (Fig. 4).

また先に伊豫らにより報告した[9]線条体における結合能 k3 と今回の前頭皮質における結合能の

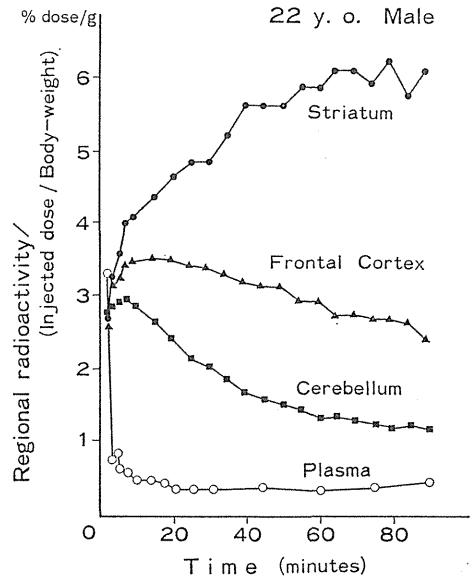

Fig. 2　Time course of radioactivity in the frontal cortex, striatum, cerebellum and plasma, following intravenous injection of ^{11}C-NMSP.

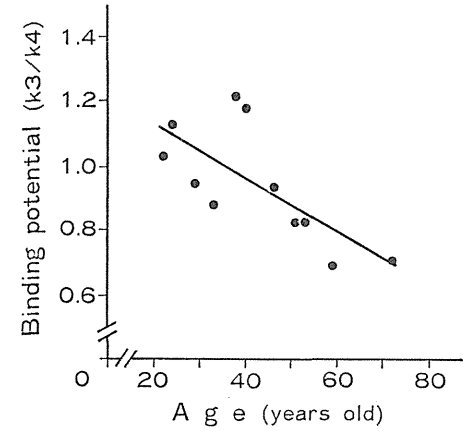

Fig. 3　Reduced binding potential (BP) of ^{11}C-NMSP in the frontal cortex with age.

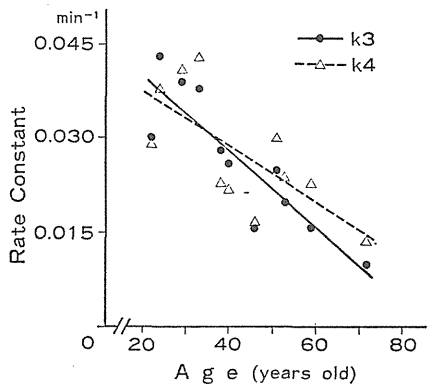

Fig. 4 Changes in the rate constants k3 and k4 values with age.

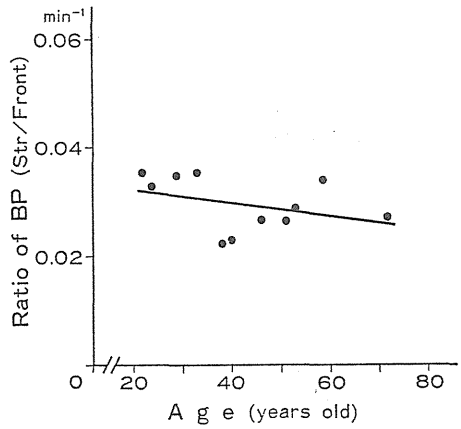

Fig. 5 The ratio of the binding potential (BP) in the striatum to the frontal cortex in individual subject.

比は，加齢に対して有意の変化は認めなかった (Fig. 5).

IV. 考　案

^{11}C-NMSP の前頭皮質での結合能の加齢変化を小脳の放射能動態を入力関数とすることで評価した．小脳の放射能動態を入力関数とすることについては (1) 標識代謝物の影響 (2) 非特異結合のパラメータの部位間での差などについて今後詳細な検討が必要であるが，被験者への負担，検査法の簡便さを考えると優れた方法と考えられる．血中遊離型リガンド濃度を入力関数とする方法は測定値の誤差や代謝物の測定法の困難さを考えると現在のところ実用的でないと考えられる．

先に伊豫らが報告した線条体での ^{11}C-NMSP の結合能の測定においては k4=0 と仮定することができたが[9,14]，前頭皮質では k4 を無視できないため非線形最小二乗法で ^{11}C-NMSP の結合能 (Binding Potential) として評価した．

NMSP の前頭皮質での結合については dopamine D2 受容体への結合とする報告[15,16] と，serotonin S2 受容体への結合とする[8,17~20] 報告がある．

最近 NMSP よりもより dopamine D2 受容体に選択性の高いとされる raclopride を用いてサルの大脳皮質に広く dopamine D2 受容体が存在することが示された[21]．しかし，解離定数 Kd は線条体のそれと比較してほぼ同程度であったが，最大結合部位数 B max は 2.3 fmol/g であり線条体での密度と比較すると約1/80しか存在しなかった[21]．結合能は B max/Kd に比例することから ^{11}C-NMSP の大脳皮質での dopamine D2 受容体との結合は非常に少ないと考えられる．事実 Farde らの報告では ^{11}C-raclopride の大脳皮質への特異的結合は非常に低いことが報告されている[22]．それにもかかわらず今回のヒト大脳皮質の ^{11}C-NMSP の放射能は線条体の約 1/2～1/3 程度の集積が認められたため，^{11}C-NMSP の大脳皮質の結合は大部分が serotonin S2 受容体の可能性が高いと考えられる．

健常者の前頭皮質での ^{11}C-NMSP の結合 (k3/k4) は加齢にともなって有意の低下が認められた．加齢により脳血流量は低下するとの報告[7] もあるが，in vivo での ^{11}C-NMSP の結合は脳局所血液量や脳局所血流量にほとんど影響をうけないこと[23]が知られており，この結合能の低下は脳血流量の低下には依存していない．速度定数 k3, k4 のそれぞれの値についてみると，k3 および k4 とも加齢に従い有意に低下しているが，結合能が低下するのは k3 の低下が k4 の低下よりも大きいためであることがわかった．ところで in vivo で，k3 は Kon・B max に比例する[13]ことが知られてい

る．したがって，k3 の低下は Kon または B max の低下のためと考えられる．線条体における結合能 (k3) の低下と前頭皮質における結合能 (k3/k4) の低下との比はほぼ一定であり加齢による結合能の低下の割合は線条体でも前頭皮質でもほぼ同じであることが明らかになった．

In vitro では加齢とともに前頭皮質での serotonin S2 受容体の最大結合数 B max は減少[24~26]し解離定数 Kd は変わらないと報告されており，Kd=Kon/Koff であることから，今回の k3 減少に起因する結合能の低下は B max の減少による可能性が高い．

最近，in vivo のリガンド－レセプター結合に関して in vitro との相違がいくつか報告されている．中でも reserpine 処理したラットを用いた ^{3}H-spiperone の結合実験で in vivo の系では結合能の低下を認めるが，in vitro の系では Kd, B max ともに変化しなかったという報告がある[27]．生体膜の流動性が受容体の結合パラメータに大きな影響を与えているという報告があり[28]，加齢ともない生体膜の特性も変化することがよく知られている[29,30]．したがって in vivo の系と in vitro の系の変化は，B max の変化以外にこの様な膜の特性の変化も含んでいる可能性も否定できない．In vivo の系では，完全なリガンド－レセプターの平衡状態は得ることができず Kd, B max は求めることができないが，飽和実験により擬似的 Scatchard plot を用いて擬似的に Kd, B max を求めることができる[22]．しかしながら，人に対する飽和実験は倫理面をふくめ難しいことが多いので，動物実験により in vivo の系での Kd, B max の加齢変化について詳細な検討が必要と思われる．

こうした前頭皮質での結合能を in vivo で測定することは正常加齢のみでなく Parkinson 病，Alzheimer 病などの種々の精神神経疾患の病態を知る上で重要であると考えられる．

謝辞　本研究の RI 生産および ^{11}C-NMSP の標識合成にあたりご協力いただいた放射線医学総合研究所サイクロトロン管理課鈴木和年氏，玉手和彦氏および三門富士夫氏に感謝いたします．また，終始本研究に対しご助言いただいた放射線医学総合研究所特別研究員樫田義彦先生，同所臨床研究部研究生の方々に感謝いたします．

文　献

1) Agnati LF, Fuxe K, Benfenati F, et al: III. Studies on aging processes. Acta Physiol Scand (Suppl) **532**: 45–61, 1984
2) McGeer PL, McGeer EG: 23, Neurotransmitters in the aging brain. The Molecular Basi of Neuropathology, pp. 631–648, Ed. by Davision AN and Thompson RHS Edward Arnold Ltd. 1981
3) Winblad B, Hardy J: Memory function and brain biochemistry in normal aging and in senile Dementia. Ann NY Acad Sci **444**: 255–268, 1985
4) Duara R, Margolin RA, Robertson-Tchabo EA, et al: Cerebral glucose utilization as measured with positron emission tomography in 21 resting healthy men between ages of 21 and 83 years. Brain **106** (Pt 3): 761–775, 1983
5) deLeon MJ, Ferris SH, George AE, et al: Positron emission tomographic studies of aging and Alzheimer disease. AJNR **4**: 568–571, 1983
6) Pantano P, Baron J-C, Lebrun-Grandie P, et al: Regional cerebral blood flow and oxygen consumption in human aging. Stroke **15**: 635–641, 1984
7) Frackowiak RSJ, Lenzi GL, Jones T, et al: Quantitative measurement of regional cerebral blood flow and oxygen metabolism in man using oxygen-15 and positron emission tomography: theory, procedure, and normal values. J Comput Assist Tomogr **4**: 727–736, 1980
8) Wong DF, Wagner HN Jr, Dannals RF, et al: Effects of age on dopamine and serotonin receptors measured by positron tomography in the living human brain. Science **226**: 1393–1396, 1984
9) 伊豫雅臣，他：加齢に伴うヒト線条体 D2 ドーパミン受容体結合能の低下――ポジトロン・エミッション・トモグラフィーによる測定――．核医学 **26**: 2, 213–220, 1989
10) Suzuki K, et al: Automatic production of N-[^{11}C]methylspiperone solution for injection and the study of its radiolysis. In Press.
11) Takami K, Ueda K, et al: Performance study of whole-body, multislice positron computed tomography-Positologica II—. IEEE Trans Nucl Sci **NS30**: 734, 1983
12) Welch MJ, Raichle MER, Kilbourn MR, et al: (^{18}F)spiroperiodol: a radiopharmaceutical for the in vivo study of the dopamine receptor. Ann Neurol **15**(Suppl): S77–S78, 1984
13) Wong DF, Gjedde A, Wagner HN Jr: Quantification of neuroreceptors in the living human brain.

I. Irreversible binding of ligands. J Cereb Blood Flow Metab 6: 137–146, 1986
14) Laduron PM, Janssen PF, Leysen JE: Spiperone: a ligand of choice for neuroleptic receptors. 2. Regional distribution and in vivo displacement of neuroleptic drugs. Biochem Pharmacol 27: 317–321, 1978
15) Liskowsky DR, Potter LT: D-2 dopamine receptors in the frontal cortex of rat and human. Life Sci 36: 1551–1559, 1985
16) Bruinink A, Lichtensteiger W, Schlumpf M: Pre- and postnatal ontogeny and characterization of dopaminergic D2, serotonergic S2, and spirodecanone binding sites in rat forebrain. J Neurochem 40: 1227–1236, 1983
17) List SJ, Seeman P: Resolution of dopamine and serotonin receptor components of [^{3}H]spiperone binding to rat brain regions. Proc Natl Acad Sci USA 78: 2620–2624, 1981
18) Burns HD, Dannals RF, Langstrom B, et al: (3-N-[^{11}C]methyl)spiperone, a ligand binding to dopamine receptors: radiochemical synthesis and biodistribution studies in mice. J Nucl Med 25: 1222–1227, 1984
19) Lyon RA, et al: 3H-3-N-Methylspiperone labels D2 dopamine receptors in basal ganglia and S2 serotonin receptors in cerebral cortex. J Neurosci 6: 2941–2949, 1986
20) Chivers J, Jenner P, Marsden CD: Pharmacological characterization of binding sites identified in rat brain following in vivo administration of [^{3}H]spiperone. Br J Pharmacol 90: 467–478, 1987
21) Lidow MS, Goldman-Rakic PS, Rakic P, et al: Dopamine D2 receptors in the cerebral cortex: Distribution and pharma cological characterization with [^{3}H]raclopride. Proc Natl Acad Sci USA 86: 6412–6416, 1989
22) Farde L, Hall H, Ehrin E, et al: Quantative analysis of D2 dopamine receptor binding in the living human brain by PET. Science 231: 258–261, 1986
23) Mintun MA, Raichle ME, Kilbourn MR, et al: A quantitative model for the in vivo assessment of drug binding sites with positron emission tomography. Ann Neurol 15: 217–227, 1984
24) Creese I, Burt DR, Synder SH: Dopamine receptor binding: differentiation of agonist and antagonist states with ^{3}H-dopamine and ^{3}H-haloperidol. Life Sci 17: 993–1001, 1975
25) Marcusson JO, Morgan DG, Winblad B, et al: Serotonin-2 binding sites in human frontal cortex and hippocampus. Selective loss of S-2A sites with age. Brain Res 311: 51–56, 1984
26) Brunello N, Riva M, Rovescalli AC, et al: Age-related changes in rat serotonergic and adrenergic systems and in receptor responsiveness to subchronic desipramine treatment. Pharmacol Toxicol 63: 150–155, 1988
27) Chugani DC, Ackermann RF, Phelps ME: In vivo [^{3}H]-spiperone binding: evidence for accumulation in corpus striatum by agonist-mediated receptor internalization. J Cereb Blood Flow Metab 8: 291–303, 1988
28) Antonian L, Lippa AS: Effect of AL721, a novel membrane fluidizer, on the binding parameters of brain dopamine receptors. Ann NY Acad Sci 515: 403–410, 1988
29) Malone MJ, Sooke MC: Neurochemical studies in aging brain. I. Structural changes in myeline lipids. J Gerontol 37: 262–268, 1982
30) Sun AY, Sun GY: Neurochemical aspect of the menbrane hypothesis of aging. I: Interdisciplaplinary Topics in Gerontology, ed. by HP von Harn, Vol. 15, pp. 34–53, S. Karger, Basser, 1979

Summary

Effect of Aging on in vivo Binding of ^{11}C-N-methylspierone in Living Human Frontal Cortex

Hisashi YONEZAWA*)**, Masaomi IYO*, Takashi ITOH***, Hiroshi FUKUDA*
Toshiro YAMASAKI*, Osamu INOUE*, Tetsuya SUHARA*, Hitoshi SHINOTOH*,
Masato NISHIO*, Hideo TOHGI** and Yukio TATENO*

**Division of Clinical Research, National Institute of Radiological Sciences*
***Department of Neurology, School of Medicine, Iwate Medical University*
****Department of Mathematics, Nippon Medical School*

Reduced in vivo binding of ^{11}C-N-methylspiperone (NMSP) with age in the living human frontal cortex was demonstrated, with positron emission tomography (PET). Eleven normal male volunteers (22 to 72 years old) were assessed.

The uptake of ^{11}C-NMSP in the frontal cortex peaked 7–15 min after intravenous injection, and then gradually decreased until the end of this study. On the other hand in the cerebellum, the uptake of ^{11}C-NMSP peaked 10 min and rapidly declined.

We analyzed the data using a three compartment model and determined rate constants k3 and k4. And the binding potential of receptors was estimated as the ratio of k3 (association rate constant) to k4 (dissociation rate constant) value. The k3 and k4 values were calculated from non-linear regression, given by the set of parameter values that minimized the deviation between the measured kinetics and model prediction. As an input function, we used the radioactivity in the cerebellum.

A significant reduction in BP with age was observed. Though both k3 and k4 values were decreased with age, this decrease of BP was found to be mainly due to the reduced k3 values. These results indicated that numbers of binding sites (Bmax) of serotonin S2 receptors in frontal cortex might be decreased with age.

Key words: PET, ^{11}C-NMSP, Serotonin S2 Receptor, Aging, Frontal cortex.

AMERICAN JOURNAL OF PHYSIOLOGIC IMAGING 5:50–54 (1990)

Carbon-13 NMR Imaging Study of In-Vivo Glucose Metabolism

HIROO IKEHIRA, MD, TAKAHIRO HASHIMOTO, MD, HIROSHI FUKUDA, MD, YASHUHIRO UESHIMA, MS, SATOSHI YAMAI, BS, TAKESHI MAKI, BS, TAKESHI A. IINUMA, PHD, AND YUKIO TATENO, MD

Division of Clinical Research, National Institute of Radiological Sciences, Anagawa-4 Chiba 260 (H.I., T.H., H.F., T.A.I., Y.T.) and Technical Center, Siemens-Asahi Medical Systems, Ltd., 221 Tanazawa, Atsugi 243-02, Kanagawa (Y.U., S.Y., T.M.), Japan

ABSTRACT **Carbon-13 NMR spectroscopy and chemical shift selective imaging studies of in vivo glucose metabolism were performed at 2.0 T. Some metabolite peaks were observed in ^{13}C NMR spectra, and carbon NMR imaging focused in the spectral region attributed to D-1-^{13}C-glucose were also performed. A ^{13}C NMR signal accumulated in the liver was detected and the average time resolution of these spectra and images were 10 and 30 minutes, respectively.**

Key words: Liver, tracer, ^{13}C spectroscopy

INTRODUCTION

Carbon-13 is one of the most interesting nuclei in the study of metabolism using NMR spectroscopy. Because the natural abundance of ^{13}C is only 1.1%, it may be used as an extra in vivo metabolic tracer [1–3], which can yield spectra that indicate very accurate information relating to the status in each molecular compound. From this point of view, NMR spectroscopic studies are completely different than other modalities such as SPECT, PET, Xray-CT, or ultrasonic imaging.

The observation of the dynamic metabolism of a biochemical substance in vivo will be very useful as a pathobiochemical diagnosis. There are some previous studies of ^{13}C imaging [4–6] but these studies were performed mainly for natural abundance ^{13}C NMR imaging, which was equivalent to fat imaging. In the case of investigating biochemical metabolism using ^{13}C as a tracer, it would be beneficial to obtain images of ^{13}C-labelled compounds without the interference of fat signal. Moreover, these images could be obtained within an appropriate scan time for a dynamic study, in spite of its low sensitivity. The aim of this study was to obtain dynamic in vivo metabolic information using not only NMR spectroscopy but also chemical shift selective imaging of the carbon-13 signal from D-1-^{13}C-glucose.

Received April 23, 1990; accepted May 3, 1990.

Address reprint requests to Dr. Hiroo Ikehira, Division of Clinical Research, National Institute of Radiological Sciences, 9-1, Anagawa-4-Chome, Chiba, 260, Japan.

The purpose of this preliminary study was to show that it is possible to obtain sufficient information from ^{13}C NMR spectroscopy and imaging with the appropriate dose and within a reasonable duration for clinical study. Our observations are based on ^{13}C NMR spectroscopy and imaging of the C3H mouse in vivo at 2.0 T.

MATERIALS AND METHODS

Ninetynine-atom% enriched D-1-^{13}C-glucose was purchased from Isotec, Inc., Miamisburg, OH, and the animals used were adult (1 year, male) C3H mice weighing approximately 30 g. They were maintained on water and chow ad lib until the day of study.

The preparation of the in vivo study was as follows; animals were anaesthetized with chloral hydrate (0.4 mg/g intra-peritoneally) and were allowed to breathe room air voluntarily. Carbon-13 labelled D-glucose (250–1,000 mg/mouse) was administrated through a stomachial cannula and the animals were placed on a horizontal platform in a room warmed to 30°C, and then positioned in the center of a cylindrical RF coil.

Carbon-13 NMR spectra and images from the whole body of the mice were then obtained at an operating frequency of 21.44 MHz on a RA-200 2.0 T system (Siemens-Asahi, Tokyo, Japan). The magnet bore size was 31 cm and contained magnetic field gradient of strength 20 mT/m. A single-tuned coil [7] and a dual-ports double-tuned coil, which could be tuned 21.44 MHz (^{13}C) and 85.26 MHz (^{1}H) simultaneously, were constructed. The latter coil joins the high-frequency channel and the low-frequency channel on

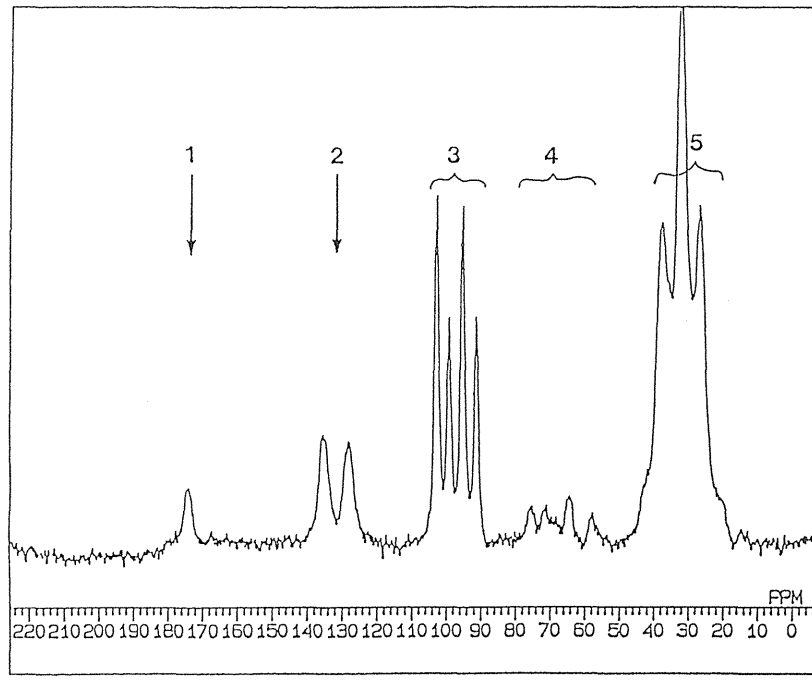

Fig.1a

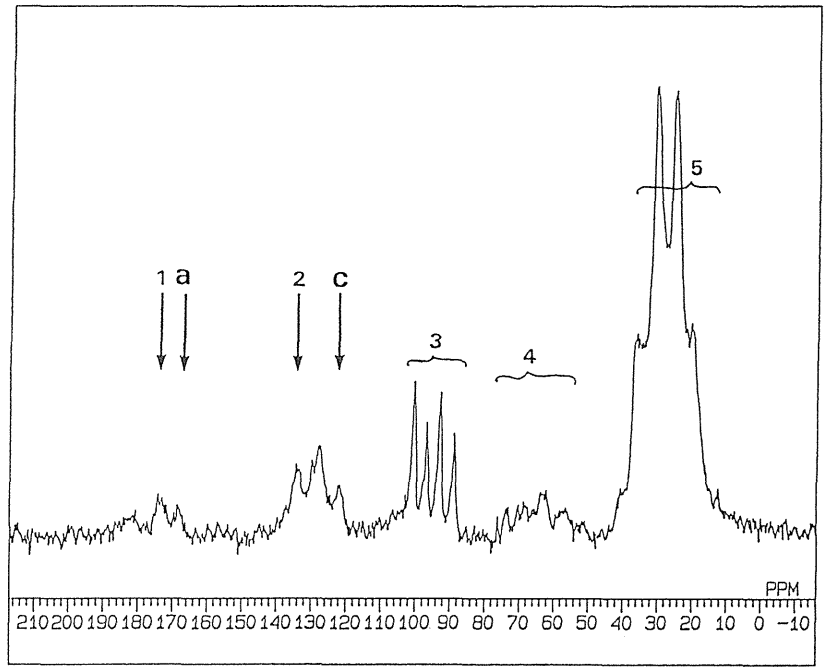

Fig.1b

Fig. 1. Carbon-13 NMR spectra post oral administration of D-1-^{13}C-glucose (1,000 mg/mouse) obtained from the whole of a C3H mouse at 2.0 T. 1a, 1b, 1c, and 1d show spectra at 5 minutes, 5, 10, and 24 hours after administration, respectively. Peak assignment: 1, COO; 2, −CH=CH−; 3, D-1-^{13}C-glucose; 4, glycerol; 5, fatty acyl chain; a, b, and c are new peaks that appeared. Figure panels 1c and 1d are on next page.

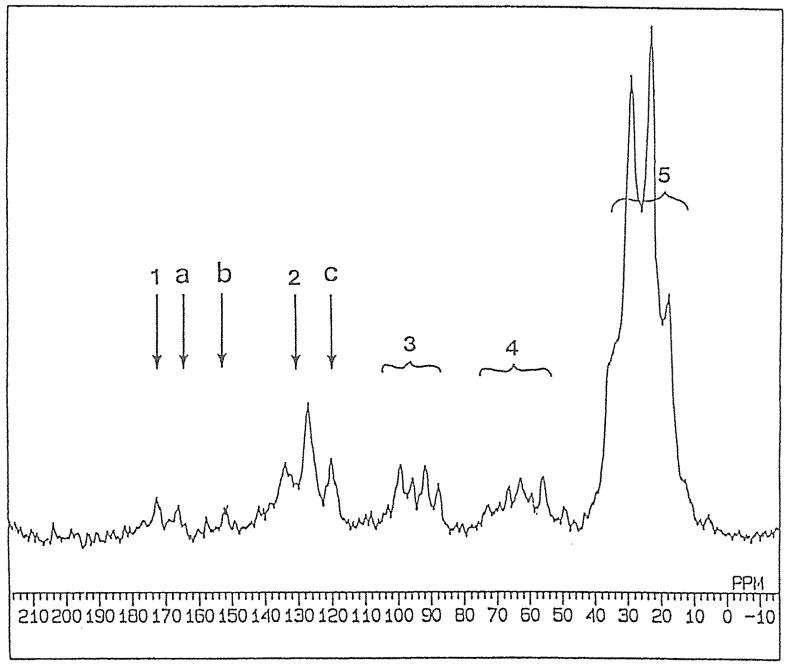

Fig.1c

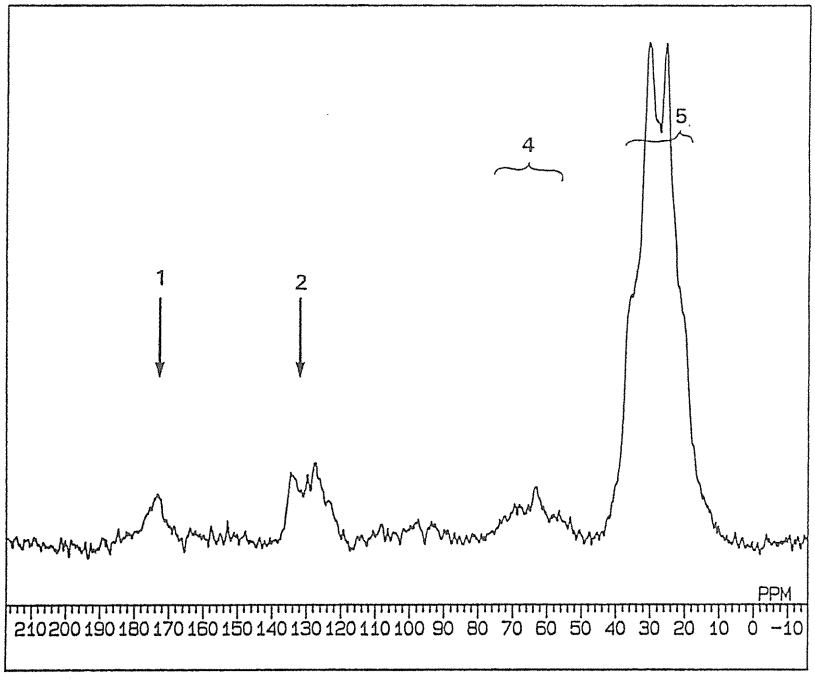

Fig.1d

Fig. 1. Carbon-13 NMR spectra post oral administration of D-1-^{13}C-glucose (1,000 mg/mouse) obtained from the whole of a C3H mouse at 2.0 T. 1a, 1b, 1c, and 1d show spectra at 5 minutes, 5, 10, and 24 hours after administration, respectively. Peak assignment: 1, COO; 2, −CH=CH−; 3, D-1-^{13}C-glucose; 4, glycerol; 5, fatty acyl chain; a, b, and c are new peaks that appeared.

the common ring. An inductive coupling was used to supply RF powers to the both channels. The physical dimensions of these coils were 7 cm in diameter and 10 cm in length. All spectra and images in this experiment were acquired without ^{1}H decoupling. The magnetic field was shimmed using the ^{1}H NMR resonances obtained from one whole body, giving a linewidth of the D-1-^{13}C-glucose that was generally in the range of 10–15 Hz. Carbon-13 NMR spectra were acquired with 5 kHz spectral width, pulse angles of 90°, and a recycle time of 0.7 sec, sampling points were 2048 and 1024 digitized signals were averaged, giving total scan time of approximately 12 minutes. Imaging experiments were performed using the field echo sequence (TR=300 msec, TE=10 msec, flip angle=90°), 2DFT technique without slice selection, therefore collected images were anterior-posterior projected shadowgrams. A gaussian shaped 4 msec 90° pulse was employed for selecting the specific spectral region, whose center frequency was adjusted to the D-1-^{13}C-β-glucose peak (92 ppm) and its bandwidth was approximately 700 Hz (30 ppm). Total phase encoding increments were 128 for a 20 cm FOV (field of view); the digitized signal was accumulated from 15 to 60 times. This resulted in total imaging times of 15 minutes for the early stage and 1 hour for the latter stages after ^{13}C-enriched glucose administration. The carrier frequency was 21.44046 MHz and the 16 kHz frequency encoded with butterworth filtering of the central 2 kHz. Proton SE (TR=500 msec, TE=30 msec, 256×256, 3 times repetitions, 7 mT/m gradient strength) images were also obtained for the reference to organ orientation.

RESULTS

Figure 1 shows the ^{13}C NMR spectra obtained after oral administration of D-1-^{13}C-glucose (1,000 mg/mouse) to a C3H mouse. Figure 1a to 1d show ^{13}C spectra at 5 minutes, 5, 10, and 24 hours, respectively, after the administration. Figure 1a shows administered D-1-^{13}C-glucose peaks in the natural abandance spectrum; then in Figure 1b there are three new peaks emerging at 120 ppm, 156 ppm, and 170 ppm. Glycerol and double-bonded carbons contributing to the increasing peak at number 4 and C peaks were observed in Figure 1b and 1C. The ^{13}C NMR signals assigned to C1-glucose were seen to decrease proportionally.

Figure 2 shows ^{13}C chemical shift selective images at 5, 65, 95, and 185 min after oral administration of D-1-^{13}C-glucose via stomachial catheter. High intensity is seen only in the stomach region until 65 min. Then a signal from the

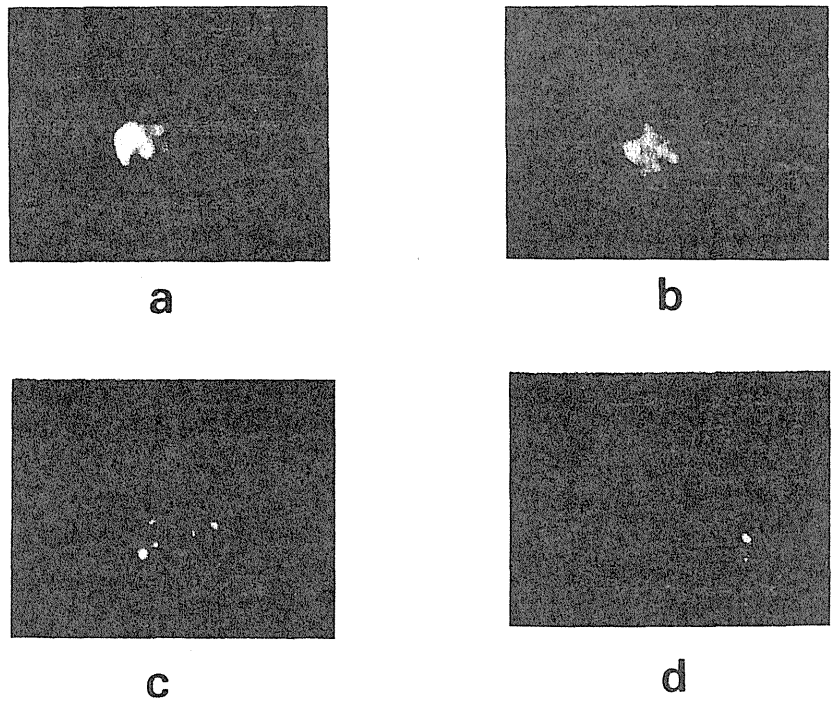

Fig. 2. Carbon-13 NMR chemical shift selective images: a shows an image 5 min after administration, b shows an image 65 min later, c shows an image 95 min later, and d shows an image 185 min later after oral administration of D-1-^{13}C-glucose 1,000 mg/mouse to C3H mouse. a and b show the stomach only, but c shows the stomach and the liver, and then a signal from liver are only visible in d.

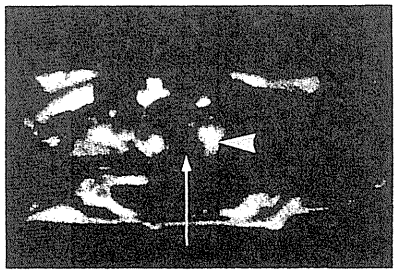

Fig. 3. A proton SE image (TR=500 msec, TE=30 msec) of C3H mouse located at the same position (coronal) and same FOV as that of the ^{13}C experiment for the anatomical reference. The small arrow points to the stomach and the large arrowhead points to the liver.

liver region is observed after 95 min with a gradual decrease of signal intensity derived from the stomach. Finally, the image intensity reduces to background level and the observed spectra returned to those obtained from natural abundance ^{13}C at 24 hours. Figure 3 shows a proton image of the same C3H mouse in the same position and of the same size as used in the ^{13}C study. This image was used for the anatomical reference to the ^{13}C study.

DISCUSSION

It is hoped that NMR spectroscopic analysis in vivo of ^{13}C-labelled compounds will be possible for the clinical study of metabolism via glycolysis and the citric acid cycle to amino acids or triglycerides etc. In particular glucose metabolism originated from glycolysis is essential for the carbohydrate metabolism [8–10]. If we try to trace in vivo whole body metabolism, it is necessary to perform imaging studies in addition to spectroscopy. However, no in vivo ^{13}C NMR imaging study for extra vivo administrated tracer metabolism exists due to its low sensitivity. In this experiment we have confirmed that in vivo metabolism study using high spatial resolution ^{13}C NMR chemical shift selective imaging is feasible. Although ^{13}C MVS (multi-voxel spectroscopy) is worthwhile for limited purpose experiments, high spatial resolution chemical shift selective imaging is preferable for dynamic studies.

There have been many previous studies concerning D-1-^{13}C-glucose metabolism observed in vivo or in vitro. Metabolism in the heart has been observed after intravenous infusion of D-1-^{13}C-glucose [11]. During infusion, myocardial glycogen (at 101 ppm) synthesis was followed and anoxia resulted in degradation of the labelled glycogen and rapid appearance of the ^{13}C label in lactic acid (at 21 ppm). A study using D-6-^{13}C-glucose in rabbit renal papillary tissue indicated the direct conversion into D-sorbitol (at 63–64 ppm) via aldose reductase [12]. Intermediate metabolites other than 3-PG/2,3-DPG can be observed in human RBC. In addition the scrambling of ^{13}C label in glucose shows that the reversal of 3-PG to glucose was in competition with its catabolism to lactate by ^{13}C-labeled C1 or C6 glucose NMR spectroscopy [13].

Our spectroscopic studies show that some peaks (55–70 ppm, 120 ppm, 128 ppm, 156 ppm, and 170 ppm) appeared. They were in proportion to the decrease of D-1-^{13}C-glucose peaks. As compared with some previously reported spectral information [9–16], we assigned these peaks. Five additional peaks at 55–70 ppm were assigned to glycerol and sorbitol. The peak at 120 ppm was assigned to an amino acid the C4 of histidine or C4/C6 of tryptophan. The peak at 128 ppm was assigned to mainly double-bonded carbon as described before but may be contaminated by some glycoprotein signal. The peak at 156 ppm was assigned to UDP-sugar C2 (UDP, uridine diphosphate) and the peak at 170 ppm was assigned to UDP-sugar C4, respectively. These assignments are shown in Figure 1b. UDP-sugar will play an important role as a glycoprotein precursor. We did not assign any glycogen peaks but these may be included with other peaks.

We observed, in ^{13}C NMR images, the transfer of 80–100 ppm signals from the stomach to the liver approximately 1 hour after oral administration of 1 g ^{13}C C1-labelled glucose. This data suggests that a glucose metabolite should be going into the liver via intestinal absorption. However, the time resolution is not high enough to detect the ^{13}C intestinal distribution.

These spectroscopic and imaging studies show that D-1-^{13}C-glucose is metabolised through the transformation to glycerol and glycoproteins during the 5- to 10-hour period after the 1 g/mouse oral administration. This study, however, may not show the natural metabolic pathway because of the high dose of 1 g/mouse, which is not physiological for the glucose metabolism of mouse. Carbon-13 imaging of these metabolites is also important, but these observations require an improvement in sensitivity, which implies the necessity of either Polarization Transfer or decoupling techniques.

ACKNOWLEDGMENTS

This study was partially supported by grants 63-11 of Ministry of Welfare, 01770807 of Ministry of Education, and Special coordination funds promoting for science and technology (Japan).

REFERENCES

1. Cohen SM, Ogawa S, Shulman RG: Proc Natl Acad Sci USA 76:1063, 1979.
2. Cohen SM, Glynn P, Shulman RG: Proc Natl Acad Sci USA 78:60, 1981.
3. Reo NV, Siegfried BA, Ackerman JJH: J Biol Chem 259:13664, 1984.
4. Kormos DW, Yeung HN, Gauss, RC: J Magn Reson 71:159, 1987.
5. Kormos DW, Yeung HN: Magn Reson Med 4:500, 1987.
6. Hall LD, Webb AG, Williams SCR: J Magn Reson 81:565, 1989.
7. Alderman DW, Grant DM: J Magn Reson 36:447, 1979.
8. Bottomley PA: Radiology 170:1, 1989.
9. Alger JR, Sillerud LO, Behar KL, Gillies RJ, Shulman RG, Gordon RE, Shaw D, Hanley PE: Science 21:660, 1981.
10. Sillerud LO, Shulman RG: Biochemistry 22:1087, 1983.
11. Neurohr KJ, Barrett EJ, Shulman RG: Proc Natl Acad Sci USA 80:1603, 1983.
12. Jans AWH, Grunewald RW, Kinne RKH: Magn Reson Med 9:419, 1989.
13. Ghai G, Gonnella, NC: Magn Reson Med 8:340, 1988.
14. Canioni P, Alger JR, Shulman RG: Biochemistry 22:4974, 1983.
15. Moonen CTW, Dimand RJ, Cox KL: Magn Reson Med 6:140, 1988.
16. Halliday KR, Fenglio-Preiser C, Sillerud LO: Magn Reson Med 7:384, 1988.

原著

In vivo ^{19}F MRI による薬物体内動態の評価（第1報）
—特に吸入麻酔剤 enflurane について—

橋本隆裕[1]，池平博夫[1]，福田　寛[1]，上嶋康裕[2]，
安藤興一[1]，舘野之男[1]，

[1] 放射線医学総合研究所臨床研究部
[2] シーメンス旭メディテック開発製造本部

はじめに

従来より薬物の吸収および排泄の過程などの生体内薬物動態を評価するには，放射性同位元素を用いた体外計測や組織を取り出しての破壊的測定を行なう必要があった．これに対しMR (magnetic resonance) 法を用いれば，薬物の生体内での挙動を非破壊的，非侵襲的にしかも経時的に捉えることが可能である．とりわけ，もともと生体内に存在する ^{19}F のほとんどがMRで検出されないため，^{19}F を含む化合物を生体内に投与してMR測定を行なえば生体内動態を捉えることが可能となり大変魅力的である．すでに，一部では臨床応用も試みられている[1]．しかし，一方 *in vivo* ^{19}F MR測定では，薬物の生体内に投与し得る量や生体内での代謝や分解といった低信号雑音比および画像化する場合のアーティファクトなどの問題が常に付きまとう[2]．

今回我々は，吸入麻酔剤として最も広く利用されている enflurane[3] を用い，より生理的状態に近い臨床麻酔で使用する濃度下（1.75-2.0%）で，かつ短時間での *in vivo* ^{19}F MR imaging (MRI) を試みた．本研究の目的は enflurane の生体内分布およびその特徴を実験的に明らかにし，また麻酔の導入ならびに覚醒時での生体組織中での挙動を単一動物にて経時的MRIにて視覚的に捉える事である．なお，F化合物の画像化の応用として，担癌マウスに放射線増感剤である KU 2285 を腹腔内投与して，^{19}F MRIによる体内動態の視覚化も試みたのでこの点についても若干述べる．

方法および対象

1）enflurane の実験では 300 gの雄性 wister ラット 12 匹を，KU-2285 の実験では左大腿皮下に NFS_a (murine fibrosarcoma) 移植後，腫瘍径が 2 cm 以上となった 35 g の C_3H 担癌マウス 4 匹を用いた．

2）使用したMR装置は 2 Tの超伝導水平型マグネットよりなる RS 200 (Siemens-Asahi Medical Systems Ltd., Tokyo, Japan) である．コイルは ^{19}Fに調整した内径 8 cm の Alderman Grant 型コイルを用いた．^{19}F, ^{1}H の共鳴周波数はそれぞれ 80.22 ならびに 85.26

キーワード enflurane, ^{19}F magnetic resonance(MR), inhalation anesthetics, KU 2285

MHzである．中心周波数および90°パルスはenflurane 5cc入りのバイアルにて決定した．enfluraneのMRスペクトルは2本の共鳴線として捉えられ，画像化にあたってはピーク高の高い低磁場側のピークに中心周波数を合わせた．サンプリングレートは8 KHzとし，2 KHzのButterworth filterによりオフセンターエリアを除いた．^{19}F MRIのパルス系列はfield echo法で，繰り返し時間は300 ms，エコー時間は10 msとした．スライス選択は行なわず，いわゆるprojection画像を撮影した．投影方向は腹臥位のラットの上下（腹側→背側）および左右方向（側方）とした．視野径は140 mm，磁場勾配は1．1 Gauss/cm，マトリックスサイズは128×128である．積算回数は5～10回，すなわち撮影時間は3.2～6.4分である．一部のラット（n＝6）ではenfluraneの解剖学的分布を明らかにするために^{19}F MRIの撮影終了後，^{19}Fのコイルの中の動物はそのままに，周波数を^{1}Hに合わせて，^{1}H MRIの撮影を行ない^{19}F MRIと比較した．^{1}H MRIの条件は，スライス幅2 mmのfield echo法（繰り返し時間/エコー時間＝300/10 ms）で，視野径は140 mm，マトリックサイズは256×256である．積算回数は2ないし4回，撮影時間は2.6～5.1分である．

3）実験のプロトコール

enfluraneの実験

他の麻酔剤の影響を避けるために，ラットを無麻酔のままゲージごと5％enflurane濃度の100％酸素を満たした袋の中にいれた．数分後ラットが不動化したところでマグネツト内に腹臥位として固定し，自発呼吸下にマスク麻酔にて維持を行なった．この間，ガス流量は1 1/minとし，酸素30％，笑気70％およびenfluraneは専用の気化器を用いて1.75～2.0％に維持した．動物をマグネツト内に固定した直後より^{19}F MRI測定を開始し，以後60分間にわたり上記の条件にて測定を続けた．その後，酸素，笑気はそのままでenfluraneの吸入を中止して動物が覚醒し自発運動を始めるまでひき続いて^{19}F MRI測定を行なった（n＝6）．enfluraneの解剖学的分布を明らかにするために半数の動物．（n＝6）ではenflurane吸入中止後20分までで^{19}F MRIの撮影を打ち切り，enflurane濃度1.75％の吸入を再開して麻酔を得て，^{19}F MRIのprojection方向に一致した^{1}H MRIを前記の条件で撮影し，^{19}F MR信号の解剖学的位置を比較検討した．

KU-2285の実験

マウスに抱水クロラール10 mgを腹腔内投与して麻酔を得た後，^{19}F用のコイルの中に腹臥位で固定した．次いで，生理食塩水で溶解したKU 2285（50 mg，1 ml）をNFSa担癌C3Hマウスに腹腔内投与して，直後より経時的に^{19}F MRIを撮影した．撮影条件は前述のenfluraneの実験と同一であり，projection方向はマウスの上下方向（腹側→背側）のみとした．

結　　果

ラットは麻酔導入後1.75～2.0％ enfluraneの一定濃度で自発呼吸下にて維持したが，導入開始後15～20分ほどで，生体より^{19}F MRの信号が見られ始めた．麻酔開始後60分を経過した時点の*in vivo* ^{19}F MRIを図1，2，3に示す．enfluraneの血中濃度はこの時点では平衡状態になっていると考えられる．

頭部の画像を図1に示す．上段は矢状方向の画像で，下段は冠状方向の画像である．図1-B，Dはenfluraneの^{19}F MRIであり，図1-A，Cは図1-B，Dに対応した^{1}H MRIである．^{19}Fの著明な信号は頸部から背部にかけて頭部側方に見られた．^{1}H MRIとの対応により，これらの高信号域はそれぞれ頸部の皮下脂肪組織ならびに唾液腺などの脂肪組織（矢印）と考えた．図1-Dの前方に見られる小さな2ヶ所の

1990年8月14日受付　1990年11月26日改訂
別刷請求先　〒260 千葉市穴川4-9-1　放射線医学総合研究所臨床研究部　橋本隆裕

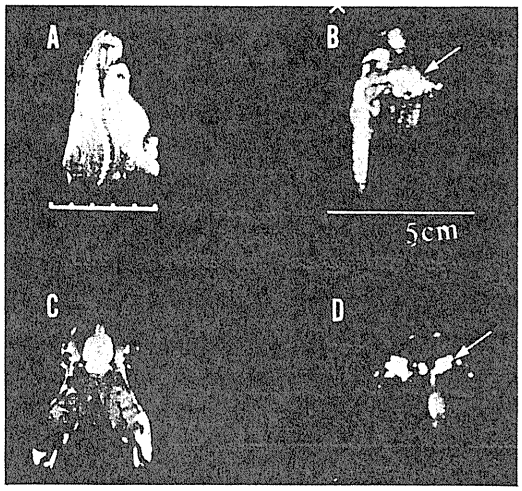

図1． 麻酔導入後，1.75%のenflurane麻酔60分経過時のラット頭部の^{1}H（図1-A,C）および^{19}F MRI（図1-B,D）示す，いずれもfield echo法で，繰り返し時間300 ms，エコー時間10 msである．前者および後者のマトリックスサイズはそれぞれ256×256，128×128である．図1-A,Bは側方から見，図1-C,Dは腹側から背側を見た像である．いずれも図の上方がrostralとなる．^{19}F MR信号は頸部背側および頭部側方に著明で，^{1}H MRIとの対比より前者は脂肪組織で，後者は唾液線の脂肪組織が主体（矢印）と考えた．図中の横線はおのおの5 cmに対応している．

図2． 1.75%のenflurane吸入麻酔60分経過時の腹部^{19}F MRI（冠状方向の像，図2-B）およびそれに対応する腹部中央での^{1}H MRI（field echo法で，繰り返し時間300 msエコー時間10 ms，スライス幅2 mm，図2-A）．図2-Aの^{1}H MRIにて胸部（肺）および腹部の領域が捉えられていることが分かる．脂肪のT_1値は短いために，高信号として捉えられる．この画像との対比で，図2-Bでの^{19}F MR信号は肝臓（小矢頭）および腹腔内脂肪組織（大矢頭）より得られていると同定できる．図中の横線はおのおの5 cmに対応している．

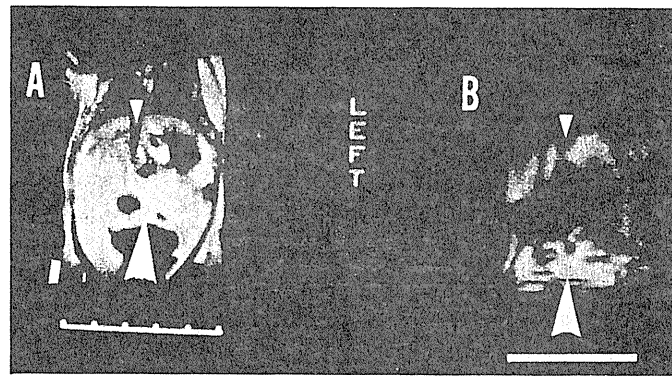

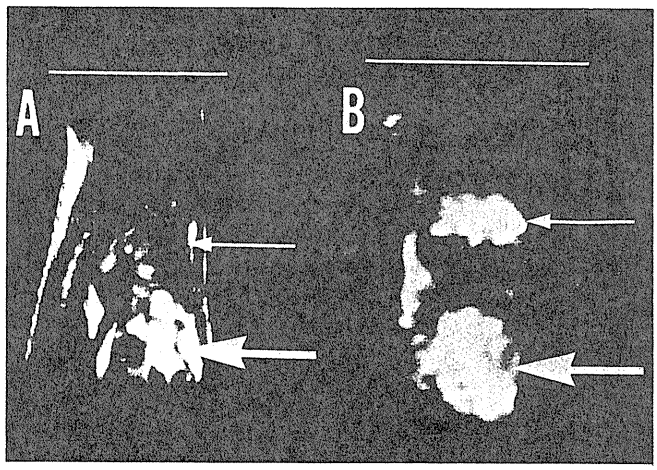

図3． 1.75% enflurane吸入麻酔60分経過時の^{19}F MRI（腹部矢状方向すなわち側方から見た像，図3-B）およびこれに対応する腹部中央での^{1}H MRI（図3-A）．図3-Bでは肝臓（小矢印）および腹腔内脂肪組織（大矢印）より^{19}F MRの高信号が得られている．肝臓の形態はこの撮影方向にて明瞭に描出されている．図中の横線はおのおの5 cmに対応している．

信号は眼窩脂肪組織と考えた．脳実質よりの ^{19}F の MR 信号は左右方向の像では重なりのために同定困難で（図1-B），上下方向の像（図1-D）では明らかでなかった．

腹部より得られた画像を図2，3に示す．腹部を下から見た画像（冠状方向）が図2であり，矢状方向から見たものが図3である．^{19}F MRI での高信号域（図2-B，3-B）は，対応する ^{1}H MRI にて肝臓ならびに腹腔内脂肪組織であると同定できる．とりわけ，脂肪は T_1 値が短く ^{1}H MRI では高信号として描出されている（図2-A，3-A）．図2の小矢頭で示したものは肝臓で，大矢頭で示したのは大網などの腹腔内の脂肪組織であり，^{19}F MR 信号強度は明らかに脂肪組織の方が肝臓よりも強かった．肝臓の形態の描出は矢状方向の像（図3小矢印）でより明らかであった．また麻酔導入後60分までの肝臓および脂肪組織よりの ^{19}F MR 信号は脂肪組織では経時的に増大したのに対して，肝臓では約30分でプラトーに達した．

1.75% enflurane による吸入麻酔を60分間維持し，その後吸入を中止して覚醒するまでの経時的な腹部の ^{19}F MRI（冠状方向）を図4に示す．左上が吸入中止直前の像で，腹腔脂肪組織（矢印）および肝臓（矢頭）より強い信号が得られている．右上の像が吸入中止後20分の像で，左下が40分後，右下図70分後の像である．40分経過すると全体の信号が低下しているが，依然肝臓からの信号も認められる．しかし，70分経過すると肝臓からの信号はほとんど認められなくなった．一方，この時点で脂肪組織からの信号は低下してはいるものの依然強く認められた．この後，ラットは麻酔より覚醒し自発運動を始めたため，^{19}F MRI 撮影を中止した．

マウスの腹腔内に投与した KU 2285 は図5に示すように捉えられた．図5-A が投与直後のもので，図5-Bが12分後，図5-Cが32分後で，図5-Dが52分後の像である．時間経過とともに腹腔内からの信号は次第に弱くなり，一方で図中の矢印に示した膀胱内に集積した KU-2285 より強い信号が捉えられた．麻酔により腸蠕動が抑制させているためか，投与後の腹腔での薬剤の移動は著明ではなかった．また，左大腿部腫瘍（図5-A，tm）からの信号は確認できなかった．

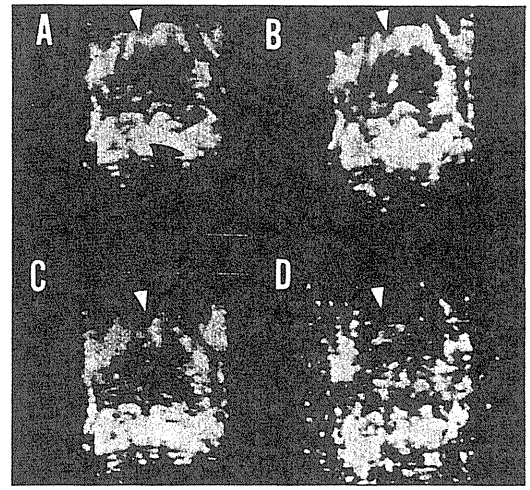

図4． 1.75% の enflurane にて60分間麻酔後，enflurane 投与を中止し，覚醒するまでの ^{19}F MRI 腹部冠状方向すなわち腹側から背側をみた像の経時的変化（投影方向は図2と同様である）．それぞれ，吸入中止直前（図4-A），中止後20分後（図4-B），40分後（図4-C），70分後（図4-D）の像である．吸入中止後 ^{19}F MR の信号は次第に弱くなり，70分後（図4-D）には肝臓（小矢頭）より信号はほとんど消失しているが，脂肪組織（矢印）からは依然信号が認められる．肝臓からの信号の低下は吸入中止後の enflurane 血中濃度の低下に対応していると考えられる．また脂肪組織は血流が少なく，かつ大量の enflurane が蓄積しているために，血中への移行が不良で信号が持続すると思われる．

考　　察

生体中に存在する F-19 は主に骨組織に組み込まれており，そのほとんどが MR にて捉えられない．一方，^{19}F の MR 感度は ^{1}H に次いで高い．そのため ^{19}F 含む物質を生体に投与して MRI 測定が可能となれば，その局在および濃度分布といった体内動態が比較的容易に画像とし

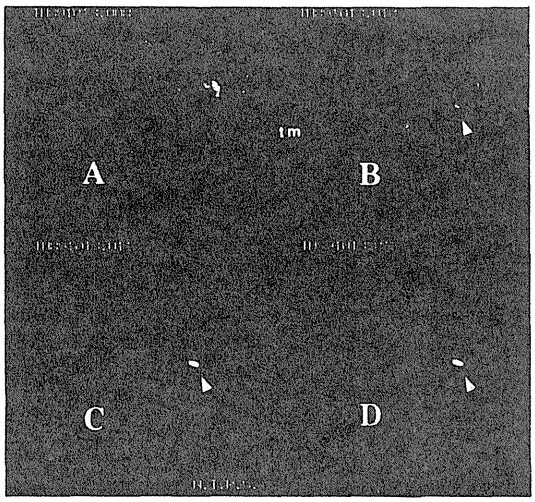

図5．放射線増感剤KU 2285（50 mg,1 ml）を左大腿に径2 cmのNFSa腫瘍を有するC3Hマウスに腹腔内投与後，経時的に^{19}F MRIを撮影した．投影方向は腹側→背側方向である．パルス系列はfield echo法（繰り返し時間/エコー時間＝300/10 ms）．それぞれ，投与2分後（図5-A），12分後（図5-B），32分後（図5-C），52分後（図5-D）の像である，12分後にすでに吸収排泄されたKU 2285の膀胱よりの^{19}F MR信号（矢頭）明らかである．しかし，腫瘍（tm）からの信号は認めない．図5-Aはマウスの腹部，下肢の輪郭を描いている．

て捉えられると考えられる．ただし実際のMRI測定に当たっては薬剤の生体組織中の濃度，分解，代謝および緩和時間が重要な因子となる．とりわけ生体投与したF化合物では組織内濃度が大きな要素となり，現実には^{1}H MRIに比べ*in vivo* ^{19}F MRIは信号雑音比が低く，空間分解能も劣る．

また，生体内での薬物の体内動態を測定するにはこれらの問題に加えて時間分解能の問題が生じる．従来報告されている*in vivo* ^{19}F MRIの撮像時間は数時間を要する例もあり[2]，分単位の経時変化を検討するには不都合である．今回の実験ではprojection画像のため，時間分解能3～6分で，薬物の生体内挙動を捉えるには満足できるものと考える．

現在まで画像化されたF化合物は血液代用剤

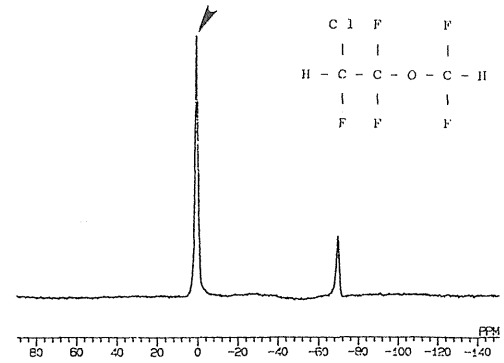

図6．Enflurane の構造式および1.75%の enflurane吸入麻酔下のラット腹部より得られた*in vivo* ^{19}F MR スペクトルを示す．今回のMRI測定にはピーク高の高い低磁場側の共鳴線（矢印）に中心周波数を合わせた．

として知られるperfluorocarbonを用いたものがほとんどである[4),5)]．しかし，実際に画像化するには極めて多量の投与が必要となり非生理的で，またこの物質は肝臓および脾臓などの網内系に蓄積し体内に長く留まるという不都合もある．そこで我々は生体内でほとんど不活性でかつ吸収および排泄が早い吸入麻酔剤を用い，その生体内での分布およびその経時的変化を画像として捉え，特徴づけることを試みた．

吸入麻酔剤のほとんどはFを含み^{19}F MRの良い対象となる[6),7)]．現在まで*in vivo* MRで検討されている麻酔剤は主としてhalothaneである[6),8)]．その理由は共鳴線が単一であるためだが，高濃度で使用する必要がある，撮像までに長時間の麻酔の維持が必要で，撮像自体にも長時間を要し，実際には生体内でかなり代謝されるなどの欠点がある[9)]．一方，enflurane（図6）は5原子のFを含み，本邦では臨床麻酔において最も使用されている吸入麻酔剤である．しかも，この薬剤は生体中ではほとんど代謝を受けず不活性であるとされている[3)]．またenflurane の*in vivo* での画像化は報告されておらずその生体内分布を捉えることは価値があると思う．図6に示すようにラット麻酔中に得たenflurane の*in*

vivo MR スペクトルは2本の共鳴線が得られ，今回の画像化にはピーク高の高い低磁場側のピーク（図6矢印）を中心周波数に合わせた．

吸入麻酔剤の組織内濃度は数 mM 以下と低いが，脂溶性が高い事はよく知られている．今回の実験でも頭頸部および腹部の脂肪組織から高信号が得られた．ただ，腹部での吸入麻酔剤の分布の画像化の報告は未だ見られない．

今回の検討で肝臓からの MR 信号について図2，3，4，に示したように興味ある知見が得られた．麻酔導入時より肝臓の信号強度は脂肪組織のそれに比べ低く，かつ早期に平衡に達した．また覚醒時には肝臓の信号は脂肪組織のそれに比べより早期に消失した（図4）．enflurane の血中濃度は開始後15分まで速やかに上昇し，60分以降平衡となる[9]．肝臓よりの信号が脂肪組織と同様に組織内蓄積に由来すると考えれば，肝臓よりの信号強度が早期に平衡に達した理由の説明が困難である．この事実は enflurane が脂肪組織のように肝臓組織中に溶解，蓄積して存在するのが主体というよりも，肝臓が豊富な血液を擁するため enfulurane の血中濃度に応じた信号を反映し，そのため enflurane 血中濃度の飽和に伴い，早期に信号強度が平衡に達したと考えたい．実際 enflurane の吸入濃度を一定にしておいてラット腹部の ^{19}F MRI 撮影中に門脈血流を急激に低下させると高信号を呈していた肝臓からの enflurane の ^{19}F MRI 信号は速やかに低下してしまうことも肝臓からの信号が主に肝臓組織中に溶解した enflurane よりも血中の enflurane に由来しているという考えを支持している（T. Hashimoto, unpublished data）．このように肝臓よりの信号が血流量を反映すると考えれば，enflurane が生体で極めて不活性であることと相まって，一定の吸入濃度の下で平衡状態に達した後に wash out時の経時的 ^{19}F MRI により，血流情報を得ることが可能となると推察される．しかし，今回の実験では臓器からの信号強度の変化のみからの考察ではあり，組織での存在状態の変化，緩和機構の変化については不明であり，今後の検討を要する．

麻酔剤を用いた ^{19}F MRで興味が持たれるのは，その脳内での分布である．A. M. Wyrwics, et al.[6] は ^{19}F MR スペクトロスコピーを用い麻酔剤が吸入中止後も脳内に長く留まることを報告している．今回の実験では画像上脳内から明らかな ^{19}F MR 信号を認めなかった．W. Chew et al.[10] も halothane を用いて兎の脳の ^{19}F MRI を試みたが，脳由来の明らかな信号は検出できなかったと報告している．この理由は，①脳組織中の濃度が周囲組織のそれに比べはるかに少ない．②T_2 緩和時間が非常に短縮している．③今回は機械の制約のためにエコー時間を 10 msとしたが，より短い設定が必要である．④より高濃度で長時間の麻酔に加え，より長い撮影を行なう必要があるなどが考えられる．

臨床的に吸入麻酔剤の体内動態を知るには血中，尿中の代謝産物の定量や呼気ガス中の定量により間接的に捉えるしかない．ましてや *in vivo* でその生体内分布を知る手段は無い．今回示したように，臨床で使用する濃度での *in vivo* ^{19}F MRI が可能であることより人体で直接 enflurane の分布を画像化できる可能性も極めて高い．

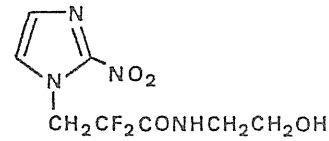

図7．KU-2285 の構造式

今回はこれまで述べてきた吸入麻酔剤に加え，^{19}F MRI を用いて放射線増感剤の KU-2285（図7）の体内動態の評価を試みた．この化合物の ^{19}F MRI 測定は現在まで報告は見られないが，図5のように担癌マウスの腹腔内投与後の拡散，吸収及び膀胱内排泄の過程を経時的に捉えることができた．R. J. Maxwell, et

al.[11]はF化されたmisonidazole類似化合物を静注投与してスペクトル測定を行ない，投与後24時間でも腫瘍では投与直後の約20%の信号が得られたの対し，他の組織でのそれは0.1%と極めて低いことより，F化放射線増感剤を用いた*in vivo* ^{19}F MR法が低酸素細胞の非侵襲的な検出手段となり得る可能性を示した．我々の実験では，腹腔，膀胱から放射線増感剤の信号は捉えられたが，腫瘍から信号の検出は出来なかった．測定条件設定の最適化の検討も今後必要であるが，薬物の体内動態に関して腫瘍内濃度が特異的に上昇していない，時間分解能より投与後早期に腫瘍組織内濃度が低下する，また腫瘍側の因子として腫瘍径の増大に伴い壊死部分が増え低酸素細胞を多く含む腫瘍実質容積が十分でなかったなどの可能性も考えられる．ただ，生体に投与した薬物を*in vivo*スペクトロスコピーで検討する際にはその信号の位置情報が得られない場合が多く，この点からも画像化を試みる意義は極めて大きいと考える．

ま と め

In vivo ^{19}F MRIを用いてF化合物である吸入麻酔剤のenfluraneおよび放射線増感剤のKU 2285 Fの画像化による体内動態の評価を試みた．臨床で使用される吸入濃度の下でenfluraneの体内分布ならびにその経時的変化をラットにおいて明瞭に描出できた．また腹腔内蔵器とりわけ肝臓の^{19}F MRIでは興味ある所見が得られた．特に肝血流とMR信号の関係については今後の検討を要する．

謝　辞

本研究の一部は科学技術振興調整費の助成を受けた．KU 2285の供与を受けたダイキン工業㈱に感謝致します．共同研究にあたり多大な御尽力を賜りましたシーメンス旭㈱開発製造本部の各位に感謝致します．

本論文の要旨は第15回日本磁気共鳴医学会大会（岐阜市，平成2年2月16日）において発表した．

文　献

1) M. C. Malet-Martino, J. P. Armand, A. Lopez. et al. : Evidence for the importance of 5'-Deoxy-5-fluorouridine catabolism in humans from ^{19}F nuclear magnetic resonance spectroscopy. Cancer Res, 46 : 2105-2112, 1986
2) E. McFarland, J. A. Koucheer, B. R. Rosen, et al.: *In vivo* ^{19}F NMR imaging. J Comput Assist Tomogr, 9 : 8-15, 1985
3) G. W. Black : Enflurane. Br J Anesth, 51 : 627-640, 1979
4) P. M. Joseph, J. E. Fishman, B. Mukher-ji, et al.: *In vivo* ^{19}F NMR imaging of the cardiovascular system. J Comput Assist Tomogr, 9 : 1012-1019, 1985
5) R. P. Mason, P. A. Antich, E. E. Babcock, et al; Perfluorocarbon imaging *in vivo* : A ^{19}F MRI study in tumorbearing mice. Magn Reson Imag, 7 : 475-485, 1988
6) A. M. Wyrwecz, C. B. Conboy, B. G. Nichols, et al. : *In vivo* ^{19}F NMR study of halothane distribution in brain. Bioch Biophy Acta, 929, 271-277, 1987
7) A. M. Wyriwicz, C. B. Conboy, K. R. Ryback, et al : *In vivo* ^{19}F-NMR study of isoflurane elimination from brain. Bioch Biophy Acta, 927 : 86-91, 1987
8) L. Litt, R. Gonzalez-Mendez, T. L. James, et al : An *in vivo* study of halothane uptake and elimination in the rat brain with fluorine nuclear magnetic resonance spectroscopy. Anesthesiology, 67 : 161-168, 1987
9) 木村邦之，神敏郎，佐藤根俊彦，他：Ethrane麻酔とその動脈血中濃度．麻酔，22：344-347, 1973
10) W. M. Chew, M. E. Moseley, P. A. Mills, et al. : Spin-echo fluorine magnetic resonance imaging at 2T : *In vivo* spatial distribution of halothane in the rabbit head. Magn Reson Imag, 5 : 51-56, 1987
11) R. J. Maxwell, P. Workman, J. R. Griffiths : Demonstration of tumor-selective retention of fluorinated nitroimidazole probes by ^{19}F magnetic resonance spectroscopy *in vivo*. Int J Radiat Oncol Biol Phys, 16 : 925-929, 1989

Evaluation of Drug Dynamics with *in Vivo* ^{19}F MRI with Special Reference to Enflurane (1st Report)

Takahiro HASHIMOTO[1], Hiroo IKEHIRA[1], Hiroshi FUKUDA[1], Yasuhiro UESHIMA[2], Koichi ANDO[1], Yukio TATENO[1]

[1]*Division of Clinical Research, National Institute of Radiological Sciences 9-1, Anagawa-4-chome, Chiba-shi 260*
[2]*Siemens-Asahi Medical Systems Ltd.*

In vivo ^{19}F magnetic resonance imaging (MRI) was examined to reveal the distribution and the dynamics of drugs containing ^{19}F. Enflurane, most commonly available inhalation anesthetics in Japan, distributed predominantly in the adipose tissue and the liver of the rats and was successfully imaged in less than seven minutes *in vivo* under the clinical concentration of 1.75-2.0%. The ^{19}F MR signal reached the plateau within 30 minutes in the liver and disappeared faster in the liver than in the adipose tissue. The MR signal from the liver was supposed to originate mainly from the enflurane in the blood. Because of low blood flow and increasing accumulation of enflurane in the adipose tissue, MR signal in the adipose tissue remained longer. *In vivo* consecutive ^{19}F MRI in the liver using enflurane might offer information of blood flow in the phase of washing out.

Radiosensitizer KU 2285 containing ^{19}F was also imaged in the C3H mouse after intraperitoneal injection. This drug was rapidly excreted in the bladder. Any MR signal was not recognized in the tumor probably due to lower concentration compared to that in the abdomen and the bladder.

The authors demonstrated and characterized *in vivo* distribution of enflurane in the rats using ^{19}F MRI. Additionally, we postulated the possibility for blood flow measurement of the liver in the washing out phase after constant inhalation of enflurane.

DEVELOPMENT OF A HIGH RESOLUTION PET

T. Yamashita, H. Uchida, H. Okada, T. Kurono, T. Takemori, M. Watanabe,
K. Shimizu, E. Yoshikawa, T. Ohmura, N. Satoh, E. Tanaka
Hamamatsu Photonics K.K.,1126-1, Ichino-cho, Hamamatsu 435, Japan
and
N. Nohara, T. Tomitani, M. Yamamoto, H. Murayama, M. Endo
National Institute of Radiological Sciences, Chiba 260, Japan

ABSTRACT

A high resolution positron emission tomograph (PET) for brain studies has been developed, which consists of 5 detector rings (240 BGO's/ring). New multi-segment photomultiplier tubes (PMT) were adopted to the system with 5mm wide BGO's. The system is designed to examine a patient sitting or lying down on a chair/bed couch. The functions of PMT auto gain control and real time image display are implemented in the system. The physical performance of the system was evaluated: the spatial resolution is 3.5mm in the transaxial plane and 5.7mm in the axial direction, and the total system sensitivity is 109kcps/μCi/ml for a 20 cm dia. uniform phantom with a pulse height threshold of 350keV.

1. INTRODUCTION

The current trends in PET systems require the improvement of spatial resolution. In order to achieve higher resolution, various ideas for detector construction have been proposed [1]-[10], which are categorized into two scintillator-PMT coupling schemes, individual coupling and group coupling. Most PET systems use group coupling detectors which are designed to make a large number of crystals coupled to a small number of PMT's [12]-[14]. In this method, however, it is often difficult to attain the spatial resolution expected from the crystal size due to the poor statistics with a limited number of scintillation photons. On the other hand, the system consisting of individual coupling detectors can accomplish high resolution performance [15]. To overcome the limitation in the size of PMT's and their arrangement for multi-ring construction, a new multi-segment PMT was developed for the application to this PET system. Several new functions are implemented in the system to attain better environment in brain studies. This paper presents the features and performance of the PET system.

2. DESIGN FEATURES

The system is specially designed for brain studies. Its features are as follows:

(1) High resolution : The resolution at the center of the field of view (FOV) is less than 4mm in the transaxial plane and less than 6mm in the axial direction.
(2) Special arrangement of detectors : High resolution is attained even in stationary mode.
(3) Axial-scan : 5 detector rings with axial-scan can provide 9 simultaneous slice images or more quasi-simultaneous slice images.
(4) Real time imaging : Real time images are displayed on a CRT monitor (40x40 pixel images) during the data acquisition.
(5) Flexible couch : The gantry has a 30cm dia. hole and tilts up to 90°. Patients can be measured sitting or lying down on the chair/bed couch.
(6) Quietness : Auditory noise is approximately 50 dB in the gantry hole during wobble mode.
(7) Auto gain tuning : PMT auto gain controller provides the system with reproducibility and reliability.

3. SYSTEM DESCRIPTION

The specifications of the system are summarized in Table 1.

Table 1. Specifications of the system

Detector	
Crystal size	5mm(w)x12mm(h)x30mm(l)
PMT size	23mm(w)x11mm(h)x68mm(l)
Number of crystals	240 / ring
Number of PMT's	60 / ring
Crystal material	BGO
PMT	Quad-PMT (R3309)
Crystal pitch	6mm
Bank spacing	3mm
Gantry	
Number of rings	5 rings
Ring diameter	473mm
Patient hole diameter	300mm
Tilt angle	-20° to 90°
Lift stroke	50cm
Scanning motion	Wobble motion Axial-scan (max 14mm)
Slice collimator	60mm(l)x5-6mm(w)
Ring pitch	16mm
Source	Orbiting ^{68}Ge rod
Couch	
Horizontal stroke	2000mm
Elevator stroke	400mm
Reclining angle	0° to 90°

Development of the PET system has been performed under contract with Research Development Corporation of Japan.

0018-9499/90/0400-0594$01.00 © 1990 IEEE

3.1 Detectors

A new multi-segment PMT (R3309) was developed for the application to this PET system, which has 4 segments in one glass envelope. The anode is common with those 4 segments in the PMT, while the last dynode is separated into 4 independent segments. The anode output is used for energy discrimination and timing pick-off. The dynode output is used for crystal identification [16]. Four BGO scintillators (5mm wide x 12mm high x 30mm deep in size) are coupled to the PMT with an individual coupling scheme. The energy resolution of this detector is 22.5% and the coincidence time resolution is 3.7ns fwhm and 7.4ns fwtm for 511keV γ-rays.

Sixteen BGO's and 4 PMT's are assembled in a detector cassette with high voltage dividers and preamplifiers. Figure 1 shows the detector structure and the cassette construction. 15 cassettes are arranged on a circular ring with a gap equal to one half the detector pitch by "a bank array concept" to obtain high resolution capability in the stationary mode [17]. The system consists of 5 detector rings (300 PMT's and 1200 BGO's). The whole PMT's are automatically tuned by an auto gain controller (AGC) in the gantry. The PMT gain tuning is executed with ^{137}Cs calibration sources set in the center of the patient hole. All PMT gain can be tuned within 3 min. AGC function provides the system with reproducibility and reliability.

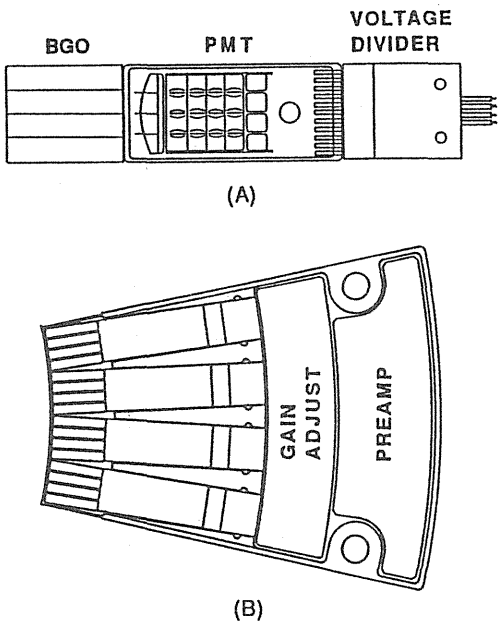

Fig.1 Detector structure (A) and detector cassette construction (B).

3.2 Electronics and Data Acquisition

Output signals from the detectors are sent to the front-end circuits which have one-to-one correspondence with each detector cassette. Anode signals are led into timing/energy discriminators which produce the timing signals. The energy threshold level can be changed by the software and is normally set to 350 keV. Dynode signals are led into comparators and coded into crystal address signals, where multi events in one cassette are rejected.

The detectors in each bank (detector cassette) are in possible coincidence with those in the opposite 6 banks both in the same ring and in the adjacent rings. In this system, 5 coincidence circuit units are installed. The width of the coincidence time window can be changed from one value to another by turning switches on the coincidence boards and is normally set to 20ns.

Coincidence detector pair signals are encoded and stored in histogram memories as a sinogram. The histogram memories consist of a pair of memory bank sets, each of which has a memory for data acquisition (2MB) and that for the real time image monitor (256kB). The data acquired on the 256kB memory are transferred onto an array processor every certain period for image reconstruction, and the real time images (40x40 pixel images) are displayed on a CRT during the data acquisition. This function reduces operation faults and consequently enhances the system reliability.

3.3 Gantry and Couch

The wobble motion and the axial scan are introduced in this system. We put emphasis on quietness in the design of those mechanical motions to reduce auditory noise during brain studies. The wobble speed is programmable and its maximum speed is 1 rotation/sec. In the axial-scan, a scan pitch and positions are selectable from 8 pre-programmed modes.

The couch can be used as a chair or a bed and the gantry tilts from -20° to 90°. A patient can be examined either in sitting or lying down on the couch. The couch can be moved perpendicularly to the gantry front face at any gantry tilt angles by computer control (axial traveling mode). According to this function, a patient can stay in a comfortable position during a long measurement and visual or auditory stimulus in physiological studies can be applied easily.

3.4 Data Processing

An array processor (HAMAMATSU M2941) was installed in the image processing unit for the image reconstruction, which is a random access type and offers easiness in the implementation of new reconstruction programs. We implemented Filtered Back Projection (FBP), Filtered Iterative Reconstruction (FIR) [18][19], EM algorithm, etc. in the array

processor. FBP requires 15sec and FIR (3 iterations) requires 2min to reconstruct an image from 160(T)x240(θ) projection data.

As a main computer for the system operation and image /data processing, we adopted an engineering work station (SUN3 260C) to the PET system and developed the software in the bases of an object oriented language: smalltalk-80.

4. PERFORMANCE

4.1 Spatial Resolution

Transaxial resolution was measured by scanning a ^{68}Ge line source, which is filled in a glass tube (internal dia. 0.55mm, external dia. 2.2mm), placed in parallel with the axis of the patient hole along the radial direction at 0, 2, 4, 6, 8, and 10cm from the center of the FOV in air. The data were acquired in both the stationary and wobble mode. The transaxial resolution, fwhm and fwtm values of a reconstructed image, was determined by taking a profile through the center of the image and making a linear interpolation. The results in both the radial and tangential direction with the wobble motion were shown in Fig. 2. Resolution in the center of the FOV is 3.5mm fwhm and 7.1mm fwtm in the wobble mode.

In the stationary mode, the resolution of 3.8mm fwhm and 8.1mm fwtm is obtained using FBP algorithm with the Shepp-Logan filter. A better resolution can generally be obtained by applying FIR algorithm with the same statistical noise. Typically, three iterations yield almost the same resolution as FBP, and further iterations yield better resolution at the cost of S/N ratio. Although the FIR method requires a longer computation time, it provides better image quality by virtue of the non-negativity.

Axial resolution (slice thickness) was measured by scanning a ^{22}Na point source parallel to the axis of the patient hole in steps of 1mm at 0, 5, 7.5, and 10cm from the center of the transaxial FOV. The count rate in each slice was recorded at each scanning point. The results were shown in Fig. 3. The axial resolution in the center of the FOV is 5.7mm fwhm, 10.4mm fwtm in the direct-plane and 5.3mm fwhm, 9.0mm fwtm in the cross-plane.

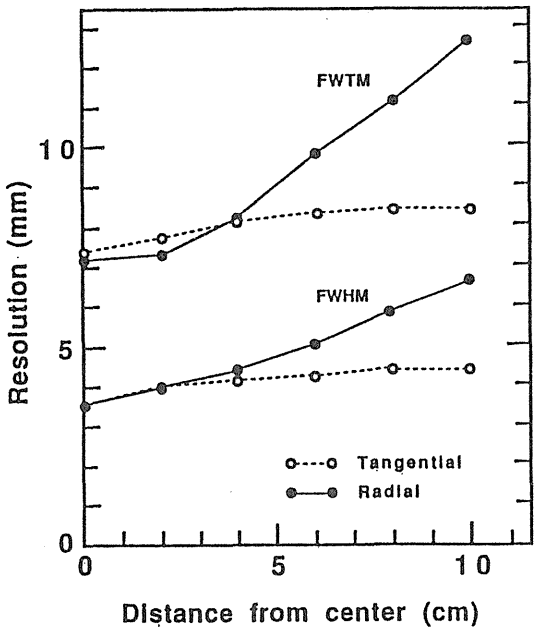

Fig.2 Radial (solid line) and tangential (dashed line) resolution with the wobble motion as a function of the distance from the center.

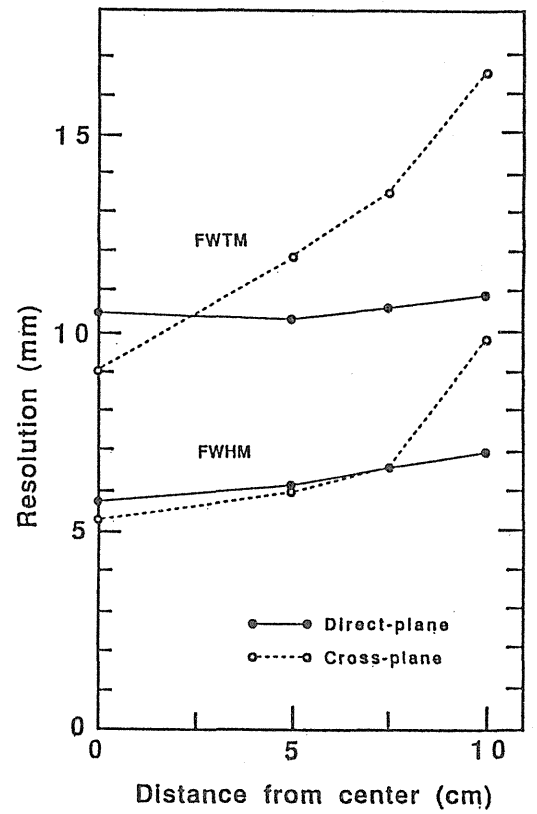

Fig.3 Axial resolution in both direct- (solid line) and cross-planes (dashed line) as a function of the distance from the center.

4.2 Axial Scan

The sampling uniformity in axial scans was tested by measuring a ^{68}Ge source in a flexible Teflon tube (2.8mm dia.) wound around the cylindrical phantom (10cm dia. x 20cm high) in spiral with 9cm pitch. The sampling uniformity was evaluated from the continuity of the circular pattern in sum of all slices. The results are shown in Fig. 4. The axial scan with 4mm pitch provides good continuous images without dead space.

4.3 Count Rate Performance

Count rate performance was measured with a cylindrical phantom (20cm dia. x 10cm high) uniformly filled with $^{13}NH_3$ solution. The initial activity was 15.9 μCi/ml and the measurements were continued for 90 minutes. The results are shown in Fig.5. The count rate loss is approximately 50% at 3μCi/ml, which is mostly caused by the dead time in the coincidence circuit. The count rate loss is corrected by using the single event rate in each ring.

4.4 Sensitivity

System sensitivity was calculated from the measurement data acquired in the above count rate performance test. The average sensitivity is 9.5kcps/μCi/ml in the direct-plane and 15.3kcps/μCi/ml in the cross-plane, and the total system sensitivity is 109kcps/μCi/ml including scatter component.

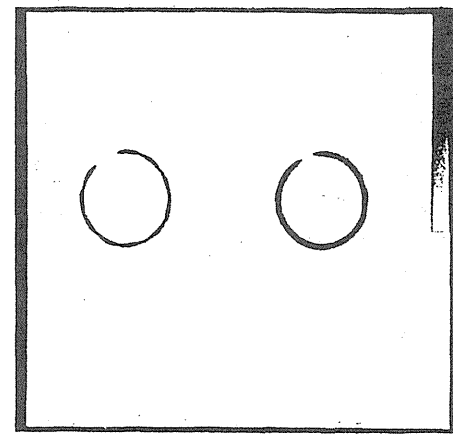

Fig.4 The circular pattern in sum of all slices with a spiral phantom. The left and right images were obtained without and with the axial-scan,respectively.

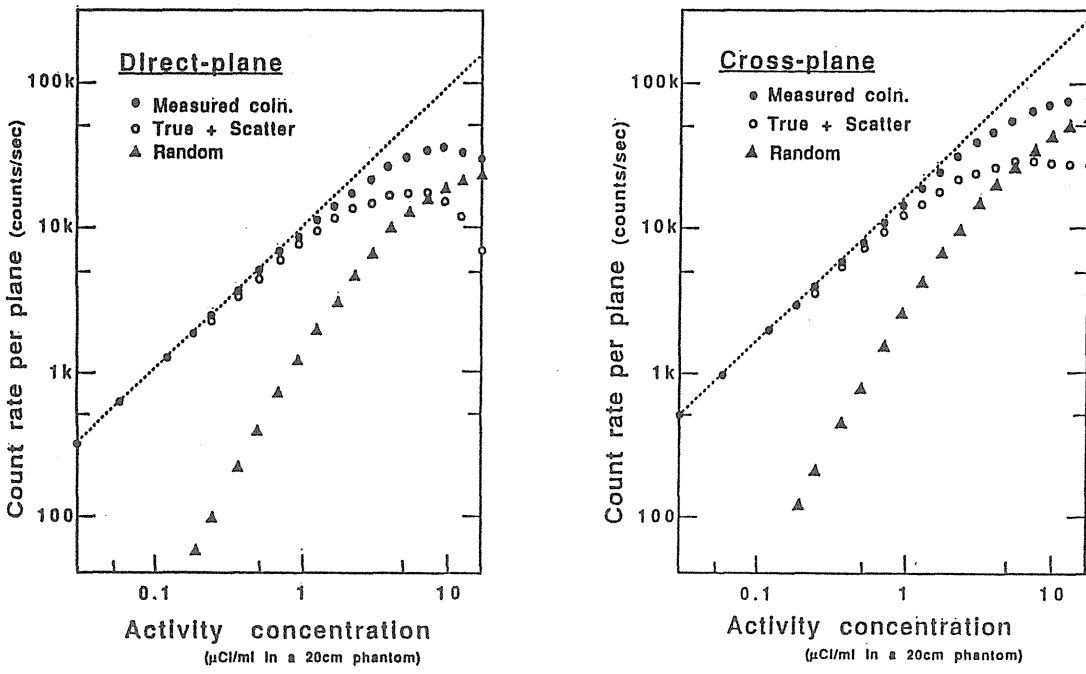

Fig.5 Count rate as a function of activity concentration in a 20 cm cylindrical phantom.

4.5 Scatter Fraction

The fraction of scattered coincidence was determined with the use of the ^{68}Ge line source, which is covered by the stainless steel tube (4mm dia.), inserted into the center of a water-filled cylindrical phantom (18cm dia. x 10cm high). The phantom was placed at the center of the FOV. In the summed projection for all angles, a central peak arising from true/scattered events and 'wing' distribution arising from scattered events were seen. The scatter component was evaluated by integrating the counts in the 'wing' distribution and in a part of the peak which was estimated by extrapolation the 'wing' distribution to the peak region, and the scatter fraction is defined by the ratio of the scatter component to the total counts in the projection. The fraction was approximately 20% in both the direct- and cross- planes.

4.6 Clinical Study

Figure 6 shows brain images of a normal volunteer measured with ^{18}F-fluoro-deoxyglucose (FDG) under an axial-scan (4mm pitch mode). Each image contains 5 to 9 million counts.

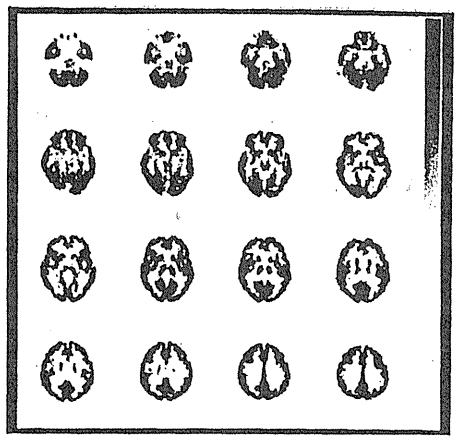

Fig.6 Brain images of a normal volunteer measured with ^{18}FDG.

5. DISCUSSION

The detector unit used in this PET system has a simple structure which is a scintillator/PMT individual coupling scheme. It offers good reliability, stability and high spatial resolution. Individual coupling detectors have a potential capability to provide the system with high count-rate performance which is particularly important in whole body PET systems. In this application, an optimum design of the signal processor and data acquisition system is necessary to reduce the count rate loss due to the dead time.

In recent years, new scintillators having fast scintillation decay and high stopping power have been proposed for PET application [20][21]. Their light output is lower than that of BGO in the state of the art. The detector system using multi-segment PMT is applicable to those new scintillators, while the crystal coding in the group coupling scheme is difficult to be applied to them because of poor statistics in those scintillation photons.

6. CONCLUSION

The high resolution PET system for brain studies has been developed. High spatial resolution in both the transaxial plane and the axial direction was accomplished by the simple detector scheme without coding method for crystal identification. Various functions implemented in this system provide the researchers with better environment for brain studies.

ACKNOWLEDGEMENTS

The authors wish to thank Dr.T.Yamasaki of National Institute of Radiological Sciences for advices for the PET development, Doctors of Chiba University for a offer of the clinical data. The authors also thank T.Hiruma, T.Hayashi of Hamamatsu Photonics K.K. for their encouragements throughout this work, and T.Katoh of Hamamatsu R&D Div., T.Watanabe, M.Ito, K.Nakamura, H.Kyushima and other people of Hamamatsu Electron Tube Div. for contribution of the design and development of the PMT.

REFERENCES

[1] S.E.Derenzo,T.F.Budinger and T.Vuletich,"High resolution positron emission tomograph using small bismuth germanate crystals and individual photosensors,"IEEE *Trans.Nucl.Sci.* NS-30, 665-670 (1983)

[2] H.Murayama et al.,"Twin BGO detector for high resolution positron emission tomograph,"*Nucl.Instr.and Meth.*vol.221,633-640 (1984)

[3] J.M.Ronye and C.J.Thompson,"Detector identification with four BGO crystals on a dual PMT,"IEEE *Trans.Nucl.Sci.* NS-31, 1022-1027 (1984)

[4] Y.Yamashita,H.Uchida,T.Yamashita et al.,"Recent development in detector for high spatial resolution positron CT,"IEEE *Trans.Nucl.Sci.* NS-31, 424-428 (1984)

[5] T.Tomitani,N.Nohara,H.Murayama,et al.,"Development of a high resolution positron CT for animal studies,"IEEE *Trans.Nucl.Sci.* NS-32, 822-825 (1985)

[6] M.E.Casey and R.Nutt,"A multicrystal two-dimensional BGO detector system for positron emission tomograph,"IEEE *Trans.Nucl.Sci.* NS-33, 460-463 (1986)

[7] H.Uchida,T.Yamashita,M.Iida et al.,"Design of a mosaic BGO detector system for positron CT,"IEEE *Trans.Nucl.Sci.* NS-33, 464-467 (1986)

[8] S.Yamamoto,S.Miura,H.Iida et al.,"A BGO detector unit for a stationary high resolution positron emission tomograph,"*J Comput Assist Tomogr*, vol.10(5), 851-855 (1986)

[9] G.Muehllehner,J.S.Karp,D.A.Mankoff et al.,"Design and performance of a new positron tomograph,"IEEE *Trans.Nucl.Sci.* NS-35, 670-674 (1988)

[10] K.Shimizu,T.Ohmura,M.Watanabe et al.,"Development of 3-D detector system for positron CT,"IEEE *Trans.Nucl.Sci.* NS-35, 717-720(1988)

[11] F.Daghighian,E.J.Hoffman and S.C.Huang,"Quality control in PET system employing 2-D modular detectors,"IEEE *Trans.Nucl.Sci.* NS-36, 1034-1037 (1989)

[12] T.J.Spinks,T.Jones,M.C.Gilardi et al.,"Physical performance of the latest generation of commercial positron scanner,"IEEE *Trans.Nucl.Sci.* NS-35, 721-725 (1988)

[13] S.Holte,L.Eriksson,J.E.Larsson et al.,"A preliminary evaluation of a positron camera system using weighted decoding of individual crystals,"IEEE *Trans.Nucl.Sci.* NS-35, 730-734 (1988)

[14] H.Iida,S.Miura,I.Kanno et al.,"Design and evaluation of HEADTOME-IV a whole-body positron emission tomograph,"IEEE *Trans.Nucl.Sci.* NS-36, 1006-1010 (1989)

[15] S.E.Derenzo,R.H.Huesman,J.L.Cahoon et al.,"A positron tomograph with 600 BGO crystals and 2.6mm resolution,"IEEE *Trans.Nucl.Sci.* NS-35, 659-664 (1988)

[16] T.Hayashi,"New photomultiplier tubes for medical imaging,"IEEE *Trans.Nucl.Sci.* NS-36, 1078-1083 (1989)

[17] E.Tanaka,N.Nohara,T.Tomitani et al.,"Stationary positron emission tomography and its image reconstruction,"IEEE *Trans.Med.Imaging*.MI-5,199-206 (1986)

[18] E.Tanaka,"A fast reconstruction algorithm for stationary positron emission tomography based on a modified EM algorithm,"IEEE Trans.Med.Imaging,vol.MI-6,98-105 (1987)

[19] E.Tanaka,"A filtered iterative reconstruction algorithm for positron emission tomography," in C.N. de Graaf and M.A. Viergever(ed.), Information Processing in Medical Imaging,Plenum Pub.Corp.,217-233 (1988)

[20] D.F.Anderson,"Properties of the high-density scintillator Cerium Fluoride,"IEEE *Trans.Nucl.Sci.* NS-36,137-140 (1989)

[21] W.W.Moses and S.E.Derenzo,"Lead carbonate,a new fast heavy scintillator,"in this volume (NS-37)

A COMPUTATIONAL FEASIBILITY STUDY OF THREE-DIMENSIONAL POSITRON EMISSION TOMOGRAPHY IN NUCLEAR MEDICINE

Hideo Murayama and Norimasa Nohara

Division of Physics, National Institute of Radiological Sciences
Anagawa-4-chome, Chiba-shi, Chiba 260, Japan

Abstract: In order to improve image quality in positron emission tomography (PET), a PET device needs to achieve full utilization of emitting photons, and it must be intimately linked to any 3D image reconstruction algorithm. Both the analytical and the iterative 3D reconstruction algorithms suitable for 3D PET systems are classified and evaluated from a computational point of view. For the analytical algorithms, the computation time is analyzed briefly and the required performances of a computer for 3D PET systems are provided. It is suggested that successful utilization of their algorithms depends not only on the performances of a computor, but also on the size of the image space to be reconstructed due to the practical constraints of detected photon counts. Some guidelines are provided for the choice of an appropriate reconstruction algorithm in a given situation.

(Keywords: Computational Feasibility, Three-dimensional Image Reconstruction, Positron Emission Tomography, Nuclear Medicine, Reconstruction Algorithm)

Introduction

Positron emission tomography (PET) has become important as a potential technique for physiological studies in nuclear medicine /1/. The technique makes it possible to non-invasively map the distribution of radioactivity by coincidence detection of annihilation photon pairs. That is, the distribution of the administered positron emitting isotope in an object is reconstructed by detecting the opposite travelling photon pairs produced by positron annihilation events.

Most current PET systems consist of cylindrical rings of detectors around a target object. The detectors are accompanied by parallel annular collimators appropriate to a section-by-section view of the object in order to eliminate oblique rays. Such PET systems involve utilization of two-dimensional (2D) section-by-section reconstruction /2/, which has allowed to use minicomputers for three-dimensional (3D) image recovery, avoiding the computational complexity of 3D problems. Since the photons are emitted isotropically from the object, the use of 2D reconstruction technique makes the great sacrifice of detection efficiency.

Toward full utilization of emitting photons, 3D reconstruction incorporating oblique rays has been studied by several authors /3-16/, and 3D reconstruction algorithms have been developed. These Fourier-based 3D reconstruction algorithms typically require a spatially invariant point spread function. A number of iterative reconstruction algorithms have been reported /20-23/ which are applicable to image reconstruction from incomplete projections. Some of the iterative algorithms may be computationally demanded for emission computed tomography because they permit accurate modeling of the imaging system and they can be derived to satisfy certain statistical performance criteria.

Recently, high sensitivity PET systems are strongly recommended to overcome the statistical limitation on the image quality, to acquire short measuring time and high spatial resolution, and to use tracers with limited specific uptake. In order to meet these demands, the 3D reconstruction algorithms must be employed to the 3D PET systems. Practical 3D PET systems, however, impose heavy burden not only to detector sets and coincidence circuitries, but also to computers in the memory requirements and the data processing /21/.

In this paper, a feasibility of 3D PET systems is described with an emphasis on the performances of a computer and the preferable algorithms for 3D reconstruction under the practical constraints of detected photon counts, ultimately aimed at 4π detection of photons.

3D PET System

In the following sections, we will use a 3D image space and 2D projection data planes of different view directions, which are digitized by the same unit size of cubic voxels and square pixels, respectively. The 3D image space is allocated with voxels on the order of N^3 in the field-of-view which is a sphere of diameter N with the center of the spherical PET at the origin. A set of detectors are assumed to be closely packed on the sphere of diameter 2N except that a part of the sphere is truncated for the practical requirements. By the truncated spherical PET with a circular opening of diameter N, looking like a jack-o'-lantern as shown in figure 1, an object can be freely accommodated in the field-of-view and subtend the coincidence detectors with 87% of the solid angle 2π.

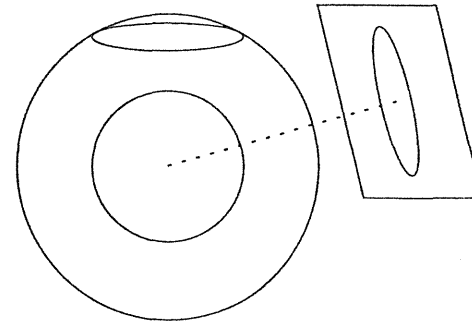

Figure 1. The geometry of a spherically bounded object and a projection plane.

For simplicity in the order estimation, the following estimates will be accomplished with a complete spherical PET system of diameter 2N, and the N will be a power of 2. To avoid the loss of resolution due to inadequate sampling, N^2 projection views are necessary. Since each projection plane has the order of N^2 pixels, the number of addresses for all the projection data is on the order to N^4, which is the same order for the total number of possible coincidence channels in the 3D PET system. In practical applications to dynamic brain studies and small animal studies, a 3D PET system with N=128 will be a powerful tool. However, to meet demands for the metabolic brain studies with high resolution of 4 mm or less, a 3D PET system with N=256 should be developed.

Because of the high stopping power, Bismuth Germanate (BGO) is currently the preferred detector material of the choice to provide 2D scintillation detector modules for 3D PET systems. Since the coincidence timing window is about 10 ns /23/, the maximum count rate of 3D PET is restricted on the order of 10^7 counts/sec or less. The maximum total count, MTC, is then restricted on the order of 10^9 or less due to the utilization of short-lived positron emitters, such as ^{11}C ($t_{1/2}$=20m), ^{13}N ($t_{1/2}$=10m), ^{15}O ($t_{1/2}$=2m), and ^{18}F ($t_{1/2}$=110m).

At present, however, MTC is limited by the maximum count rate of data acquisition systems. Recently, a data acquisition system with software controlled processes has been proposed /24/, which consists of an array of processors connected over a VME bus, operating asynchronously and in parallel. The device will be able to attain the maximum count rate of 2.5×10^6 coincidence events per second for raw data of the processing unit. Such a software-based system is preferable to 3D PET because the data acquisition system for 3D PET must be flexible enough to accomodate several reconstruction methods and different geometries in detector arrangement.

3D Reconstruction Algorithms

Analytical Methods

A set of two-dimensional projections $p(\hat{\mathbf{u}},\mathbf{s})$ of a density $f(x)$ in the 3D image space $\mathbf{R}^3$ is defined by

$$p(\hat{\mathbf{u}},\mathbf{s}) = \int_{-\infty}^{+\infty} dl\, f(\mathbf{s}+l\hat{\mathbf{u}}) \qquad (1)$$

where $\hat{\mathbf{u}}$ is the unit vector of projection direction and $\mathbf{s}=x-(x\cdot\hat{\mathbf{u}})\hat{\mathbf{u}}$ is the two-dimensional vector in the projection plane. It is assumed to be shift invariant for a set of directions of Ω with $\hat{\mathbf{u}}\in\Omega$, and the line integrals are measured for all positions in the central plane normal to $\hat{\mathbf{u}}$, i.e., for all $\mathbf{s}\in\mathbf{R}^3$ satisfying $\mathbf{s}\cdot\hat{\mathbf{u}}=0$. By the central slice theorem, the relationship (1) between the density f and the projections p is described in Fourier space as follows,

$$F(\nu) = \iiint_{-\infty}^{+\infty} d^3x f(x)\exp(-2\pi i x\cdot\nu)$$

$$= P(\hat{\mathbf{u}},\nu) \qquad (2)$$

with $\nu\cdot\hat{\mathbf{u}}=0$, where $F(\nu)$ is the Fourier transform of $f(x)$, and $P(\hat{\mathbf{u}},\nu)$ is the two-dimensional Fourier transform of the projection, namely,

$$P(\hat{\mathbf{u}},\nu) = \iint_{\mathbf{s}\cdot\hat{\mathbf{u}}=0} d^2\mathbf{s}\,\exp(-2\pi i\mathbf{s}\cdot\nu)p(\hat{\mathbf{u}},\mathbf{s}) . \qquad (3)$$

As shown by Defrise et al /7/, we can obtain

$$F(\nu) = \iint_{\Omega} d^2\hat{\mathbf{u}}\,\delta(\hat{\mathbf{u}}\cdot\nu)H(\hat{\mathbf{u}},\nu)P(\hat{\mathbf{u}},\nu), \qquad (4)$$

where $\delta(x)$ is the Dirac distribution function, and $H(\hat{\mathbf{u}},\nu)$ is a specific Fourier space filter, which must satisfy

$$\iint_{\Omega} d^2\hat{\mathbf{u}}\,\delta(\hat{\mathbf{u}}\cdot\nu)H(\hat{\mathbf{u}},\nu) = 1 \qquad (5)$$

for any ν in $\mathbf{R}^3$.

Because of a redundancy of the measured data in 3D PET, the recovery procedure is not unique and a number of distinct algorithms are available which may provide different noise properties. The algorithms for analytical 3D reconstructions from projections can be classified into two categories. The first category, named by FILBK, is based on 2D filtering in projection planes prior to backprojecting into a 3D image space. The second category, named by BKFIL, implies that the projection data are backprojected into a 3D image space, followed by 3D filtering in the image space. The FILBK and BKFIL are corresponding to two families of filters, defined by Defrise et al /7/: those which are not factorisable and those which are factorisable, respectively. A filter $H(\hat{\mathbf{u}},\nu)$ is said to be factorisable if it can be written as the product of a filter function $H'(\nu)$ defined on $\mathbf{R}^3$, with an even positive integrable function $w(\hat{\mathbf{u}})$ defined on Ω, that is,

$$H(\hat{\mathbf{u}},\nu) = H'(\nu)w(\hat{\mathbf{u}}). \qquad (6)$$

From a theoretical point of view, the FILBK is general because the BKFIL algorithms can be mathematically transferred to a part of the FILBK algorithms. From a computational point of view, however, the FILBK is possessed of inevitable limitation in counting statistics of data at each projection address. Projection data with a system of N=256 may be very sparsely distributed among the possible addresses on the order of 256^4 ($\sim4\times10^9$), because the number of possible addresses is larger than MTC. Therefore, the FILBK algorithms should be employed

for N less than or equal to 128. A set of projection data with the system of N=256 needs a non-practically large storage capacity. The BKFIL algorithms, however, have the possibility of reduction in storage capacity of the projection data, if coincidence data are backprojected directly into the 3D image space with an event-by-event technique.

In applications of nuclear medicine, we often encounter to evaluate small regions of interest in the field-of-view, which obviates the need for reconstruction of the whole 3D image. In such a situation, the FILBK algorithms take the advantage of saving memory capacity and computation time in the 3D backprojection step, while the BKFIL algorithms always require the whole image space due to the successive 3D filtering.

An example of BKFIL is the Colsher's algorithm /4/, which uses the following 3D filter in Fourier space on the condition that $\Omega = \{\hat{u} \in S^2 | |\hat{u}_z| < \sin\theta_0\}$ and $w(\hat{u}) = 1$ for some fixed acceptance angle θ_0:

$$H'(\nu) = \begin{cases} \dfrac{|\nu|}{2\pi} & \text{if } |\Psi| < \theta_0 \\ \dfrac{|\nu|}{4} \dfrac{1}{\sin^{-1}(\sin\theta_0/\sin\Psi)} & \text{if } |\Psi| \geq \theta_0. \end{cases} \quad (7)$$

An example of FILBK is the Ra's algorithm /6/, which uses the following 2D filter in Fourier space:

$$H(\hat{u},\nu) = \begin{cases} \dfrac{|\nu|}{2\pi(1-\cos\theta_0)} \left(1 - \dfrac{\cos\theta_0 \cos\Psi}{u_p^2}\right) & \text{if } |\Psi| < \theta_0 \\ \dfrac{|\nu|}{2\pi(1-\cos\theta_0)} \left(1 - \dfrac{\cos^2\theta_0}{u_p^2}\right)^{1/2} \left(1 - \dfrac{\cos^2\Psi}{u_p^2}\right)^{1/2} & \text{if } |\Psi| \geq \theta_0, \end{cases} \quad (8)$$

where $\cos\Psi = |\nu_z|/|\nu|$ and $u_p^2 = 1 - \hat{u}_z^2$.

Under the condition of full angular acceptance ($\theta_0 = \pi/2$) and N = 64, numerical computation for imaging a phantom was performed with both the FILBK (Colsher's algorithm) and BKFIL (Ra's algorithm). Figure 2(A) is a set of sliced original images of the phantom. The emission density of the crust for the phantom is a half that of the ellipsoid in the hollow sphere. Figures 2(B) and (C) are reconstructed images of the corresponding planes to figure 2(A) with the BKFIL algorithm and the FILBK algorithm, respectively. In this simulation, we used 2D line integral projection data (128x128 in pixel size) of 92 orientations without statistical noise. Although the Gibb's phenomenon appears more distinctly in the reconstructed image with the BKFIL than the FILBK, these figures demonstrate the good image recovery with both the algorithms for the noiseless data. It took computation time about 75 minutes for the BKFIL, and 108 minutes for the FILBK on a micro VAX II.

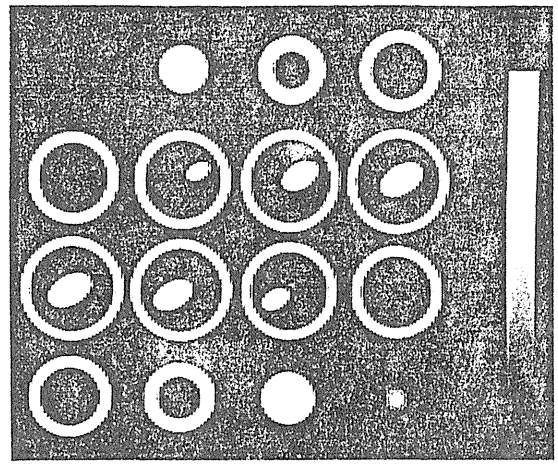

A

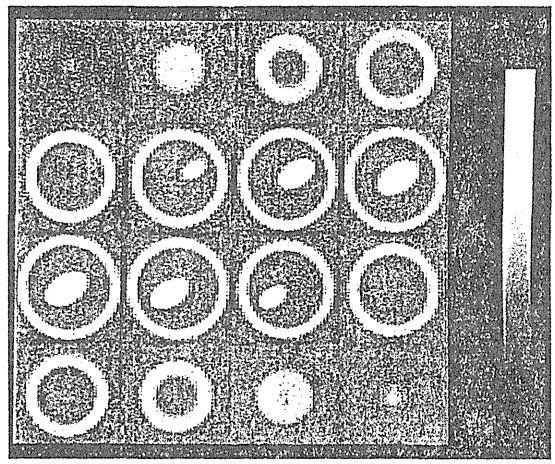

B

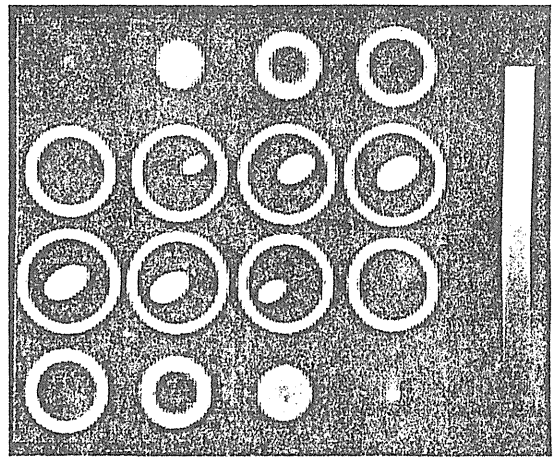

C

Figure 2. Original sliced images of a phantom in (A), and reconstructed volume images resulting from the BKFIL in (B) and the FILBK in (C) without statistical noise in the projection data.

Iterative Methods

Recently, iterative reconstruction methods have received considerable attention for their use in emission computed tomography because the iterative methods are useful in cases not only where the point spread function is not spatially invariant, but also where it is easy to incorporate a priori information about the emission distribution, such as non-negativity. Compared to analytical reconstruction methods, they have advantages in that they are tolerant to incomplete sampling of projection data. They are also promising methods for a stationary PET system with fine spatial resolution and high sensitivity using a 3D detector arrangement, in which undesireable gaps among the detector banks are inevitable or the finite distance between the adjacent detector elements restricts the spatial resolution of the image over the intrinsic detector resolution /26/.

The iterative algorithms are categorized into two families, which we call IPRA and ISRA. The IPRA algorithms perform evaluation of each iteration on the projection planes, while the ISRA algorithms do on the image space. The IPRA algorithms should be employed for the system of N less than or equal to 128 due to the counting statistics of projection data, which is the same cause as the limitation of N for the FILBK algorithms. Similar to the BKFIL algorithms, the ISRA algorithms have the possibility of reduction for storage of the projection data with an event-by-event technique on 3D backprojection, prior to the iterative procedure.

We assume that a set of I measurements y_i ($1 \le i \le I$) are available, where y_i is the number of events counted in the i-th projection address. The basic problem is to estimate the emission density x_j ($1 \le j \le J$) from the measurements, where j is a source voxel in a set of J elements. Let us denote the normalized probability that an event emitted from voxel j is assigned to projection i by a_{ij}. Then for each j,

$$\sum_{i=1}^{I} a_{ij} = 1 \tag{9}$$

and a set of I elements z_j ($1 \le i \le I$), which are the expected values of y_i, are obtained by

$$z_i = \sum_{j=1}^{J} a_{ij} x_j. \tag{10}$$

An example of IPRA is the expectation maximization algorithm (EM) method /20/. The iteration step for this method is given by

$$x_j^{(n+1)} = x_j^{(n)} \sum_{i=1}^{I} (a_{ij} y_i / z_i). \tag{11}$$

The virtues of the EM method are not only that convergence to the maximum likelihood estimate can be proven theoretically, but also that automatic inclusion of non-negativity constraints and preservation of total image counts in every iteration are possible.

Since its convergence rate is low, modified versions of the EM method have been developed by several authors, one of which is the filtered iterative reconstruction algorithm (FIRA) method /22/. This method uses the following iteration step,

$$x_j^{(n+1)} = \begin{cases} x_j^{(n)} C_j^{\alpha} U_j^{\beta/A_j} & \text{if } U_j \le 1 \\ x_j^{(n)} \{C_j^{\alpha} + (U_j - 1)\beta/A_j\} & \text{if } U_j > 1, \end{cases} \tag{12}$$

where α and β are constants, and

$$C_j = \sum_{i=1}^{I} (y_i a_{ij}) / z_i^{(n)},$$

$$U_j = \sum_{i=1}^{I} [\{y_i a_{ij} (z_i^{(n)} * h)_s / \{z_i^{(n)} (y_i * h)_s\}],$$

$$A_j = (x_j + \rho) \sum_{i=1}^{I} [\{a_{ij} (z_i^{(n)} * h)_s / \{z_i^{(n)} (y_i * h)_s\}]. \tag{13}$$

Here ρ is a small positive constant, and h is a low-pass filter, namely,

$$h \equiv h(s) = (s^3 + 2s^2 + 3)^{-1} \quad (-10 \le s \le 10), \tag{14}$$

where s is the bin number of the projections in the same view angle of the projection i. Two convolutions, $(z_i^{(n)} * h)_s$ and $(y_i * h)_s$, are performed on the sampling points on the s axis.

An example of ISRA is the muitiplicative simultaneous iterative reconstruction technique (MSIRT) /28/. The iteration step for this method is given by

$$x_j^{(n+1)} = x_j^{(n)} \sum_{i=1}^{I} (a_{ij} y_i / b_i) \Big/ \sum_{i=1}^{I} (a_{ij} z_i^{(n)} / b_i),$$

$$b_i = \sum_{j=1}^{J} a_{ij}, \tag{15}$$

where b_i's are normalization factors and the MSIRT is the same algorithm as the one proposed by M.E. Daube-Witherspoon, et al /21/ if $b_i = 1$.

Under the condition of 2D image reconstruction in a 64x64 square matrix, numerical computation for imaging a 2D phantom was performed with these iterative methods. Figures 3(A) and (B) are the original image of the phantom and a reconstructed image by using the Shepp-Logan convolution method (CONVO)/2/, which is one of the 2D analytical reconstruction methods. Image recovery for the iterative reconstruction methods depends on the iteration number, ITN. Figures 3(C), (D) and (E) are images reconstructed with the EM of ITN=20, the FIRA of ITN=4, and the MSIRT of ITN=20, respectively. In this simulation, we used 68 line integral projection data of 240 orientations, which are based on the noisy data with a total count of 1×10^6. These figures demonstrate that iterative methods such as the EM, FIRA and MSIRT provide superior images as compared with the analytical CONVO method.

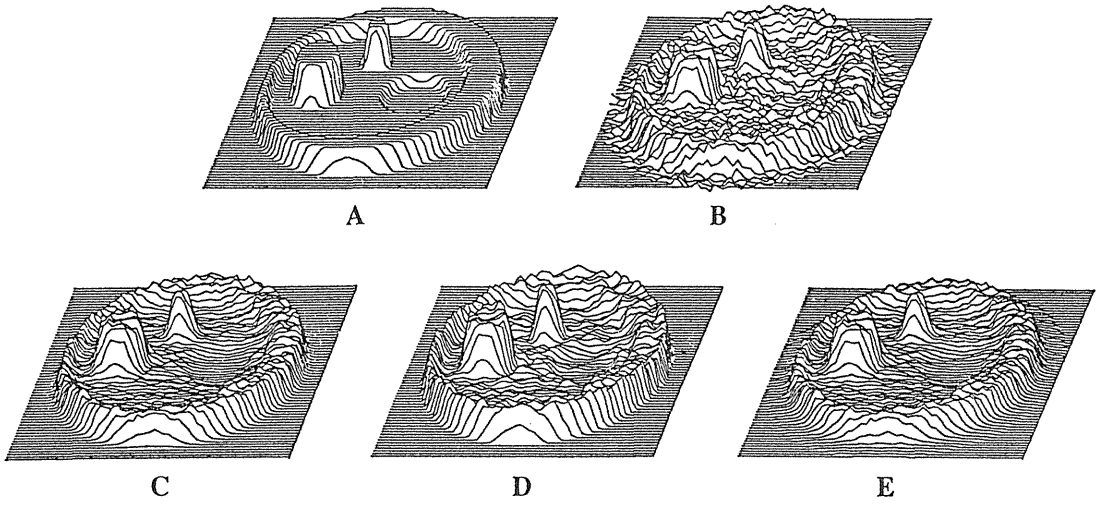

Figure 3. Original image of the 2D phantom in (A) and the reconstructed image by using the Shepp-Logan convolution method for noisy data set with the total count of 1×10^6 in (B); reconstructed images by using the EM of ITN=20 in (C), the FIRA of ITN=4 in (D), and the MSIRT of ITN=20 in (E) for noisy data set with the total count of 1×10^6.

Data Processing

For simplicity, a computer used for the image reconstruction is assumed to run under the full pipeline operation, which provides the ideal throughput rate, namely, maximum floating-point operation per cycle time.

A FILBK algorithm mainly consists of 2D filtering processes for 2D projections using 2D Fast Fourier Transform (FFT), and process of 3D backprojection. The most time-consuming step in FILBK is the 3D backprojection, which may take time about

$$\mathrm{TBACK(N)} = \mathrm{LB} \times \mathrm{TM} \times \mathrm{N}^5, \tag{16}$$

where TM is a single cycle time of the computer used and LB is the number of machine cycles to proceed the kernel do-loop which executes rotation of coordinates and 2D interpolation. Since LB is about 30,

$$\mathrm{TBACK(N)} = 30 \times \mathrm{TM} \times \mathrm{N}^5. \tag{17}$$

The computation time for 2D filtering process in FILBK is given by

$$\mathrm{TFIL2(N)} = 8 \times \mathrm{TM} \times \mathrm{N}^4 \times \log_2 \mathrm{N}. \tag{18}$$

A BKFIL algorithm consists of 3D backprojection and 3D filtering process for the backprojected data using 3D FFT. The computation time for 3D filtering process in BKFIL is given by

$$\mathrm{TFIL3(N)} = 12 \times \mathrm{TM} \times \mathrm{N}^3 \times \log_2 \mathrm{N}. \tag{19}$$

Due to the higher order dependence of TFIL2(N) on N compared with TFIL3(N), the BKFIL algorithms require less computation time than the FILBK. Nevertheless the time difference is not distinct owing to the heavy burden of TBACK(N) in both the algorithms.

In the case that TM=100ns, corresponding to a computer with 10 MFLOPS, the computation time for 3D backprojection is given by

$$\begin{aligned} &\mathrm{TBACK(256)} = 915\ \mathrm{h}, \\ &\mathrm{TBACK(128)} = 28\ \mathrm{h}, \\ &\mathrm{TBACK(64)} = 55\ \mathrm{m}. \end{aligned} \tag{20}$$

This suggests that the 3D backprojection process for the image size of the order of 256^3 is not practical. If a computer or a special hardwired backprojector with the effective computation speed of 30 GFLOPS is available, the computation time TBACK(256) is about 20 minutes, which is tolerable in certain clinical use. For the image size of the order of 128^3, the computation time of 20 minutes will be achieved with a powerful parallel computer or a backprojector of 1 GFLOPS, which is expected to be a type of workstation in clinical site.

In applications of evaluating the regions of interest, the computation time for 3D backprojection may be largely reduced by using the FILBK algorithms. In these cases the computation time for 3D reconstruction is dominated by 2D filtering processes, as follows:

$$\begin{aligned} &\mathrm{TFIL2(128)} = 25\ \mathrm{m}, \\ &\mathrm{TFIL2(64)} = 1.4\ \mathrm{m}. \end{aligned} \tag{21}$$

A BKFIL algorithm can involve the event-by-event backprojection instead of the ordinary 3D backprojection. The computation time for event-by-event backprojection process is given by

$$\mathrm{TEVEB(MTC)} = \mathrm{LW} \times \mathrm{TM} \times \mathrm{MTC}, \tag{22}$$

where LW is the average number of machine cycles to deposit proper densities onto the voxels along the path of each coincidence line. A real-time event-by-event backprojector will be available if TM x LW is less than 100 ns, due to the maximum countrate of a 3D PET system with MTC=10^9. Since LW is approximately proportional to N, the event-by-event backprojector is more powerful for a larger image space, namely, for the system of N=256.

The iterative methods involve not only backprojection processes but also forward-projection processes. For the IPRA algorithms, each step of both the processes takes time about TBACK(N), and then the total computation time is approximately given by 2 x ITN x TBACK(N), where ITN is the iteration number to get the final reconstructed image. Disadvantage of the iterative methods is mainly due to their slow convergence rate. The EM algorithm, one of typical examples for IPRA, needs ITN of more than 15, dependent on the statistics of photon counts and emission distribution. The IPRA algorithms, however, have been successfully modified to obtain faster speed of convergence. The FIRA method, one of modified EM versions, needs ITN of less than 5.

The iteration number required to get a final image with the ISRA algorithms is larger than that with the EM algorithm, and accelerated algorithms for ISRA have not found yet. However, the ISRA algorithms have the advantage of reduction in the number of projection views for both the forward-projection steps and the backprojection steps after the first event-by-event backprojection step.

Discussion and Conclusion

In this work, the effect of attenuation in the object does not be considered, and problems of scattered events and the accidental events are neglected. A 3D PET system, however, implies an increase in the singles rate as well as in the true coincidence rate, and consequently in the randoms rate /18/. Removal of parallel annular collimators in front of detectors on a 3D PET device increases scattered and accidental coincidences. In development of a correction algorithm for scattered radiation and accidental coincidences, or in examining the performances of different 3D PET configurations, Monte Calro simulation study /27/ may be a powerful tool, which demands the same powerful computer as the one used for data processing in practical 3D reconstruction.

Toward practical 3D PET systems, 3D reconstruction algorithms have been classified and evaluated from a computational point of view. For the analytical algorithms, the computation time has been analyzed briefly and the required performances of a computer for 3D PET systems have been provided. For the iterative algorithms, it is suggested that successful utilization of their algorithms depends on the developments for not only fast backprojectors but also fast forward-projectors in the 3D image space. They are characterized and summarized, as follows:

1) FILBK and IPRA algorithms should be used for the image space of 128^3 or less, due to maximum photon counts.
2) BKFIL and ISRA algorithms may be useful for the image space of 256^3. For these algorithms, a real-time event-by-event backprojector is preferable.
3) In certain clinical use, a computer with the effective computation speed of 30 GFLOPS is needed for the image space of 256^3 on the 3D reconstruction process. For the image space of 128^3, a computer of 1 GFLOPS is expected.

Acknowlegement

This work was supported in part by a grant from the Ministry of Education, Japan. We gratefully acknowlege Dr. K. Kawashima for his kind support of this work.

References

1. H.N. Wagner, Jr: J. Nucl. Med., 29, 1329-1337 (1988)
2. L.A. Shepp and B.F. Logan: IEEE Trans. Nucl. Sci., NS-21, 21-43 (1974)
3. N.J. Pelc and D.A. Chesler: J. Comput. Assist. Tomogr., 3, 385-395 (1979)
4. J.G. Colsher: Phys. Med. Biol., 25, 103-115 (1980)
5. B. Shorr, D.W. Townsend and R. Clack: Phys. Med. Biol., 28, 305-312 (1983)
6. J.B. Ra, C.B. Lim, Z.H. Cho, et al: Phys. Med. Biol. 27, 37-50 (1982)
7. M. Defrise, D.W. Townsend and R. Clack: Phys. Med. Biol., 34, 573-587 (1989)
8. Z.H. Cho, J.B. Ra and S.K.Hilal: IEEE Trans. Med. Imag., MI-2, 6-18 (1983)
9. M. Defrise, S. Kuijk and F. Deconinck: Phys. Med. Biol., 33, 43-51 (1988)
10. P.E. Kinahan, J.G. Rogers, R. Harrop, et al: IEEE Trans. Nucl. Sci., NS-35, 635-638 (1988)
11. J.G. Rogers, R. Harrop, P.E. Kinahan, et al: IEEE Trans. Nucl. Sci., NS-35, 680-684 (1988)
12. P.E. Kinahan and J.G. Rogers: IEEE Trans. Nucl. Sci., NS-36, 964-968 (1989)
13. S.S. Orlov: Kristallografiya, 20, 511-515 (1975)
14. S.S. Orlov: Kristallografiya, 20, 701-709 (1975)
15. O. Nalcioglu and Z.H. Cho: Proc. IEEE, 66, 1584-1585 (1978)
16. E. Tanaka: Phys. Med. Biol., 24, 157-161 (1979)
17. G. Muehllehner, J.S. Karp, D.A. Mankoff, et al: IEEE Trans. Nucl. Sci., NS-35, 670-674 (1988)
18. D.W. Townsend, T. Spinks, T. Jones, et al: EEE Trans. Nucl. Sci., NS-36, 1056-1065 (1989)
19. P.K. Marsden, R.J. Ott, J.E. Bateman, et al: Phys. Med. Biol., 34, 1043-1062 (1989)
20. L.A. Shepp and Y. Vardi: IEEE Trans. Med. Imag., MI-1, 113-122 (1982)
21. M.E. Daube-Witherspoon and G. Muehllehner: IEEE Trans. Med. Imag., MI-5, 61-66 (1986)
22. E. Tanaka: IEEE Trans. Med. Imag., MI-6, 98-105 (1987)
23. H. Murayama: Nucl. Instr. Meth., 177, 433-440 (1980)
24. N.A. Wilkinson, M.S. Atkins and J.G. Rogers: IEEE Trans. Nucl. Sci., NS-36, 1047-1051 (1989)
25. M. Dahlbom, L. Erikson, G. Rosenqvist, et al: IEEE Trans. Nucl. Sci., NS-36, 1066-1071 (1989)
26. E. Tanaka, N. Nohara, T. Tomitani, et al: IEEE Trans. Med. Imag., MI-5, 199-206 (1986)
27. C.J. Thompson: IEEE Trans. Nucl. Sci., NS-36, 1072-1077 (1989)
28. H. Murayama, E. Tanaka and N.Nohara: Med. Imag. Tech., 7, 315-333 (1989)

3．治　　療

日放腫会誌 *J. Jpn. Soc. Ther. Radiol. Oncol.* 3: 27-33, 1991

FAST NEUTRON RADIOTHERAPY FOR SUPERIOR SULCUS, PANCOAST TUMOR

Shinroku MORITA, Hiroshi TSUNEMOTO, Tadaaki MIYAMOTO, Shinichiro SATO and Kenjiro FUKUHISA

(*Received 24 August 1990, accepted 22 November 1990*)

Abstract Thirty-two previously untreated patients suffering from superior sulcus Pancoast tumors of the lung were treated with fast neutron beams (30 MeV d-Be) between 1975 and 1988 at the NIRS. A high irradiation dose (average dose: TDF 113) was administered with a large field to cover subclinical deposits utilizing a shrinking field technique. Local control of the tumor mass was observed in 44% of the patients, greatly improving chances for prolonged survival. Median survival was 21.1 months for patients with local control versus 10.4 months for those with local failure. The relative five-year survival rate was 20% for the total (n=32), 34% for stage III A (n=12), 15% for stage III B (n=16) and 0% for stage IV (n=4). Radiation therapy achieved pain relief for 62.5% of patients. Radiation myelopathy developed in one long-surviving patient, but complications from radiation were, otherwise, mild to moderate

Key words: Fast neutron irradiation, Superior sulcus lung cancer, Pancoast cancer.

INTRODUCTION

Fast neutron radiotherapy was started in November 1975 at the NIRS, Chiba, Japan. A total of 1805 patients with localy advanced or radioresistant malignant tumors were treated through the end of 1989.

Fast neutrons have the following radiobiological properties of high LET (Linear Energy Transfer) radiation: ① lower Oxygen Enhancement Ratio (OER), ② less variation in radiosensitivity among cell lines and conditions of cells (in a cell cycle or in the degree of oxygenation), ③ greater RBE (Relative Biological Effectiveness) in slow growing tumors which are commonly radioresistant to photons.

Tumors located at the apex of the lung have been well described by Pancoast[1,2]. These tumors characteristically invade surrounding structures including the pleura, posterior part of the ribs, vertebrae, and brachial or cervical sympathetic nerve plexuses. Thus, most patients suffer from severe pain in the shoulder, chest or arm, numbness or atrophy of the arm, and Horner's syndrome.

Treatment of choice has been a controversial subject. As curative resection was generally not feasible due to the tumor location[3], preoperative radiotherapy was employed[3-6].

The postoperative complication rate was, however, unacceptably high[5,6], and no five-year survivor among those patients with positive mediastinal nodes were reported[3,4]. Radiotherapy alone with high energy, high dose and wide field was prefered[7] with some recommended surgery, either alone or combined with interstitial irradiation[8,9]. The purpose of this paper is to evaluate the efficacy and radiobiological advantages of fast neutrons in the treatment of Pancoast tumor of the lung.

METHODS AND MATERIALS

1) Characteristics of neutrons

The fast neutron beams used were produced by bombarding a thick beryllium target with 30 MeV deuterons. A distribution of lineal

森田 新六, 恒元 博, 宮本 忠昭, 佐藤 眞一郎, 福久 健二郎
Hospital Division, National Institute of Radiological Sciences (NIRS), 4-9-1, Anagawa, Chiba-shi 260, Japan.

Table 1. Clinical stages by TNM classification of 32 previously untreated patients

Stage	No.	T2	T3				T4			
		N2	N0	N1	N2	N3	N0	N1	N2	N3
III A	12	1	5	4	2	-	-	-	-	-
III B	16	-	-	-	-	4	1	-	5	6
IV	4	-	-	-	1	1	1	-	1	-
Total	32	1	17				14			

* Sites of tumor invasion in T4 cases: mediastinum; 3 patients; vertebral body; 11 patients.

energy transfer in the neutron beam ranged from 10 to 1000 KeV/μm, which was high LET radiation.

The depth dose, and dose distribution obtained at a source skin-distance (SSD) of 175 cm were about the same as those of Co-60 gamma rays at SSD 65 cm. The maximum build-up was 5 mm below the surface. The output dose rate was 42 cGy/min. (n. γ.) for an 11.4 cm×11.4 cm field at a source-target-distance (STD) of 200 cm. Gamma ray contamination was estimated to be less than 4%. Target doses were prescribed with the biologically equivalent TDF (Time Dose and Fractionation). For cases with curative intent TDF 110-120 were delivered, either with neutrons alone or in a mixture with photons, called a mixed beam schedule or neutron boost.

2) Patients

Thirty-two previously untreated patients were treated between 1975 and 1988. There were 28 men four women. Ages ranged from 31 to 71 years with an average of 60.1 years. Patients were classified according to the UICC TNM classification (1987). Twelve patients had stage III A disease, one T2N2, five T3N0, four T3N1, and two T3N2. Sixteen patients had stage III B disease, four T3N3, one T4N0, five T4N2, and six T4N3. Four patients had stage IV disease, T3N2M1, T3N3M1, T4N0M1, and T4N2M1. T4 lesions invaded to mediastinum in three patients and vertebral body in 11 patients (Table 1). Histological classification was ① adenocarcinoma: 17 patients (53%), including eight with a poorly differentiated type, ② squamous cell carcinoma: 10 (31%), ③ large cell carcinoma three (9%), and ④ small cell carcinoma: two (6%).

3) Irradiation methods

Three patients (9%) were treated with fast neutrons alone and the others (91%) with a mixture with photons. A target volume included the primary tumor, supraclavicular nodes area, vertebral bones, nerve plexuses, upper and midmediastinal and hilar nodes area, and irradiated with anterior-posterior parallel opposed ports with an average size of 169.6 cm^2. The spinal cord and the hilum were spared after TDF 66 (40 Gy equivalent), and a boost dose of TDF 49 (30 Gy equivalent) was delivered to cover the gross tumor with an average portal size of 102 cm^2.

As neutron beams were available three days a week, the standard dose with neutrons alone was determined to be 1620 cGy/18 Fx./6 weeks (TDP 100), based on an RBE value of 3.0.

The average prescribed dose was TDF 113.7 in total patients, TDF 113.2 in mixture with photons and TDF 118.0 in the neutrons-alone group.

RESULTS

1) Local control rate

Complete disappearance or possibly a scarred tumor mass about six months after treatment was observed in 14 patients (44%) and local residual or recurrence of tumor occurred in 18 patients (56%). Local control rate of each stage was 33% (4/12) for stage III A, 50% (8/16) for stage III B and 50% (2/4) for stage IV. (Table 2)

2) Survival

The median survival of the six surviving

Table 2. Local control rates by stage

Local status	Stage			Total
	III A	III B	IV	
Controlled or scarred	33%(4/12)	50%(8/16)	50%(2/4)	44%(14/32)
Residual or Recurrence	67%(8/12)	50%(8/16)	50%(2/4)	56%(18/32)

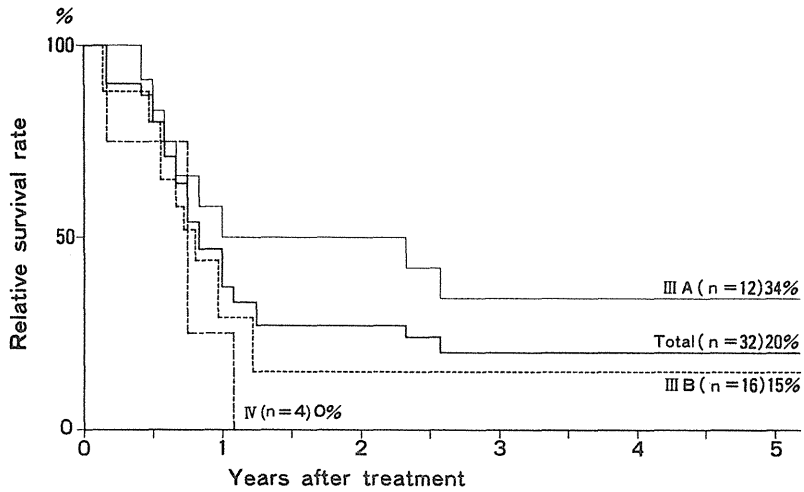

Fig. 1. The relative survival curves of fast neutron irradiated patients with Pancoast lung cancer (1975-1988, NIRS). No significant statistical differences were observed between III A vs III B (χ^2 test=1.226), III A vs IV (χ^2 test=2.374), or III B vs IV (χ^2 test=0.451).

patients is 55.3 months (6 to 96 months), 73.2 months for the four patients whose cancers were locally controlled, and 19.5 months for the two patients with local failure.

Twenty six patients died in one to 69 months. The median survivals were 14.8 months for all patients, 21.9 months for 10 with local control, and 10.4 months for 16 with local failure.

Five patients survived over 60 months (67 to 106 months). The relative five-year survival rates were 20% for all patients, 34% for stage III A, 15% for stage III B and 0% for stage IV (Fig. 1).

Considering the T factor, the five-year survival rates were 29.8% for T3 patients and 8.6% for T 4 (Fig. 2). Considering the N factor, the five-year survival rates were 27.5% for N0 and N1 patients, 22.5% for N2, and 11.4% for N3. (Fig. 3)

3) Histologic type

No statistical difference in patient distribution was found in two histologic type groups of adenocarcinoma (Ad) vs squamous cell carcinoma (Sq). Local control was achieved in eight of 17 Ad patients (47%) and two of 10 Sq (20%). Four Ad patients are still living 6 to 100 months after their treatment, but there are no survivors among the Sq patients. The median survival rate was 19.8 months for Ad patients and 10.8 for Sq patients (Table 3).

4) Symptomatic relief

Symptomatic releif was obtained for 20 patients (62.5%). Five patients (15.6%) experienced complete relief and the remaining 15 (46.8%) had partial relief. Four patients (12.5 %) had no change and six (18.7%) developed aggravated symptoms after short term relief. No data was available for the remaining two patients.

5) Causes of death

Twenty six patients were examined, 10

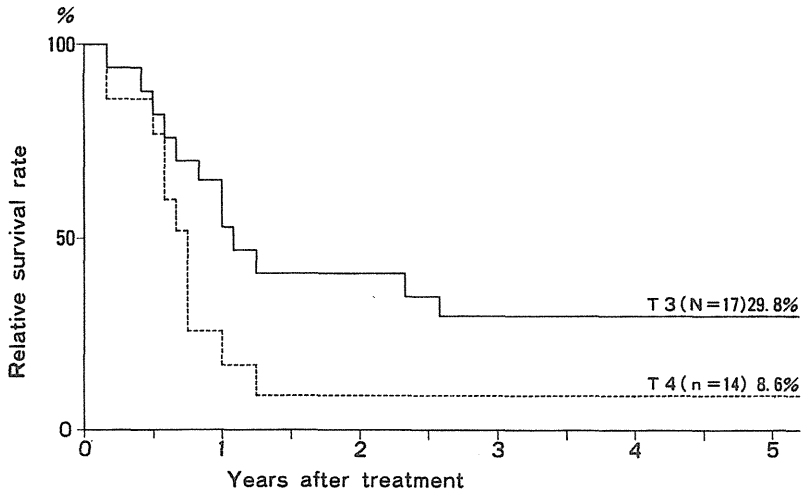

Fig. 2. The relative survival curves related to T factor. Differences at 90% level of risk (χ^2 test=3.418) was statistically significant.

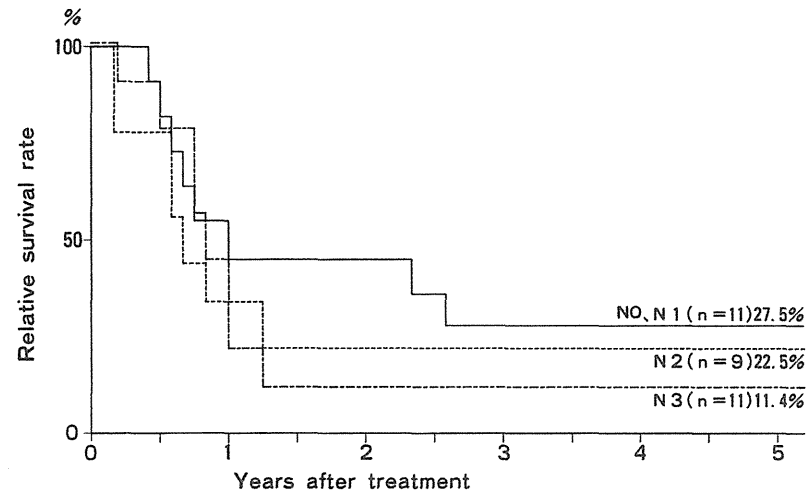

Fig. 3. The relative survival curves related to N factor. No significant statistical differences were observed between N0 and N1 vs N2 (χ^2 test=0.1233), N0 and N1 vs N3 (χ^2=0.5099), or N2 vs N3 (χ^2 test=0.0068).

patients (38.4%) died from a residual or recurrent tumor.

Distant metastasis caused the death in 11 (42.3%). Other diseases accounted for the death of the five remaining patients (15.3%), two from pneumonia, one from heart failure, one from uterine cervix cancer, and one from hemoptysis.

6) Complications

There were no major complications to the skin or subcutaneus tissue. Although moderate fibrotic changes developed in irradiated lung tissue in most patients, no serious symptoms were observed.

Radiation myelopathy with paraplegia developed in one patient in the mixture with photons group almost 2 years after irradiation. Dose to the spinal cord was estimated to be TDF 62 (4000 cGy).

Hemoptysis in the patient mentioned above occurred at 5 years and 7 months after the treatment presumably caused by irradiation.

Table 3. Clinical results of fast neutron therapy for Pancoast tumor by histologic type

(NIRS, 1989)

	Adeno ca	Squamous cell ca
No. of patients	17	10
Average age Stage Average TDF	61.5 III A: 7, III B: 9, IV: 1 113.6	65.0 III A: 4, III B: 5, IV: 1 114.9
Local Control[1)]	8/17(47%)	2/10(20%)
Alive	4 (6-100 months)	0
Deceased[2)] Median Survival	13 (19.8 months)	10 (10.8 months)

1) $\chi^2=0.987$, 2) $\chi^2=1.212$, no significant statistical difference

DISCUSSION

The efficacy of fast neutrons in the treatment of relatively slow-growing tumors was argued by Battermann et al.[10]. They revealed an RBE of 5.7 for a single fraction and an RBE of 8.0 for multiple fractions of neutrons in the treatment of metastatic adenoidcystic carcinoma of the lung. RBE for most normal human tissue is in the 3.0-3.3 range. So this difference in RBE values could indicate an advantage with neutrons. Actually, salivary gland tumors and prostatic adenocarcinomas, which are slow-growing tumors, were clearly revealed to benefit from neutron therapy in various centers[11].

Pancoast tumors are considered to be relatively slow-growing[3,4], and our neutron therapy proved to be beneficial. Our study is not a randomized trial but is comparable to the results of studies concerning the various methods of treatment of Pancoast tumors.

Paulson[3] combined 30 Gy of preoperative radiation with block resection of the chest wall (completed for 67% of patients), and obtained a five-year survival rate of 34.7%, and a 10-year rate of 29%. However, when hilar or mediastinal nodes were involved, none of the patients survived three years.

Hilaris[4] reported that six of 38 patients (16%) survived five years or more after interstitial irradiation treatment for unresectable tumors. His emphasis was on a dose two or three times as high as the safe external irradiation dose level.

Komaki[7] recommended a wider field and higher dose irradiation of photons. Although there were fewer adenocarcinoma patients (8%) and more squamous cell carcinoma patients (38.8%) in her study than ours, the five-year survival rate was 23% (36 patients) with a median dose of 58 Gy over six weeks. She also reported that the most important determinant of survival was local control. The median survival and five-year survival rates of patients with local control were 26.5 months and 45% compared with 6.5 months and 0% for those with local failure. Houtte et al.[12]suggested that a high dose, 50 Gy or more, of external radiation is not only an alternative to surgery, but may occasionally be curative. The five-year survival rate and median survival were 18% and 17 months. However, survival went up to 40% in the group of patients without bone erosion or scalene lymph node involvement. Ahmad et al.[13] reported that five year survival rate was directly related to the radiation dose: 4.5% for patients with doses less than 50 Gy, and 20.9% for those with doses of 50 to 60 Gy. The survival rate was also related to the size of the primary tumor (24.9% for T2 tumors compared with 7.9% for T3 tumors), presence of regional adenopathy (5.2% with adenopathy vs 30.2% for T2N0 and 11.6% T3N0), and extent of local spread (osseous and nerve root involvement).

Our five-year survival rate results were: 20% for all patients, 29.8% for T3, and 8.6% for T4. They were 27.5% for N0 and N1 patients, 22.5%

for N2, and 11.4% for N3. These are rather better than the results of the above studies, whereas most of our patients suffered from adenocarcinoma tumors.

We chose fast neutron therapy for following reasons: ① Pancoast tumors are located peripherally in the apex of the lungs, so it is possible to give high doses with little risk of lung complication. ② Neutron RBE is higher in slow-growing tumor, so Pancoast tumors, especially of adenocarcinoma, are more likely to respond well to fast neutron therapy. As the neutron RBE for the spinal cord was reported to be as high as 5.2[14], we encountered one case (3.1%) of radiation myelopathy. Several authors have reported that no major complications occured in patients treated with photon irradiation alone[6,7,12]. Special care must be taken to ensure that irradiating neutrons not to exceed the tolerance of the spinal cord.

CONCLUSIONS

1) Thirty-two patients with Pancoast tumors were treated by fast neutron radiotherapy.
2) Five patients survived over 60 months.
3) Local control was the most important factor for prolonged survival. The median survival was 21.1 months for patients with loal control compared with 10.4 months for those with local failure.
4) The relative five-year survival rate was 20% for all patients, 34% for stage III A, 15% for stage III B and 0% for stage IV.
5) Fast neutrons were more effective for adenocarcinoma than for squamous cell carcinoma.
6) Symptomatic relief was one important result of radiation therapy. This was achieved in 62.5% of the patients.
7) Radiation myelopathy developed in one patient, however, complications on the lung were relatively mild to moderate, despite the larger field and higher doses involved.

REFERENCES

1) Pancoast, H. K: Importance of careful roentgen ray investigations of apical chest tumors. *JAMA* **83**: 1407-1411, 1924.
2) Pancoast, H, K: Superior pulmonary sulcus tumor. *JAMA* **99**: 1391-1396, 1932.
3) Paulson, D. L.: Carcinomas in the superior pulmonary sulcus. *The J. of Thoracic and cardiovascular surgery* **70**: 1095-1130, 1975.
4) Hilaris, B. S., Luomanen, R. K., Beattie, E. J.: Integrated irradiation and surgery in the treatment of apical lung cancer. *Cancer* **27**: 1369-1373, 1971.
5) Attar, S., Miller, J. E., Satterfield, J. *et al*: Pancoast's tumor: irradiation or surgery? *The Annals of Thoracic Surgery* **28**: 578-586, 1979.
6) Devine, J. W., Mendenhall, W. M., Million, R. R. *et al.*: Carcinoma of the superior pulmonary sulcus treated with surgery and/or radiation thrapy. *Cancer* **57**: 941-943, 1986.
7) Komaki, R., Roh, J., Cox, J. *et al.*: Superior sulcus tumor: results of irradiation of 36 patients. *Cancer* **48**: 1563-1568, 1981.
8) Hilaris, B. S., Martini, N.: Interstitial brachytherapy in cancer of the lung, a 20 year experience. *Int. J. Radiat. Oncol. Biol. Phys.* **5**: 1951-1956, 1979.
9) Takagi, I.: Application of interstitial brachytherapy using afterloading technique for the intra thoracic deep sheated residual malignant tumors. *Nippon Kyobu Geka Gakkai Zasshi* **33**: 2095-2101, 1985.
10) Battermann, J. J., Breur, K., Hart, G. A. *et al.*: Observations on pulmonary metastasis in patients after single doses and multiple fractions of fast neutrons and cobalt-60 gamma rays. *Europ. J. Cancer* **17**: 539-548, 1981.
11) Griffin T. W., Wambersie, A., Laramore, G. *et al.*: High LET: heavy particle trials. *Int. J. Radiat. Oncol. Biol. Phys.* **14**: S 83-S 92, 1988.
12) Houtte, P. V., MacLennan. I., Poulter, C. *et al.*: External radiation in the management of superior sulcus tumor. *Cancer* **54**: 223-227, 1984.
13) Ahmad, K., Fayos, J. V., Kirsh, M. M. Apical lung carcinoma. Cancer **54**: 913-917, 1984.
14) Hornsey, S., Morris, C. C., Myers, R. *et al.*: Relative biological effectiveness for damage to the central nervous system by neutrons. *Int. J. Radiat. Oncol. Biol. Phys.* **7**: 185-189, 1981.

要旨：1975年から1988年迄に32例のパンコスト型肺尖部癌の速中性子線治療を行った．癌の浸潤範囲を含む比較的広い照射野に平均線量TDF 113を照射した．局所制御（44%）は生存率を良くする重要な因子であり，局所制御群の平均生存月数は21.1カ月で，非制御群の10.4カ月より優れていた．全体の5年生存率は20%であったが，III A期では34%（12例），III B期は15%（16例），IV期0%（4例）で，5例が5年以上生存した．疼痛の除去は大切な治療目的であり，62.5%に一時的又は完全な効果をみた．放射線脊髄炎は1例の長期生存例に発生したが，肺野の放射線障害は一般的に軽度から中等度であった．

Int. J. Radiation Oncology Biol. Phys., Vol. 19, pp. 1011–1019
Printed in the U.S.A.

0360-3016/90 $3.00 + .00

Brief Communication

HISTOLOGICAL AND IMMUNOHISTOCHEMICAL PREDICTION FOR LOCAL CONTROL OF CERVICAL SQUAMOUS CELL CARCINOMA TREATED WITH RADIOTHERAPY ALONE

TAKASHI NAKANO, M.D., KUNIYUKI OKA, M.D. AND TATSUO ARAI, M.D.

Division of Hospital, National Institute of Radiological Sciences, 4-9-1 Anagawa, Chiba 260, Japan

Predictability of local control following radiotherapy was evaluated with morphological methods such as histology and immunohistochemistry for 36 cervical squamous cell carcinomas. All these patients showed viable cancer cell predominance on the specimens excised with drill biopsy after radiation therapy. These specimens were stained with routine haematoxylin and eosin staining as well as with antibodies against epithelial membrane antigen (EMA), carcinoembryonic antigen, and S-100 protein. Five histological features, the number of the cancer nests per 22.5mm^2 section, stromal reaction, space formation in the cancer nests, foamy cell or foreign body giant cell (FBG) clusters, and epithelial membrane antigen reactivity on the specimens excised after radiation therapy, were significantly related to the local control probability. Namely, less than 20 cancer nests, granulomatous stroma, presence of the space formation, absence of the foamy cell or foreign body giant cell clusters, and epithelial membrane antigen negativity were favorable for local control of the cervical cancer with radiation therapy. These data suggested that radiation sensitivity of cancer and stromal reaction for drainage of the degenerated cancer debris were important for local control of the tumors.

Cervical cancer, Drill biopsy, Prediction for local control, Histological and immunohistochemical studies, Epithelial membrane antigen.

INTRODUCTION

Many histological investigations have been made to predict a prognosis following radiotherapy for the patients with cervical cancer (2, 6, 13, 15, 19, 24, 27, 32). These were essentially based on the specimens excised before radiotherapy. Now, there are many controversial arguments on their prognostic values (9, 10, 20).

Few investigators have attempted to predict a local control probability by histological effects on the specimens excised after radiotherapy. Shimozato *et al.* (24) have described histological gradings for the effects of radiotherapy or chemotherapy on carcinomas based on H&E staining. However, the correlation between this histological grading and local control has not been clearly proven. Actually, we often experienced that cancers disappearing in the patients showed residual viable cancer cells on the specimens excised after radiotherapy. Thus, histological prediction for local control probability requires more reliable histological grading systems.

Carcinoembryonic antigen (CEA) is especially interesting for being a tumor-related antigen (7, 30). Epithelial membrane antigen (EMA) is regarded as an activation antigen of tumors (3). Infiltration of Langerhans cells, identified as S-100 protein positive dendritic cells, in tumor tissues has been reported to show some prognostic value (8, 16, 17, 29).

The present study attempted to evaluate the predictability of the local control using routine H&E as well as immunohistochemical staining for the residual squamous cell carcinoma on the cervical specimens excised with drill biopsy after radiotherapy (i.e. post-RT specimens).

METHODS AND MATERIALS

One hundred fifty patients with invasive squamous cell carcinomas of the cervix received a drill biopsy after radiotherapy from 1975 to 1986. They were treated with radiotherapy alone. In the majority of biopsies, no or few

Reprint requests to: Takashi Nakano, M.D.

Acknowledgment—The authors thank Dr. Ando, K. for his kind editing, Dr. Otsu, H., Dr. Morita, S. and Dr. Tsunemoto, H. for their appropriate advice, Mr. Oouchi, R. and Mrs. Suzuki, Y. for their excellent technical support, and Mrs. Sakurai, M. and Mrs. Fujita, H. for their secretarial assistance.

Accepted for publication 26 April 1990.

nests of cancer cells were found. This study, however, is concerned with those 36 patients with Stage II and III diseases whose post-RT specimens were diagnosed as being predominant for viable cancer cells. The patients' ages ranged from 32 to 79 years old (mean age, 58.8 years old). Eight patients had Stage II disease and 28 patients Stage III disease. Prognosis of all patients was traced for the period ranging from 2 to 13 years (mean 4.5 years). The patients who survived without evidence of local disease for over 2 years were defined as local control. According to this definition, 25 patients achieved local control and 11 patients developed recurrence.

Drill biopsy technique

Punch biopsy, which is commonly used for untreated tumors, is not useful for irradiated cervical cancer because viable cancer cells often remain about 1cm beneath the surface of the portio after radiotherapy. The drill biopsy technique* (23) has been applied to irradiated cervical cancer since 1975, and can obtain specimens 1.3 mm in diameter and 15mm–20mm in length from the cervix (Fig. 1). The drill biopsy technique was developed originally for a biopsy of mammary carcinomas and was applied to cervical cancer biopsy in our hospital. Patients were laid on the examination bed and the drill biopsy was performed after the direction of drill insertion was confirmed by probe through the cervical canal. The cotton sponge was packed into the vagina to stop bleeding. With this technique, two to three cervical tumor specimens were excised after radiation therapy (i.e., post-RT specimens) to reduce the sampling bias.

Histopathological examination

The pre-RT and post-RT specimens from 36 patients were fixed with formalin and embedded in paraffin. The specimens were stained with the following immunohistochemical methods (14, 28) using anti-EMA monoclonal antibody,† anti-CEA monoclonal antibody‡ (12). They were also stained with anti-S-100 protein polyclonal antibody‡ on the trypsin-treated sections (14). S-100 protein is one of the reliable markers for Langerhans cells infiltrating into tumors. All the pre-RT specimens were histologically classified according to the WHO classification (18) on H&E sections. The H&E sections of the post-RT specimens served to investigate the several histological features as follows: (a) the number of cancer nests per 22.5mm^2 section classified as fewer or more than 20, (b) the stromal reaction around the nests; granulomatous (Fig. 2a) or fibrous stroma (Fig. 2b), (c) the appearance of a free space around and/or within the cancer nests; positive (Fig. 2a) or negative (Fig. 2b), (d) the residual non-viable cancer cells as defined below in cancer nests; positive or negative (less than 10% of all), (e) the presence of the keratinoid substances or calcification (Fig. 3a) or cholesterol crystals (Fig. 3b); positive or negative, (f) the presence of foamy cell or foreign body giant cell clusters (FBG) (Fig. 3b); positive or negative.

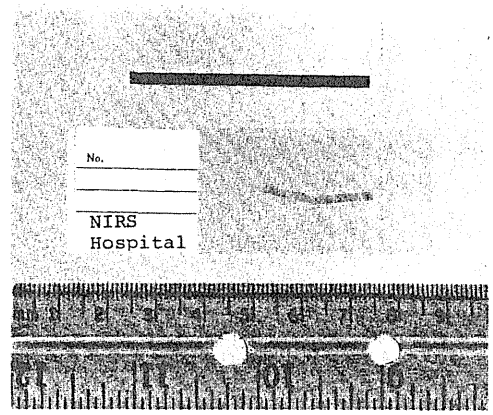

Fig. 1. A cylindrical edge of the drill (top) and H&E section excised with drill biopsy (bottom).

Assessment of cancer morphology

We employed here the classification and criteria proposed by Shimozato *et al.* (24) to assess morphological change of the tumor cells caused by radiotherapy. Nonviable cancer cells were defined as those showing either pyknosis (Fig. 4a), karyorrhexis (Fig. 4b), karyolysis (Fig. 4c), or bizarre shape (Fig. 4d) of the nuclei and excessive swelling of cytoplasms (5, 21, 22). Cancer cells which showed either slight swelling of the nuclei and cytoplasms, vacuole formation in tumor cells, multilobulated nuclei, or giant cell formation were regarded as the viable cancer cells. The 36 patients were diagnosed as having viable cancer cell predominance on Post-RT specimens. The viable cancer cell predominance means that cancer nest structures are moderately destroyed and the viable cancer cells consist of more than one-fourth of all cancer cells within nests.

Radiation therapy

Radiotherapy protocol is shown in Table 1. All patients were treated with a combination of high dose-rate intracavitary irradiation and external irradiation. The intracavitary irradiation was performed§ four to five times during the period of external irradiation (1). The patients with Stage II were treated with a combination of external irradiation (central shielding pelvis fields to deliver 50 Gy

* Using Biostar, Nipro Medical Ind. Ltd., Japan.
† Dakopatts, Denmark.
‡ BioGenex Lab, CA.
§ With RALSTRON, Simazu Co., Japan.

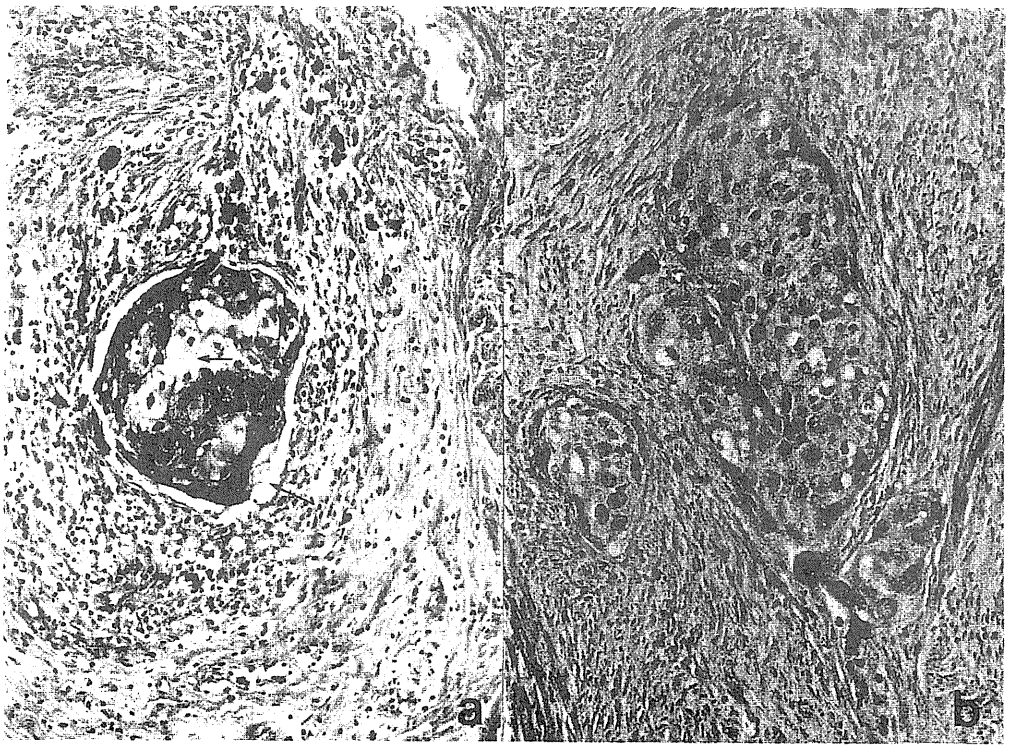

Fig. 2. The specimens excised with drill biopsy after radiotherapy. ×165. H&E. (a) shows the granulomatous stroma and the space formation in or around cancer nests (arrows). (b) shows the fibrous stroma and no space formation in cancer nests.

to the external iliac lymph nodes) and five intracavitary insertions for a total of 29 Gy at Point A. The patients with Stage II with large tumors and Stage III diseases were treated with a combination of external irradiation (20 to 30 Gy whole pelvis and additional parametrial dose to deliver 50 Gy to the external iliac nodes) and four intracavitary insertions for 23 Gy at Point A. The patients with Stage III with large tumor were treated with increase in external dose and decrease in intracavitary dose as shown in Table 1. External irradiation was performed with 10 MeV X ray, giving fraction dose of 1.8 Gy to 2 Gy daily, five fractions per week.

Distances between the portion of the specimens excised with drill biopsy and tandem sources were approximately 1cm. Then, the cervical specimens were exposed to a dose range from 100 Gy to 120 Gy by combination of the external and intracavitary irradiation, though accurate doses of the specimens could not be calculated because of a rapid decrease in dose near intracavitary sources.

Statistical analysis

Chi-square test was utilized for the following analysis: a) the correlation between histological or immunohistochemical features and local control probability, and b) the correlation among the features. The rank of the features for local control probability was analyzed by multiple regression analysis. The standard partial regression coefficients (i.e., SPRC in Tables 2 and 3) of each feature were calculated and compared for estimating the rank.

RESULTS

Since the 36 patients were selected for having residual cancer in the cervical specimens after radiotherapy, local control was not associated significantly with clinical stage, histological subtype, and tumor volume (Table 2).

The results of histological findings on the post-RT specimens are summarized in Table 3. The local control group showed a significant increase in space formation ($p < 0.001$) and a smaller number of cancer nests ($p < 0.025$) compared with the recurrent group. As to the stromal reaction, granulomatous reaction was significantly frequent ($p < 0.025$) for the control group than the recurrent group. Contrary to expectations, the clusters of the foamy cell or FBG (Fig. 3b) and the proportion of non-viable cancer cells remaining in the cancer nests ap-

Fig. 3. The specimens excised with drill biopsy after radiotherapy. ×165. H&E. (a) shows keratinoid (arrow head) and calcification (arrow). (b) shows cholesterol crystals (arrow), foreign body giant cells, and keratinoid substance.

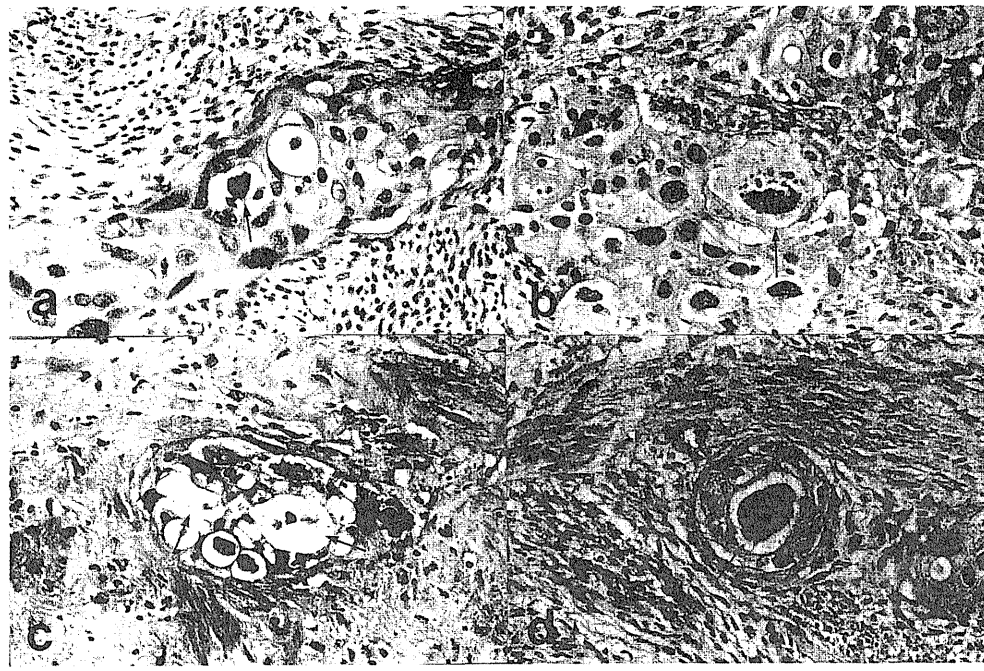

Fig. 4. Non-viable cancer cells among viable cancer cells, showing pyknosis (a, arrow), karyorrhexis (b, arrow), karyolysis (c, arrow), and bizarre shape (d, arrow). ×230. H&E.

Table 1. Treatment policy of combined radiotherapy with external and intracavitary irradiation for cervical carcinoma

Stages	Tumor diameter	External irradiation WP (Gy)	CS (Gy)	Total (Gy)	Intracavitary irradiation Point A dose (Gy/Fraction)
I		—	45	45	29/5
II	<5 cm	—	50	50	29/5
	>5 cm	20	30	50	23/4
III	<5 cm	20–30	30–20	50	23/4
	>5 cm	30–40	25–15	50–55	15–20/3–4
IV		40–50	0–15	50–60	15–20/3–4

Note: External irradiation is performed five fractions weekly, giving fraction doses of 1.8 Gy for whole pelvis irradiation and 2.0 Gy for central shielding pelvic field.
WP = Whole pelvis field; CS = Central shielding field.

peared more frequently in the recurrent group compared with the local control group (p = 0.04 and 0.09, respectively). Also, the foreign body substances such as keratinoid, calcification (Fig. 3a), or cholesterol crystals (Fig. 3b) appeared more frequently in the recurrent group compared with the local control group.

The results of immunohistochemical staining on the pre- and post-RT specimens are summarized in Table 4. EMA was detected in the cytoplasms and on the surface membranes of the cancer cells (Fig. 5a) irrespective of the cancer cell viability. The specimens in which more than 90% of the cancer cells failed to show any EMA were defined as EMA negative (Fig. 5b). On the post-RT specimens the local control group showed significantly lower EMA positivity compared with the recurrent group ($p < 0.02$). Of 14 patients showing EMA negativity on the post-RT specimens, 13 patients achieved local control. Of 11 patients with recurrence, only one showed EMA negativity on the post-RT specimens.

CEA was also observed both in the cytoplasms and on the surface membranes of the cancer cells, irrespective of the cancer cell viability. Both local control and recurrent groups showed almost similar CEA positivity both on the pre-RT and post-RT specimens (Table 3). The CEA positivity in both groups did not decrease at all after radiation therapy.

S-100 protein was observed both in cytoplasms and nuclei of dendritic cells, the equivalent of Langerhans cells, in cancer nests. The local control group showed rather frequent Langerhans cell infiltration on both the pre- and post-RT specimens compared with the recurrent group (Table 3). However, a significant difference was not demonstrated between the two groups.

From our data described above, the local control group showed the following five histological findings on the Post-RT specimens, which were defined as favorable for local control: EMA negativity of cancer cells, fewer than 20 cancer nests per 22.5mm^2 section, the granulomatous stroma, the space formation in the cancer nests, and absence of foamy cell or FBG clusters. In reverse, the following five findings were defined as unfavorable for local control: EMA positivity of cancer cells, more than 20 cancer nests per 22.5mm^2 section, the fibrous stroma, no space formation in the cancer nests, and the foamy cell or FBG clusters. All 14 patients showing the four or five favorable findings achieved local control. Conversely, all seven patients showing the four or five unfavorable findings died of recurrence.

The standard partial regression coefficients are shown in Tables 3 and 4. They show the rank of features for local control probability: a) the space formation in cancer nests, b) the EMA reactivity of cancer cells, c) the stromal reaction, d) the number of the cancer nests, and e) the foamy cells or FBG clusters.

The correlations among the three histological features are summarized in Table 5. The stromal reaction, the number of the cancer nests, and the space formation were significantly associated with each other. That is, the granulomatous stroma tended to be accompanied by fewer cancer nests per field and the formation of a free space in or around them. In reverse, the fibrous stroma was more

Table 2. Correlation between local control and Stage, histologic subtype, or tumor volume for 36 patients with cervical cancer

	Local control	Recurrence
Stage		
II	4	4
III	21	7
Histology		
Keratinizing	1	1
Non-ker. small	0	0
Non-ker. large	24	10
Tumor diameter		
3–4 cm	3	3
4–6 cm	14	5
6 cm <	8	3
Total	25	11

Non-ker. small = Small cell, non-keratinizing type; Non-ker. large = Large cell, non-keratinizing type.

Table 3. Histological findings of cervical drill biopsy specimens excised after radiation therapy

	Local control (n = 25)	Recurrence (n = 11)	p	SPRC
No. of Ca nests				
20>	15	2	<0.025	0.035
20<	10	9		
Stromal reaction				
Granulomatous	19	4	<0.025	0.052
Fibrous	6	7		
Space formation in Ca nests				
Positive	19	0	<0.001	0.179
Negative	6	11		
Non-viable Ca cells in Ca nests				
Positive	13	9	0.09	—
Negative	12	2		
Foreign body residue				
Positive	8	6	NS	—
Negative	17	5		
Foamy cells and FBG clusters				
Positive	2	4	<0.04	0.012
Negative	23	7		

SPRC = Standard partial regression coefficient; FBG = foreign body giant cells; NS = No significant difference; Ca = Cancer.
* p-value between local control and recurrent groups in each findings.

likely to be accompanied by many cancer nests per field and no space formation. However, EMA reaction was independent of the other three features.

DISCUSSION

The present study demonstrated that five histological features on the Post-RT specimens, EMA reactivity of cancer cells, the number of the cancer nests per 22.5mm^2 section, the stromal reaction, the space formation in cancer nests, and the foamy cell or FBG clusters, were significantly related to the local control probability. Specifically, EMA negativity, less than 20 cancer nests per 22.5mm^2 section, the granulomatous stroma, presence of the space formation, and absence of the foamy cell or FBG clusters were favorable for local control following radiation therapy.

EMA has been recognized as one of the markers characteristic of epithelial cells (11, 25), and most of the carcinoma cells express EMA. Moreover, EMA is regarded as an activation antigen similar to Ki-1, HLA-DR, and interleukin-2 receptor antigen (3, 4, 26). The present study demonstrated that the local control group showed a significant decrease in EMA expression on the post-RT specimens compared with the recurrent group. In particular, EMA negativity of cancer cells on the post-RT spec-

Table 4. Immunohistochemical staining for EMA, CEA, and S-100 protein on the pre- and post-RT specimens

	No. of specimens							
	Pre-RT				Post-RT			
	Cont (n = 25)	Rec (n = 11)	p	SPRC	Cont (n = 25)	Rec (n = 11)	p	SPRC
EMA								
Positive	23	11	NS	—	12	10	P < 0.02	0.115
Negative	2	0			13	1		
CEA								
Positive	18	7	NS	—	18	8	NS	—
Negative	7	4			7	3		
S-100 protein								
Positive	17	5	NS	—	4	4	NS	—
Negative	8	6			21	7		

EMA = Epithelial membrane antigen; CEA = Carcinoembryonic antigen; Pre-RT = Before radiotherapy; Post-RT = After radiotherapy; Cont = Local control group; Rec = Recurrence group; p-val = p-value between local control and recurrent group. SPRC: standard partial regression coefficient; NS = No significant difference.

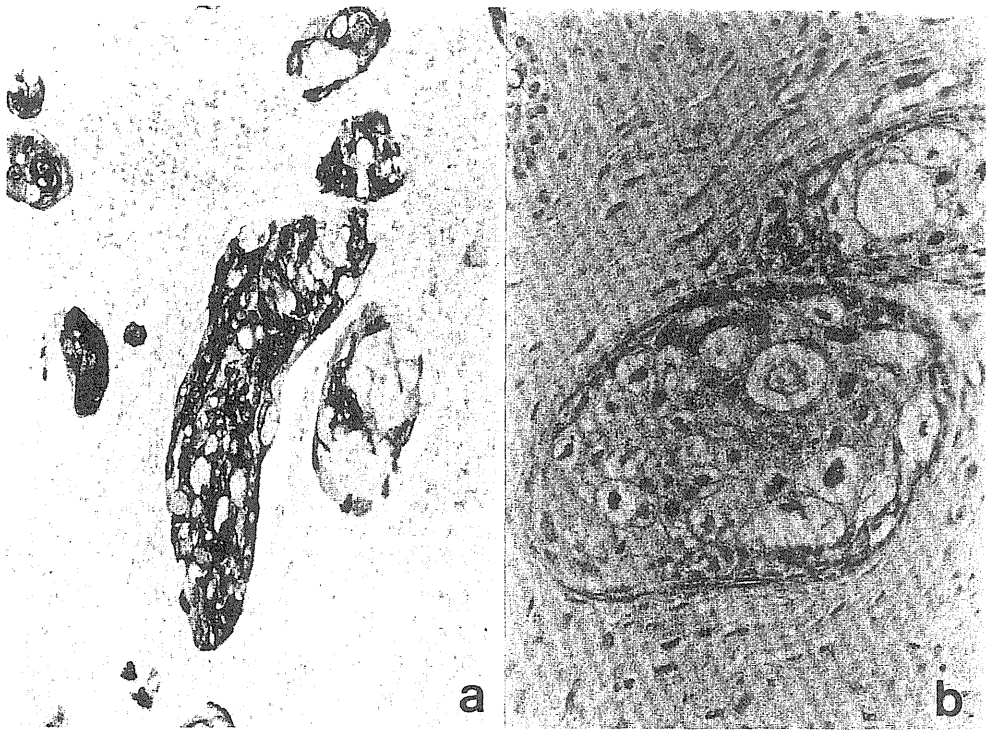

Fig. 5. Epithelial membrane antigen (EMA) staining of the specimen excised with drill biopsy after radiotherapy, showing EMA positivity (a, × 165) and EMA negativity (b, ×330). ABC method.

imens was associated with a high probability of local control. However, about half of the EMA positive patients were also locally controlled. It may be possible that EMA disappears late in the course of tumor degeneration, though the biological significance of EMA is unclear. Further investigations are required to develop monoclonal antibodies which can recognize the viability of cancer cells.

Seventy percent of the cervical carcinomas were positive for CEA in cancer cells in the present study. However, no correlation was observed between the CEA positivity on the Pre-RT specimens and the local control. Moreover, the present study also demonstrated that the CEA expression did not decrease at all by radiation therapy. Hence, we consider that CEA is not a useful marker for predicting proliferating ability of the cancer cells and the local control probability following radiotherapy.

Table 5. Correlation between three features predictable for local control

	No. of cancer nests		Space formation	
	<20	20<	+	–
Stromal reaction				
Granulomatous	14	9	16	7
Fibrous	3	10	3	10
p	<0.02		<0.02	
Space formation				
Positive	13	6		
Negative	4	13		
p	<0.02			

Langerhans cells are thought to play a important role in anti-tumor immune reactions and the Langerhans cell infiltration in cancer nests has been reported to relate to the prognosis in cervical cancer (16) and other cancers (8, 17, 29, 31). However, the present study failed to demonstrate a significant value for local control probability on the pre-RT specimens, although there was a much greater decrease of the Langerhans cell infiltration in local controls than in the recurrent patients.

The local control group showed a smaller number of cancer nests. This fact may indicate that these cancers are sensitive to radiation and the residual small amount of cancer cells will gradually disappear. The presence of granulomatous stroma appears to be favorable for draining the degenerated cancer debris as the granulomatous stroma is abundant in capillaries and lymphatic circulation. In reverse, the fibrous stroma appears to be unfavorable for the clearance by the lymph-vascular system. The space formation in or around cancer nests may be

caused by faster clearance of the degenerated cancer debris than the fibrotic repair by connective tissues. Conversely, the recurrent group may show delayed clearance of degenerated cancer by the fibrous stroma, as indicated by the presence of many remaining non-viable cancer cells and many clusters of foamy cell or FBG and no space formation. These findings suggest that the recurrent group may show coagulation necrosis more frequently than the local control group. Thus, we consider that radiation sensitive cancers show predominantly liquefacted necrosis and that the stroma with high activity for drainage of the degenerated cancer may be necessary for the local control of cervical squamous cell carcinomas.

It is suggested that the space formation in or around cancer nests was the product of clearance activity for cancer debris and liquefacted necrosis of cancer cells rather than fixation artifacts, as the space formation was associated with the granulomatous stroma and a fewer residual cancer nests (Table 5).

Since 1975, we have been using the drill biopsy technique to assess radiation effects in cervical cancer. This technique is carried out without major trouble except for acceptable pain and bleeding which can be easily managed. Hence, this technique might be used more widely to assess the therapeutic effects of radiation therapy or chemotherapy for cancers of various organs.

REFERENCES

1. Arai, T.; Morita, S.; Iinuma, T.; Masubuchi, K.; Tsuya, A.; Onai, Y.; Ito, Y.; Tazaki, E. Relationship between total iso-effect dose and number of fractions for the treatment of uterine cervical carcinoma by high dose-rate intracavitary irradiation. In: Bates, T. D., Berry, R. J., eds. High dose-rate afterloading in the treatment of cancer of the uterus. Br. J. Radiol. special report No. 17:89–92; 1978.
2. Beecham, J. B.; Halvorsen, T.; Kolbenstvedt, A. Histologic classification, lymph node metastases and patient survival in stage Ib cervical carcinoma. An analysis of 245 uniformly treated cases. Gynecol. Oncol. 6:95–105; 1978.
3. Delsol, G.; Alsaati, T.; Gatter, K. C.; Gerdes, J.; Schwarting, R.; Caveriviere, P.; Rigal-huguet, F.; Robert, A.; Stein, H.; Mason, D. Y. Coexpression of epithelial membrane antigen (EMA), Ki-1, and interleukin-2 receptor by anaplastic large cell lymphomas. Am. J. Pathol. 130:59–70; 1988.
4. Delsol, G.; Gatter, K. C.; Stein, H.; Erber, W. N.; Pulford, K. A. F.; Zinne, K.; Mason, D. Y. Human lymphoid cells express epithelial membrane antigen. Implications for the diagnosis of human neoplasms. Lancet 2:1124–1128; 1984.
5. Fajardo, L. F. Morphologic changes in irradiated tumors. In: Pathology of radiation injury. New York: Masson; 1982: 244–251.
6. Finck, F. M.; Denk, M. Cervical carcinoma. Relationship between histology and survival following radiation therapy. Obstet. Gynecol. 35:339–343; 1970.
7. Fray, R. E.; Husain, O. A. N.; To, A. C. W.; Watts, K. C.; Lader, S.; Rogers, G. T. The value of immunohistochemical markers in the diagnosis of cervical neoplasia. Br. J. Obstet. Gynecol. 91:1037–1041; 1984.
8. Furukawa, T.; Watanabe, S.; Kodama, T.; Sato, Y.; Shimosato, Y.; Suemasu, K. T-zone histiocytes in adenocarcinoma of the lung in relation to postoperative prognosis. Cancer 56:2651–2656; 1985.
9. Goellner, J. R. Carcinoma of the cervix. Clinicopathologic correlation of 196 cases. Am. J. Clin. Pathol. 66:775–785; 1976.
10. Gunderson, L. L.; Weems, W. S.; Hebertson, R. M.; Plenk, H. P. Correlation of histopathology with clinical results following radiation therapy for carcinoma of the cervix. Cancer 120:74–87; 1974.
11. Hilkens, J.; Buijs, F.; Hilgers, J.; Hageman, P.; Calafat, J.; Sonnenberg, A.; Van Der Valk, M. Monoclonal antibodies against human milkfat globule membranes detecting differentiation antigens of the mammary gland and its tumors. Int. J. Cancer 34:197–206; 1984.
12. Hsu, S. M.; Raine, L.; Fanger, H. Use of avidin-biotin-peroxidase complex (ABC) in immunoperoxidase techniques: A comparison between ABC and unlabeled antibody (PAP) procedures. J. Histochem. Cytochem. 29:577–580; 1981.
13. Hugh, R. K.; Facog, B.; Sommers, S. C.; Rotterdam, H.; Kwon, T. Vascular invastion as a prognostic factor in stage Ib cancer of the cervix. Obstet. Gynecol. 52:343–348; 1978.
14. Isaacson, P.; Wright, D. H.; Judd, M. A.; Mepham, B. L. Primary gastro intestinal lymphomas. A classification of 66 cases. Cancer 43:1805–1819; 1979.
15. Kato, H.; Morioka, H.; Aramaki, S.; Tamai, K.; Torigoe, T. Prognostic significance of the tumor antigen TA-4 in squamous cell carcinoma of the uterine cervix. Am. J. Obstet. Gynecol. 145:350–354; 1983.
16. Nakano, T.; Oka, K.; Arai, T.; Morita, S.; Tsunemoto, H. Prognostic significance of Langerhans's cell infiltration in radiation therapy for squamous cell carcinoma of the uterine cervix. Arch. Pathol. Lab. Med. 113:511–515; 1989.
17. Nomori, H.; Watanabe, S.; Nakajima, T.; Shimosato, Y.; Kameya, T. Histiocytes in nasopharyngeal carcinoma in relation to prognosis. Cancer 57:100–105; 1986.
18. Poulsen, H. E.; Taylor, C. W.; Sobin, L. H. Histological typing of female genital tract tumours. Geneva: WHO; 1955: 55–59.
19. Prenpree, T.; Patanaphan, V.; Sewchand, W.; Scott, R. M. The influence of patients' age and tumor grade on the prognosis of carcinoma of the cervix. Cancer 51:1764–1771; 1983.
20. Randall, M. E.; Constable, W. C.; Hahn, S. S.; Kim, J.; Mills, S. E. Results of the radiotherapeutic management of carcinoma of the cervix with emphasis on the influence of histologic classification. Cancer 62:48–53; 1988.
21. Robbins, S. L.; Angell, M. Basic pathology, 2nd edition. Philadelphia: WB Saunders; 1976:22–23.
22. Rubin, P.; Casarett, G. W. Radiation cytopathology in clinical radiation pathology, Vol 1. Philadelphia: WB Saunders; 1968:16–18.
23. Samejima, N.; Nakajima, S. New electric drill biopsy apparatus for breast tumors. Surgery 79:590–591; 1976.
24. Shimosato, Y.; Oboshi, S.; Baba, K. Histological evaluation of effects of radiotherapy and chemotherapy for carcinomas. Jap. J. Clin. Oncol. 1:19–35; 1971.
25. Sloane, J. P.; Ormerod, M. G. Distribution of epithelial membrane antigen in normal and neoplastic tissues and its value in diagnostic tumor pathology. Cancer 47:1786–1795; 1981.
26. Stein, H.; Mason, D. Y.; Gerdes, J.; O'Connor, N.; Wainscoat, J.; Pallesen, G.; Gatter, K.; Falini, B.; Delsol, G.;

Lemke, H.; Schwarting, R.; Lennert, K. The expression of the Hodgkin's disease associated antigen Ki-1 in reactive and neoplastic lymphoid tissue. Evidence that Reed-Sternberg cells and histiocytic malignancies are derived from activated lymphoid cells. Blood 66:848–858; 1985.
27. Swan, D. S.; Roddick, J. W. A clinical-pathological correlation of cell type classification for cervical cancer. Am. J. Obstet. Gynecol. 116:666–670; 1973.
28. Taylor, C. R. An immunohistological study of follicular lymphoma, reticulum cell sarcoma and Hodgkin's disease. Eur. J. Cancer 12:61–75; 1976.
29. Tsujitani, S.; Furukawa, T.; Tamada, R.; Okamura, T.; Yasumoto, Y.; Sugimachi, K. Langerhans cells and prognosis in patients with gastric carcinoma. Cancer 59:501–505; 1987.
30. VanNager, J. R.; Donaldson, E. S.; Gay, E. C.; Hudoson, S.; Goldenberg, D. M. Carcinoembryonic antigen in carcinoma of the uterine cervix. 2 Tissue localization and correlation with plasma antigen concentration. Cancer 44:944–948; 1979.
31. Watanabe, S.; Sato, Y.; Kodama, T.; Shimosato, Y. Immunohistochemical study with monoclonal antibodies on immune response in human lung cancer. Cancer Res. 43: 5883–5889; 1983.
32. Wentz, W. B.; Reagan, J. W. Survival in cervical cancer with respect to cell type. Cancer 12:384–388; 1959.

「粒 子 線 治 療」

5. 速中性子線治療の臨床評価

放射線医学総合研究所 病院部
宮本 忠昭、佐藤真一郎、坂下 邦雄、中野 隆史
久保田 進、向井 稔、森田 新六、恒元 博
放射線医学総合研究所 臨床研究部
中村 譲
放射線医学総合研究所 病院部
福久健二郎

1. はじめに

放医研の速中性子線（ＦＮ）治療は1975年11月に開始された。現在まで約15年間余りの間に各種のがん患者1800名余りがすでに治療された。治療成績は対象疾患毎に内外の学会で報告され論文にまとめられている。表１は、これらの成果を「評価」し、まとめた速中性子線治療の適応疾患をランクづけたものである[1]。唾液腺腫瘍、骨、軟部肉腫、前立腺癌、パンコースト腫瘍は良い適応とされる。悪性髄膜腫、頭頸部腫瘍、食道癌、子宮頸癌は対象を厳しく選べば治療成績の向上に役立たせることができる。しかし、多発性神膠腫、膵癌については未確定である。現在、放射線によるがん治療はほとんど高エネルギー光子線（以下Ｘ線と称する）で行われている。腫瘍のＴとＮが正確に記載されていれば病期別のＸ線治療による局所効果はほぼ一定している。放射線治療医はこの効果を熟知しているので新しい治療法が在来の治療法より優れているか否かを判断できることが多い。表１で「明らかに有利」と判定された疾患は基本的にこれによっている。ＦＮは欧米でトライアルが先行しており、唾液腺、頭頸部、前立腺、子宮頸癌はランダマイズ・トライアルが行われた。この結果、適応疾患については国際的合意が得られている[2]　ことも表１を作ることを容易にした。ＦＮはこれを生み出す装置の能力により線量分布やＲＢＥが異なる。放医研のサイクロ（30MeV d→Be）によりＦＮ治療も基本的には自前のデータでその抗腫瘍効果を判断しなければならない。放射線治療は局所治癒であるから、局所療法を評価することが最も大切である。局所再発のない転移が死因の症例は評価の対象から外すべきである。局所再発および放射線障害が死因になった場合にのみ生存率と治療が結びつく。放医研のＦＮによる治療の論文では近接効果については腫瘍計測あるいは病理組織的検討などにより比較的きちんと調べられている。しかし、効果の継続、言い換えれば再発に関しては充分な記載がなされていない。生存例でも照射後手術により剔出されてしまえば、照射の効果を評価することは難しい。死亡例でも再発なのか転移または他の原因なのか不明瞭な症例もかなりある。照射内容もＦＮ単独、mixed beam、boost 治療と三種ある。子宮頸癌以外はランダマイズのないトライアルであるからＦＮがＸ線よりすぐれているかどうかは局所制御に関する客観的データに頼る他はない。これを完備したデータは予想外に少ない。一方、同じことが障害、ことに晩期障害についてもいえる。この

〒260 千葉市穴川4－9－1

表1. 速中性子線30（d）+Be による治療適応

	RT−only	Preop. RT	Postop. RT
brain astrocytoma	—	—	○
meningioma	—	—	○
glioblastoma	—	—	—
head and neck	○	—	—
salivary gland	◎	—	◎
lung：adenocarcinoma	○	—	—
Pancoast tumor	◎	—	—
esophagus	○	○	○
pancreas	—	—	—
uierine cervix	○	—	—
prostate	◎		
urinary bladder	—	—	—
osteosarcoma	◎	◎	—
soft tissue sarcoma	○	◎	○
melanoma	○	◎	—

◎：速中性子線治療が明らかに有利。
○：線量分布が改善されれば高ＬＥＴ放射線治療の効果がさらに明確になる。
—：速中性子線の効果はまだ明らかでない。

場合は事は一層複雑である。放医研のＦＮの線量分布はコバルト並である。深部腫瘍に必要な線量を当てると表面線量は30〜40%高くなる。晩期皮膚障害を調べる前に表面線量を再調査する必要がある。どの位の線量が入ったか判らないのでは障害の評価は出来ない。他の臓器、組織も同じである。これらは速中性子線治療の問題の一部である。放医研では平成5年度より重粒子臨床トライアルが始まる。これらを充分検討して教訓にしたいと思っている。しかし、それではＦＮが余り効果がないのかと勘違いされては困る。表1で「明かに有利」とされている疾患は欧米ではランダマイズトライアルで実証しているのである。放医研のトライアルで見つけた肺パンコースト腫瘍[3]も世界で認めつつある。重粒子とは別途にきちんとしたデータ解析にもとづき必要なら新しくトライアルを組み、全ての治療医が納得できるデータを提供するつもりである。本報告はこのための序論と考えている。

2. 速中性子線治療の臨床評価の視点

ＦＮの線量分布はコバルト並なので深部病巣に必要線量を集中させることは容易でない。利点は高いＲＢＥと低いＯＥＲにある。高いＲＢＥは腫瘍のみならず照射野内の正常組織をも直撃する。治療における利益（Therapeutic Gain Factor：ＴＧＦ）は以下のバランスによって決まる。

$$TGF=\frac{\text{腫瘍のＲＢＥ}}{\text{障害決定臓器のＲＢＥ}}\cdot\frac{\text{種類、サイズ*}}{\text{部位、照射野}}$$

表2. ＦＮ単独症例（37）の解析

ＴＤＦ≧80

癌種	評価数	レスポンス CR	PR	NR	制御例 ≧2年（CR）	生存例 ≧5月
肺癌	9	7	1	1	5（7）	4（9）
前立腺	6	6	0	0	6（6）	3（6）
頭頸部	6	4	2	0	1（4）	1（5）
軟部肉腫	5	3	2	0	2（3）	0（5）
黒色腫	4		3	1	0	0（4）
皮膚癌	2	1	1	0	1（1）	1（2）
その他	5	3	2	0	2（3）	1（5）
	37	24	11	2	17（24）	10（37）
		ＣＲ率			制御率（CR）	5生率
		64％			70％	27％

〔X〕線量（D）・分割回数（F）・照射期間（T）

＊低酸素細胞の割合も含む。

線量分布が同じ場合決定臓器のＲＢＥより腫瘍のＲＢＥが高ければＴＧＦは高くなる。唾液腺癌、骨肉種、前立腺癌などはこの典型である。パンコースト肺癌なども比較的体表面に近くよい線量分布が得られるのでかなり大きな腫瘍まで制御できる。しかし、肺の深部にある腺癌は線量分布が悪いので図2に示すように4㎝以下のサイズに限られる。線量分布の悪い深部腫瘍については未検討でありリニヤックと同等の線量分布が達成されればまだ有効な適応がみつかる可能性が高い。欧米ではこのような視点にそって、回転式の速中性子照射装置が作成され、臨床トライアルが行われている。深部臓器の癌のなかに耳下腺、前立腺癌、骨肉種に匹敵するＦＮに有効な癌のある可能性は高い。これは回転式の装置や重粒子によって明かになるであろう。

3. 速中性子線単独照射による局所効果、局所制御率および局所治癒率の検討

放医研のコンピュータに登録されている1578名の速中性子治療患者を治療内容別に検討すると単独：11.7％、ブースト：10.5（167）％、mixed beam：35.9（567）％、外科との合併：40.6（640）％、腔内照射との併用：1.2（19）％となる。今回は先ず単独症例について次のような条件の下に患者を選び、抗腫瘍効果を検討した。①ＴＤＦ換算で80以上照射されている。②計測可能病変を有する。③完全寛解例では照射後手術による剔出がない。④照射後最低2年まで生存していて再発の有無を観察している。更に経過観察がなされていて、5年生存例でこの間に局所再発が認められない。

以上を完全に満足する症例は以外と少なく、全例でわずか37症例でＦＮ単独症例の約20％であった。その結果を表2に示した。疾患別にすると肺癌、前立腺、頭頸部、軟部肉腫、黒色腫、皮膚癌などでそれぞれ10名以下である。全症例のＣＲ率は64％であり内でも前立腺、肺癌のＣＲ率が高い傾向にあった。2年局所制御率をＣＲ例にかぎって評価すると70％であった。同様に前立腺、肺

癌、軟部肉種の制御率が高かった。局所治療癒率を明らかにするため60カ月以上にわたって経過観察しえた34例の局所再発を調査した。結果は図1に示すように44カ月まで再発が見られ62%でプラトーに達した。局所治癒率は38%となる。5生率は約27%なので当解析では10%が遠隔転移などで死亡していることになる。以上の解析から速中性子治療による局所治癒を判定するには少なくとも約4年間経過観察を必要とすることがわかる。局所制御率を記載するには必ず照射後の観察期間を明示することが必要となる。局所治癒に言及するには経時的な再発蓄積曲線を添えることが望ましい。どの時期に局所治癒が達せられたかは恐らく疾患別に異なってくるであろう。

肺癌の単独照射例は12名であり表3に示したように当評価の対象となった症例は9名であったが1例においては再発腫瘍を2回治療観察できたので評価可能10腫瘍となった。これらに対して、組織型、病期、線量、腫瘍サイズ、寛解率および制御期間を詳しく検討した。その結果は表3に示してある。この内、腫瘍制御期間と腫瘍サイズ、線量との関係をわかり易く図2に示した。速中性子線による治癒症例は腫瘍サイズが4cm以下の腺癌であり、線量は20 Gy又はTDFで140以下であった。腫瘍直径5cm以上の症例には治癒例はなく必ずしも線量依存傾向が見られなかった。しかし 4cm以下の腫瘍では依存性がみられ再発、再治療の症例の調査では同一腫瘍で同一制御期間を得るために2cmの腫瘍ではTDFで80でよいのに4cmの腫瘍では120以上必要となる。腫瘍体積が倍加するごとにTDFで40／8（4^3／2^3）＝5，X線で約3 Gy に相当する線量を増やすことを要することがわかった。肺癌では照射開始時の腫瘍サイズの大きさが高LET，高RBE放射線でも治癒可能性の限界の目印であることが明らかになった。

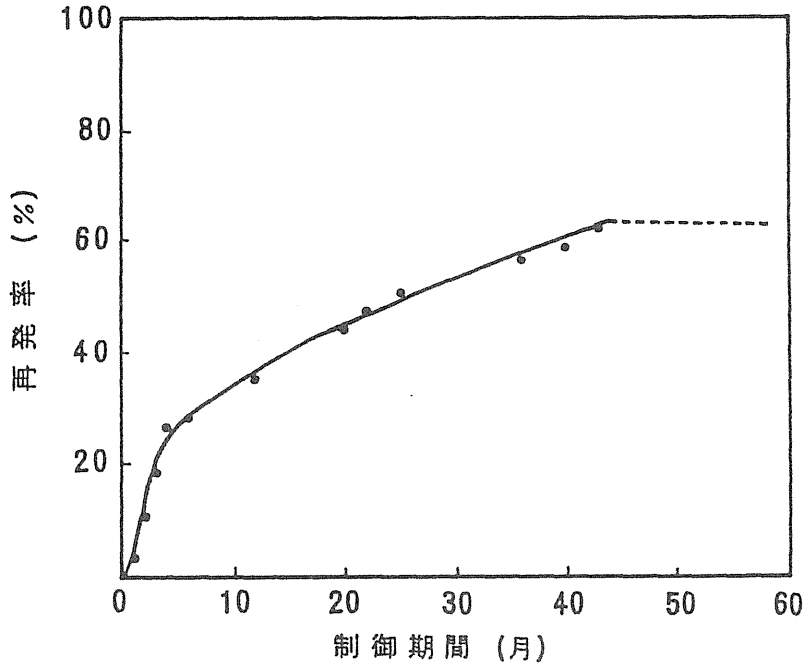

図1. FN単独照射による局所再発率と期間
（FN単独治療評価可能34例）

表 3.　ＦＮ単独肺癌治療（ＴＤＦ＞80）症例の腫瘍制御の解析

＊単独照射　12症例
　　評価可能症例　9　　評価可能腫瘍数　10
　　評価不能症例　3

番号	組織	病期	線量 cGy	線量 TDF	腫瘍サイズ φ cm	レスポンス	制御期間（年） 1 2 3 4 5
1	腺	Ⅰ	1782	107.8	15×15	CR	→
2	腺	Ⅰ	2145	138.6	13×12	CR	→
3	腺	Ⅱ	2200	133.1	30×30	CR	→
4	腺	ⅢA	2200	134.2	30×40	CR$\bar{cs}$	→
5a	腺	Ⅱ	1936	121.0	37×57	CR	⊣
b		再発	1320	80.3	30×30	CR	⊣
6	腺	ⅢA	2147	127.6	52×75	MR	⊣
7	扁平	Ⅱ	1402	80.3	40×40	CR$\bar{cs}$	⊣
8	扁平	ⅢA	1881	117.7	40×60	CR$\bar{cs}$	⊣
9	扁平	ⅢA	1900	121.0	＞60	PR	⊣

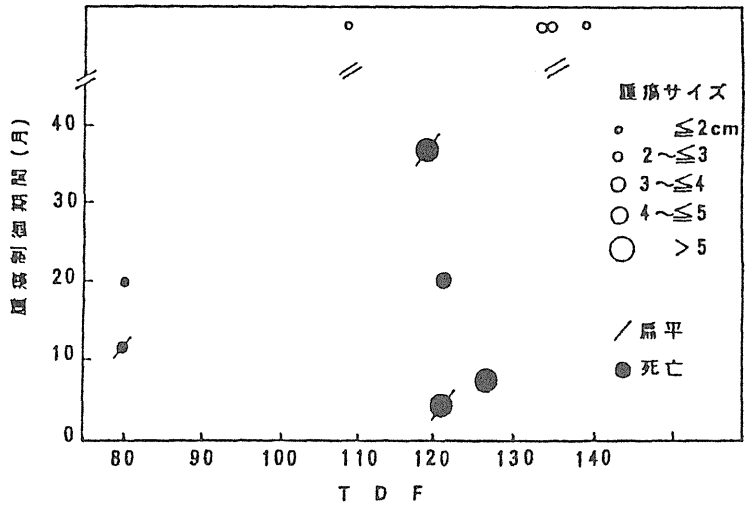

図 2.　腫瘍制御期間・腫瘍サイズ・線量

4. 術前照射例の組織学的検討による速中性子線と高エネルギー光子線の効果の比較

必ずしもランダマイズでないが速中性子線の単独効果を高エネルギー光子線と比較するために食道癌、膀胱癌の対照は照射量を共にTDFで60にしてある。結果は表4に示した。それぞれの研究の報告者と報告年代が記入されている[4,5,6]。食道癌は食道癌取扱い規約による組織分類、膀胱癌は

表4. FNによる組織学的効果

食道癌 （ ）内：%

	症例	Ef1	Ef2	Ef3
Co TDF 60	39	21 (53.9)	13 (33.3)	5 (12.8)
FN TDF 60 910 cGy×7回／14−17日	15	6 (40.0)	7 (46.7)	2 (13.3)

（石川 1983）

膀胱癌

	症例	GI	GIIa	GIIIb	GIII
Liniac TDF 60 300 cGy×5回／7日	26	7 (26.9)	8 (30.7)	11 (42.3)	1 (3.8)
FN TDF 60 910 cGy×7回／14−17日	20	3 (15.0)	6 (30.0)	10 (50.0)	1 (5.0)

（井坂 1990）

骨肉腫

		症例	I	II	III
Co or Liniac	＜ 99 Gy	9	4 (44.5)	3 (33.2)	2 (22.2)
	≧100 Gy	8	1 (12.5)	1 (12.5)	6 (75.0)
FN	＜17.90 Gy	15	2 (13.3)	5 (33.3)	8 (53.4)
	≧18.Gy	6	0	0	6 (100)

（高田 1984）

大星、下里分類、骨肉腫は千葉県がんセンターの分類による。詳細は別にしてそれぞれの分類のランクを縦に合せたが大差はないと思われる。食道癌、膀胱癌では両者の間に有意差は認められていない。骨肉腫では historical control を用いている。X線照射線量は 100 Gy を境にして分けている。極めて高線量で照射している。照射後、切断することを前提とし癌細胞の Total kill を目指している。FNは18 Gy を境に分けており、TDFで100に相当する。組織学的効果をⅢ以上（腫瘍細胞なし）でみるとFNでTDF80～100では53.4％と高エネルギーX線 100 Gy の75％より高いが100～120では全例がⅢ以上でX線よりすぐれている。ちなみにX線で100 Gy をTDFに換算すると166となる。FNでⅢ以上の効果を得る同等の線量をTDFで100とすると骨肉腫はX線に比べてFNに対し1.6（166／100）倍高い感受性を示すことがわかった。FNの皮膚の耐容線量は10×10 cmの照射野でTDF で100, RBE 3.0なので対向2門で照射すれば大腿骨骨端の骨肉腫のRBEは4.8（3.0×1.6）となりTGFは4.8／3.0＝1.6 倍以上となると概算される。食道癌、膀胱腫瘍で差が出なかったのは線量不足かあるいは腫瘍本来の固有感受性の相違か今後の検討が必要である。また、放射線による組織学的効果判定には大星－下里分類が使われることが多いが日本国内でも疾患によっては異なった分類法が用いられており、国際的にも認められていない。組織学的効果判定は腫瘍計測にも匹敵する近接効果判定法なので病理学者の協力を得て国際的にも通じる統一した判定基準をつくる努力をすべきである。

5. 放医研の無作為対照試験、子宮頸癌Ⅲ、Ⅳb期の膀胱、直腸および皮フ障害にもとづく速中性子線のRBEの検討。

放医研の子宮頸癌Ⅲ、Ⅳa 期に対するランダマイズクリニカルトライアルは1975年から1982年まで7年間に速中性子線例は64名、対照射は81名で計145例を対象に行われた。この結果は、すでに荒居等[7]によって詳しく報告されている。当論文では上記症例のうち1975年から1980年までの症例に絞って検討した。

ランダマイズのスケジュールは表5に示した。1975～1979年までは mixed deam のFNの量を80 cGyとしたが腸管の障害が対照群に比べて強いので10％減らして72 cGy としてトライアルを続けた。これが72 cGy と80 cGy群の意味である。この間の61例に対する転帰解析の結果を表

表5. 子宮頸癌（Ⅲ, Ⅳa）に対する mixed beam ランダマイズ例のスケジュール

		WP		A点 RALS
X-対照群	X	180 cGy×5回×5.5W	5,000 cGy	1000 cGy/2回/2W
	TDF	77.99		21.14　計 99.13
72 cGy 群	N	72 cGy × 2 × 5W	720	
	X	170 × 3 × 5	2,250	
	TDF	82.89		計 104.03
80 cGy 群	N	80 cGy × 2 × 5	800	
	X	170 × 3 × 5	2,250	
	TDF	88.73		計 109.87

$$*\ TDFn = 30.0 \times 10^{-3} \Sigma d^{1.1765} X^{-0.1294}$$
$$TDFx = \Sigma d^{1.5385} X^{-0.1693} / 10^{3}$$

(Y. NAKAMURA)

表 6. 転帰解析と局所制御率

（子宮頸癌 mixcd beam）

	症例数	制御	再・再転	転	障害	局所制御率 %		生存率 %
						粗	修正	
X対照群	17	12	3	1	1	70.5 (12／17)	80.0 (12／15)	70.5
72 cGy群	24	10	5	9		41.6 (10／24)	66.6 (10／15)	41.6
80 cGy群	20	10	5	4	1	50.0 (10／20)	66.5 (10／15)	50.0

（1975～1980）

修正：転移・障害を除く。

表 7. 子宮頸癌（Ⅲ, Ⅳa）に対する mixed beam によるランダマイズ症例の障害率の比較

（1975～1980）

	症例数	スコア記載率	5生率	評価	障害臓器組織					
					膀胱	直腸	S状結腸	小腸	皮下硬結	浮腫
X線照射	17	70 (12／17)%	70 (12／17)%	≧2 %	2 16.6	4 33.3	1 8.0	0	3 25.0	1 8.3
				≧3 %	0	3 25.0	0	0	0	0
72 cGy群	24	50 (12／24)%	42 (10／24)%	≧2 %	4 33.3	2 16.6	0	0	2 16.6	0
				≧3 %	16.6	1 8.3	0	0	1 8.3	0
80 cGy群	20	60 (12／20)%	50 (10／20)%	≧2 %	5 41.6	8 66.6	2 16.6	1 8.3	7 58.3	2 16.6
				≧3 %	2 16.6	5 41.6	0	0	6 50.0	0

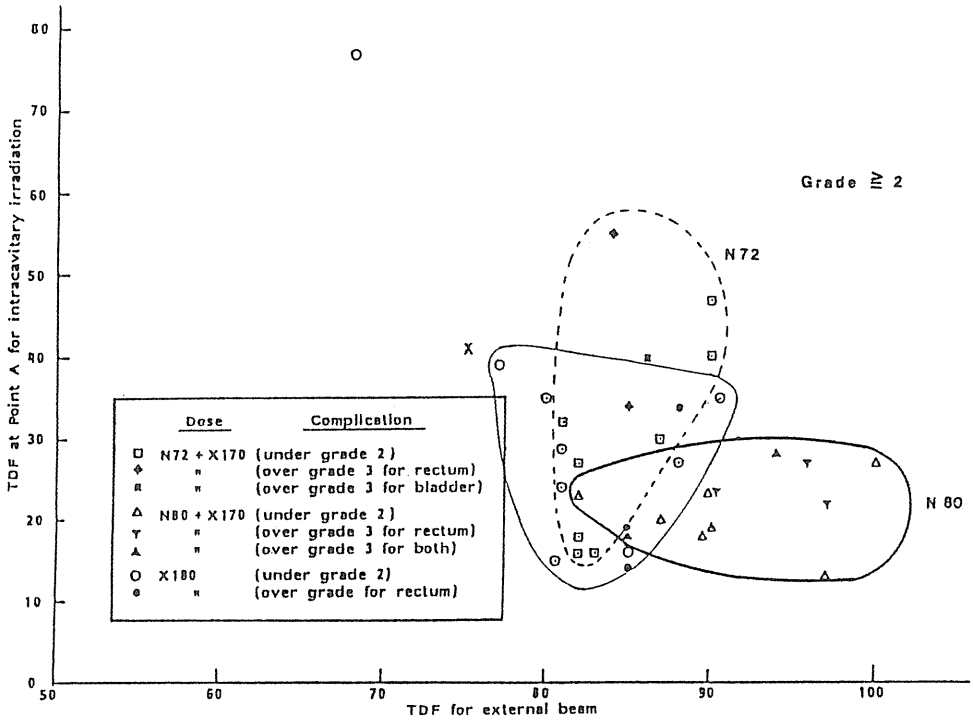
TDF at Point A for intracavitary irradiation
TDF for external beam
Grade ≧ 2
N72
X
N 80
Dose
Complication
N72 + X170 (under grade 2)
" (over grade 3 for rectum)
" (over grade 3 for bladder)
N80 + X170 (under grade 2)
" (over grade 3 for rectum)
" (over grade 3 for both)
X180 (under grade 2)
" (over grade for rectum)

図3

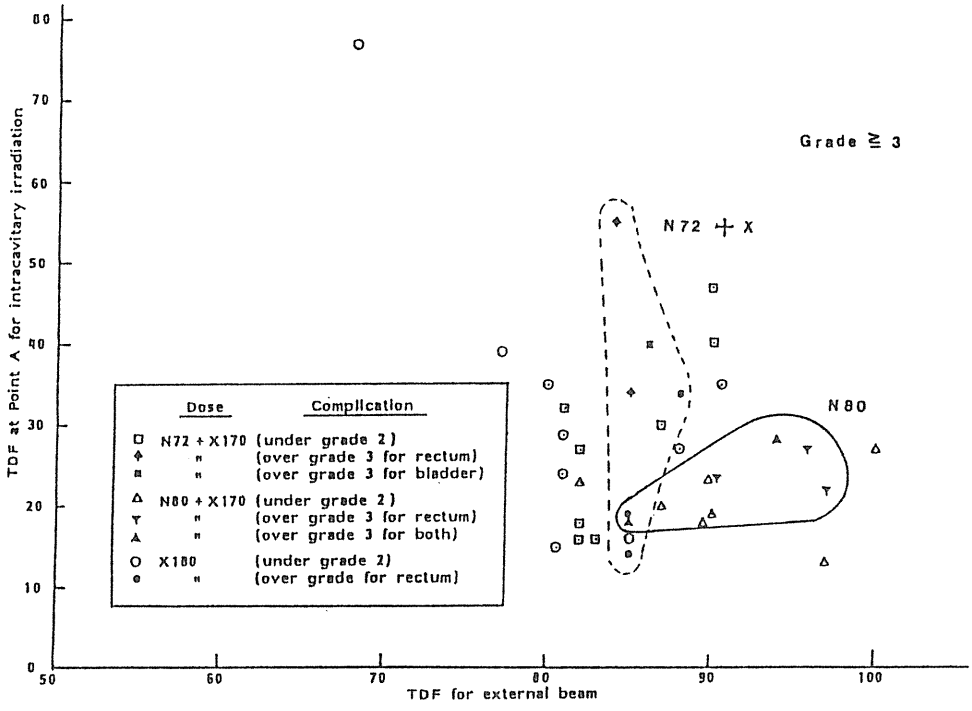
TDF at Point A for intracavitary irradiation
TDF for external beam
Grade ≧ 3
N72 + X
N80
Dose
Complication
N72 + X170 (under grade 2)
" (over grade 3 for rectum)
" (over grade 3 for bladder)
N80 + X170 (under grade 2)
" (over grade 3 for rectum)
" (over grade 3 for both)
X180 (under grade 2)
" (over grade for rectum)

図4

6に示す。

5生存率はX対照射群がかなり息好であるがこれは転帰解析によりFN群に転移死亡例がかたよって配分されたためと判ったのでこれを除いて局所制御率のみでみるとX線群80%に対してFN群66%づつと大差はない。この局所の差は全症例をまとめて評価した荒居等の論文に5生率にしてFN群の成積有意とはいえないが若干よくない結果で反映している。一方、これらの症例に対して放医研の障害判定スコア表にもとづいて照射野内の各臓器の障害のスコアを判定した。スコアは照射後5年以内の最大のスコアをリストした。その結果を表7に示した。スコア≧2と≧3に分けて評価した。X線対照群と72cGy 群の間では共に差はないが、80 cGyでは明らかに多くの障害が出現していることがわかる。この内、膀胱、直腸障害のみをピックアップし腔内照射と全骨盤外部照射とを分離し、全骨盤にのみmixされたFNの影響をよりわかり易く解析し図3、4に示した。縦軸はA点におけるTDE、横軸は外部照射のTDFである。障害のポイントが上にあるほど腔内照射の影響が強く、右横にあるほど外部照射の影響が強いことを示す。図3のようにスコア2以上をとるとX線対照群とFN 72 cGy 群はほぼ障害の分布が重なるが、FN80 cGy 群は明らかに分離してくる。更に図4でスコア3以上をとってみる。ここではX線対照群と72 cGy をまとめ80 cGy と比較してみた。この2群で外部照射量をみるとX＋72 cGy 群では84〜88 cGy に分布し平均は約85 cGy に対し80 cGy群は85 cGy から95 cGy に分布しその平均は約94 cGy 附近となる。

mixed beamにおけるX線の寄与は同じであるからX＋72 cGy群は80 cGy群より10%線量が少なくなっていることが障害の解析からも推定された。当初80 cGy を割りふったのは皮フの耐容線量より計算してRBEは3.26であり、X線に260 cGyに匹敵するとして mixed beamのスケジュールをつくりX線対照群と同等としたが途中で障害が多いため72 cGyに減らした。実際、今回の解析からも膀胱、直腸障害からはX線で約10%だけ余分照射したことになっていることが判ったのでこの処置は正しかったことが証明された。そこで、骨盤照射のモデルとして20cmの厚さのファントムに20×20cmの照射野でX線単独、72cGy，80 cGy

mixed beamの線量分布をモジュレックスを用いて描いてみると図5のようになった。分布はTDFで表示してある。これてみるとX線と72 cGy群の分布は全く同一であるが、80 cGy 群は膀胱、直腸に相当する部分がTDFで85〜90 cGyの分布内にあり、前者が80〜85 cGy群に分布しているから5〜10%の後者の方が多く照射されたことになる。モジュレックスによる線量分布計算は生物、医学的データを考慮してFNのTDFと値を定め物理実験データをもとに導いたものだが、今回ヒトにおける障害研究の解析からもその正しさが証明されることとなった。同時にFNの膀胱、直腸のRBEは皮フのRBEとほぼ同等であるか若干高いことが推定された。今後も高RBEや組織透過性の異なる新しい線源を用いて治療する場合、色々な生物、医学的、データをもとに物理計算を行い線量分布を求め、これを治計の指針とすることになろう。線量分布計算がヒトにおいて正しいか否かは検証を要する。当研究は諸臓器、組織の障害を臨床的に正しく観察しスコアをしておけばこれが可能であることを証明した。また、ヒト諸臓器のRBEも知ることが出来ることを示した。

考　察

放医研では速中性子線単独治療の線量配分を1560 cGy／12F／4Wを基本として臨床トライアルを開始した[8]。これはTDFで100に相当し、皮膚の耐容線量である。FNは加速器の性能により線量分布とLETを変える。放医研のサイクロから出されるFN（30 MeV d−Be）は、固有の線量分布とLETを有する。物理学者達の線量測定法の創意と工夫により脂肪、骨、肺など不均一な電子密度の物質を通過するときのエネルギーの減弱が明らかになり精度の高い線量分布がわかるようになった。一方、生物学者は培養細胞、動物

X対照群　　72 cGy 群

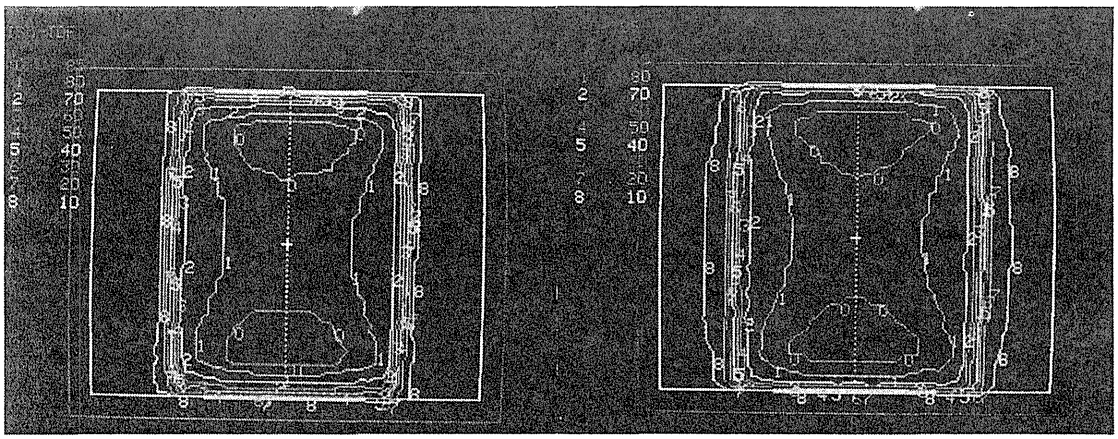

80 cGy 群

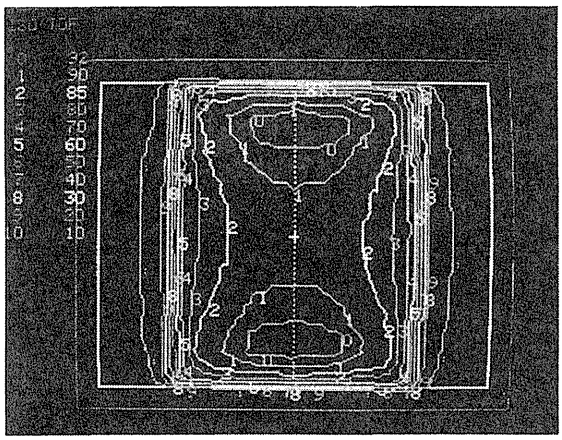

図5

腫瘍、動物の正常組織の反応などから1回照射と分割照射のＲＢＥとその関係を明らかにした。臨床ではこのような基本的知見にもとづき頭頸部腫瘍患者28名の皮膚反応によりＮＳＤを求め、当ＦＮのＴＤＦのαとβのべき乗数を定めた[9]。これによってＸ線とＦＮはＴＤＦを介して容易に翻訳が出来るようになった[10]。この結果、腫瘍の制御に必要な照射線量をＴＤＦによって示すようになった。Ｘ線による局所治療線量はＴとＮ因子が定まればほぼ明らかになっている。正常組織の障害も照射野のサイズが決れば耐容線量は定まる。ＦＮが耐容線量の限度内でどのようながんに有効かは、それぞれのがんに対するＦＮの単独治療の局所治癒率を明らかにできれば、 historical control を比べることで検討がつく。そのうち、FNがかなり有効と思われる小数例をランダマイズして有意差を出せばよい。これがうまく成功したのが唾液腺がんのトライアルである[11]。しかし、ＴＤＦが腫瘍の治療線量を決めるのに用いられるようになった一方で、ＦＮがコバルト並みの線量分布しかな

いという意識が薄れ、深部病巣に isocenter をとり必要線量を照射したため皮膚又は体表面に近い臓器の線量は20～40%も超過し重篤な障害に至った例も経験することとなった。当論文で検討した子宮頸癌の場合、mixed beam ですら直腸、膀胱障害は有意に上昇した。線量分布を求めてみればその原因は一目瞭然であった。また、放医研のＴＤＦのα、βの値は皮膚の急性障害にもとづいている。しかし、障害が問題となるのは子宮頸癌の場合と同様に晩期障害である。ＦＮは急性より晩期障害が強いといわれる。すなわち、ＦＮによる正常組織の障害の再評価は先ず症例ごとに線量分布を再現し、評価対象臓器の正しい照射線量を求めることである。第二は長期生存例などを対象に晩期障害の調査を行い、正しい線量ごとにスコアをつけることである。当論文で分析した頸癌に関する解析結果はその第一歩である。現在、体表面に近いがんに対するＦＮの適応の評価は実質的に終わったと考えられる。しかし、深部の腫瘍については悪い線量分布による障害に妨げられ充分な評価がされたとはいえない。今後、放医研の１800例の症例に対してこのようなアプローチで解析をすすめることによってその一端がおのずから明らかになるであろう。この結果、見当のついたがん種について小数例のランダマイズを行い、効果を客観的に明らかにすることによってＦＮを研究用のビームから医療用のビームに認めさせたいと考えている。

参考文献

1）森田新六：速中性子線治療　医学のあゆみ　**150**：1036－1039, 1989.

2）Gribfim, T. W., Wambersie, A., Laramore, G., *et al*：High LET：Heavy Particle Trials. *Int. J. Radiation Oncology Biol. Phys*. **14**：583－592, 1988.

3）沢田勤也、福間誠吾、関保雄　他：Pancoast型肺癌に対する速中性子線治療について、癌の臨床　**29**：111－114, 1983.

4）石川達雄：食道癌に対する速中性子線術前合併療法の効果－組織学的効果について－日本消化器外科学会　**16**：1738－1786, 1983.

5）井坂茂夫、五十嵐辰男、伊藤晴雄：進行膀胱腫瘍に対する術前照射の近接効果、日泌尿会誌　**74**：1778－1783, 1983.

6）高田典彦、保高英二、梅田透　他：放射線医学総合研究所編、特別研究「粒子加速器の医学利用に関する調査研究」最終報告書、pp. 37－45, 1984.

7）荒居竜雄、森田新六、中野隆史　他：子宮頸癌の速中性子線治療、産婦人科の実際　**35**：47－53, 1986.

8）恒元博：速中性子線治療の臨床評価、日医放　**42**：823－847, 1982.

9）恒元博、森田新六、佐方周防：多分割照射法(2)放射線治療効果の評価、癌の臨床　**33**：1579－1589, 1987.

10）中村譲：速中性子線治療における生物学的等価ＴＤＦによる治療計画法、日医放　**38**：950－960, 1978.

11）Griffin T. W., Pajak, T. F., Laramore, G. E., Neutron vs photon irradiation of inoperable salivary gland tumor：results of an RTOG－MRC cooperative randamized study. *Int. J. Radiation Oncology Biol. Phys*. **15**：1085－1090, 1988.

4．そ　の　他

平成２年度 第１回粒子線治療研究委員会
議 事 概 要

日　　時　　平成２年８月３日（金）　　１３：００～１７：００
場　　所　　科学技術庁分室第７会議室
出 席 者　　恒元委員長、梅垣、田崎、鎌田、稲田、辻井、増田、北川、森田（皓）、坂本、入江（五）、鈴木、井上、春日、山下（橋本代）、野口（入江實代）、平尾、舘野、森田（新）、宮本、大原、飯沼、近藤

説明者及びオブザーバー
設楽（東大脳外）、安藤、向井、中野、佐藤、高橋、遠藤、中村、河内、金井、野原、
管理部長、丑山、河合

配付資料

１．平成２年度研究計画
ａ．重粒子線治療のための物理・生物学的基礎研究
ｂ．重粒子線治療における核医学に関する基礎的研究
ｃ．重粒子線治療に関する臨床的研究
ｄ．重粒子線がん治療の総合的研究

２．重粒子線治療臨床試行
ａ．重粒子線治療における生物効果
ｂ．重粒子線治療システム
ｃ．重粒子線治療の方針

議事概要

１．平成２年度の研究計画に関する討議：

重粒子線治療を行う場合に、Peak 巾を拡大する ridge filter は不可欠である。理化学研究所の重粒子線ビームライン等を利用して ridge filter の製作に必要な生物・物理学的研究を重点的にすすめること、並びに速中性子線治療成績を詳細に分析することを基本とする研究計画を示し、討議が行われた。

さらに、平成３年度には国際ワークショップを開催して、重粒子線治療臨床トライアルに必要な前臨床的研究の方針と内容を討議する計画が紹介された。

２．重粒子線治療臨床試行に関する討議：

重粒子線治療を開始するに先立って、重粒子線治療効果比を予測して治療、照射スケジュールを定めて、精度の高い治療計画法を整備し、臨床試行の実行計画を具体的に立

案しなければならない。

重粒子線の治療効果比を予測する場合、先ず主たる治療ビームを定めること、重粒子線治療システムの精度に見合った治療技術を確立することが急務であることが指摘された。

重粒子線治療を行うに当たり、研究方針にしたがって患者を選択するばかりではなく、医療としての側面を十分に生かして試行を行うことも必要であるとの意見があった。

平成２年度 第２回粒子線治療研究委員会
議 事 概 要

日　　時　　平成３年３月１５日（金）　１３：３０～１６：３０
場　　所　　科学技術庁分館第８会議室
出 席 者　　恒元委員長、梅垣、入江、井上、稲田、鎌田、坂本、鈴木、橋本、増田、大原、平尾、森田、宮本各委員
（説明者及びオブザーバー）
河内、安藤、山崎、野原、富谷、向井、佐藤、坂下、
松平所長、戸張科学研究官
（事務局）
丑山、河合

配布資料

１．治療システムの整備について
２．粒子線治療研究委員会臨床部会の検討内容

議事概要

１．重粒子線治療システムに関する討議

理研の生物研究用ビームポートを利用して行われた研究成果と重粒子線治療システムに関して討議が行われた。

a.重粒子線治療用のリッジフィルターの作製がカーボンビームを利用して始まった。ＮＦＳａ繊維肉腫を用いた実験結果をもとにフィルターを作製したが、基本になる実験系とフィルターの製作方法につきさらに研究を重ねる必要がある。

b.重粒子線治療に関する前臨床的基礎研究の進め方についての討議の中で、先ず皮膚早期反応を定量的に評価することが重要であり、さらに分割照射の方法に関しては、基礎と臨床の両面から検討することが必要であることが強調された。

c.重粒子線治療照射系のシステムに関しては、臨床トライヤルと合わせて全体的なシステム構成の見直しが必要であるとの指摘に基づき討議が行われた。

２．速中性子線治療成績に関する討議

平成３年２月２２日の臨床部会において討議された速中性子線が有効な腫瘍の順序は以下のとおりである。

１）耳下腺癌、骨肉腫
２）肺腺癌、前立腺癌、軟部肉腫、悪性黒色腫
３）局所進行扁平上皮癌

臨床部会の報告をもとに討議が行われ、脊髄等中枢神経系は速中性子線に対して感受性が高く、治療技術を改善することが効果を確認するために重要な因子となることを強調した。

以上の論議を踏まえ、放医研としては適応疾患を厳しく選定し、プロトコールを定め速

中性子線による治療実績の向上を目標に、組織をあげて臨床トライアルを再度取組むので委員各位には一層の協力をお願いする旨の報告があった。

3．最後に松平所長より挨拶があり、粒子線治療研究委員会としてはこれが最後の会議であり、これまでの委員各位の絶大なるご支援・ご協力に関して謝辞が述べられ、また今後は中性子・陽子線治療については評価委員会を新しく設け、重粒子線治療に関しては重粒子線治療ネットワーク会議を中心に新体制のもとでのなお一層のご協力方についてお願いの言葉が述べられた。

平成2年度　第1回短寿命および陽電子RIの医学利用に関する研究委員会
議　事　概　要

日　　時　　平成3年3月14日（木）　13：30～16：30
場　　所　　科学技術庁5階　特別会議室
出 席 者　　委員長：舘野（放医研）
委員：安東（実中研）、佐々木（東京大学）、佐藤（千葉県衛生短大）、
寺尾（国立衛生試験所）、野崎（北里大学）、増田（千葉大学）、
町野（上智大学）、山崎（放医研）、吉川（メジフィジックス、葉杖代理）
オブザーバー：田中（浜松ホトニクス）、伊藤（日本医大）、西尾（下総療養所）、
伊豫（精神保健研究所）、鈴木、根本、入江、井上、須原（以上放医研）

資料配付

1．サルを用いた研究計画について
2．Ro15-1788 を用いた臨床研究計画について
3．Ro15-1788 を用いた臨床研究計画に用いる説明書、承諾書

議事概要

1．サルを用いた研究計画について
井上より資料に基づいて説明があった。質疑応答の後、研究計画は承認された。
2．Ro15-1788 を用いた臨床研究計画およびその説明書、承諾書について
須原より資料に基づいて研究計画、および説明書、承諾書について説明があった。
質疑応答の結果、承諾書原案の語句のうち
［副作用］を［危険性の有無］に変更した。
また説明書については［Ro15-1788 は有害な作用がなく、ヨーロッパでは医薬品として使用されている］［針を刺す際に、痛みを感じることがあります］という語句を追加することとした。
以上の手直しの後、研究計画および説明書、承諾書について承認された。
3．成果報告
以下の研究について成果報告が行われた。
1）躁うつ病のDIレセプターについて
2）変性疾患のDIレセプターについて
3）薬物依存について
4）ポジトロンカメラの物理について

特別研究「重粒子線によるがん治療法に関する調査研究」
平成２年度　班員名簿

（班　長）	恒　元　　博	病院部長
（副班長）	川　島　勝　弘	物理研究部長
	舘　野　之　男	臨床研究部長
	平　尾　泰　男	医用重粒子線研究部長
（顧　問）	梅　垣　洋一郎	特別研究員
	樫　田　義　彦	〃
	田　中　栄　一	〃
	福　田　信　男	〃

１．重粒子線治療のための物理・生物学的基礎調査研究

（１）重粒子線の線量評価および線量分布に関する研究

平　岡　　武	物理研究部第２研究室長
川　島　勝　弘	物理研究部長
星　野　一　雄	物理研究部第２研究室
福　村　明　史	〃　　〃
白　貝　彰　宏	〃　第３研究室
喜多尾　憲　助	〃　第４研究室
中　村　　譲	臨床研究部第２研究室
古　川　重　夫	〃　第４研究室
河　内　清　光	医用重粒子線研究部第３研究室長
遠　藤　真　広	〃　第３研究室
金　井　達　明	〃　第３研究室
中　野　隆　史	病院部医務課
佐　藤　眞一郎	〃　〃
坂　下　邦　雄	〃　〃

（２）重粒子線の初期課程および生物作用モデルに関する研究

丸　山　隆　司	物理研究部第３研究室長
星　野　一　雄	〃　第２研究室
山　口　　寛	〃　第３研究室
野　田　　豊	〃　〃
中　島　敏　行	〃　第４研究室長
大　原　　弘	障害基礎研究部第３研究室長
小　川　博　嗣	医用重粒子線研究部第１研究室長
佐　藤　幸　夫	〃　第１研究室
佐　藤　健　次	〃　第２研究室長
河　内　清　光	〃　第３研究室長
金　井　達　明	〃　第３研究室
隈　元　芳　一	技術部サイクロトロン管理課

根井　充	養成訓練部指導室

（３）重粒子線治療関連機器に関する研究

河内清光	医用重粒子線研究部第３研究室長
平尾泰男	医用重粒子線研究部長
小川博嗣	医用重粒子線研究部第１研究室長
山田孝信	〃　第１研究室
山田　聰	〃　〃
佐藤幸夫	〃　〃
佐藤健次	〃　第２研究室
金澤光隆	〃　〃
遠藤真広	〃　第３研究室
金井達明	〃　〃
河野俊之	〃　〃
平岡　武	物理研究部第２研究室長
福村明史	〃　第２研究室
野田　豊	〃　第３研究室
中村　譲	臨床研究部第２研究室
森田新六	病院部医務課長
久保田進	〃　医務課
中野隆史	〃　〃
坂下邦雄	〃　〃

（４）重粒子線に対する細胞感受性および障害回復に関する研究

大原　弘	障害基礎研究部第３研究室長
坪井篤	〃　第１研究室長
小島栄一	〃　第１研究室
笠井清美	〃　第３研究室
山口寛	物理研究部第３研究室
松本信二	薬理化学研究部第１研究室
青木芳朗	障害臨床研究部長
大山ハルミ	障害臨床研究部第２研究室
金井達明	医用重粒子線研究部第３研究室
根井　充	養成訓練部指導室

（５）治療効果比の早期判定法に関する実験的・臨床的研究

安藤興一	臨床研究部第４研究室長
福田寛	〃　第３研究室長
古川重夫	〃　第４研究室
小池幸子	〃　〃
古瀬　健	生理病理研究部第２研究室
大原　弘	障害基礎研究部第３研究室長
松本恒弥	技術部動植物管理課

松　下　　悟	技術部動植物管理課
上　島　久　正	養成訓練部指導室
宮　本　忠　昭	病院部医務課
向　井　　稔	〃　〃
久保田　　進	〃　〃
中　野　隆　史	〃　〃
佐　藤　眞一郎	〃　〃
岡　　邦　行	〃　検査課長

2．重粒子線治療における核医学に関する基礎的研究

（1）標識薬剤の開発に関する研究

山　崎　統四郎	臨床研究部第1研究室長
入　江　俊　幸	〃　第1研究室
井　上　　修	〃　〃
福　士　　清	〃　〃
福　田　　寛	〃　第3研究室長
安　藤　興　一	〃　第4研究室長
鈴　木　和　年	技術部サイクロトロン管理課

（2）高分解能ポジトロンＣＴに関する研究

野　原　功　全	物理研究部第1研究室長
富　谷　武　浩	〃　第1研究室
山　本　幹　男	〃　〃
村　山　秀　雄	〃　〃
山　崎　統四郎	臨床研究部第1研究室長
福　田　　寛	〃　第3研究室長
遠　藤　真　広	医用重粒子線研究部第3研究室

（3）ラジオアクティブビーム等の利用に関する調査研究

富　谷　武　浩	物理研究部第1研究室
野　原　功　全	〃　第1研究室長
山　本　幹　男	〃　第1研究室
村　山　秀　雄	〃　〃
山　田　　聰	医用重粒子線研究部第1研究室
佐　藤　幸　夫	〃　〃
金　井　達　明	〃　第3研究室

3．重粒子線治療に関する臨床的研究

（1）重粒子線治療の評価法に関する研究

森　田　新　六	病院部医務課長
恒　元　　博	病院部長
宮　本　忠　昭	病院部医務課
向　井　　稔	〃　〃
久保田　　進	〃　〃

中野隆史	病院部医務課
佐藤眞一郎	〃　〃
野本靖	〃　〃
坂下邦雄	〃　〃
熊谷和正	〃　〃
柴山晃一	〃　〃
千尾武彦	〃　〃
石居隆義	〃　〃
平岡武	物理研究部第２研究室長
星野一雄	〃　第２研究室
福村明史	〃　〃
舘野之男	臨床研究部長
飯沼武	臨床研究部第２研究室長
中村譲	〃　第２研究室
安藤興一	〃　第４研究室長
古川重夫	〃　第４研究室
青木芳朗	障害臨床研究部長
河内清光	医用重粒子線研究部第３研究室長
遠藤真広	〃　第３研究室
金井達明	〃　〃
福久健二郎	技術部技術課

（２）重粒子線治療システムの開発に関する研究

遠藤真広	医用重粒子線研究部第３研究室
河内清光	〃　第３研究室長
金井達明	〃　第３研究室
福村明史	物理研究部第２研究室
飯沼武	臨床研究部第２研究室長
中村譲	〃　第２研究室
福田寛	〃　第３研究室長
池平博夫	〃　第３研究室
古川重夫	〃　第４研究室
福久健二郎	技術部技術課
森田新六	病院部医務課
久保田進	〃　〃
佐藤眞一郎	〃　〃
坂下邦雄	〃　〃
熊谷和正	〃　〃
柴山晃一	〃　〃
千尾武彦	〃　〃
石居隆義	〃　〃

（３）ポジトロンＣＴ・ＭＲＩ等の臨床応用に関する研究

福田　寛	臨床研究部第３研究室長
舘野之男	臨床研究部長
山崎統四郎	臨床研究部第１研究室長
飯沼　武	〃　第２研究室長
池平博夫	〃　第３研究室
井上　修	〃　第４研究室
青木芳朗	障害臨床研究部長
遠藤真広	医用重粒子線研究部第３研究室
鈴木和年	技術部サイクロトロン管理課
中野隆史	病院部医務課
久保田進	〃　〃
佐藤眞一郎	〃　〃
坂下邦雄	〃　〃

４．重粒子線がん治療の総合的調査研究

（１）重粒子線がん治療研究の総合評価に関する調査研究

川島勝弘	物理研究部長
大原　弘	障害基礎研究部第３研究室長
舘野之男	臨床研究部長
山崎統四郎	臨床研究部第１研究室長
飯沼　武	〃　第２研究室長
中村　譲	〃　第２研究室
平尾泰男	医用重粒子線研究部長
恒元　博	病院部長
森田新六	病院部医務課

特別研究「重粒子線によるがん治療法に
関する調査研究」論文集　第２集
平成４年３月
千葉市穴川４－９－１
放射線医学総合研究所
Tel.0472-51-2111(代)